Copy No. 71
NCHRP 10-48

ASSESSING PAVEMENT LAYER CONDITION USING DEFLECTION DATA

APPENDICES

Prepared for
National Cooperative Highway Research Program
Transportation Research Board
National Research Council

Y. R. Kim, S. R. Ranjithan, J. D. Troxler, B. Xu
North Carolina State University

November 2000

ACKNOWLEDGMENT OF SPONSORSHIP

This work was sponsored by the American Association of State Highway and Transportation Officials, in cooperation with the Federal Highway Administration, and was conducted in the National Cooperative Highway Research Program, which is administered by the Transportation Research Board of the National Research Council.

TABLE OF CONTENTS

APPENDIX A

FINITE ELEMENT MODELING

INTRODUCTION

Consideration of non-linearity in unbound layers is necessary for accurate modeling of a flexible pavement structure. The necessity of non-linear consideration in rigid pavements has not been studied as closely. Many problems arise from the assumption of elastic layer properties for unbound layers. For example, granular layers may have a lower modulus than the subgrade, and measured vertical strain at the top of the subgrade may be twice the theoretical value. Nazarian and Stokoe (A-1) have shown that non-linear behavior occurs in FWD testing. An increase in the load magnitude of the FWD results in an increase in deflection that is greater than one to one. Nazarian, et. al. (A-2) also showed the effect of non-linearity with depth in a farm-to-market test road.

Several procedures have been developed to try to handle the non-linearity of unbound layers in pavement structures. Some analyses attempt to model the non-linearity by considering the plastic behavior of subgrade soils. Others approximate non-linear effects through iterative linear elastic procedures. Most recently, finite element code has been utilized in modeling the stress state dependency of granular base layers, and the strain level dependence of subgrade materials.

As stresses and strains are used more and more to determine the relative condition of layers in a pavement structure, the need for consideration of non-linear material behavior becomes increasingly important. Linear elastic approximations of unbound material behavior are no longer acceptable in pavement analysis. Errors from such approximations have been noted and documented. The stress state dependency of granular materials, and strain based subgrade soil models must be considered for an accurate estimation of true pavement response.

GENERAL FINITE ELEMENT (FEM) MODEL

ABAQUS, a commercial finite element modeling (FEM) program, has been widely applied for pavement analysis. Chen et al. (A-3) have made a comprehensive study of various FEM pavement analysis programs and showed that the results from ABAQUS program were comparable to those from other programs. Zaghloul et al.(A-4) simulated the pavement responses under FWD loading for flexible pavements using 3-dimensional dynamic analysis in ABAQUS. Uddin et al. (A-5) investigated the effects of pavement discontinuities on the surface deflections of rigid pavements for 3-dimensional dynamic analysis using ABAQUS. The main capabilities of ABAQUS in solving pavement engineering problems include:

- linear and nonlinear elastic, viscoelastic, elastio-plastic material modeling,
- 2-Dimensional and 3-Dimensional calculation,
- static, harmonic dynamic, and transient dynamic loading simulation,
- interface modeling with friction,
- cracking propagation modeling.
- thermal gradient analysis

ABAQUS provides many element models that are useful for pavement analysis. Infinite element model can be used to model the infinite boundary conditions in horizontal and vertical directions in pavement systems. Interface element model can be used to simulate the cracking or debonding within pavements. Lee (A-6) has investigated the effects of initial gap and friction coefficient of interface model on surface deflections, and concluded that an initial gap of 0.01 inch and a friction coefficient of 0.5 were suitable for cracked pavement analysis. ABAQUS also includes many material models, such as linear elastic model, viscoelastic model, hypoelastic

model, and Drucker-Prager plastic model. ABAQUS allows static and dynamic analysis capabilities.

LINEAR ELASTIC MODEL

In this research, the finite element models were designed particularly for FWD testing configuration. A typical FWD test is performed by dropping a 9000 pound load on the top of circular plate with a radius of 5.91 inches resting on the pavement surface. The loading duration is about 30 ms. The deflections at distances of 0, 8,12, 18, 24, 36, and 48 inches from the center of the load are measured.

Two-dimensional, axi-symmetric finite element structure was used to model pavements. The horizontal and vertical boundaries were modeled using infinite elements. No displacement in horizontal direction along the symmetry axis was allowed. An extra pavement layer was modeled at the bottom of subgrade. A large modulus value of 5000 ksi was assigned to this layer, which represents the stiff layer. If subgrade is infinite, the same modulus as that of subgrade was assigned to this layer. The FEM mesh was designed finer at the loading area where the larger stress and strain gradients occur. At locations farther from the load, the mesh was modeled to be coarser to reduce the number of elements and, therefore, the computation burden. Figure A-1 shows a typical finite element mesh configuration. Figure A-2 shows typical deflection vs. time history curves resulting from FWD loading. The peak deflections at the seven sensors did not occur at the same time. The time-lag between peak deflections comes from the nature of wave propagation and damping effect.

ABAQUS can be applied to simulate material discontinuities (cracking, stripping and debonding) in pavements. ABAQUS allows the user to define the modulus for each element. In

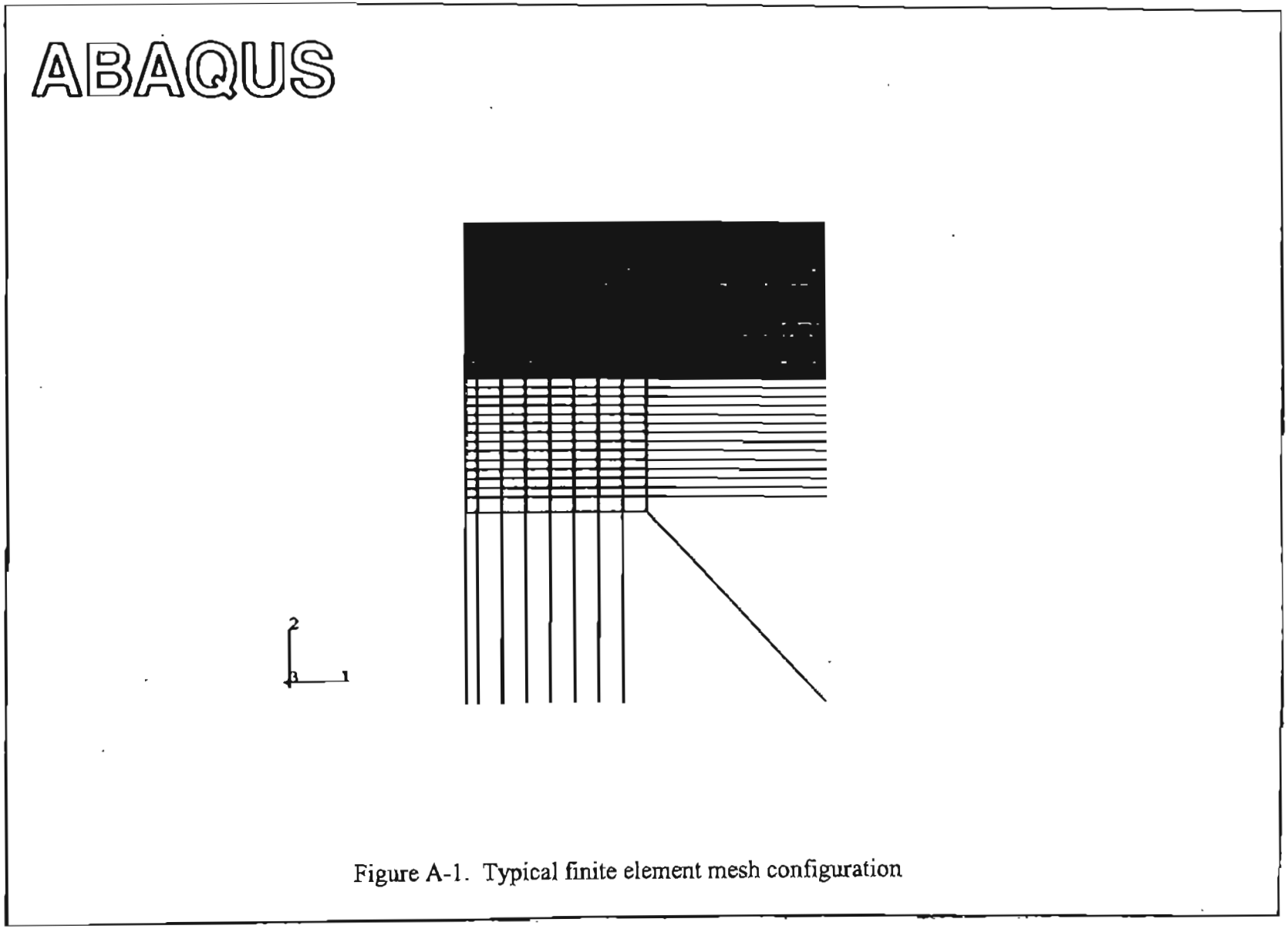

Figure A-1. Typical finite element mesh configuration

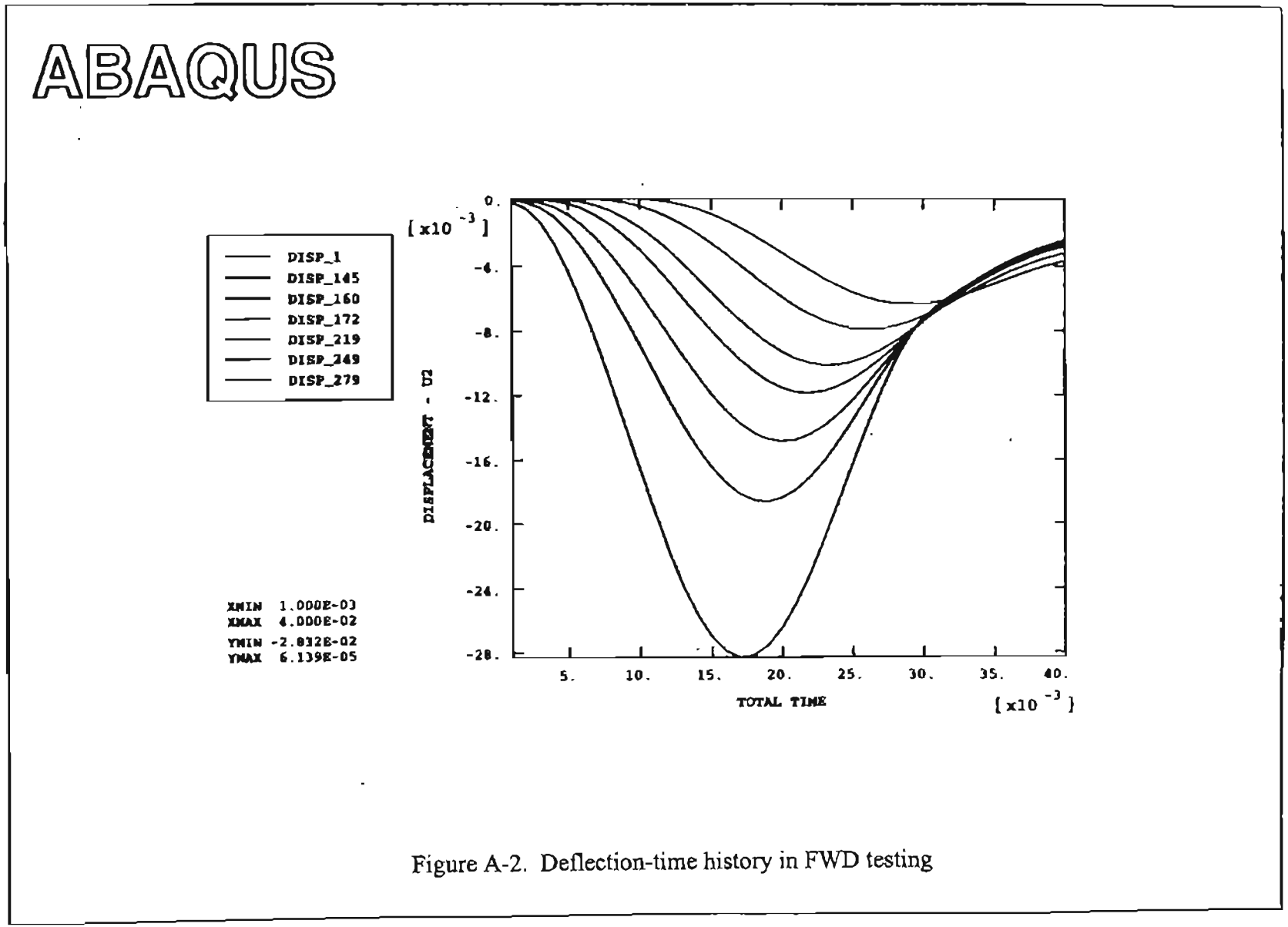

Figure A-2. Deflection-time history in FWD testing

this way stripping is simulated by assigning a low modulus value (70 ksi) to materials within the stripped area. ABAQUS provides the interface element for cracking and debonding discontinuity applications. A friction coefficient of 0.5 is used for both cracked and debonded pavements. An initial gap of 10 mils and 0.5 mils are used, for cracking and debonding, respectively. Figure A-3 shows the results. It can be seen that discontinuities cause larger deflections. The cracked pavements seemed to have a significant different deflection shape than the intact pavement, while the deflection shapes from stripped and debonded pavements are not unusual from the intact pavement.

NONLINEAR ELASTIC MODEL

KENLAYER was used to find stress and strain values of certain types of pavements at different positions throughout the depth of the pavement structure. These points were located directly under the load and at an eight inch offset. This analysis was completed for the full-depth, aggregate base, and rigid pavement cases. Extreme cases in full depth, aggregate base, and rigid pavements taken from the synthetic database were used as models for analysis in the KENLAYER pavement analysis program. In the full depth case, an infinite subgrade depth was assumed and weak and strong modulus values were assigned. The AC layer modulus remained constant while the layer thickness changed from thin to thick. The aggregate base and rigid pavements were more complicated as there were three layers to consider. In this case the subgrade and AC layer assumptions were the same as those in the full depth case, however, the base layer thickness was changed from thin to thick as well. Although a PCC (rigid) layer is present in the analysis, KENLAYER was chosen over KENSLABS because the error between the two models is negligible if loads are applied at the center of the slab. So, there were four

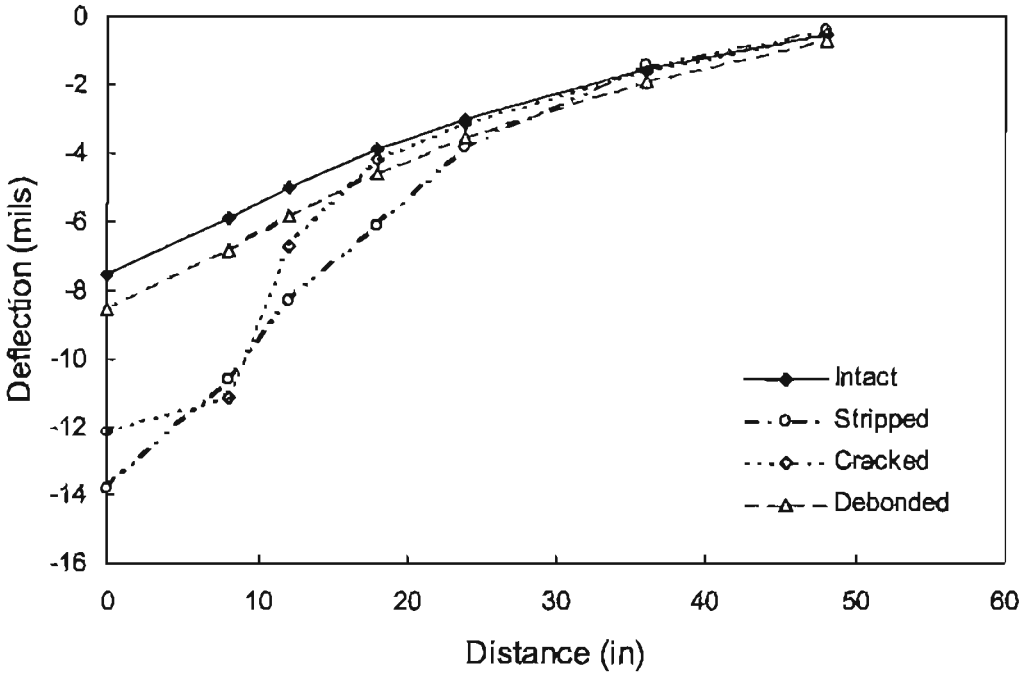

Figure A-3. Comparison of deflection basins from intact and distressed pavements

two-layer pavement cases considered, and eight three-layer cases. For each case, stress and strain information was gathered for the first 30 inches of subgrade depth, in 3 inch increments. Pavement thickness and moduli information are described in Table A-1.

FLEXIBLE PAVEMENTS

Compressive stress, compressive strain, bulk stress, and deviatoric stress were calculated for each flexible pavement case listed in Table A-1. Strain values found from this KENLAYER study were compared to values found in the work done by Shao and Borden (Figure A-4). The strain values fell in the nonlinear portion of the E/Emax curve, therefore nonlinear behavior needed to be added to the existing linear elastic forward model. Figures A-5 through A-12 show the stress and strain information generated for each flexible pavement case.

Once the need for nonlinear modeling was determined, the investigation on how to include nonlinearity of unbound layers into the existing ABAQUS finite element forward model began. Literature review showed that the Drucker-Prager Plasticity model had been used to represent nonlinear behavior in granular and cohesive soils. Comparison of an existing linear elastic aggregate base pavement structure with the same structure using the Drucker-Prager Plasticity model for base layer properties was performed. Five different sets of Drucker-Prager parameters were chosen based on results from triaxial testing of aggregate base materials at the Mn/ROAD test site. The results of this preliminary study indicated that the inclusion of the plastic model had a negligible effect on the deflections, and hence the strains, computed by the finite element forward model. One possible reason why there was no difference in output generated by the two models was because the aggregate base pavement layer thicknesses were so great that the strains were too low to show any nonlinear effects. For this reason, three of the

Table A-1. Kenlayer structures used in nonlinear analysis

Pavement Type	Asphalt Layer	Base Layer	Subgrade Layer
Full-Depth	H_{ac}=4, 18 in. E_{ac}=400 ksi ν=0.30	N/A	H_{sg}=infinite E_{sg}=5, 25 ksi ν=0.45
Aggregate Base	H_{ac}=4, 13 in. E_{ac}=400 ksi ν=0.30	H_{abc}=6, 18 in. E_{abc}=75 ksi ν=0.35	H_{sg}=infinite E_{sg}=5, 25 ksi ν=0.45
AC/PCC	H_{ac}=2, 6 in. E_{ac}=400 ksi ν=0.30	H_{pcc}=6 in. E_{pcc}=4,000 ksi ν=0.20	H_{sg}=infinite E_{sg}=5, 25 ksi ν=0.45

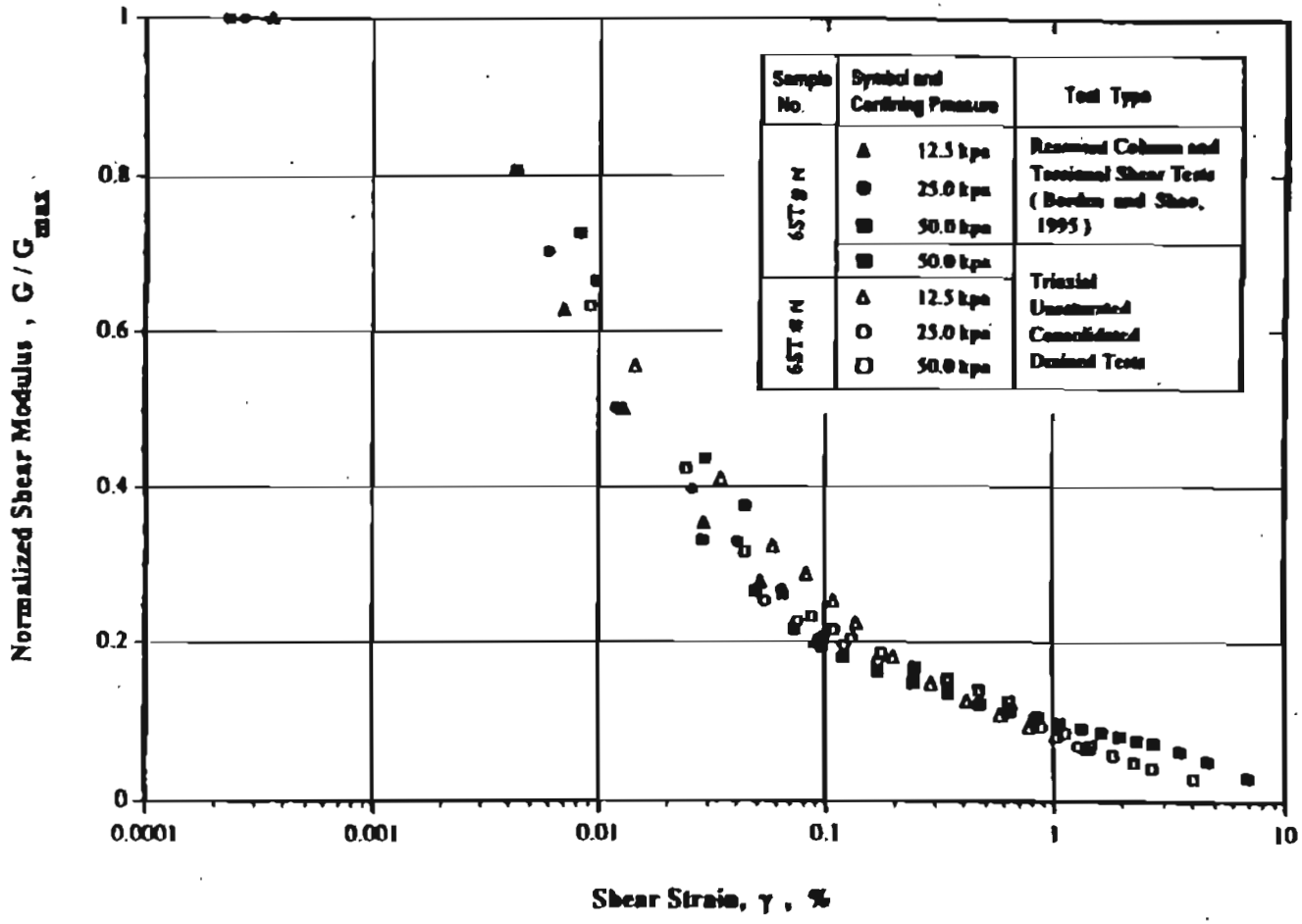

Figure A-4. Normalized shear modulus as a function of shear strain for samples obtained from Selma, NC

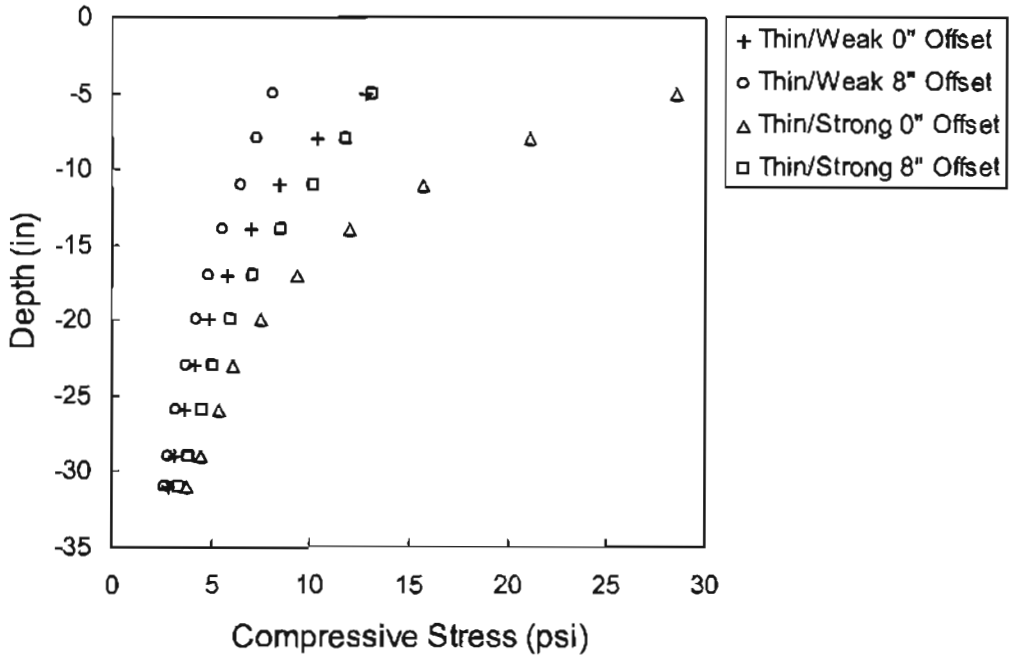

Figure A-5. KENLAYER compressive stress results for full-depth pavements

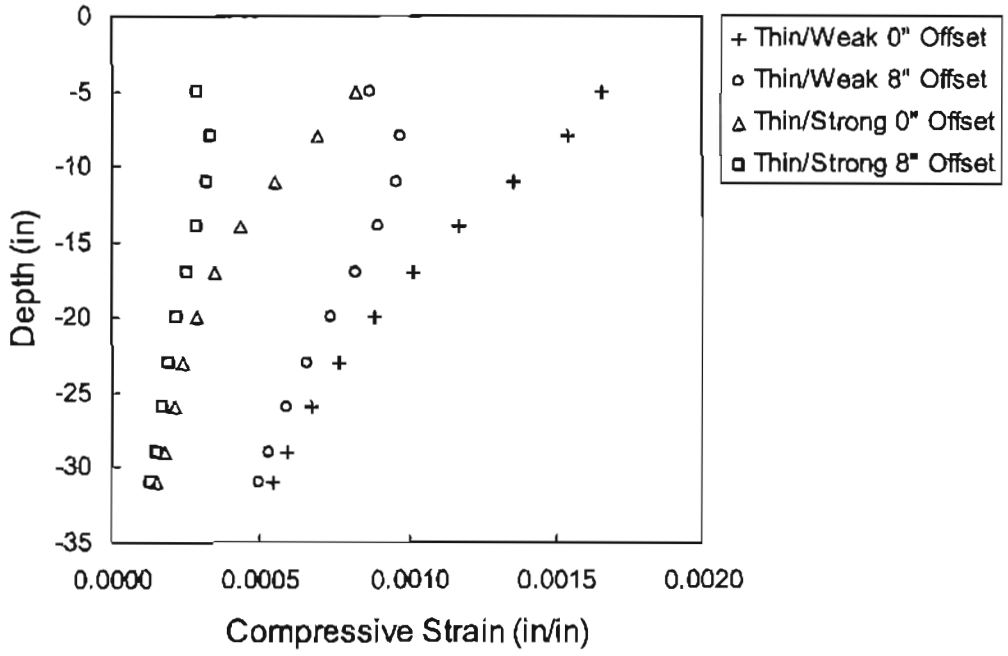

Figure A-6. KENLAYER compressive strain results for full-depth pavements

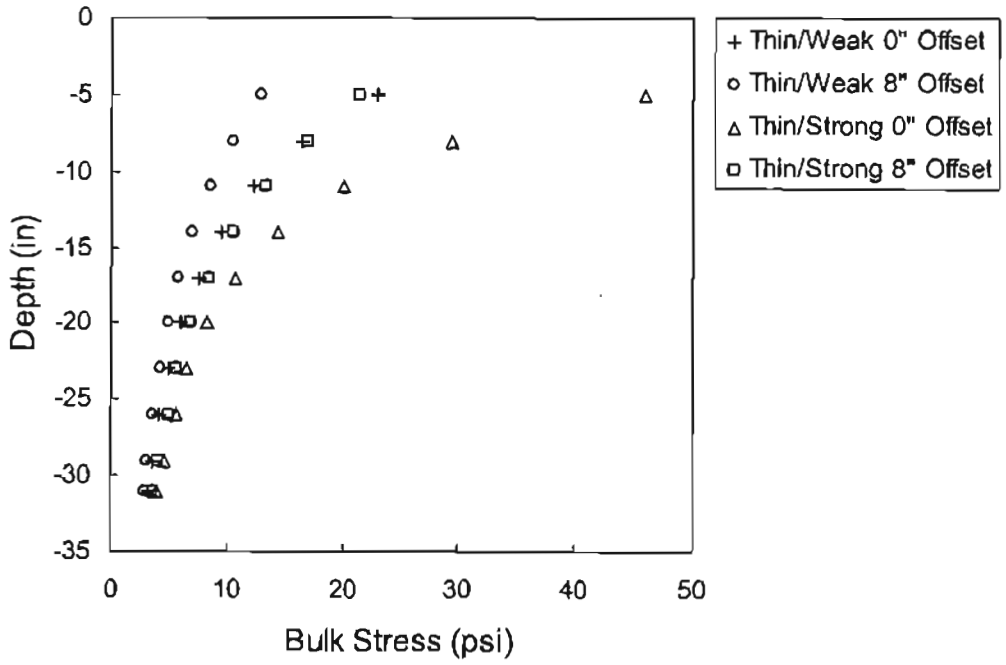

Figure A-7. KENLAYER bulk stress results for full-depth pavements

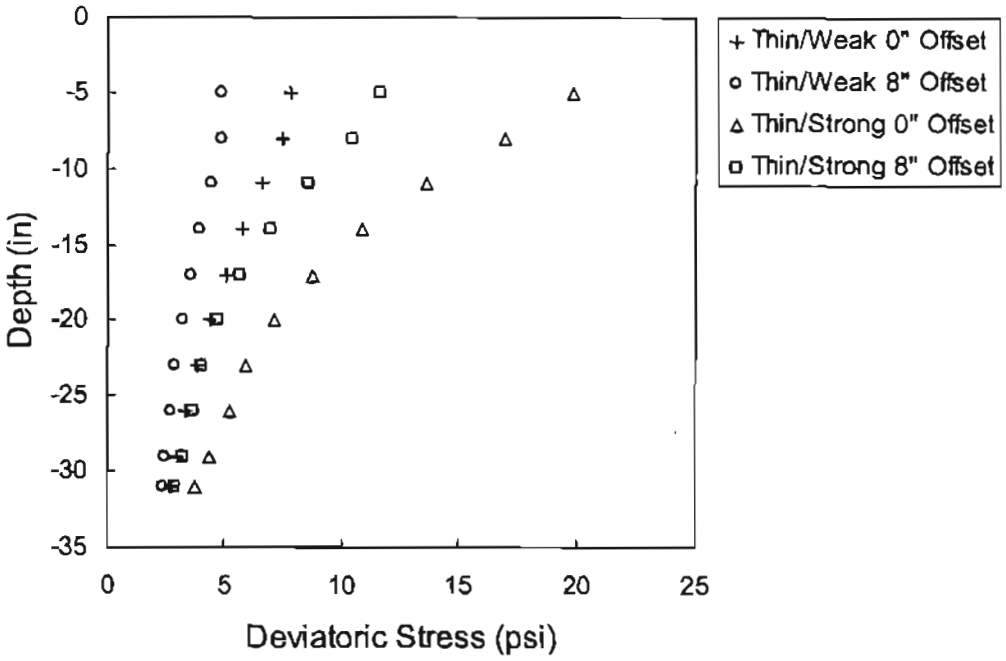

Figure A-8. KENLAYER deviatoric stress results for full-depth pavements

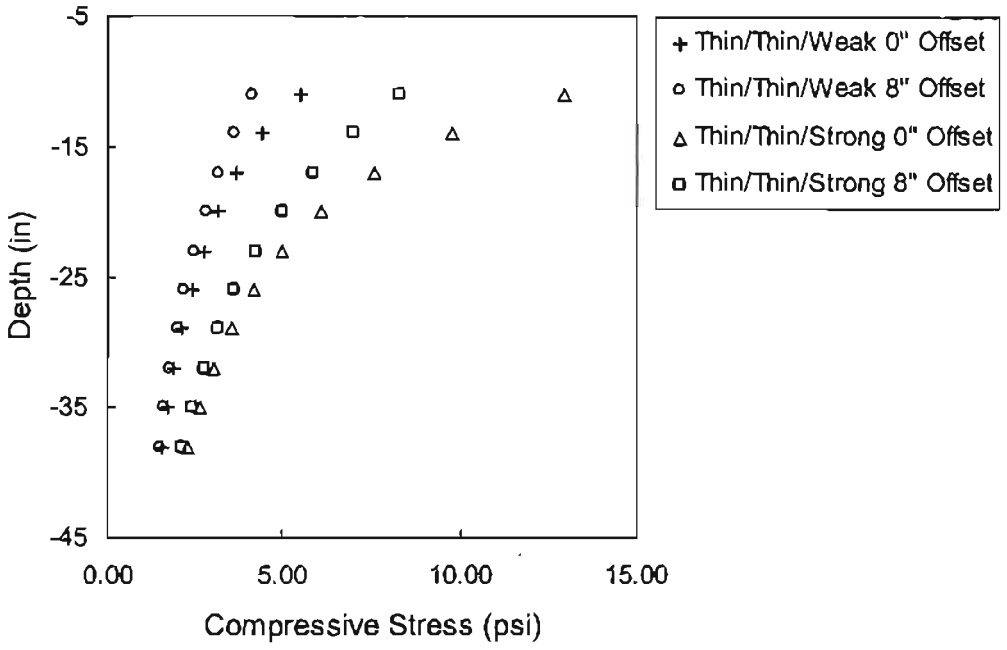

Figure A-9. KENLAYER compressive stress results for aggregate base pavements

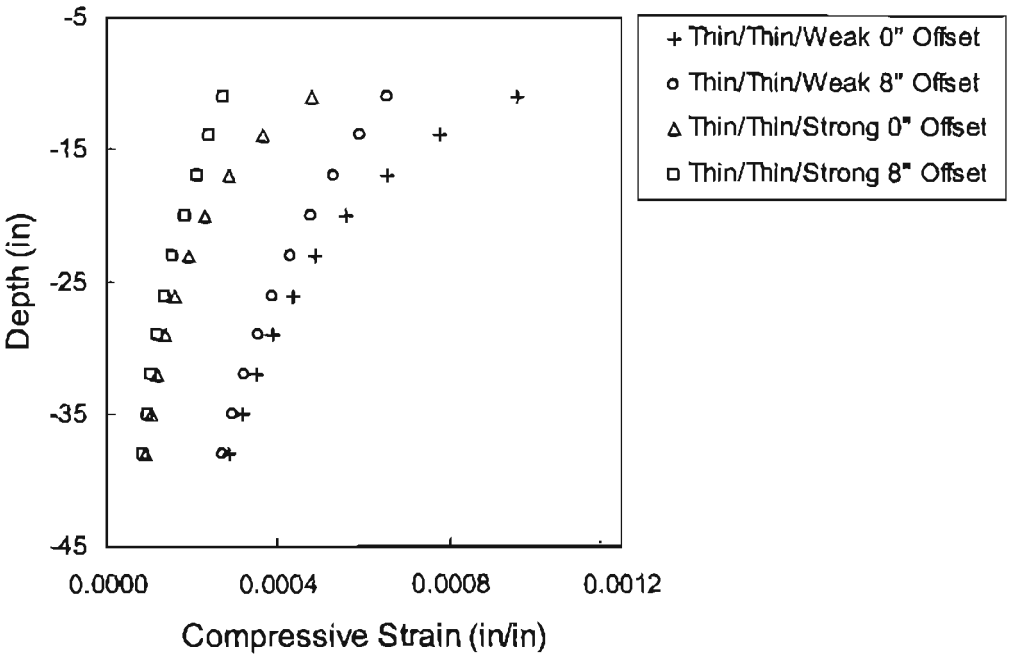

Figure A-10. KENLAYER compressive strain results for aggregate base pavements

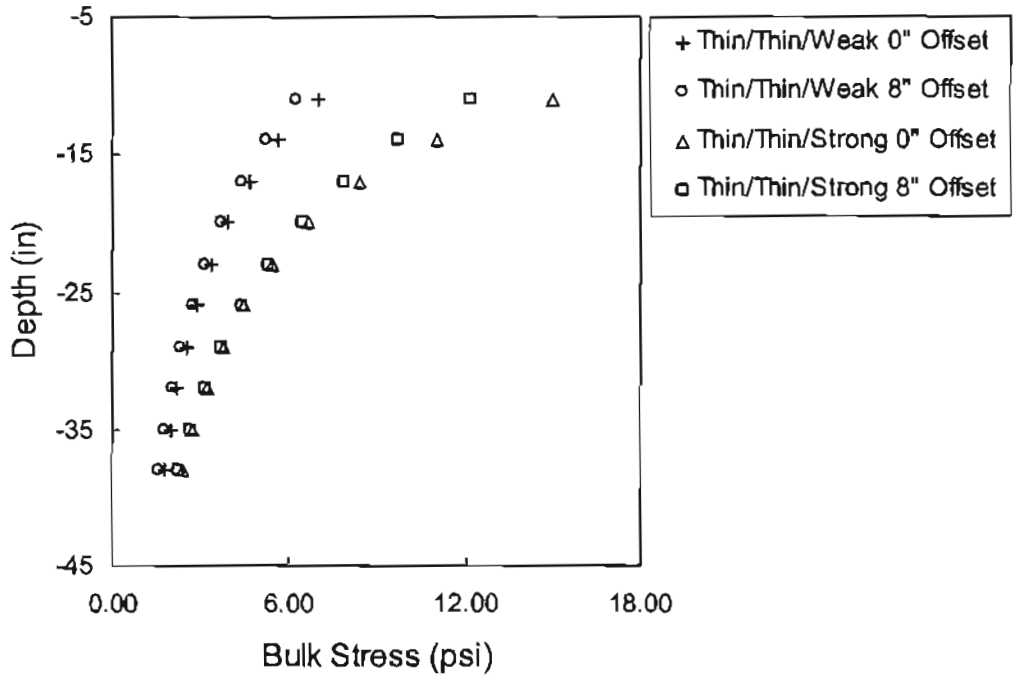

Figure A-11. KENLAYER bulk stress results for aggregate base pavements

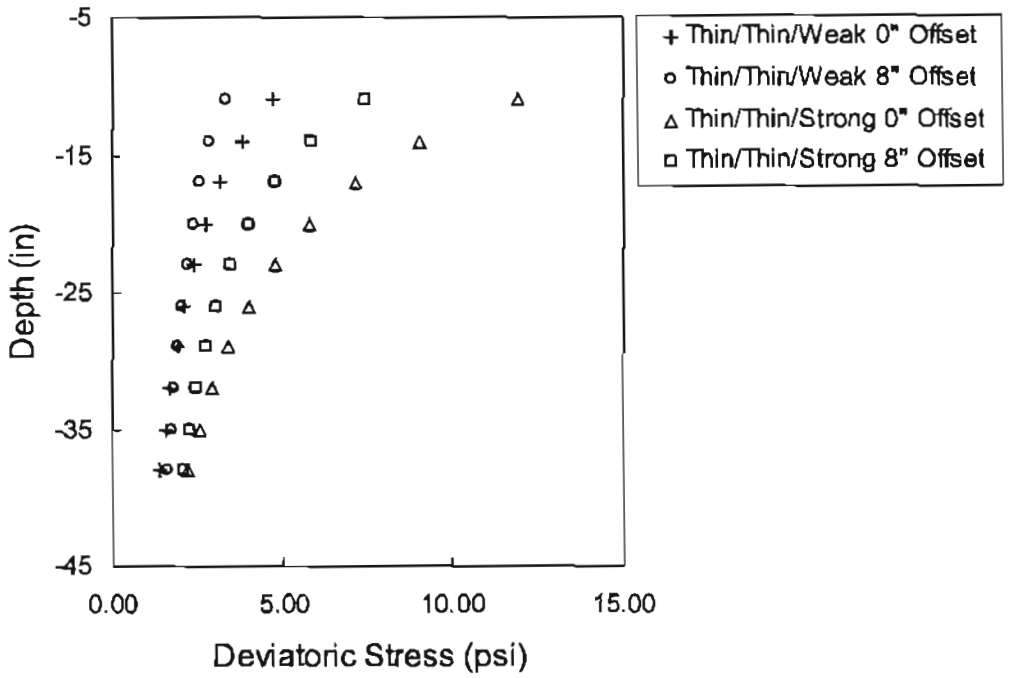

Figure A-12. KENLAYER deviatoric stress results for aggregate base pavements

five original Drucker-Prager property sets were added to an existing thin aggregate base pavement structure. The results from this analysis set showed some deviation from the linear elastic deflections, indicating that the inclusion of nonlinear parameters had some effect on the strains in the system. However, the differences in deflection were, at maximum, on the order of ten percent. The results from the case with maximum deflection difference is shown in Figure A-13. Ten percent is a very small effect considering the asphalt layer chosen was the thinnest available in the synthetic database, and the modulus of that layer was also the least available, 100 ksi. Further literature review showed that the Drucker-Prager material parameters might not be reasonable. The cohesion value used in the plasticity models seemed high. Another set of runs were analyzed, using only a fraction of the cohesion values used in the first set of runs, and the results showed an effect closer to 15 percent. The effects of the dilatation angle were also studied. The Drucker-Prager approach, if used in cohesive soil applications, would require the addition of the dilatation angle parameter. For this reason, one of the three current Drucker-Prager cases were run with three different dilatation angles, and the results compared. The effect of the dilatation angle, at maximum was less than three percent. These results were again from the thinnest, weakest upper layer condition available in the synthetic database.

An asphalt layer modulus of 100 ksi is extremely low and may even be considered unreasonable except in the case of extreme damage or extreme heat, so the Drucker-Prager Plasticity cases were analyzed again with an asphalt layer modulus of 400 ksi. The observed results were a reduction in the effect of plasticity in the base layer. With an asphalt layer modulus of 400 ksi, the effect of including plasticity effects in the base layer were about five percent, at maximum.

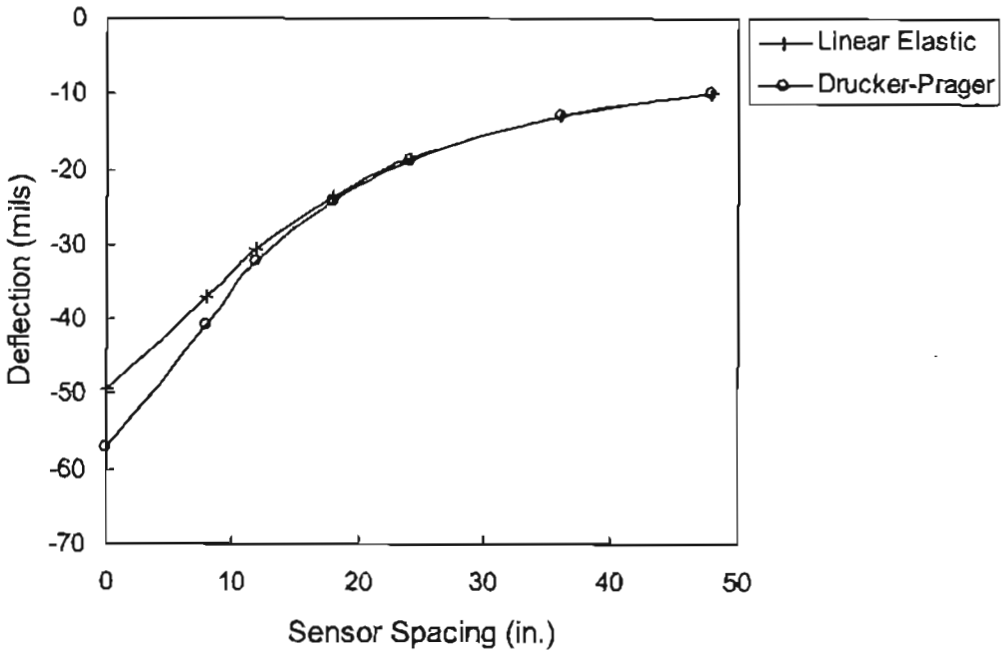

Figure A-13. Plasticity effect of base layer material on deflections

The Drucker-Prager plasticity model was then added to the subgrade layer. In this way, both unbound layers would be defined according to the plasticity model found from ortland test data. Three of the extreme cases in the Drucker-Prager base study were run again, with the addition of Drucker-Prager coefficients in the subgrade layer. The coefficients used were taken from field specimens tested using the ortland testing configuration. Results obtained where plasticity was included in the base and subgrade were compared to those calculated with only base plasticity. The results showed a maximum difference of just over 11 percent. Results from the case with the maximum difference are shown in Figure A-14.

The maximum difference in strain when the Drucker-Prager plasticity model was considered for unbound layers was on the order of 10-15 percent. This difference was found in the thinnest and weakest pavement structure in the synthetic finite element database. In addition, the 10-15 percent difference considered only the center deflection. There was practically no change in deflection in any cases after the fifth sensor. A much greater difference is expected when nonlinearity is included in unbound layers. For these reasons, the research team felt that the Drucker-Prager Plasticity model could not accurately represent the nonlinearity of the unbound layers in a pavement structure.

Since the Drucker-Prager Plasticity model was deemed unfit for nonlinear modeling, a comprehensive review of all remaining models available in the ABAQUS nonlinear model library was performed in the attempt to find another model readily available for use that would adequately represent nonlinear behavior in unbound layers. One such method was the Hypoelasticity option. The hypoelastic model has been used quite extensively in geotechnical applications with cohesive subgrade. Hypoelastic model parameters were found in some geotechnical textbooks based on ortland testing of field specimens. A trial set of ABAQUS

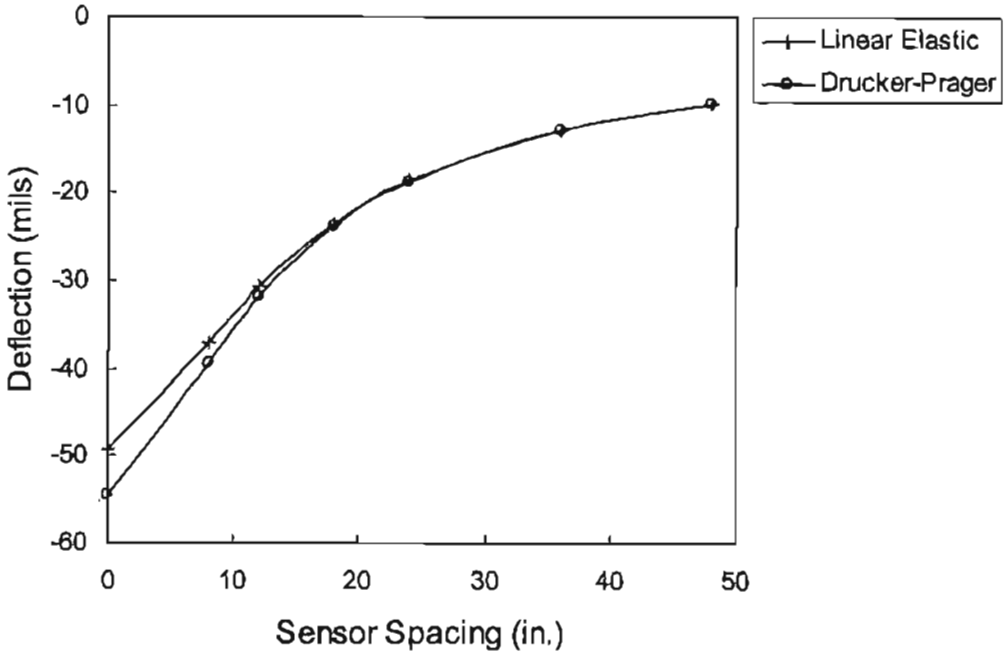

Figure A-14. Plasticity effect of base and subgrade layer materials on defelctions

finite element forward model runs was set up for full depth pavement structures with asphalt layer moduli of 100 ksi and 300 ksi, and layer thicknesses of 4.41 inches and 13.31 inches. This gave a set of four linear elastic models for study. These four models were run again with the Hypoelastic model parameters replacing the linear elastic parameters in the subgrade layer. The linear elastic results were then compared to the Hypoelastic nonlinear results. The comparison showed that the Hypoelastic model gave deflections 60 percent less than those recorded in thin asphalt layer linear elastic cases, and 80 percent less than those recorded in thick asphalt layer linear elastic cases. The difference was substantial for all seven sensors, and the results for a typical relationship are shown in Figure A-15. The Hypoelastic model may be suitable for cohesive subgrade nonlinear modeling. One problem, however, was that finding a set of Hypoelastic parameters corresponding to strong, medium, and weak subgrades would be quite difficult. Since the distinction between subgrade conditions is vital to the success of the synthetic database accuracy, and since the Hypoelastic model could only be used for cohesive subgrade cases, the Hypoelastic model was left as a possible option in lieu of a better approach.

GRANULAR MATERIAL MODELING

Various nonlinear elastic models, derived from cyclic ortland testing, have been proposed to describe the response of granular materials under loading. Several widely used models are summarized in Table A-2.

The $k-\theta$ model was the most popular model in the past due to its simplicity. In this model, the resilient modulus of granular materials is expressed as a function of the bulk stress (θ). Only two material constants, k_1 and k_2, are required, which can be regressed from the experimental data. One drawback of this model is that it neglects the effect of the shear stress on the resilient modulus, which can result in inaccurate prediction of material behavior. Uzan's

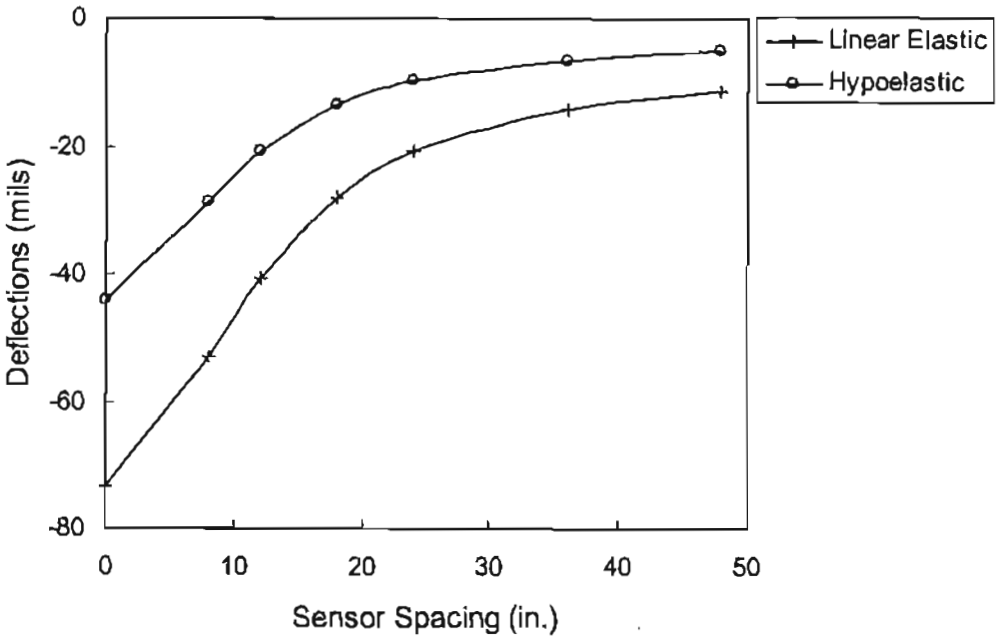

Figure A-15. Hypoelasticity effect on deflections for full-depth pavements

Table A-2. Resilient modulus models for granular materials.

Model	Model Expression	Model Constants
$k-\theta$	$M_R = k_1\theta^{k_2}$	k_1, k_2
Uzan	$M_R = k_1\theta^{k_2}\sigma_d^{\ k_3}$	k_1, k_2, k_3
UT-Austin	$M_R = k_1\sigma_d^{\ k_2}\sigma_3^{\ k_3}$	k_1, k_2, k_3
UT-El Paso	$M_R = k_1\theta^{k_2}\varepsilon_a^{\ k_3}$	k_1, k_2, k_3
Boyce	$M_R = \frac{9KG}{3K+G}$ $K = K_a(\frac{p}{p_a})^{(1-n)}\left[1-\beta(\frac{q}{p})^2\right]^{-1}$ $G = G_a(\frac{p}{p_a})^{(1-n)}$ $\beta = \frac{(1-n)K_a}{6G_a}$	K_a, G_a, n

Note: θ = bulk stress = $\sigma_1 + \sigma_2 + \sigma_3$;

σ_d = deviator stress = $\sigma_1 - \sigma_3$;

σ_d q = deviator stress = $\sigma_1 - \sigma_3$;

q σ_3 = confining stress = σ_2;

σ_3 p = mean normal stress = $\frac{1}{3}(\sigma_1 + \sigma_2 + \sigma_3)$;

p M_R = resilient modulus;

M_R K = bulk modulus; and

K G = shear modulus.

G ε_a = axial strain;

ε_a p_o' = initial effective mean normal stress before cyclic loading or the magnitude of the suction at zero confined stress;

E_{max} = maximum modulus of cohesive soils varying with soil type; and

E_{max} M_R = resilient modulus.

M_R

Model and the UT-El Paso model overcome this problem by adding either the measured deviator stress (σ_d) or axial strain (ε_a) as the extra parameter to predict the resilient modulus. The UT-Austin model directly relates two independent variables, the deviator stress (σ_d) and the confining pressure (σ_3) to the resilient modulus. Compared to the $k-\theta$ model, Uzan's model, the UT-El Paso model, and the UT-Austin model all show better agreement with the experimental data. Boyce's model widely used in European countries is one of the advanced models for granular materials. Although the better results may be obtained from this model, more complicated testing and material constant evaluation procedures are required. Thus, it is not considered practical in routine uses.

COHESIVE MATERIAL MODELING

The resilient modulus of cohesive soils mainly depends on the deviator stress and the moisture content (or suction). For partially saturated soils (such as compacted soils), the negative pore pressure contributes significantly to the effective confining pressure. The suction is often so significant that practitioners generally consider that confining pressure has a minor influence on the behavior of fine-grained soils. The models that have been proposed for cohesive materials are summarized in Table A-3.

The bilinear model, based on cyclic ortland tests at a single confining pressure, was successfully used in the ILLI-PAVE and MICH-PAVE computer programs for fine-grained soils. In this model, the value of k_1, representing resilient modulus at the breakpoint in the bilinear curve, is considered as a major indicator of material behavior. The other constants, k_2, k_3, and k_4 "display less variability and have smaller influences on pavement response than k_1." The power $k-\sigma_d$ model considers the resilient modulus as a power function of the deviator stress.

Table A-3. Resilient modulus models for cohesive soils

Model	Model Expression	Model Constants
Bilinear $k-\sigma_d$	$M_R = k_2 + k_3(k_1 - \sigma_d) \quad k_1 > \sigma_d$ $M_R = k_2 + k_4(\sigma_d - k_1) \quad k_1 < \sigma_d$	k_1, k_2, k_3, k_4
Power $k-\sigma_d$	$M_R = k_1 \sigma_d^{k_3}$	k_1, k_3
Dawson and Correia	$M_R = k_1 + k_2 p_o' - k_3 \sigma_d$	k_1, k_2, k_3
$E/E_{max} - \varepsilon_a$	$M_R = f(E_{max}, \varepsilon_a)$	E_{max}

Note: σ_d = deviator stress = $\sigma_1 - \sigma_3$;

Compared to the bilinear model, this model has the advantage of having fewer material constants. The drawback of both the bilinear model and the power model is that confining pressure is not considered. Dawson's model not only takes into account the deviator stress but also the suction, and therefore this model shows better agreement with the results from laboratory testing. However, since determining the moisture content of a soil in the field is much more difficult than in the lab, this model seems to be impractical for routine uses. The $E / E_{max} - \varepsilon_o$ model, also named the strain level dependent model, describes the modulus as a function of axial strain. Unlike other models which are only derived from the cyclic ortland test, the resonant column test and torsional shear test are also performed to formulate the $E / E_{max} - \varepsilon_a$ model. Thus, this model has a larger range of application, which is able to represent the nonlinearity of cohesive soils at as low as 0.001 percent axial strain level.

Based on the investigation of all these available models for granular materials and cohesive soils, Uzan's universal model, initially proposed for granular materials, is chosen as the model for the nonlinear analysis. The general expression of this model is:

$$M_R = k_1 \theta^{k_2} \sigma_d^{k_3} \qquad \text{(A-1)}$$

where M_R is resilient modulus, θ is bulk stress, σ_d is deviator stress, k_1, k_2, k_3 are model constants. It is noted that k_1 and k_2 are always positive and k_3 is usually a negative constant.

The advantage of the universal model is that it can represent all pavement layers with a single expression. When k_1, k_2, and k_3 are all non-zero values, the model represents granular materials in base layer or subgrade. When both k_2 and k_3 are set to zero, this model represents linear elastic materials. When only setting k_2 to zero, the model represents fine-grained materials in subgrade.

However, one should note that, according to Eq. A-1, if a very small deviator stress (close to zero) is applied, the calculated resilient modulus becomes a very large value approaching infinity, which is obviously unrealistic. The universal model is derived from cyclic o r tland testing, where the minimum deviator stress is usually 1 psi. This indicates that one has to be careful when using this model at the deviator stress level less than 1 psi. In order to overcome this problem, an arbitrary maximum resilient modulus is assigned to the material if the deviator stress is less than 0.5 psi. For fine-grained cohesive soils, E_{max} in the strain level dependent model may be assigned as the maximum resilient modulus value.

UMAT SUBROUTINE

User defined subroutine UMAT is a powerful option in ABAQUS, which provides an interface that allows the user to define any mechanical constitutive model within ABAQUS input files. For the nonlinear A- analysis, an UMAT program was coded in Fortran language to simulate Uzan's universal model as defined in Eq. A-1. It should note that, in laboratory o r tland tests, because σ_2 is equal to σ_3, the deviator stress is defined as follows:

$$\sigma_d = \sigma_1 - \sigma_3 \tag{A-2}$$

However, in a pavement system, σ_2 may not be equal to σ_3. Therefore, the average value of σ_2 and σ_3 is considered as an approximation of σ_3, that is,

$$\sigma_d = \sigma_1 - \frac{1}{2}(\sigma_2 + \sigma_3) \tag{A-3}$$

The resilient modulus derived from the lab testing is usually considered as the secant Young's modulus E_t (the ratio of total stress to total strain). For dynamic analysis, the tangent Young's modulus (the ratio of small changes of stress to small changes of strain) is required, which can be estimated from the following equation:

$$E_t = \frac{K_t}{(1-2\nu)} = \frac{\Delta\theta}{k_1(\theta+\Delta\theta)^{k_5}(\sigma_d+\Delta\sigma_d)^{k_3} - k_1(\theta)^{k_5}(\sigma_d)^{k_3}} \quad \text{(A-4)}$$

where $k_5 = 1+k_2$, and k_1, k_2, and k_3 are material constants.

UMAT has two major functions: it updates the stresses at the end of each time increment, and it provides the material Jacobian matrix for the mechanical constitutive model. UMAT is executed for each material integration point at each iteration in each time increment. Modulus of each integration point is calculated based on the stress level at the beginning of each time increment. The accuracy of the results depends on the size of the time increment. A smaller time increment will yield better results, but result in longer computation time.

INITIAL STRESSES

Before an FWD load is applied, a pavement already has stresses due to geostatic pressure, pore pressure (which could be positive or negative depending on whether the material is totally or partially saturated) and residual pressure from compaction. These stresses will affect the initial moduli of the layer materials. Since some of these stresses are very difficult to be measured in the field, only geostatic stresses are considered in the nonlinear analysis. The vertical geostatic stress σ_v is calculated based on the thickness and unit weights of pavement layers. The horizontal stress σ_h is calculated based on the coefficient of earth pressure at rest, K_o, which is defined as the ratio of horizontal stress to vertical stress under zero lateral strain condition. These relationships are:

$$\sigma_v = \gamma z \quad \text{(A-5)}$$

$$\sigma_h = K_o \sigma_v \quad \text{(A-6)}$$

where γ is the density of layer materials, z is the depth of material point from the pavement surface, and K_0 is the coefficient of earth pressure at rest, which can be established, depending on material types, from the following equations:

Linear elastic materials:

$$K_o = \frac{\nu}{1-\nu} \tag{A-7}$$

Granular materials:

$$K_o = 1 - \sin\phi \tag{A-8}$$

Fine-grained, normal consolidated soils:

$$K_o = 0.44 + 0.42\left[\frac{PI(\%)}{100}\right] \tag{A-9}$$

where ν is Poisson's ratio, ϕ is the drained frictional angle, and PI is the plastic index.

For pavement materials, especially the base layer and the upper layer of subgrade, the coefficient of earth pressure at rest should be in the range of 0.8 to 2.0 due to compaction and frequent loading. In this research, the coefficient of 0.8 is assigned to all stress-sensitive layers.

As the geostatic stresses do not yield strains in pavement system, in the ABAQUS model, the load induced stresses and strains are calculated separately from the calculation of the geostatic stresses. The geostatic stresses are only used to establish the material modulus at the beginning of each time increment.

FAILURE CRITERION

Mohr-Coulomb failure envelope, demonstrated in Figure A-16, is employed in the nonlinear finite element analysis. According to this criterion, failure occurs when the load induced stresses exceed the material strength, which is defined based on the maximum principal

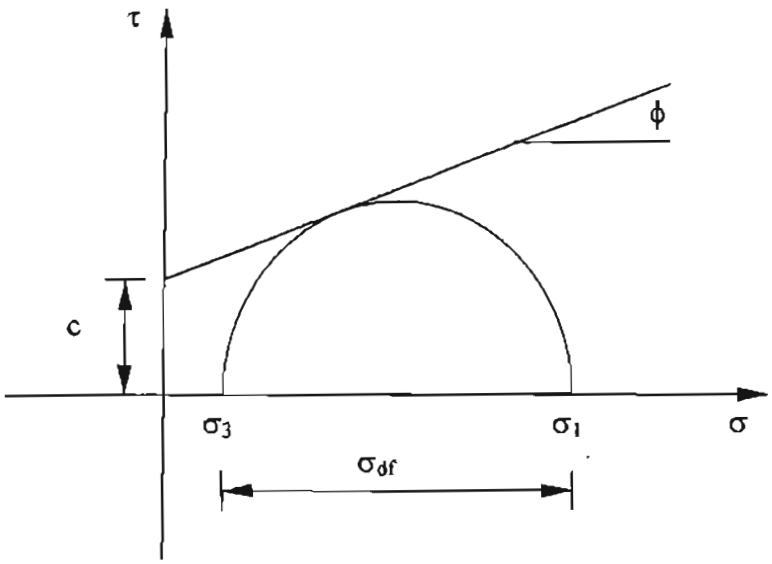

Figure A-16. Mohr-Coulomb failure curve

stress ratio for granular materials and as the maximum shear stress for fine-grained materials. The relationship between major and minor principal stresses at failure can also be expressed as:

$$\sigma_1 = \sigma_3 \tan^2(45 + \frac{\phi}{2}) + 2c\tan(45 + \frac{\phi}{2}) \quad \text{(A-10)}$$

where σ_1 and σ_3 are major and minor principal stresses, respectively, and c and f are stress parameters corresponding to cohesion and frictional angle, respectively.

Usually, the failure modulus is assigned to the failed element. Since this failure modulus value is arbitrarily decided, however, different numbers used in the analysis may result in sufficiently different pavement stress and strain responses. Raad and Figueroa (A-7) proposed a technique that ensures the stresses do not exceed the failure envelope, in which the principal stresses in the base materials and subgrade are modified at the end of each increment. This is achieved by using the vertical stress, σ_v, to calculate the limit values for major and minor principal stresses, $(\sigma_1)_{max}$ and $(\sigma_3)_{min}$, respectively.

$$(\sigma_1)_{max} = \sigma_v \tan^2(45 + \frac{\phi}{2}) + 2c\tan(45 + \frac{\phi}{2}) \quad \text{(A-11)}$$

$$(\sigma_3)_{min} = \sigma_v \tan^2(45 - \frac{\phi}{2}) - 2c\tan(45 - \frac{\phi}{2}) \quad \text{(A-12)}$$

At any time increment, the current σ_1 value is not allowed to exceed $(\sigma_1)_{max}$, while σ_3 value is not allowed to be smaller than $(\sigma_3)_{min}$. In addition, σ_1 also is not allowed to exceed σ_1', which is defined as:

$$\sigma_1' = \sigma_3 \tan^2(45 + \frac{\phi}{2}) + 2c\tan(45 + \frac{\phi}{2}) \quad \text{(A-13)}$$

Modified stresses are then used to predict the resilient modulus for the subsequent time increment.

Note that the principle of the stress modification is very similar to Rankine's theory of lateral active and passive pressure without earthquake. It is reasonable to consider that the stress modification in dynamic analysis should be different from that in static analysis. For example, when c is set to 0 for granular materials, the expressions of $(\sigma_3)_{min}$ and $(\sigma_1)_{max}$ in dynamic analysis may be expressed as:

$$(\sigma_1)_{max} = \sigma_v \frac{\cos^2(\phi-\beta)}{\cos^3\beta\left\{1-\left[\frac{\sin\phi\sin(\phi-\beta)}{\cos\beta}\right]^{1/2}\right\}^2} \tag{A-14}$$

$$(\sigma_3)_{min} = \sigma_v \frac{\cos^2(\phi-\beta)}{\cos^2\beta\left\{1+\left[\frac{\sin\phi\sin(\phi-\beta)}{\cos\beta}\right]^{1/2}\right\}^2} \tag{A-15}$$

where ϕ is frictional angle, and β is expressed as:

$$\beta = \tan^{-1}\left(\frac{k_h}{1-k_v}\right) \tag{A-16}$$

where $k_h = \frac{g_h}{g}$, $k_v = \frac{g_v}{g}$, g_h is horizontal acceleration, g_v is vertical acceleration, and g is acceleration from gravity.

It is evident from Eqs. A-9 and A-10 that $(\sigma_1)_{max}$ in dynamic analysis is larger than that in static analysis, and $(\sigma_3)_{min}$ in dynamic analysis can be smaller or larger than that in static analysis.

In both static analysis and dynamic analysis, neglecting the horizontal acceleration results in β being equal to 0. Eqs. A-9 and A-10 are then similar to Eqs. A-6 and A-7.

RIGID PAVEMENTS

Compressive stress, compressive strain, bulk stress, and deviatoric stress were calculated for each rigid pavement case listed in Table A-1. Strain values found from this KENLAYER study were compared to values found in the work done by Shao and Borden (Figure A-1). The strain values fell close to the linear elastic portion of the E/E_{max} curve, therefore nonlinear behavior did not need to be added to the existing linear elastic forward model. Figures A-17 through A-20 show the stress and strain information generated for each rigid pavement case.

Field data was next used to determine if nonlinear modeling in rigid pavements was necessary. The DataPave field database was searched to find pavement cases with varying layer thicknesses and subgrade strengths for a nonlinear comparison. Pavements that would represent weak and strong subgrade strengths, thick and thin PCC layers, and thick and thin subgrade layers were chosen. Extremes of these cases were chosen for analysis. Table A-4 shows the pavement structures selected for use in this study. Deflection data were gathered and consolidated for each pavement structure. In each case, tests were taken every 25 feet throughout a 500-foot test section. Tests were performed at two or more different times. In most cases, testing was performed with loads of 6, 9, 12, and 15 kips. In some cases, the 6 kip test run was omitted. To test the nonlinearity of the rigid pavement structures, the center and seventh deflection normalized with respect to the load was plotted versus load level. A horizontal line would indicate a linear relationship between load and pavement response. A line with a non-zero slope would indicate a nonlinear relationship. Figure A-21 shows a typical plot of the normalized deflection versus load level for the field structures.

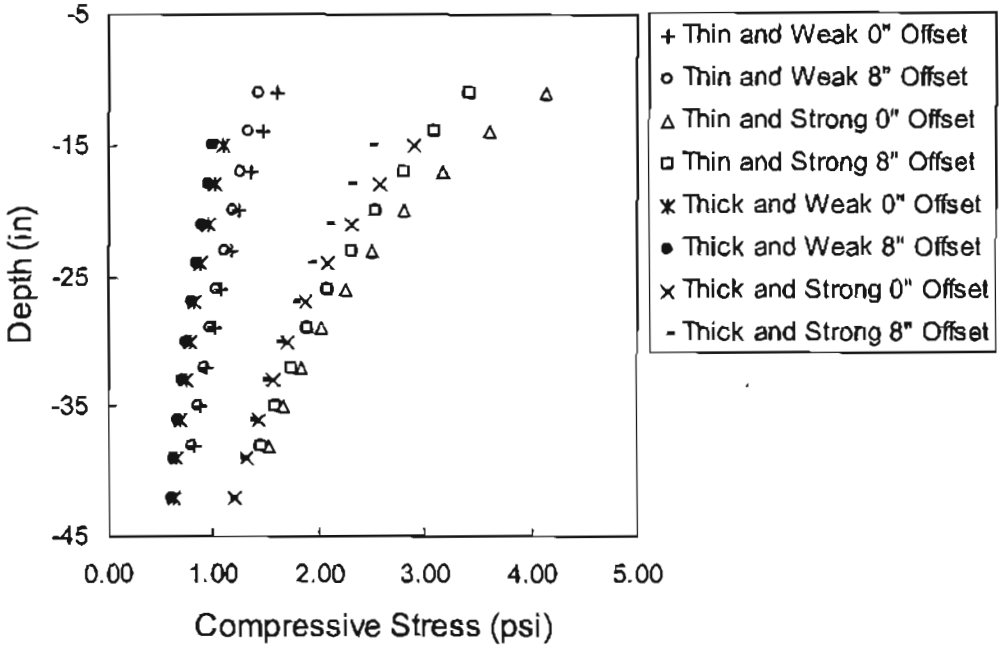

Figure A-17. KENLAYER compressive stress results for rigid pavements

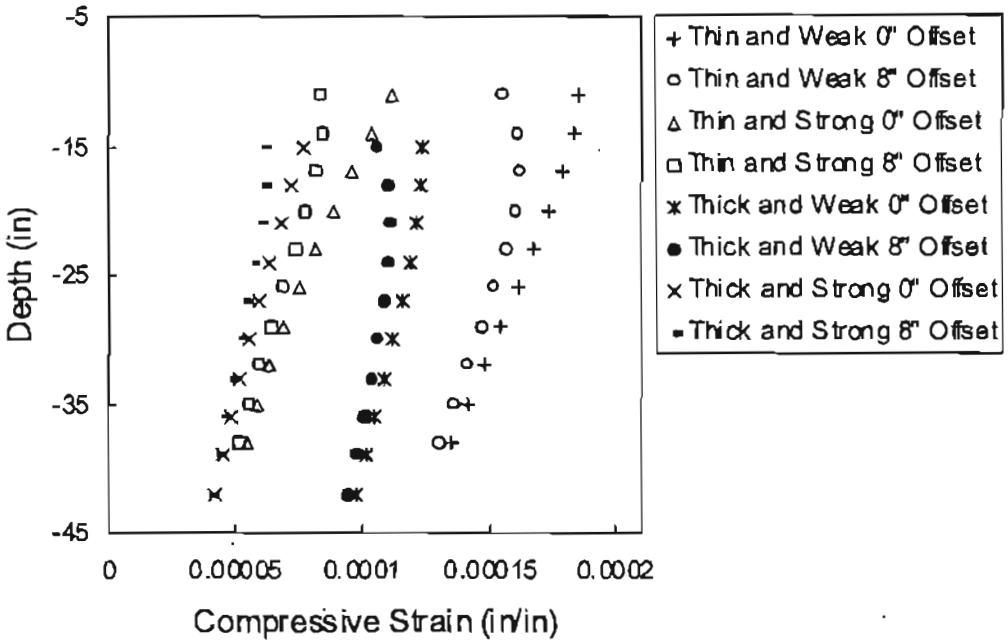

Figure A-18. KENLAYER compressive strain results for rigid pavements

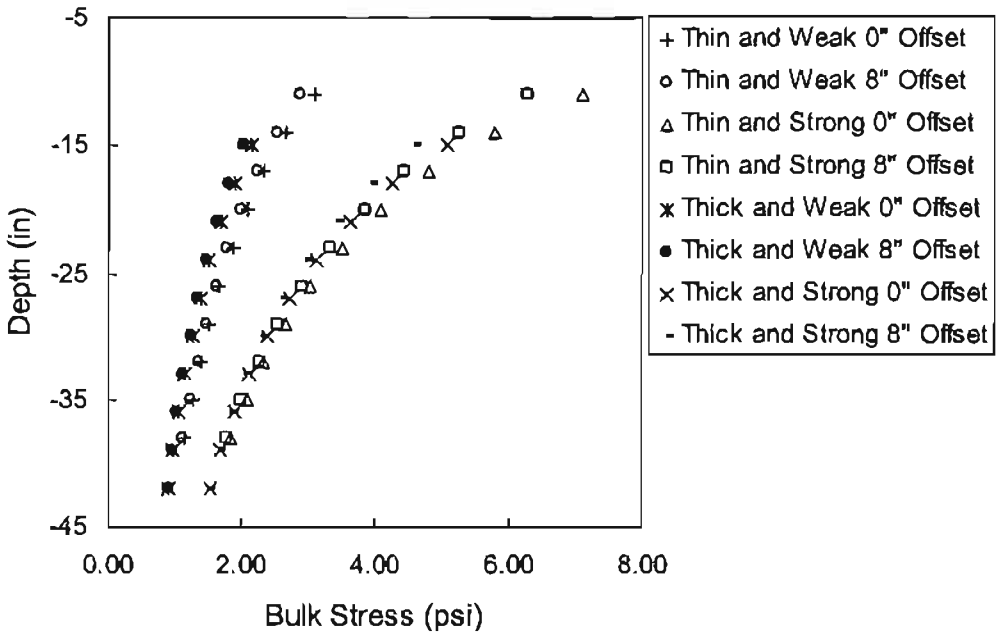

Figure A-19. KENLAYER bulk stress results for rigid pavements

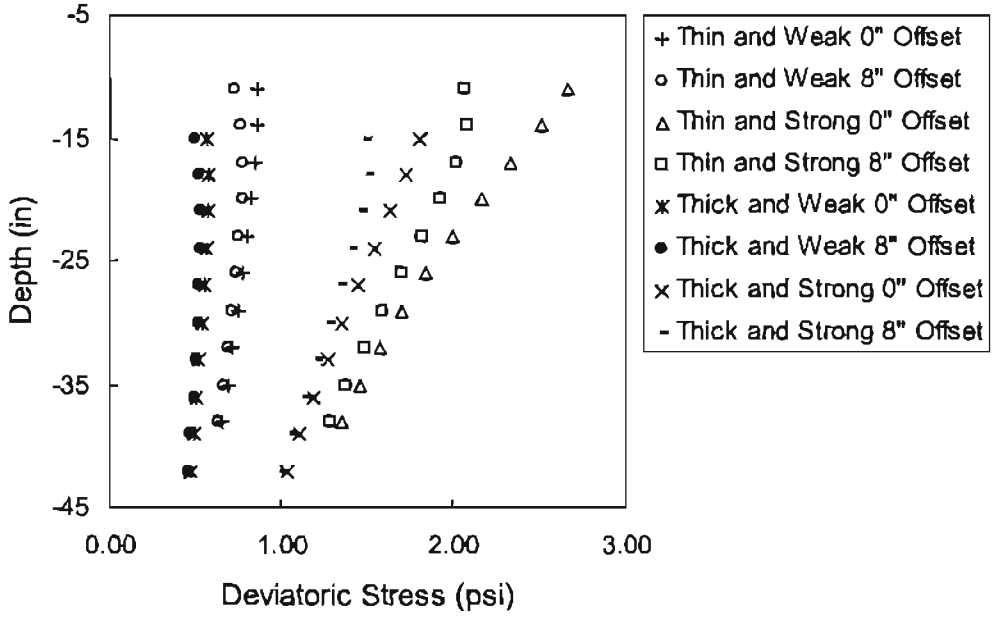

Figure A-20. KENLAYER deviatoric stress results for rigid pavements

Table A-4. Data used for rigid FEM verification

	State of Origin	PCC thickness	SG thickness
Soil Classification A-2-5			
SHRP 7035	Colorado	8"	3'
SHRP 9327	Illinois	10.4"	8'
Soil Classification A-2-6			
SHRP 7090	Minnesota	7"	12'
SHRP 7012	Mississippi	9"	6'
Soil Classification A-7-5			
SHRP 9116	Iowa	8"	24'
SHRP 9126	Iowa	10"	24'

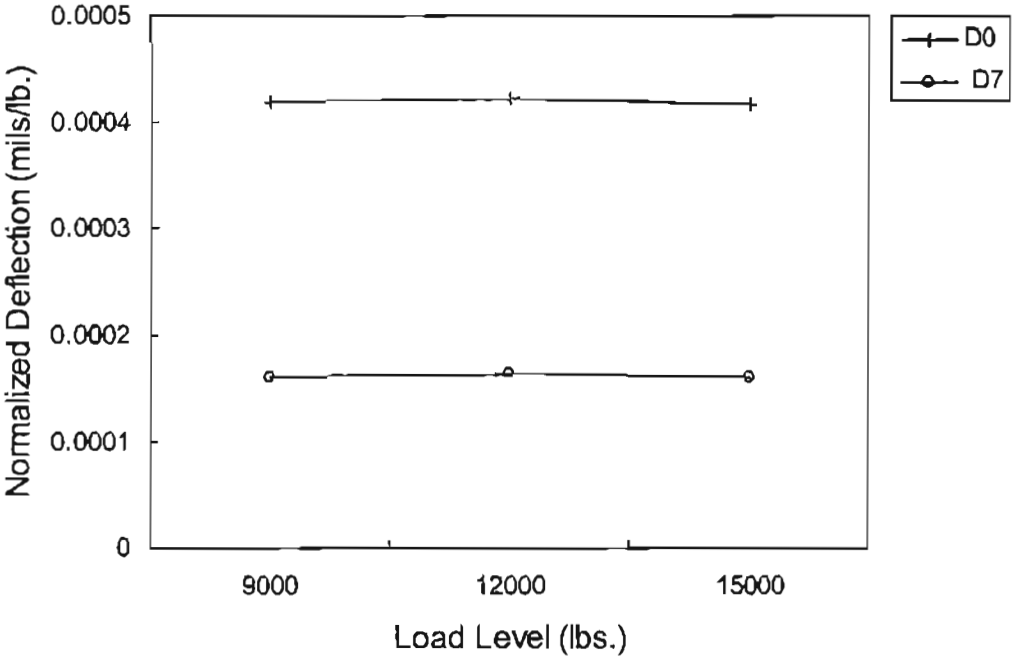

Figure A-21. Rigid pavement linearity check using multiple load levels

In every case considered, a linear relationship for both the center and seventh deflection exists. For all thicknesses of PCC and subgrade and for all three soil classifications, nonlinearity does not appear to exist. According to the extreme cases of field data analyzed here, nonlinear modeling of the subgrade in overlaid rigid pavement structures is not warranted.

Finally, the synthetic database was examined. Three FEM structures were created with stiff layer depths of 30, 39, and 79 inches, respectively. For each of these cases, a subgrade modulus of 5, 15, and 25 ksi were assigned. The upper layers in each case were given a constant thickness and modulus, resulting in a total of nine synthetic cases. Each of these cases was analyzed and the compressive stress and compressive strain values at the top of the subgrade were recorded. Table A-5 shows the results of this analysis. The percent strain values were compared to the S-shaped curve developed by Shao and Borden (Figure A-3) to check for nonlinearity in the subgrade layer. Only the cases with shallow stiff layer depths and low modulus values appeared well into the nonlinear range.

Table A-5. Results of nonlinear study for rigid pavements

		6000 lbs.		9000 lbs.		12000 lbs.		15000 lbs.	
DSL (in)	Esg (ksi)	Stress (psi)	Strain %	Stress (psi)	Strain %	Stress (psi)	Strain %	Stress (psi)	Strain %
30	5	0.7312	0.00669	1.0960	0.01000	1.4620	0.01330	1.8280	0.01670
	15	0.9604	0.00330	1.4390	0.00496	1.9180	0.00661	2.4010	0.00829
	25	1.0950	0.00244	1.6420	0.00365	2.1880	0.00486	2.7240	0.00608
39	5	0.5879	0.00588	0.8992	0.00910	1.2010	0.01210	1.5010	0.01520
	15	0.8702	0.00332	1.3040	0.00497	1.7400	0.00663	2.1750	0.00828
	25	1.0020	0.00243	1.5020	0.00364	2.0050	0.00486	2.5060	0.00607
79	5	0.3311	0.00364	0.4959	0.00543	0.6621	0.00725	0.9338	0.01150
	15	0.5850	0.00257	0.8763	0.00384	1.1700	0.00513	1.4620	0.00648
	25	0.7754	0.00218	1.1620	0.00328	1.5510	0.00437	1.9400	0.00547

FEM MODEL VERIFICATION

FLEXIBLE PAVEMENTS

The data from AASHTO Sherrard test section were used to validate the dynamic finite element modeling approach used in this research. Two data sets for Sherrard test section were available from the study by Shoukry et al. (A-8). The first set is the actual measured deflection basin under FWD testing, and the second is the set of the values of layer moduli and other material properties measured from laboratory tests. Table A-6 shows the pavement profile of Sherrard test section.

The FWD test was performed with a peak pressure of 70 psi and a duration of 40 ms. Figure A-22 shows the deflections that resulted from different models using the layer properties listed in Table A-1. The deflection bowl obtained from the FEM model used in this research agreed well with the actual measured deflection bowl.

RIGID PAVEMENTS

All pavement structures were modeled in a two-dimensional (2-D), dynamic, axisymmetric manner. A roller-type boundary condition was employed at the load center side of the model, and infinite elements were used to model the lateral extent of the pavement structure. Fine elements were used to model the area around the load plate, and the elements were biased laterally and vertically away from the load center where the same detail in accuracy was not required. This model was first incorporated for flexible pavement studies. With the inclusion of rigid pavement systems, namely cement treated base and ortland cement concrete base with asphalt overlay pavements; the model used in flexible pavement modeling needed to be proven accurate for rigid applications.

Table A-6. Pavement profile of Sherrard test section

Layer	Thickness (in)	Modulus (ksi)	Poisson's Ratio	Density (pcf)	Damping Ratio
AC layer	4	500	0.35	145	5%
Base Layer	14	35	0.40	140	5%
Subgrade	720	10	0.45	115	5%

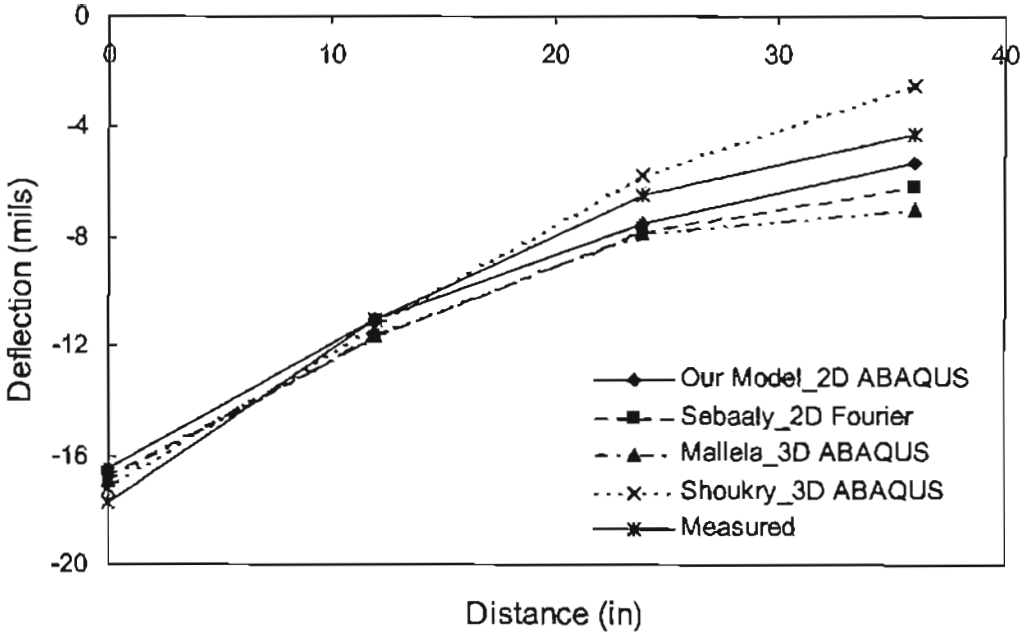

Figure A-22. Verification of FEM model for Sherrard test section

Cho, McCullough, and Weismann tested the finite element model in a 2-D plane strain, 2-D axisymmetric and 3-D arrangement. The 2-D axisymmetric study was split into three separate models. The first model had a 1" square mesh system at the load center, and a discontinuous boundary 90" from the load center. The second model had a 2" square mesh system at the load center, and a discontinuous boundary 90" from the load center. The third model had a 1" square mesh system at the load center, and infinite elements instead of a discontinuous boundary at the simulated slab edge. The results from the finite element simulation showed that the model with the infinite elements at the slab edge gave less stiffness to the structure and deflections closer to layered theory solutions. In general, it was concluded that the axisymmetric model is a "...reasonable approach for simulating pavement response..." It was also noted that the 3-D model required more computing time than did the 2-D axisymmetric model.

Intuitively, the 2-D axisymmetric infinite element model results should agree with the actual field condition better than results of those models with a lateral discontinuity. The axisymmetric formulation is based on the assumption that the two-dimensional mesh form is valid for three-dimensions. This means that if a discontinuity is modeled at the 2-D slab edge, in three dimensions a discontinuity will surround the load center at the given lateral dimension.

With the ultimate goal being the accurate prediction of pavement response in the field through synthetic finite element modeling, the best way to validate a forward model is to match synthetic data and field data where all variables are the same for both data sets. For rigid pavement validation, deflection data from the I-71 Ohio test track was used. The Ohio test track was part of a 7.8 mile Break and Seat (B/S) rehabilitation project that was included in the Federal Highway Administration (FHWA) project SP-202 entitled "Break and Seat of Jointed Reinforced

Concrete Pavement." The test is was broken into four 1000-foot sections. One section was designated a control section, one section was designated a 6" B/S section, one section was designated an 18" B/S section, and one section was designated a 30" B/S section. Each section consisted of sixteen 60' slabs. All sections originally had a 3" asphalt overlay over a 9" PCC slab. The construction project called for the existing asphalt overlay to be milled the B/S procedures to take place, and then an 8.5" overlay to be placed. The overlay was constructed in three lifts, a 4.5" base lift, a 2" intermediate lift, and a 2" wearing lift. Deflection testing was performed before milling, before B/S operations, and after each lift of overlay.

The asphalt thickness was known as the overlay was measured as it was constructed. Asphalt modulus information was obtained through testing at the time of mixing and of cores taken in four selected locations throughout the project length. The asphalt modulus was estimated to be a constant 448,000 psi. PCC slab thickness information was obtained through the original construction plans and was observed to be a constant 9" throughout the length of the project. Cores were also taken to verify the construction plan thickness. The modulus of the PCC slab was not known, so MODULUS was used to estimate the PCC modulus. The subgrade thickness was also listed in the construction plans, although no coring was performed to verify the stiff layer depth. No modulus information for the subgrade was available so again, MODULUS was used to estimate the subgrade modulus. Several approaches were used to try to estimate PCC modulus, subgrade depth, and subgrade modulus, all with moderate success. The PCC modulus estimates ranged from 5,000 ksi to over 6,000 ksi. The subgrade depths were assumed to be correct as listed in the construction records. The subgrade modulus varied from 4 ksi to 26 ksi.

To model the field pavement structures some decisions had to be made concerning the PCC, and subgrade modulus values, and the subgrade thickness values. Since no other records were available, the recorded subgrade depths present in the construction documentation were used. The PCC modulus was modeled as a constant 5,000 ksi because this is a typical value used to model intact PCC layers, and because it is on the conservative side of the MODULUS estimation. The subgrade modulus was modeled as 5, 15, and 25 ksi to account for the full range of estimated values back-calculated using MODULUS. Only the control sections were used for verification of the forward model. A visual survey was done on the PCC slabs before overlay procedures took place, and some of the sixteen control slabs showed signs of cracking. For this reason, only slabs 1,2,3,5,6,7,8,9,12,13,and 16 were considered.

Figures A-23 and A-24 are typical examples of the comparison of the finite element forward model results and the measured field data. Subgrade modulus plays an important role in the prediction of pavement response. In the cases shown, the field data seems to match the 15 and 25 ksi synthetic deflection bowls. Although the data points do not match exactly, the deflection curves are quite similar.

Preliminary studies show that the 2-D axisymmetric model does a reasonable job of simulating rigid pavement behavior. It was also observed that an axisymmetric model with infinite lateral elements would give a less stiff pavement structure and results closer to those obtained from layer theory. Intuition suggests that the infinite element approach in lieu of a modeled discontinuity, in a 2-D axisymmetric situation, would more closely approximate an actual pavement configuration. Matching the synthetic deflection data points to those measured in actual field conditions for structures with similar layer properties showed a good correlation in most cases. In all cases, the deflection curve trends were quite similar, indicating a reasonably

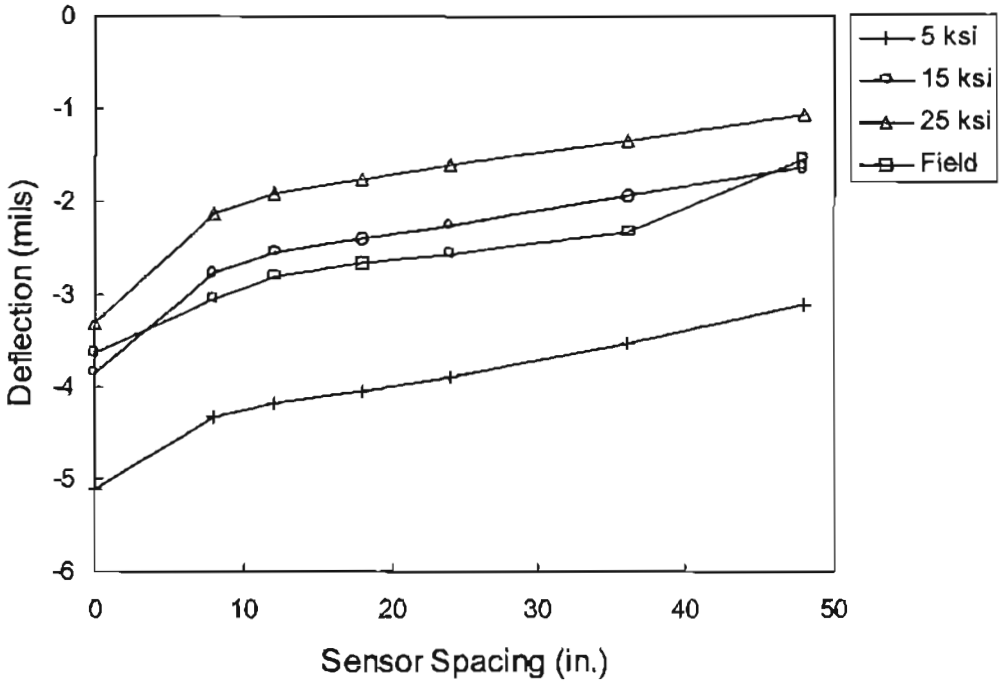

Figure A-23. Deflection comparison of synthetic and field rigid pavements

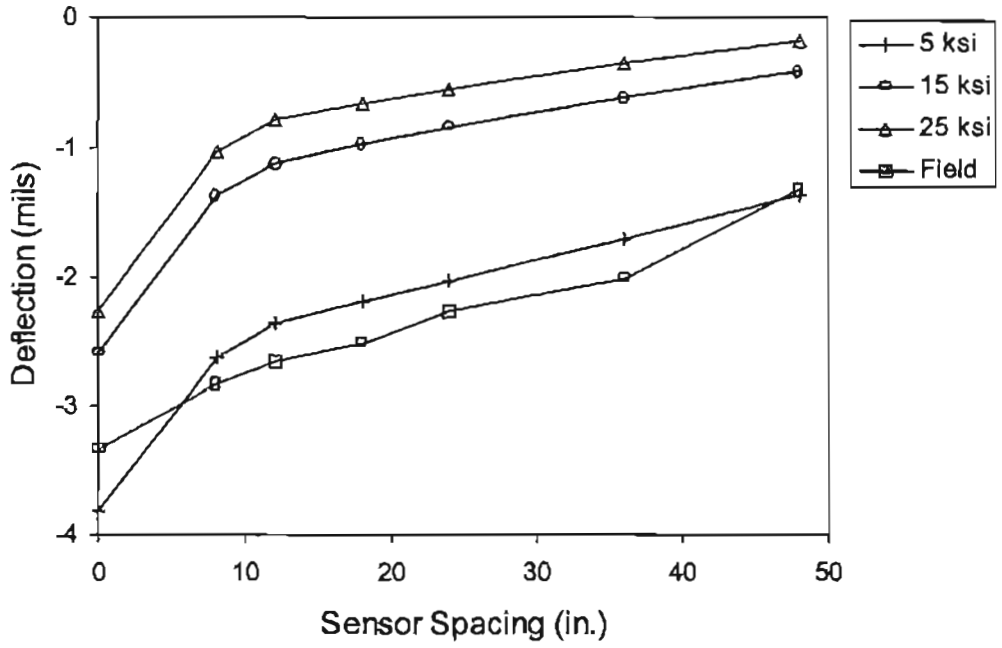

Figure A-24. Deflection comparison of synthetic and field rigid pavements

accurate response prediction. It appears that the 2-D dynamic axisymmetric finite element forward model does a good job of predicting pavement response in actual field conditions.

REFERENCES

A-1 Nazarian, S. and K. M.. Boddspati,"Pavement-Falling Weight Deflection Interaction Using Dynamic Finite Element Analysis," In Transportation Research Record 1449, TRB, National Research Council, Washington, D.,C., 1995, pp.123-133.

A-3 Chen, D-H., M.Zaman, J.Laguros, and A. Soltani, "Assessing of Computer Programs for Analysis of Flexible Pavement Structure," In Transportation Research Record 1482, TRB, National Research Council, Washington, D.,C., 1995, pp.123-133.

A-4 Zaghloul, S.M., and T.D., White, "Use of a three-dimensional, Dynamic Finite Element Program for Analysis of Flexible Pavement," In Transportation Research Record 1388, TRB, National Research Council, Washington, D.,C., 1993, pp.60-69.

A-5 Uddin, W., R.B. Hackett, A. Joseph, Z. Pan, and A.B. Crawley, "Three Dimensional Finite Element Analysis of Jointed Concrete Pavement with Discontinuities," In Transportation Research Record 1482, TRB, National Research Council, Washington, D.,C., 1995, pp.26-32..

A-6 Lee, Y.C., Condition Assessment of Flexible Pavements Using FWD Deflections," Doctor of Philosophy Dissertation, North Carolina State University, Raleigh, NC, 1997.

A-7 Raad, L. and J.L. Figueroa, (1980), "Load Response of Transportation Support Systems," Transportation Engineering Journal, ASCE, Volume 106, No. TE1, January

A-8 Shoukry, S.N., D.R. Marttinelli, and O.I. Selezeneva, "Dynamic Performance of Composite Pavements Under Impact.", In Transportation Research Record 1570, 1996, Transportation Research Board, National Research Council, Washington, D.C., pp. 163-171.

APPENDIX B

FIELD DATABASE

FIELD DATABASE

Tables B-1 through B-4 show the full depth, aggregate base, CTB, and AC/PCC pavement cases chosen from DataPave, respectively. The FWD test data available in DataPave 2.0 represented all the pavement cases considered in this approach. The DataPave database includes FWD test information from all states in the contiguous United States and some International locations. Due to the tremendous quantity of information available, all the data in DataPave 2.0 could not be used in this study. The database was made more manageable by considering only those sections tested on at least three separate occasions. Some general trends were derived from the pavement history described by the difference in the deflection information as a function of test date. However, the database continues to be updated and was void of much needed condition information at the time of this research. To accurately test for the condition of pavement layers, detailed information is needed concerning specific pavement layers. Cores were taken at each of the test sites, but only outside the pavement section. Due to possible significant variations along the site, these data cannot be used reliably to develop prediction procedures. For these reasons, DataPave information was used as a test set where some general conclusions regarding subgrade strength and depth to a stiff layer could be made.

Field data from state DOTs were less abundant. There was little quality field data for any pavement types. Tables B-5 through B-8 show the full depth, aggregate base, CTB and AC/PCC state field databases, respectively. In the CTB database, the Florida, Nevada, and Texas data sets only contained layer thickness information. The subgrade

Table B-1. Selected full depth pavements DataPave field data

State	Pavement ID	H_{ac} (in)	H_{sg} (in)
21	1034	15	120
4	1025	8	84
46	9106	7	300
47	9024	12.8	132
81	8529	6.5	60

Table B-2. Selected aggregate base pavements DataPave field data

State	Pavement ID	H_{ac} (in)	H_{abc}(in)	H_{sg} (in)
21	1010	6.3	8	180
47	3101	9.6	5	144
51	1002	5.4	8	72
1	101	6.6	7.9	-
1	102	3.9	11.9	-
51	113	4	13.9	-
51	114	6.8	17.9	-
10	102	5.5	50.8	-
4	113	4.2	7.5	-
4	114	7.1	12	-
32	101	7.1	31.3	-

Table B-3. Selected CTB pavement DataPave field data

State	SHRP ID	AC Layer	Base Layer	Subgrade
		Thickness (in)	Thickness (in)	Depth (in)
Arizona	1062	18	6	-
California	8149	4.7	6	-
Florida	3997	3	22	100
Maryland	2805	9.1	12	3.5
Mississippi	2807	10.5	6	100
North Dakota	2001	2.5	8	100
Oklahoma	4088	12.5	6	100
Texas	1050	1.8	18	100
Texas	3749	2.3	16	100
Virginia	1023	9.9	14	100
Wyoming	2019	3.8	10	28

Table B-4. Selected AC/PCC pavement DataPave field data

State	SHRP ID	AC Layer	Base Layer	Subgrade
		Thickness (in)	Thickness (in)	Depth (in)
Colorado	7035	5	8	-
Georgia	7028	6	9	-
Nebraska	7050	5	9	-
South Dakota	7049	4.5	8	-
Ontario	2812	3	7	-

Table B-5. Complete information listing of available field data for aggregate base pavements

State	Section	AC Layer	Base Layer	Subgrade	AC Layer	Base Layer	Subgrade
	Identification	Thickness (in)	Thickness (in)	Thickness (in)	Condition	Condition	CBR (%)
North Carolina (2427)	1	3.5	9.5	60	-	-	-
	2	3.5	9.5	60	-	-	-
	3	3.5	9.5	144	-	-	-
	4	3.5	9.5	144	-	-	-
North Carolina (264)	1	8	6	-	-	Weak	Weak
North Carolina (2026)	1	4	12	-	-	110	Weak
	2	4	12	-	-	50	Weak
	3	4	12	-	-	70	Weak
	4	4	12	-	-	60	Weak
North Carolina (421)	1.1	3.5	12	-	good	237	11.9
	1.3	3.5	12	-	good	329	12.5
	16.2	5	8	-	good	196	17
	16.5	5	8	-	good	122	23
	17.1	3.5	8	-	good	129	58
	17.6	3.5	8	-	good	105	167
	17.9	3.5	8	-	good	134	22
	23.5	3.5	12	-	good	167	43
	23.7	3.5	12	-	good	270	28
	24.4	2	12	-	good	631	138
	24.8	2	12	-	good	357	42
	2	2	12	-	good	568	very strong
	2.6	2	12	-	good	513	very strong
	2.8	2	12	-	good	468	very strong
	5.4	3.5	8	-	good	270	very strong
	5.7	3.5	8	-	good	252	very strong

Table B-6. Complete information listing of available field data for full-depth pavements

State	Section Identification	AC Layer Thickness (in)	Subgrade Thickness (in)	AC Layer Condition	Subgrade CBR (%)
North Carolina (2427)	1	7.75	-	-	9.8
	2	6.5	-	-	9
	3	7	-	-	5
	4	7.25	-	-	9.6
	5	7	-	-	18.5
North Carolina (421)	11.1	4	-	good	19.9
	11.3	4	-	cracking	16.4
	11.7	4	-	stripping	26
	11.8	4	-	good	42
	12.2	3.5	-	stripping	28
	12.3	3.5	-	good	27
	13.8	5	-	good	62.2
	14.1	5	-	cracking	24.4
	14.6	3.5	-	cracking	19.4
	20.1	3.5	-	good	16
	20.4	3.5	-	cracking	18.5
	22.2	3.5	-	stripping	13.7
	22.5	2	-	stripping	15.9
	22.6	2	-	good	58

Table B-7. Complete information listing of available field data for CTB pavements

State	Section Identification	AC Layer Thickness (in)	Base Layer Thickness (in)	Subgrade Thickness (in)	AC Layer Condition	Base Layer Condition	Subgrade CBR (%)
Florida	106	5	4	7.3	.	.	.
	109	5.2	11.7	6.8	.	.	.
North Carolina (49)	A9	4.75	.	.	Debonded	.	.
	A12	4.25	7.25	.	Intact	Intact	.
	A21	4.5	8.25	.	Intact	Intact	.
	A30	4.5	3.5	.	Intact	Cracked	.
	A40	4.38	7.5	.	Intact	Intact	.
North Carolina (58)	1	1.5	7	.	Intact	Intact	.
	2	5	7	.	Intact	Intact	.
	3	7.5	7	.	Intact	Intact	.
North Carolina (421)	4.3	3.5	5.5	.	Stripping	.	41.15
	4.7	3	9	.	Single Crack	Single Crack	16.02
	4.8	3.5	.	.	Stripping	.	13.8
	6.1	7.25	5.75	.	Stripping	.	20.63
	6.2	.	.	.	Broken	Broken	.
	6.4	5	8.5	.	.	Good	34.37
	6.6	4.5	5.5	.	Good	Good	.
	6.8	.	.	.	.	.	46
	8.5	6.25	.	.	.	.	46
	8.9	.	.	.	Broken	Broken	.
	10.5	3.75	5.25	.	Good	Good	.
	10.8	3.5	5.5	.	Stripping	.	25.3
	15.1	6.5	.	.	Stripping	.	14.29
	15.2	.	.	.	.	.	24.31
	18.3	4	.	.	Stripping	Broken	14.95
	18.4	4	.	.	Good	Good	
	18.6	3.75	7.5	.	Good	Good	24.4
	18.7	4.75	7.25	.	Good	Good	.
	18.9	4	.	.	Good	Good	.
	19.1	6	.	.	Stripping	.	18.76
	19.3	2.375	.	.	Good	Good	.
	19.4	2.375	.	.	Good	Good	.
	19.6	7	.	.	.	.	35
	19.8	7.25	.	.	Good	Good	.
	19.9	7.625	.	.	Good	Good	22.8)
	21.2	5	5.25	.	Good	Good	17.2
	21.4	5	5.25	.	.	Broken	13.71
	21.8	5	5.5	.	.	.	16.03
Nevada	104	12.4	12	100	.	.	.
Ohio	390159	4	4	300	Intact	Intact	.
Texas	113	2	12	100	.	.	.
	115	5	12	100	.	.	.
	116	3.3	12	100	.	.	.
	123	9.1	12	100	.	.	.
	124	9.3	12	100	.	.	.

Table B-8. Complete information listing of available field data for AC/PCC pavements

State	Section	AC Layer	Base Layer	Subgrade	AC Layer	Base Layer	Subgrade
	Identification	Thickness (in)	Thickness (in)	Thickness (in)	Condition	Condition	M_r (ksi)
Ohio	0107192e	8.5	9	300	-	-	9.4
	0407912e	8.5	9	300	-	-	9.2
	0107091f	7	9	300	-	-	-
Montana	00090_p	4.8	8	-	-	-	16
Washington	Was-195-8	3	7	-	-	-	28

depth information was included, so these data sets were used for the determination of depth to a stiff layer. The Ohio data was reportedly tested on a newly constructed pavement and included all layer thickness information. Therefore it was considered intact. The Ohio field report showed some of the Ohio data to be erroneous, and therefore those data points were excluded from this study. Arrowood Road in Charlotte, North Carolina (NC 49) contained upper layer thickness information and core data that gave insight into the layer condition. Subgrade soil type was given with no condition information. The NC 58 test section data set contained core information (including layer thicknesses) and had been open to traffic only one year at the time of testing, and therefore considered intact.

The NC 421 field record is the most complete received in this study. Twenty-four pavement sections were constructed in 1989 to study the performance of different pavement types. Figure B-1 shows the section profiles of the pavements constructed for the NC 421 project. Sections 1, 3, 16, and 23 are aggregate base pavements, sections 7, 9, 20, and 22 are full depth pavements, sections 2, 5, 11, 12, 13, 14, 17, and 24 are flexible pavements with stabilized subgrade, and sections 4, 6, 8, 10, 15, 18, 19, and 21 are CTB pavements, with lime stabilized subgrade in sections 8, 10, 15, and 19. The layer thicknesses varied for each section type. In August of 1993, cores were taken at several locations in each test section. Cores extracted yielded information including layer thickness and condition information. Therefore deflection testing information corresponding to core information is available at several locations in each section. Figure B-2 shows a typical pavement cross-section. Strain gauges, moisture sensors, pressure cells, and thermocouples were imbedded in each test section so that detailed information

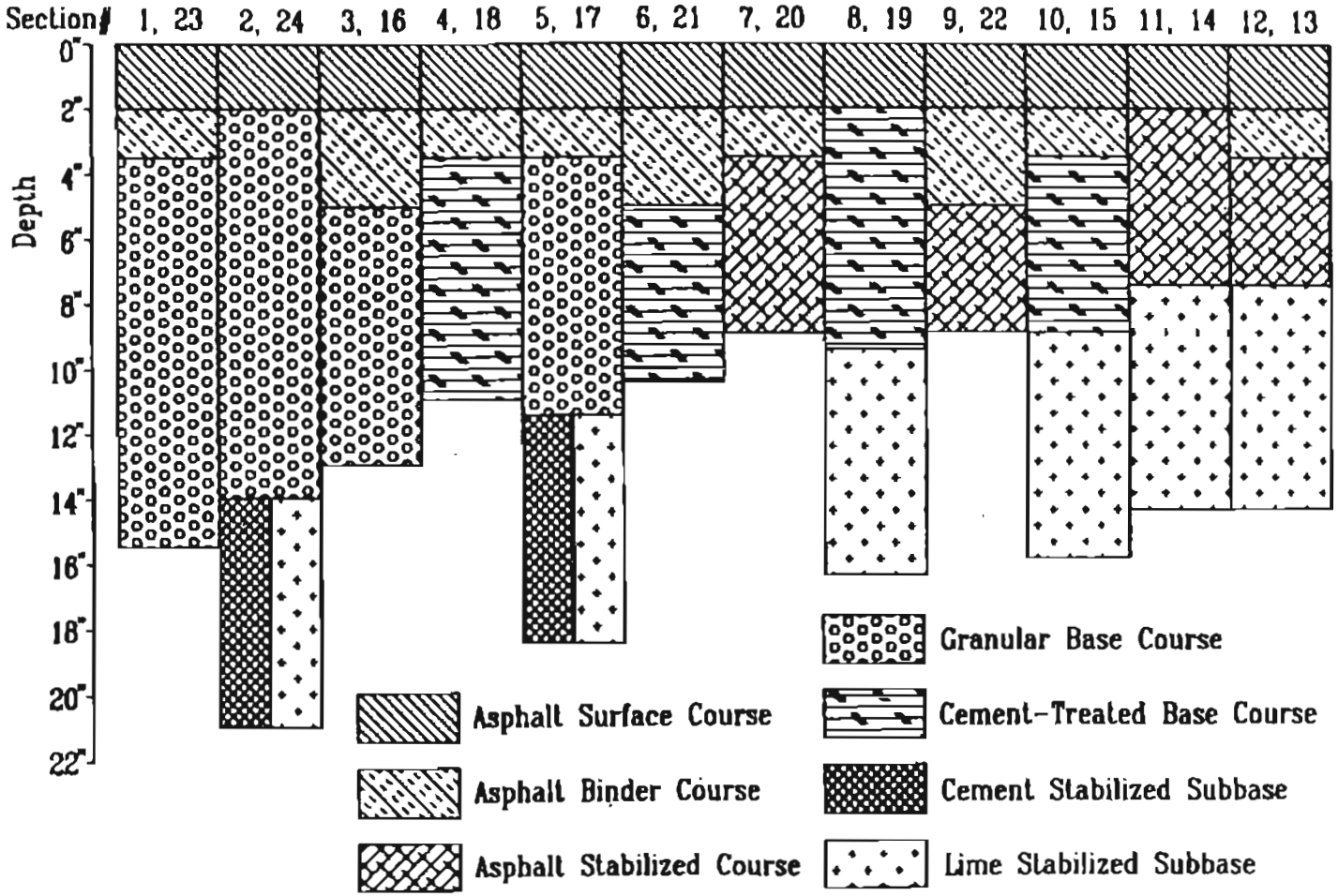

Figure B-1. NC 421 test section layout

Sections 1 & 23

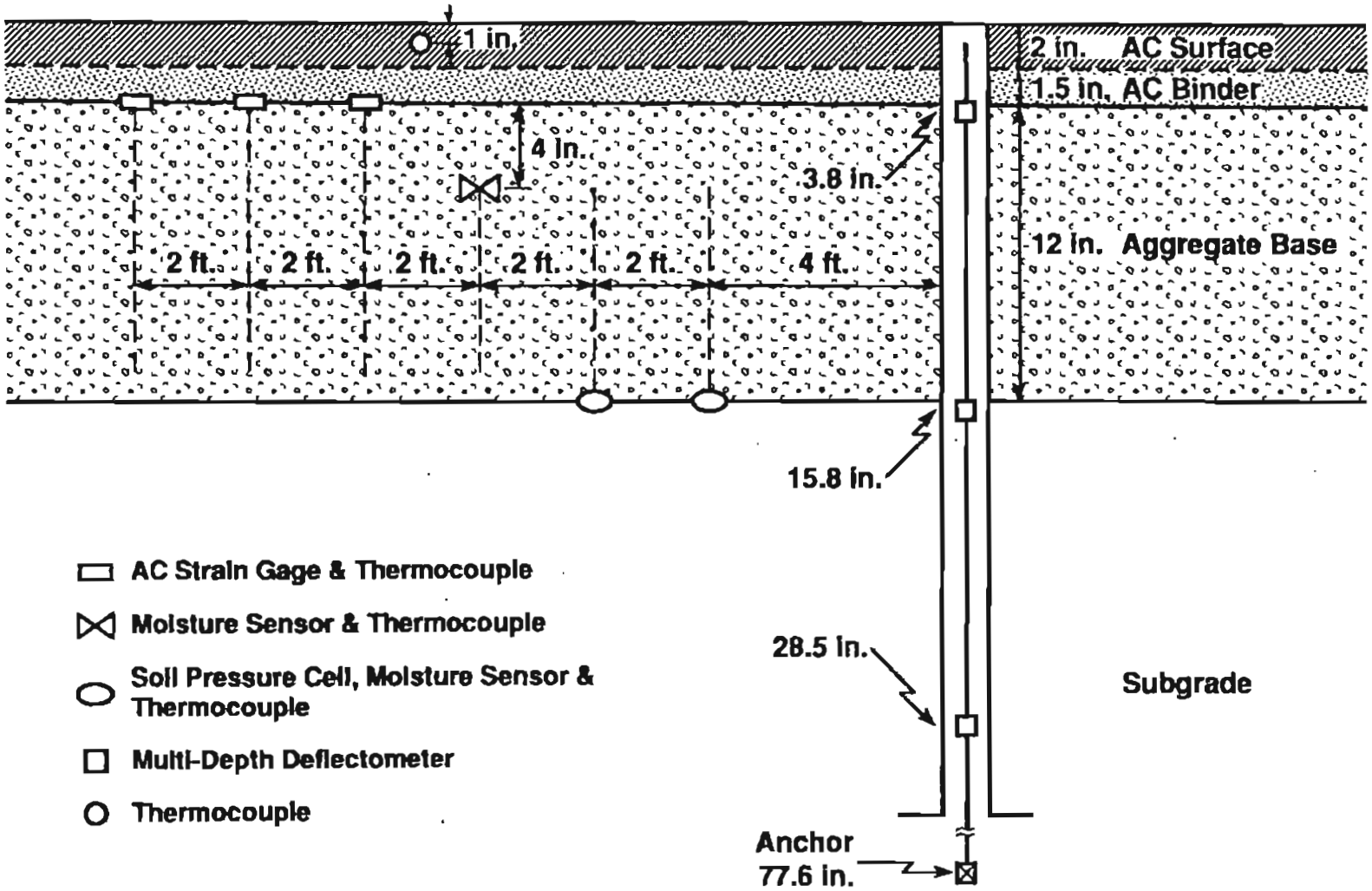

Figure B-2. Typical NC 421 pavement cross-section

could be collected during FWD testing. Field records from February 1990, November 1990, May 1991, October 1991, February 1992, March 1992, June 1992, October 1992, February 1993, June 1993, and August 1993 were available. The distressed data set used in the analysis consisted of each point in August where core logs showed distresses. At locations where core logs showed intact layers, all previous FWD results were also considered intact. DCP testing was performed at several locations in each test section. The data from those tests were recorded and percent CBR values were estimated. Therefore, in the NC 421 field database at several points in each test section deflection data, core information, and CBR subgrade information was known.

In the AC/PCC state field database, the Ohio data were the most complete. Field reports were available and included detailed information on site conditions, layer thicknesses, and laboratory tests of cored subgrade materials. Upper layer condition at the time of testing was unknown. The Montana field data included upper layer thicknesses and backcalculated subgrade resilient moduli values. Washington field data were accompanied with a field report that listed site conditions, construction procedures, upper layer thicknesses, and resilient modulus of subgrade materials.

APPENDIX C

DEFLECTION BASIN PARAMETER AND SURFACE MODULUS METHODS

DEFLECTION BASIN PARAMETER ANALYSIS

Deflection basin parameters (DBPs), which are derived from FWD deflection measurements, are established to be good indicators of selected pavement properties and conditions. Their effective use, instead of the deflection measurements alone, in pavement analyses has been generally documented in the literature. In this research we investigated a range of DBPs (a list is given in Table 2 in the "Introduction" chapter) in conjunction with other information as condition indicators. This investigation, which was carried out based on synthetic database, first examined the sensitivity of DBPs to pavement parameters, such as modulus values, layer thickness, stress and strain values, which are critical for describing the condition. Based on the sensor location of the deflection information used in deriving a DBP, the pavement layer that is best characterized by that DBP can be predicted, and therefore narrow the number of combinations to explore. For example, if the outer sensor measurements define a DBP, then that DBP better characterizes the condition of the lower layers. Using the sensitivity information, the DBPs that best describe the changes in pavement parameters are identified as potential condition indicators. Instead of just the most sensitive DBP, a small set of DBPs that showed significant sensitivity was identified. Conceptually, a sensitive DBP could be used to indicate any change in the pavement parameter to which that DBP is most sensitive, enabling a mechanism for identifying the pavement condition that contributes to the change.

As these sensitive DBPs were identified using synthetic data, their sensitivity to field data may not necessarily be similar. In some cases the most sensitive DBP as

identified above did not show the anticipated response to changes in the corresponding pavement parameter or condition.

These sensitive DBPs are then incorporated into the condition evaluation procedures and analyses. This is accomplished by developing the association between the DBPs and condition indicators. For each indicator, a functional relationship is identified using an empirical approach based on the synthetic database. The following sections describe the details and results of this investigation for each type of pavement. Although the results are specific to the data sets used in this investigation, the approach adopted here should be viewed as a sufficiently general approach applicable to future studies using other data sets.

Full-depth and Aggregate Base Pavements

Development of prediction approaches for layer condition indicators for each pavement layer is described below:

AC Modulus (E_{ac})

The deflection basin parameter *SCI* is understood to better represent the condition of upper layers, especially AC layer. An interesting finding from the synthetic database is that, for a certain thickness of AC layer, E_{ac} and *SCI* exhibits an approximately linear relationship in log-log scale. A stiff layer, if exists, has little or no effect on the *SCI* value, while the condition of subgrade has a minor effect, especially when AC layer is strong. Figures C-1 and C-2 show the relationship between E_{ac} and *SCI* for full-depth

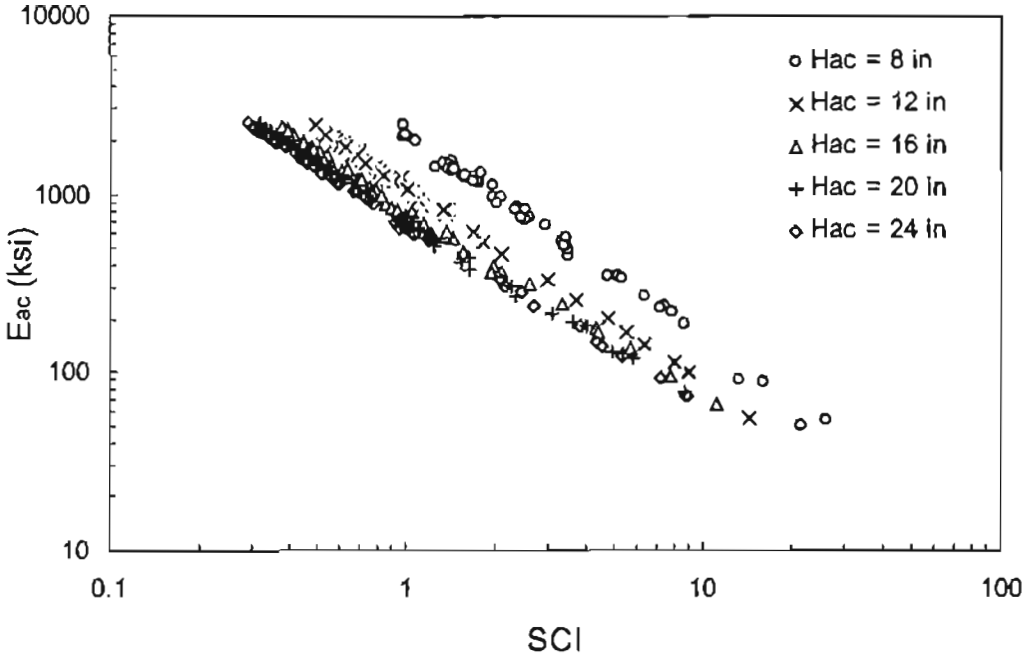

Figure C-1. E_{ac} vs. *SCI* for various H_{ac} for full-depth pavements from the synthetic data

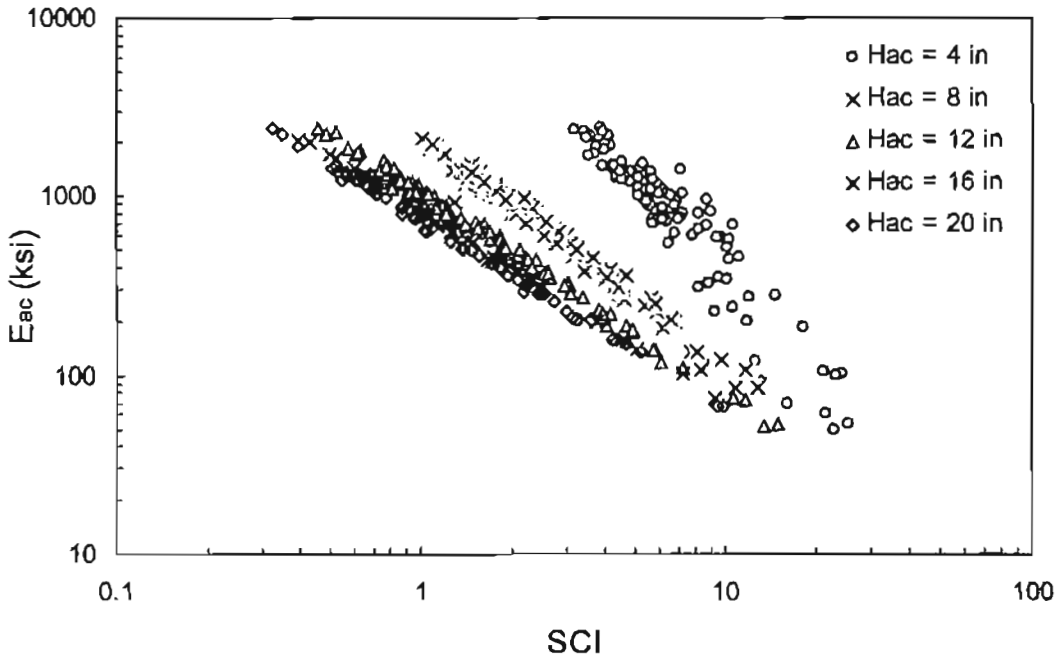

Figure C-2. E_{ac} vs. *SCI* for various H_{ac} for aggregate base pavements from the synthetic data

pavements and aggregate base pavements, respectively, for different values of AC thickness. It is noted that when AC layer is weaker (e.g., when H_{ac} is equal to 4 inches for aggregate base pavements as shown in Figure C-2), more deviations can be seen in the *SCI vs.* E_{ac} relationship, which may be due to the increased influence from the lower layers. As both AC thickness and E_{ac} increase, the influence from lower layers decreases. When AC thickness is larger than 16 inches, H_{ac} no longer influences *SCI*, resulting in a relationship for *SCI* only in terms of E_{ac}. For full-depth pavements, AC thickness is usually greater than 6 inches. Thus, the effect of lower layers can be negotiable. For aggregate base pavements with AC thickness less than 6 inches, *BDI* is added into the regression equation below to reflect the increased influence from lower layers. The following relationships were established between E_{ac} and *SCI* for full-depth and aggregate base pavements:

For full-depth pavements,

$$\log(E_{ac}) = -1.0831 * \log(SCI) - 2.6210 * \log(H_{ac}) + 0.0482 * H_{ac} + 5.2961 \quad \text{(C-1)}$$

$R^2 = 0.994 \qquad SEE = 0.028$

For aggregate base pavements,

when $H_{ac} \geq 6$ inches,

$$\log(E_{ac}) = -1.1435 * \log(SCI) - 2.5635 * \log(H_{ac}) + 0.0498 * H_{ac} + 5.2005 \quad \text{(C-2)}$$

$R^2 = 0.988 \qquad SEE = 0.039$

when $H_{ac} < 6$ inches,

$$\log(E_{ac}) = -2.4527 * \log(SCI) + 1.4116 * \log(BDI) - 2.1621 * \log(H_{ac}) + 0.0013 * H_{abc} + 5.123 \quad \text{(C-3)}$$

$R^2 = 0.965 \qquad SEE = 0.099$

AC Tensile Strain (ε_{ac})

Based on ILLI-PAVE analysis, Hill and Thompson (C-1) established a simple regression equation to predict the tensile strain at bottom of AC layer directly from the value of *AUPP*. Based on the synthetic database developed in this research, the relationship between ε_{ac} and *BDI* was found to give better correlation. Figure C-3 shows the approximately linear relationships that were found between ε_{ac} and *BDI* in the log-log scale for full-depth pavements. For aggregate base pavements, the relationship between ε_{ac} and *BDI* are as shown in Figure C-4. It must be noted that, for aggregate base pavements, when the ratio of H_{ac} to a, the radius of load area, is less than 1 ($H_{ac} < 6$ inches), more variations were found in the ε_{ac}-*BDI* relationship. This can be attributed to the presence of the weaker AC layer, and therefore the increased influence from lower layers on ε_{ac}. The relationships between ε_{ac} and *BDI* are as follows:

For full-depth pavements,

$$\log(\varepsilon_{ac}) = 0.9977 * \log(BDI) + 1.7142 \qquad \text{(C-4)}$$

$R^2 = 0.987 \qquad SEE = 0.049$

For aggregate base pavements,

when $H_{ac} \geq 6$ inches,

$$\log(\varepsilon_{ac}) = 1.023 * \log(BDI) + 1.7127 \qquad \text{(C-5)}$$

$R^2 = 0.981 \qquad SEE = 0.052$

when $H_{ac} < 6$ inches,

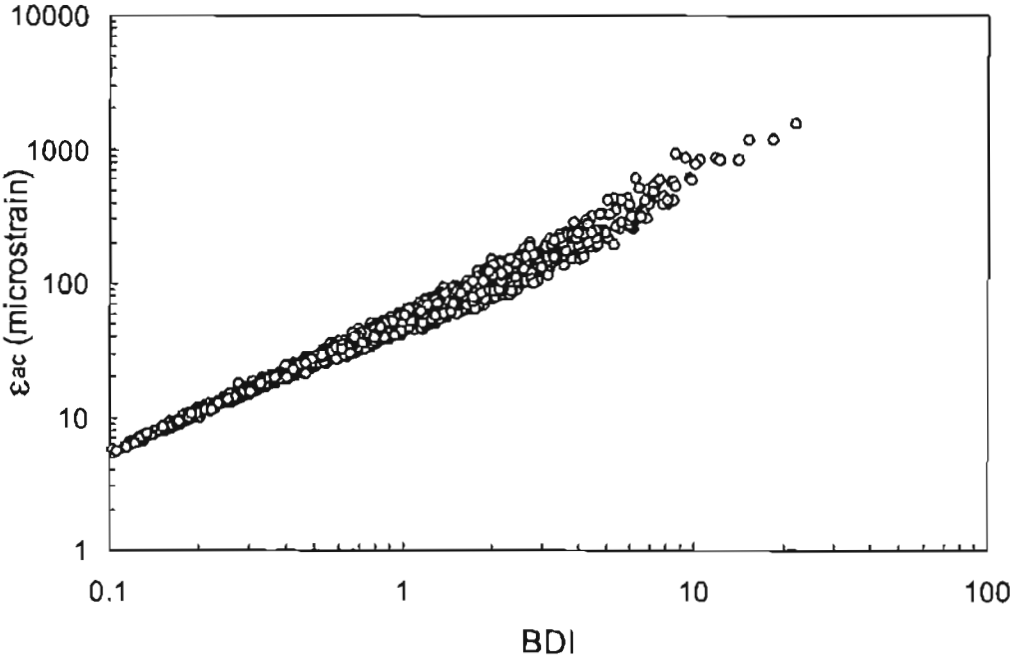

Figure C-3. ε_{ac} vs. *BDI* for full-depth pavements from the synthetic data

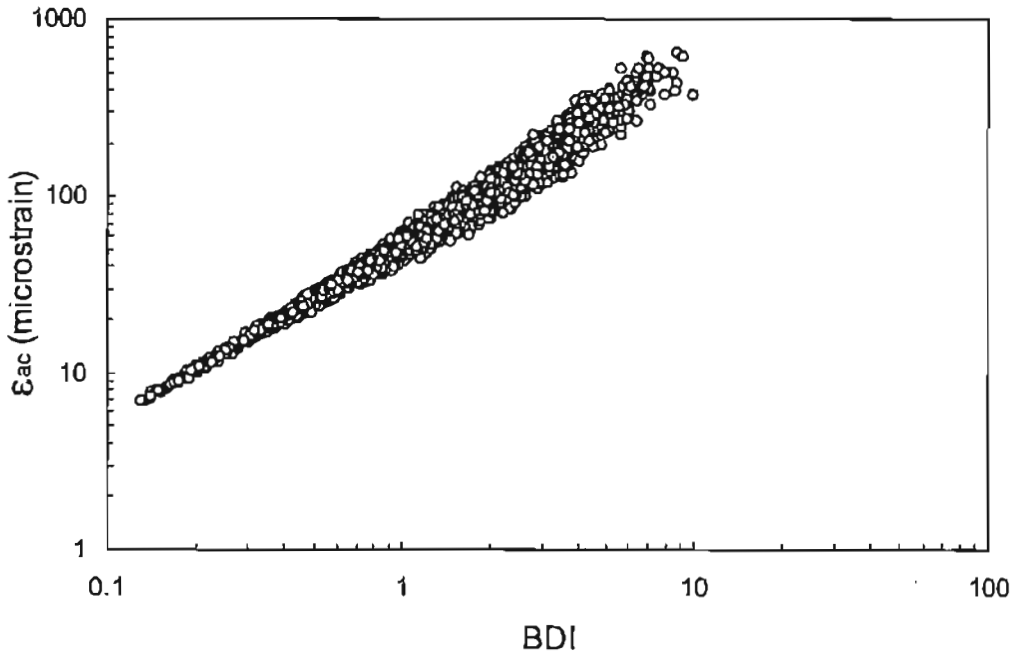

Figure C-4. ε_{ac} vs. *BDI* for aggregate base pavements from the synthetic data

$$\log(\varepsilon_{ac}) = 0.7798 * \log(SCI) + 0.2279 * \log(BDI) + 0.5736 * \log(H_{ac}) + 0.0410 * \log(H_{abc}) + 1.1604 \quad \text{(C-6)}$$

$R^2 = 0.969 \qquad SEE = 0.041$

Compressive Strains of Base and Subgrade (ε_{abc} and ε_{sg})

For intact pavements, the layer interfaces can be considered to be fully bonded, and the strains at the interfaces to be therefore continuous. Based on this, the following relationships can be established:

For full-depth pavements,

$$\frac{\varepsilon_{ac}}{\varepsilon_{sg}} = \nu \quad \text{(C-7)}$$

For aggregate base pavements,

$$\frac{\varepsilon_{ac}}{\varepsilon_{abc}} = \nu \quad \text{(C-8)}$$

where ν is Poison's Ratio. Since ε_{ac} is a linear function of *BDI* in log-log scale as described previously, the relationships between ε_{abc} and *BDI* for aggregate base pavements, and between ε_{sg} and *BDI* for full-depth pavements in log-log scale are expected to be linear as well. Figure C-5 shows the relationship between *BDI* and ε_{sg} for full-depth pavements, and Figure C-6 shows the relationship between *BDI* and ε_{abc} for aggregate base pavements. For full-depth pavements, the relationship between ε_{sg} and *BDI* is represented by:

$$\log(\varepsilon_{sg}) = 0.9823 * \log(BDI) + 2.1460 \quad \text{(C-9)}$$

$R^2 = 0.978 \qquad SEE = 0.063$

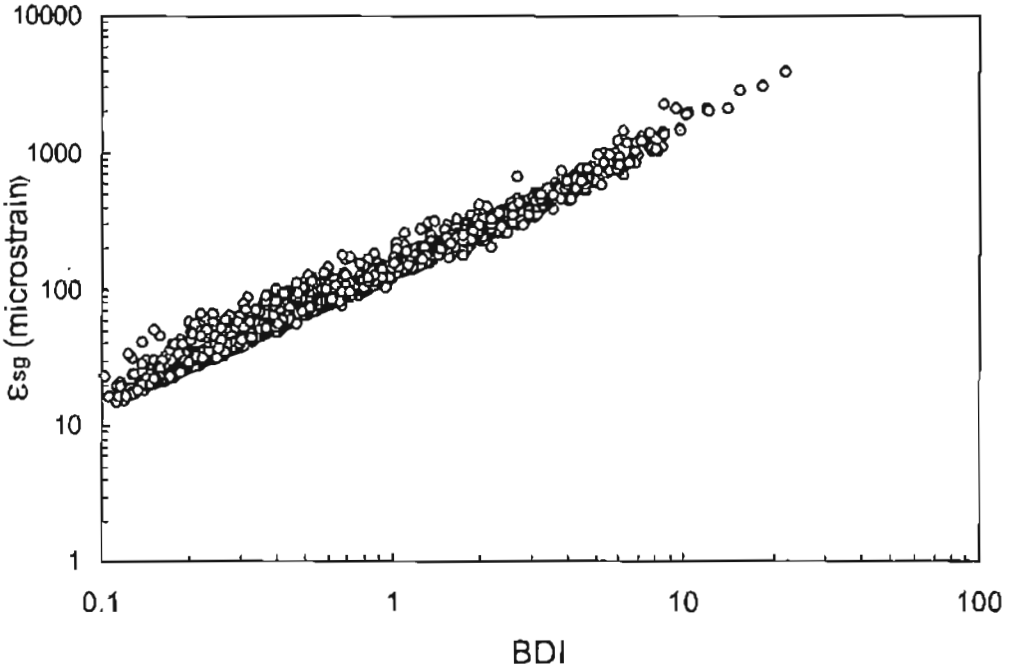

Figure C-5. ε_{sg} vs. *BDI* for full-depth pavements from the synthetic data

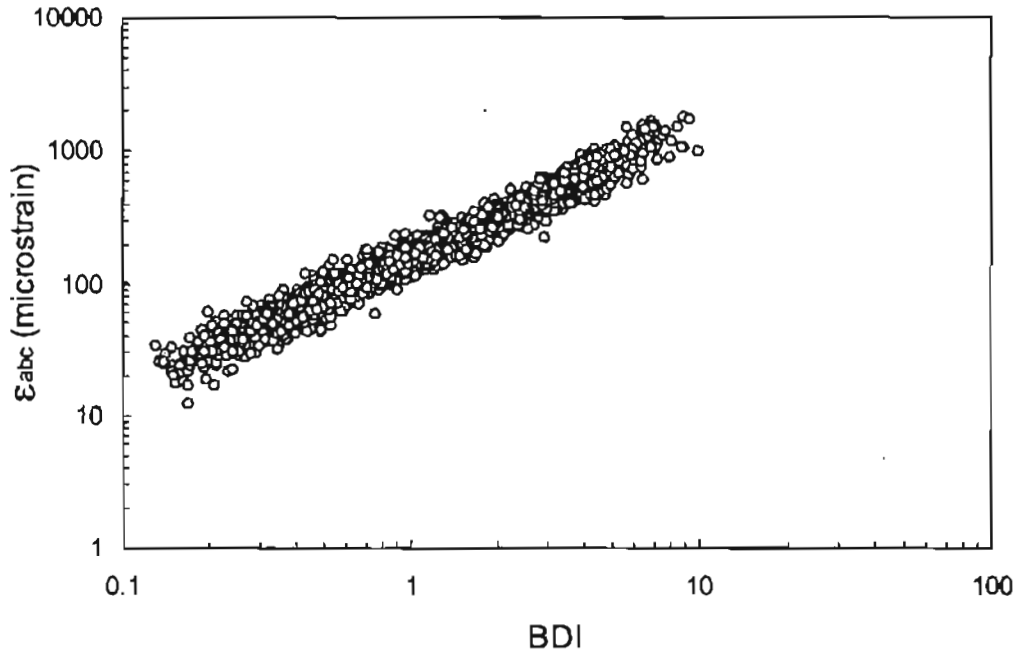

Figure C-6. ε_{abc} vs. *BDI* for aggregate base pavements from the synthetic data

For aggregate base pavements, ε_{abc} and ε_{sg} are represented in terms of *BDI* and *BCI* as follows.

For $H_{ac} \geq 6$,

$$\log(\varepsilon_{abc}) = 0.9958 * \log(BDI) + 2.1955 \qquad \text{(C-10)}$$

$$R^2 = 0.976 \qquad SEE = 0.052$$

$$\log(\varepsilon_{sg}) = 0.2811 * \log(BDI) + 0.6788 * \log(BCI) - 0.0135 * \log(H_{ac}) - 0.0123 * H_{abc} + 2.2083 \qquad \text{(C-11)}$$

$$R^2 = 0.988 \qquad SEE = 0.016$$

For $H_{ac} < 6$,

$$\log(\varepsilon_{abc}) = 0.7357 * \log(SCI) + 0.1043 * \log(BDI) + 0.1240 * \log(H_{ac}) + 0.0648 * \log(H_{abc}) + 2.0730 \qquad \text{(C-12)}$$

$$R^2 = 0.963 \qquad SEE = 0.054$$

$$\log(\varepsilon_{sg}) = 0.8835 * \log(BDI) + 0.1526 * \log(BCI) - 0.0995 * \log(H_{ac}) - 0.0185 * H_{abc} + 2.2461 \qquad \text{(C-13)}$$

$$R^2 = 0.976 \qquad SEE = 0.010$$

In summary, based on the synthetic database from dynamic, nonlinear analysis, *SCI* was found to have a high correlation with E_{ac}, and *BDI* was found to have a high correlation with ε_{ac}. *BDI* was also found to correlate well with ε_{abc} for aggregate base pavements and with ε_{sg} for full-depth pavements. For aggregate base pavements, ε_{sg} was described as function of *BCI* and *BDI*. It should be noted that these findings agree very well with the conclusion from the sensitivity study that was based on the synthetic

database from dynamic, linear elastic analysis, suggesting that the effects of layer properties on deflection parameters are consistent between linear and nonlinear analyses.

Cement Treated Base (CTB) Pavements

Development of prediction approaches for layer condition for each pavement layer is described below.

Debonding in Asphalt Layer

The deflection basin parameter approach in the case of debonding in the asphalt layer in CTB pavements was inconclusive, as no field data from state DOTs with known debonding in the asphalt layer was received until well into the third year of the project. As Appendix B shows, North Carolina highway 49 section A9 was the only field data submitted with known debonding in the asphalt layer. This NC-49 data consists of a total of six data points. With such a small amount of information, a meaningful relationship could not be developed.

Cracking in Cement Treated Base Layer

The "Findings" chapter shows the five deflection basin parameters most likely to represent cement treated base layer condition to be BDI, BCI, AUPP, F2, and SCI. Therefore, these DBP's were investigated using available field data to develop a relationship that would best represent actual layer condition. Figures C-7 through C-11 show each DBP versus test date for all available field data. BDI appears to be the DBP that best distinguishes between intact and cracked pavement cases. The parametric study based on synthetic data also identified BDI as the DBP most capable of representing CTB

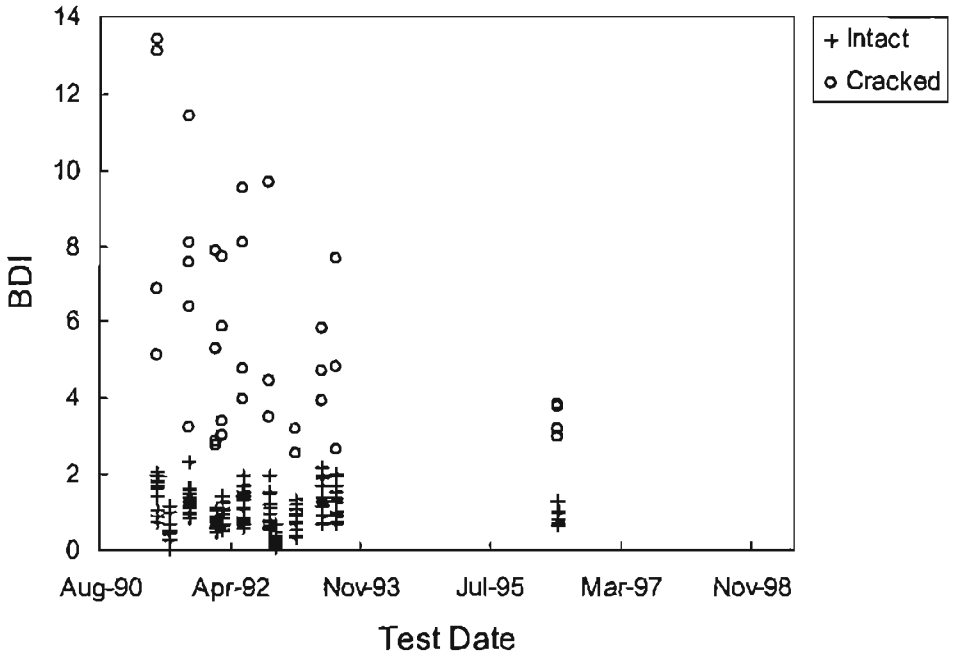

Figure C-7. BDI vs. test date for CTB state field data

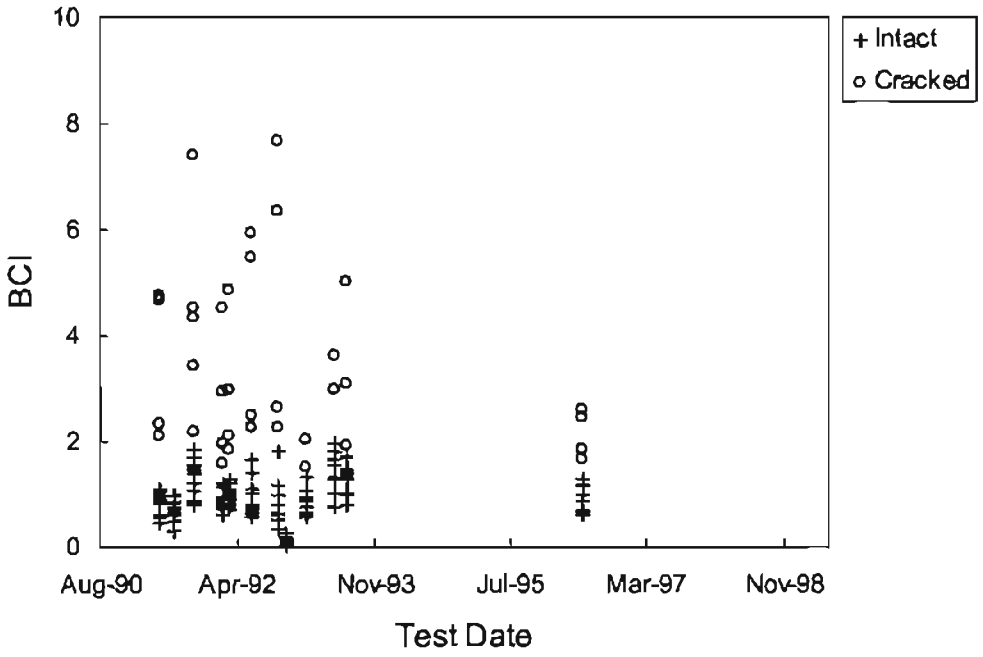

Figure C-8. BCI vs. test date for CTB state field data

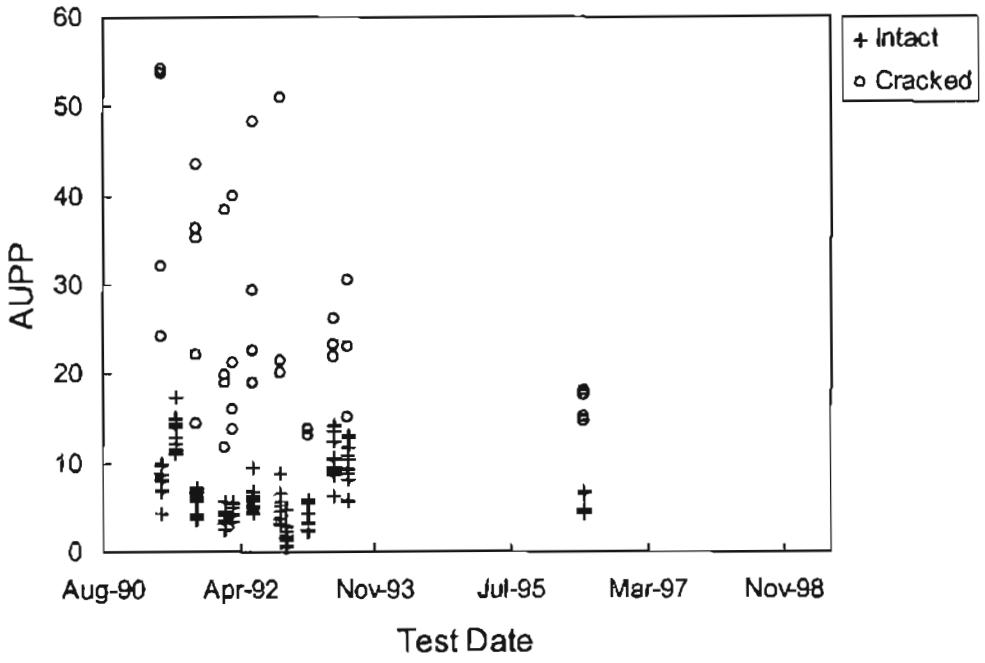

Figure C-9. AUPP vs. test date for CTB state field data

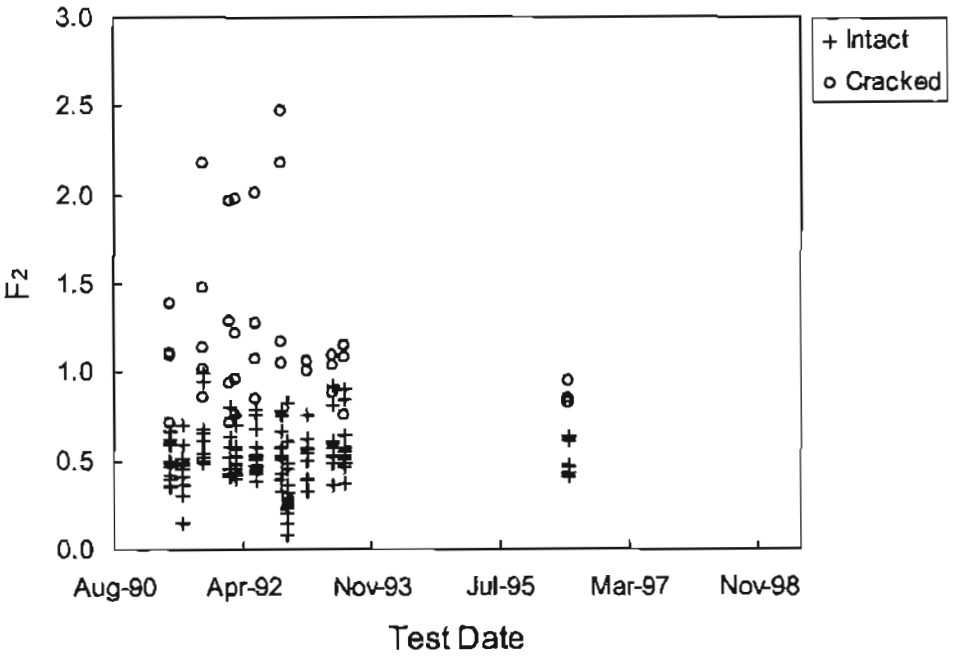

Figure C-10. F_2 vs. test date for CTB state field data

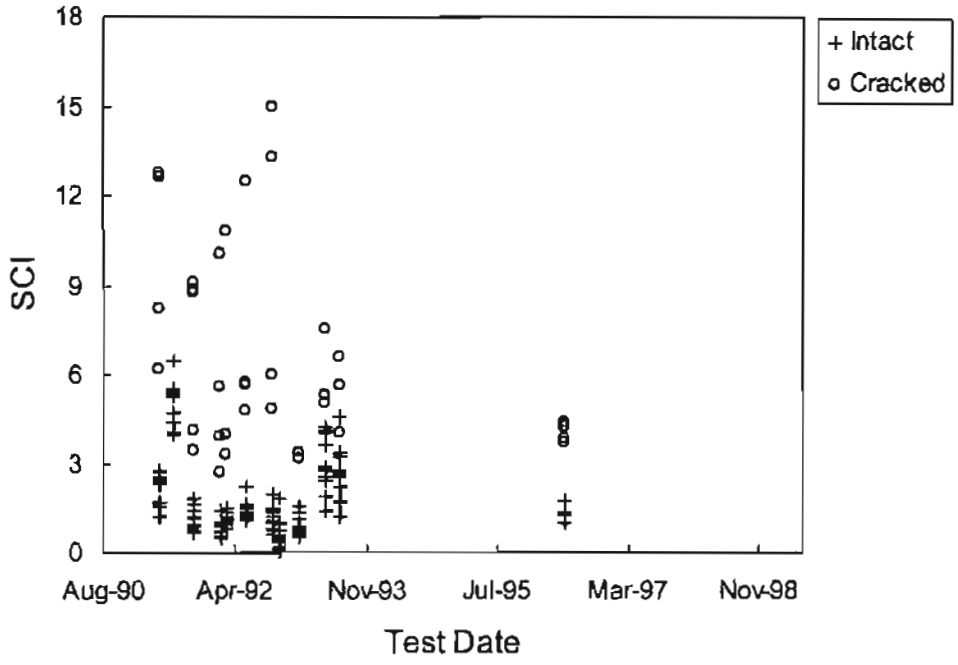

Figure C-11. SCI vs. test date for CTB state field data

layer condition. Test data with known CTB layer condition supported the parametric study results. Therefore, BDI was chosen as the DBP to indicate the CTB layer condition.

The synthetic database was then revisited to determine a meaningful BDI value to be used as a test criterion. Core data from field records, listed in Appendix B, showed that the strength of intact base layers ranged between 1500 and 2000 ksi. Base layer moduli values in synthetic cases were set to 500, 1000, 1500, 2000, and 2500 ksi. All synthetic cases with a CTB layer modulus of 1500, 2000, and 2500 ksi were separated and their respective BDI values calculated. Figure C-12 illustrates this relationship. The maximum value of BDI for the 1500, 2000, and 2500 ksi CTB layer modulus conditions is 2.5, 2.3, and 2.0, respectively. The BDI value matching the lowest field core test was chosen as the BDI value representing intact CTB layer condition. Therefore, and value of BDI less than or equal to 2.5 is considered to indicate intact condition. When the BDI criteria value of 2.5 is added to the field data in Figure C-13, it is clear that all available field data are properly distinguished.

Subgrade Strength

The deflection basin parameter approach to determine subgrade condition in CTB pavements began with the parametric study described previously. The five deflection basin parameters identified in the parametric study were D_{48}, LSI, D_{18}, $AREA_3$, and BCI. Field data from NC 421 were the only points made available with known subgrade condition. This information was used to develop an indicator for subgrade layer condition in CTB pavements. Deflection basin parameters deemed most promising in

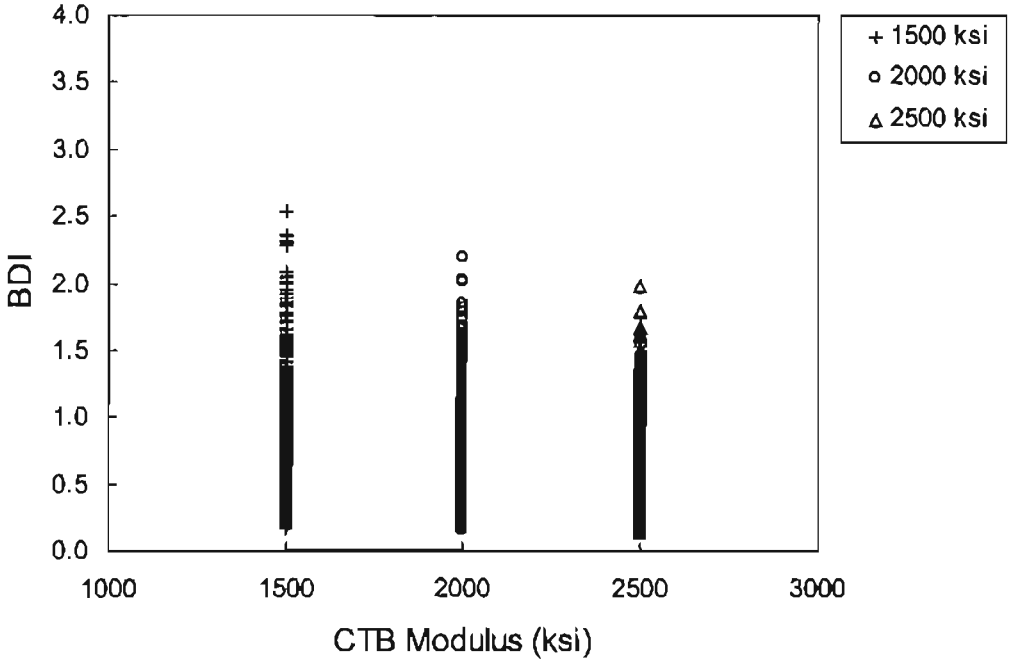

Figure C-12. BDI vs. CTB modulus for CTB synthetic cases

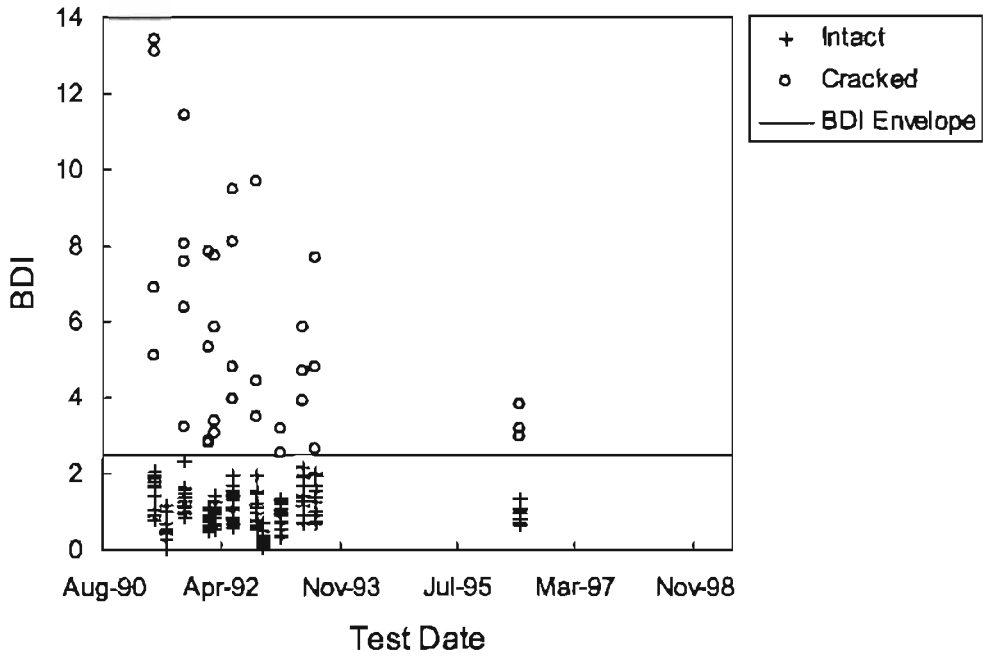

Figure C-13. BDI vs. test date for CTB state field data with BDI envelope

finding a subgrade strength indicator were plotted against the CBR values estimated from the DCP results for the test data set described in Appendix B. Figures C-14 to C-18 show this relationship. For each deflection basin parameter investigated, the best-fit curve with the highest R-squared value was generated. In each plot, a line corresponding to a CBR value of 10 was included. The NCDOT recognizes 10 as a CBR value consistent with poor subgrade behavior. Of the five deflection basin parameters considered, D_{48} correlates most strongly with the CBR values. D_{48} is the deflection four feet from the load center. Theoretically, the last sensor in FWD testing represents lower layer condition. Therefore, it is reasonable that D_{48} is a quality measure of subgrade condition. Figure C-14 shows that following FWD testing, the CBR value can be estimated by plotting the deflection value four feet from the load center against the regression curve. As D_{48} decreases, CBR increases. This would imply that a low deflection value would correspond to a strong subgrade. Established theory, the synthetic parametric study, and regression analysis indicate that D_{48} is a promising DBP for the determination of subgrade condition in CTB pavements.

Depth to a Stiff Layer

Depth to a stiff layer in CTB pavements can be estimated using the F_3 deflection basin parameter. The parametric study showed F_3 to be the most sensitive to changes in stiff layer depth. The field data from Florida, Nevada, Ohio, and Texas described in Appendix B was used to develop a relationship between deflection basin parameters and stiff layer depth. Each deflection basin parameter listed in the parametric study was plotted against stiff layer depth. Regression was performed to determine the best-fit

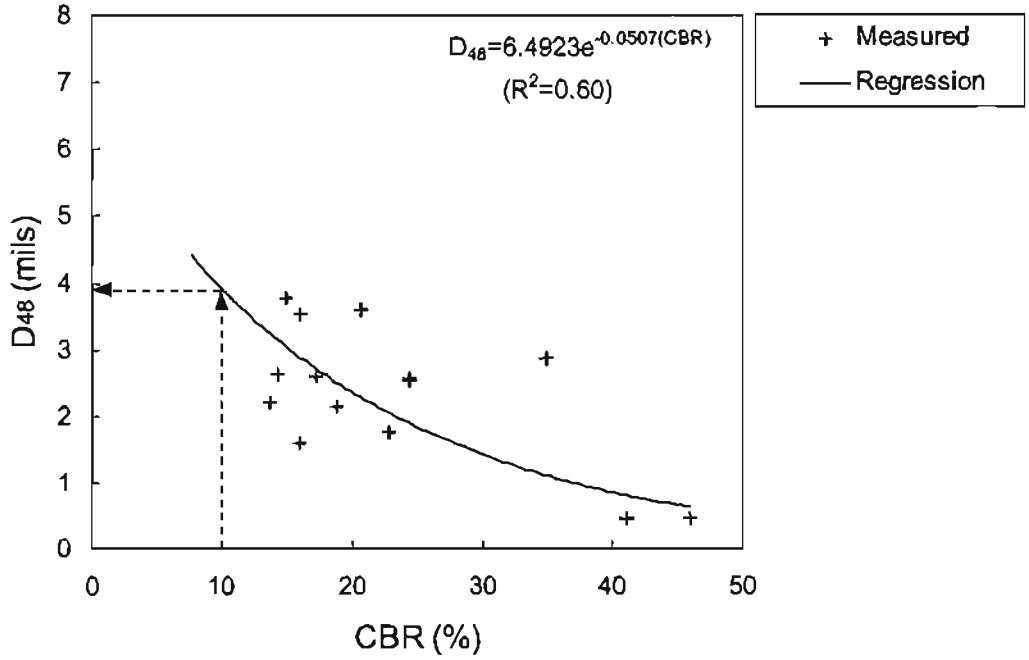

Figure C-14. D_{48} vs. CBR for NC421 CTB pavements

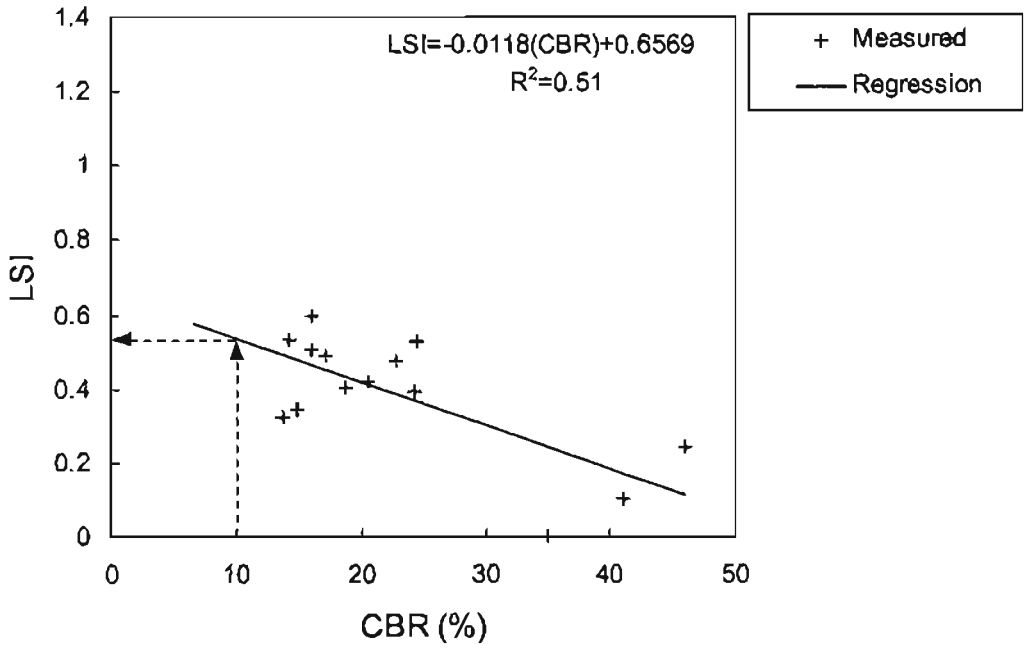

Figure C-15. LSI vs. CBR for NC421 CTB pavements

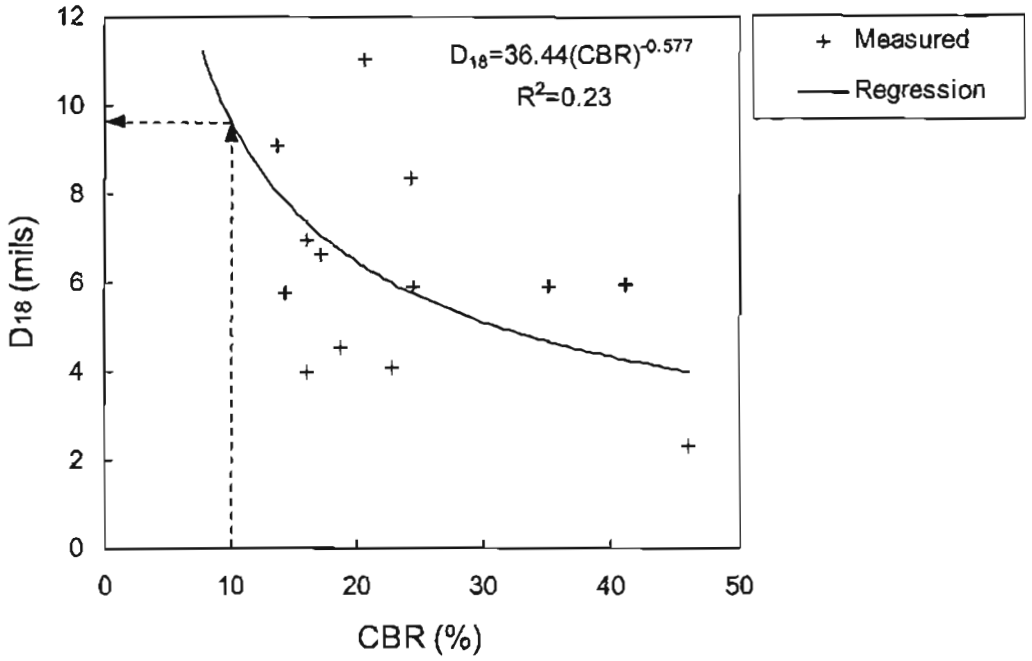

Figure C-16. D_{18} vs. CBR for NC421 CTB pavements

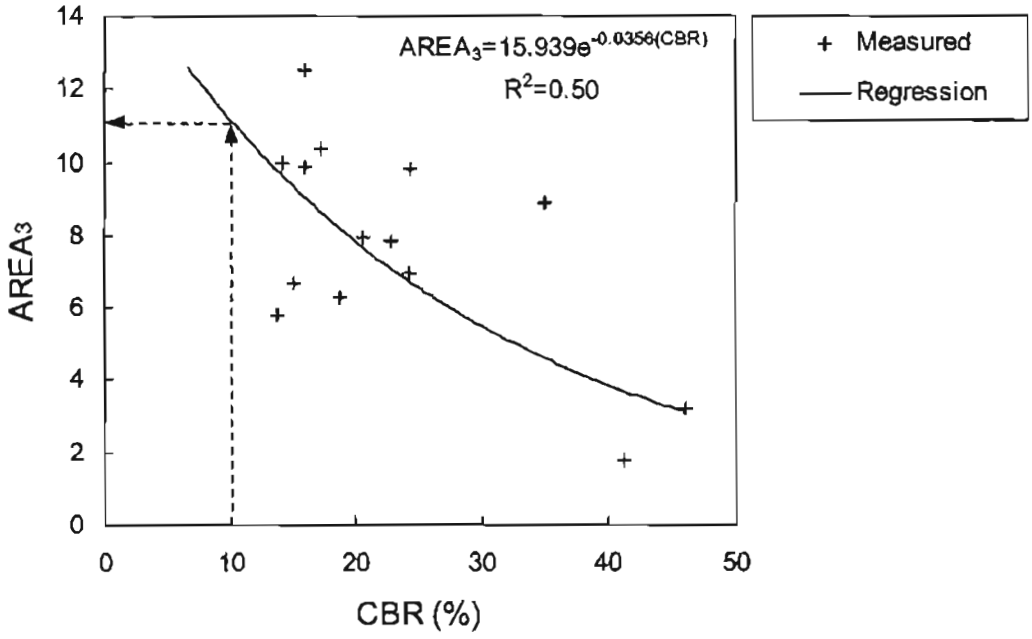

Figure C-17. $AREA_3$ vs. CBR for NC421 CTB pavements

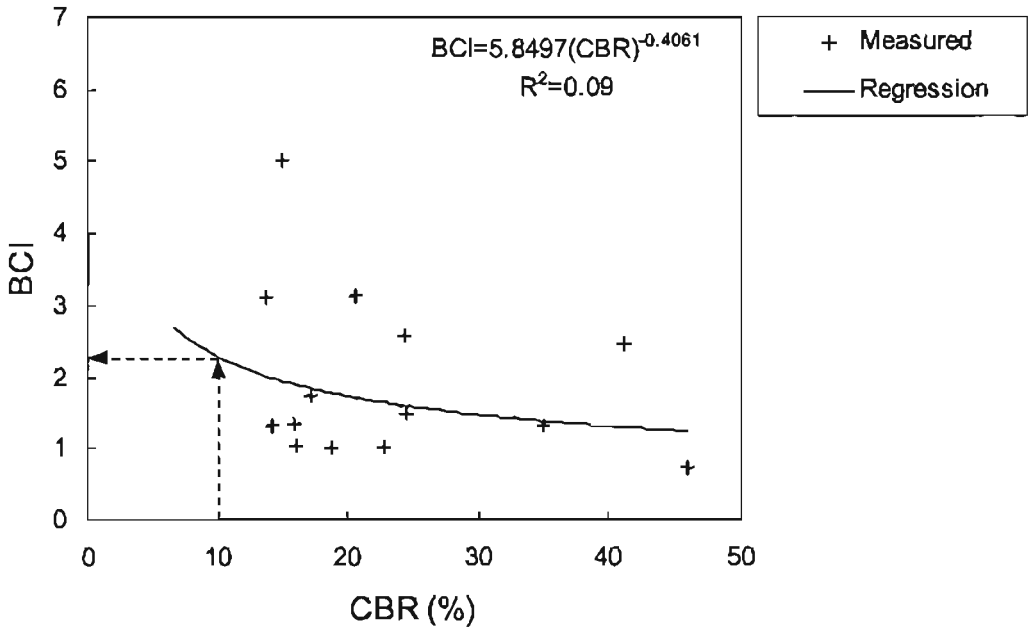

Figure C-18. BCI vs. CBR for NC421 CTB pavements

curve to represent each relationship. The regression curves for each parameter is shown in Figures C-19 to C-23. F_3 was linearly related to stiff layer depth and had the highest R-squared value among all parameters except D_{48}. Since the R-squared values were quite close and D_{48} was chosen as the indicator for subgrade condition, F_3 was chosen as the indicator for depth to a stiff layer. F_3 is inversely related to stiff layer depth. This behavior is expected since F_3 is a shape factor that describes the tail of the deflection basin. Essentially, F_3 is the slope of the deflection basin between the sensors two feet and four feet from the load center. These deflections are known to describe the properties of the lower layers. A small F_3 would correlate to a deep lower layer, such that the slope of the last two feet of the deflection bowl approaches the horizontal.

Asphalt Concrete Overlain Portland Cement Concrete (AC/PCC) Pavements

Subgrade Strength

The parametric study of synthetic data in AC/PCC pavements revealed that D_{48}, D_{18}, $AREA_3$, LSI, and $AREA_2$ were the DBPs that were most sensitive to changes in subgrade condition. The field database contained only two pavement sections with laboratory test results. Both these pavement sections were located in Ohio and were constructed on the same material. Therefore, resilient moduli values for the two test sections are nearly identical (9.141 and 9.213). Because there are only two sections with known subgrade information, and because those two sections are so similar, a relationship meaningful for all AC/PCC pavements can not be developed from the existing database. Theoretically, however, we know that D_{48} represents the lower

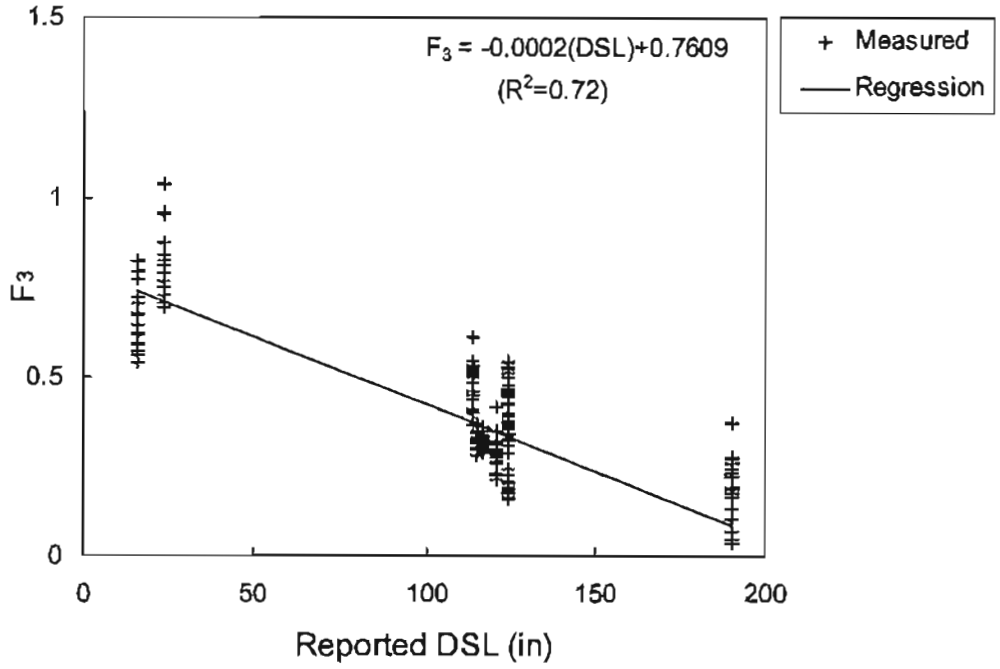

Figure C-19. F_3 vs. DSL for CTB from DataPave

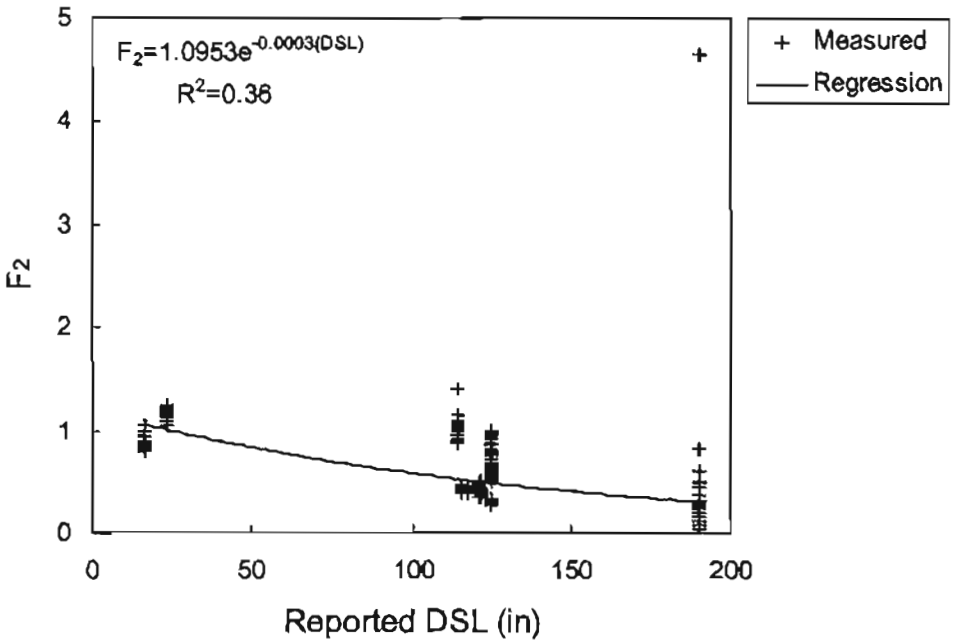

Figure C-20. F_2 vs. DSL for CTB from DataPave

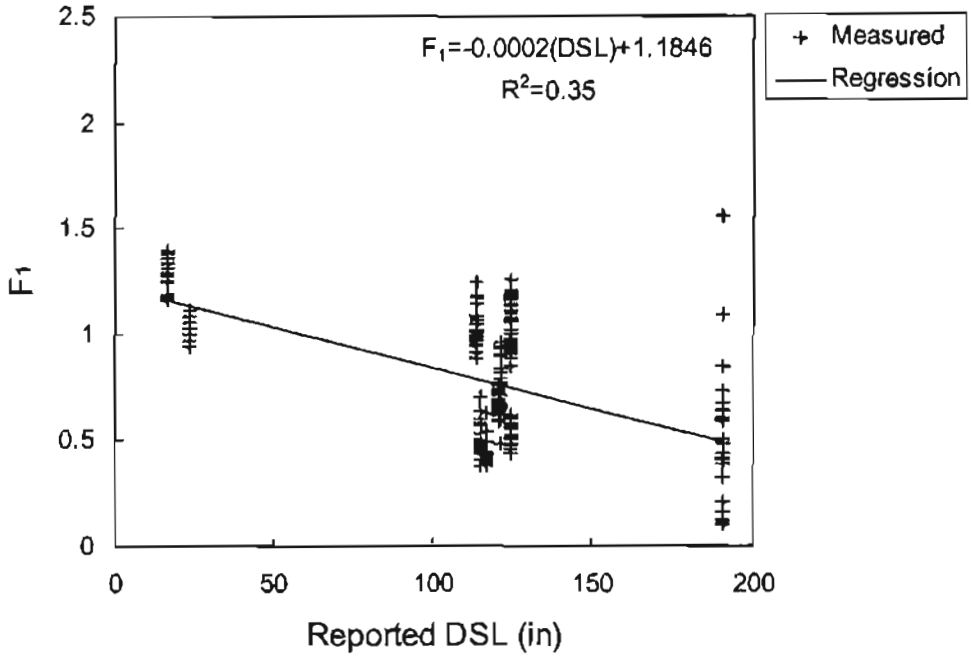

Figure C-21. F_1 vs. DSL for CTB from DataPave

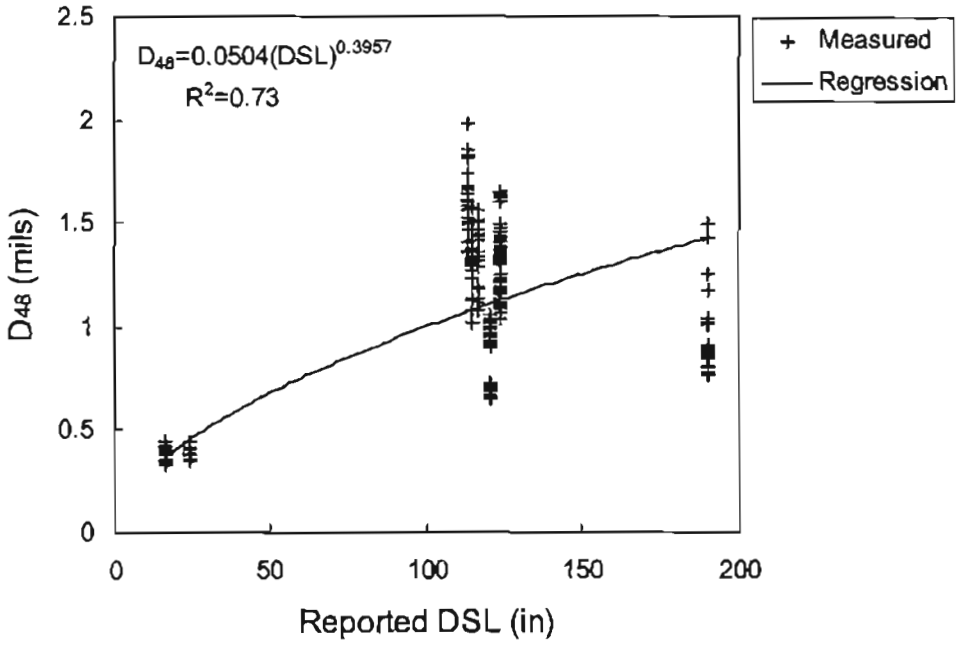

Figure C-22. D_{48} vs. DSL for CTB from DataPave

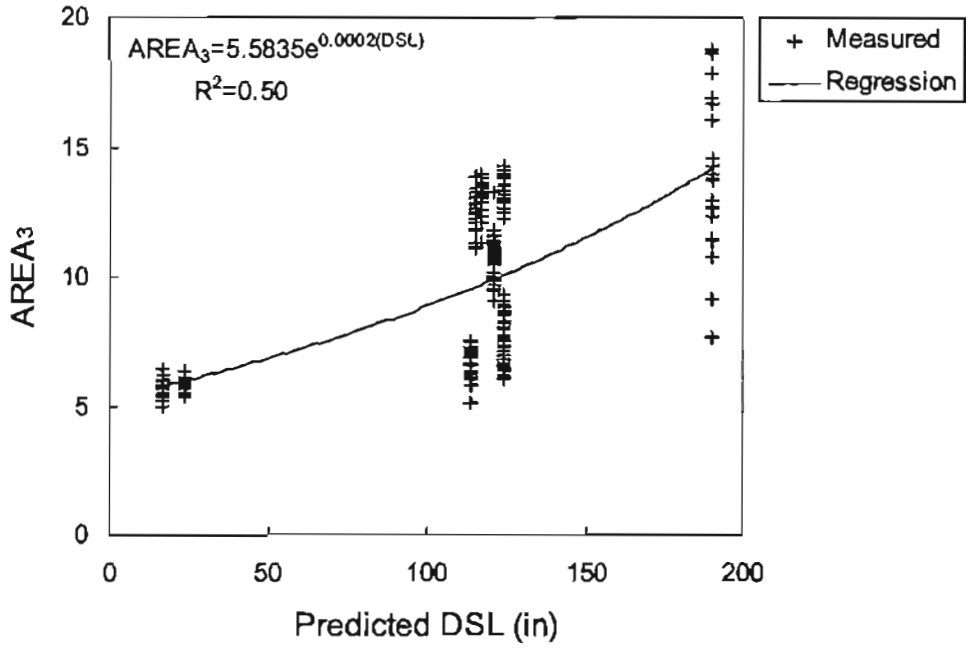

Figure C-23. $AREA_3$ vs. DSL for CTB from DataPave

pavement layers, which supports its performance as a good indicator of subgrade condition.

Since the field data could not be used to develop a relationship between D_{48} and subgrade condition, an additional synthetic database study was performed. The synthetic database was separated based on assigned subgrade modulus values 5, 10, 15, 20, 25, 50, and 100 ksi. The D_{48} values for each were averaged, and this average was plotted against subgrade modulus. Figure C-24 shows the resulting relationship. As in the field database, a low D_{48} value corresponds to a strong subgrade condition. Each grouping of subgrade modulus deflection information contained the full permutation of thickness and modulus for all layers other than the subgrade layer. Therefore, each group contained deflection information of all combinations of intact and distressed, and thick and thin layers. Because these values were averaged before plotting, D_{48} values shown in Figure C-24 are quite small. For this reason, the synthetic database cannot be used to predict subgrade strength numerically. The synthetic study can be used to make a general observation in which a distinction between poor subgrade and good subgrade can be made. The average synthetic D_{48} value corresponding to an E_{sg} value of 10 ksi is shown in Figure C-24 with a dashed line. When the Ohio field data is plotted against this D_{48} curve, all pints fall just above the critical line (Figures C-25 and C-26). This would suggest that the Ohio test sections have a subgrade condition that just falls into the poor range. This conclusion is confirmed by laboratory test data from core samples. The D_{48} test was performed on all remaining AC/PCC state field data, and results are shown in Figures C-27 through C-29.

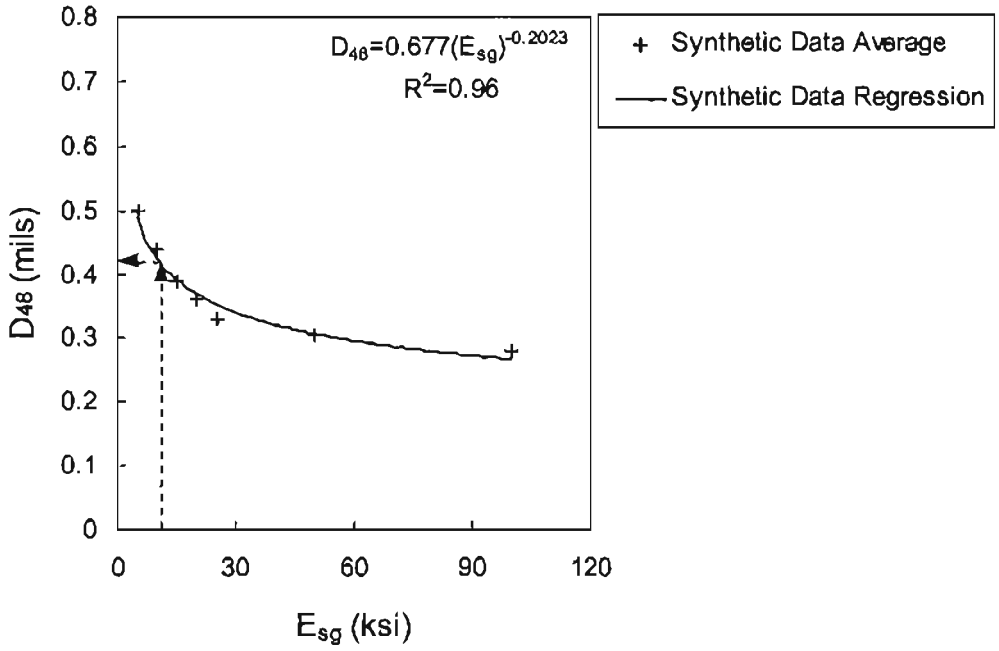

Figure C-24. D_{48} vs. E_{sg} for AC/PCC synthetic data regression analysis

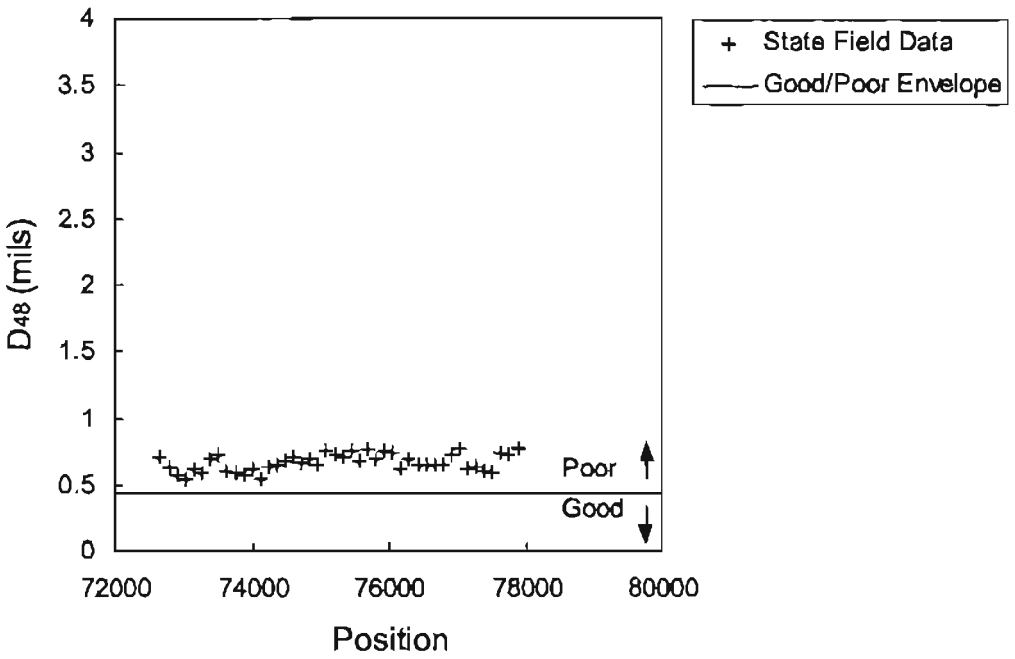

Figure C-25. D_{48} vs. position for subgrade condition determination in Ohio test section

0107192e

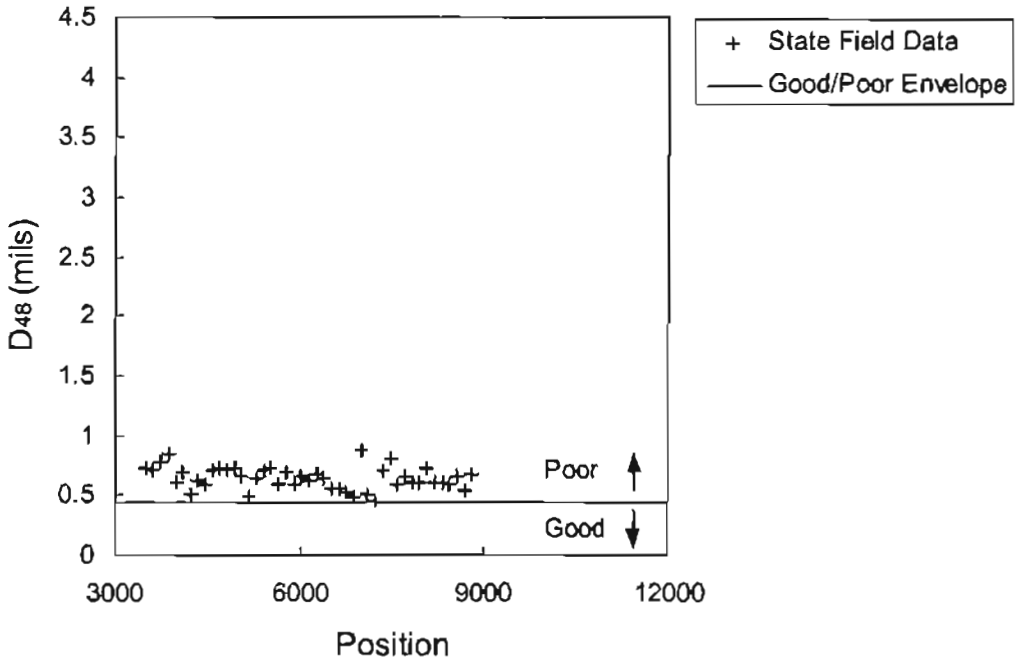

Figure C-26. D_{48} vs. position for subgrade condition determination in Ohio test section 0407192e

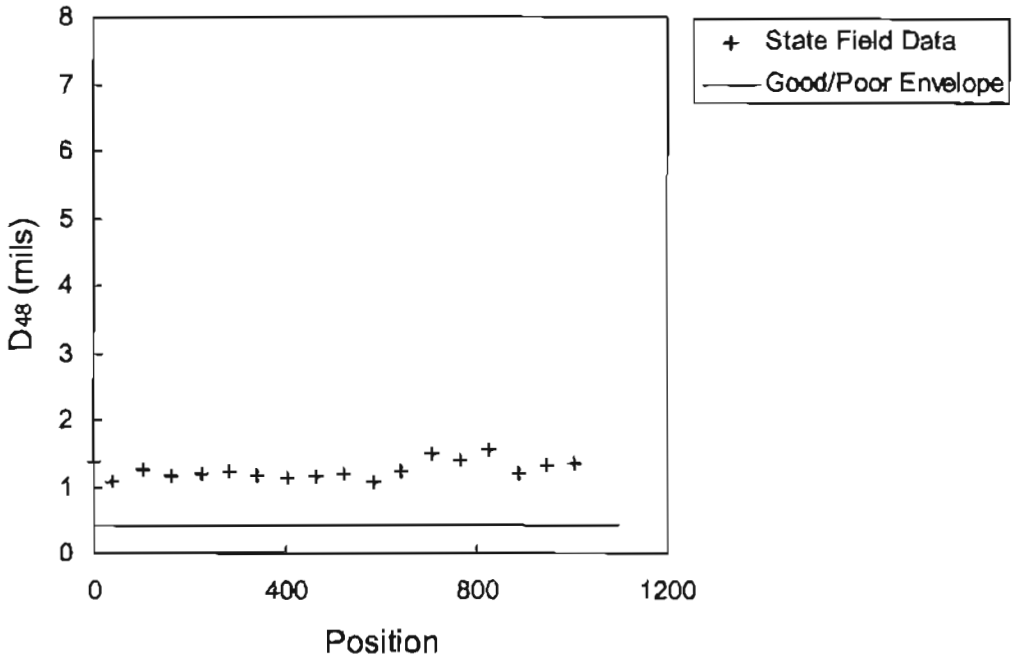

Figure C-27. D_{48} vs. position for subgrade condition determination in Ohio test section 0107091f

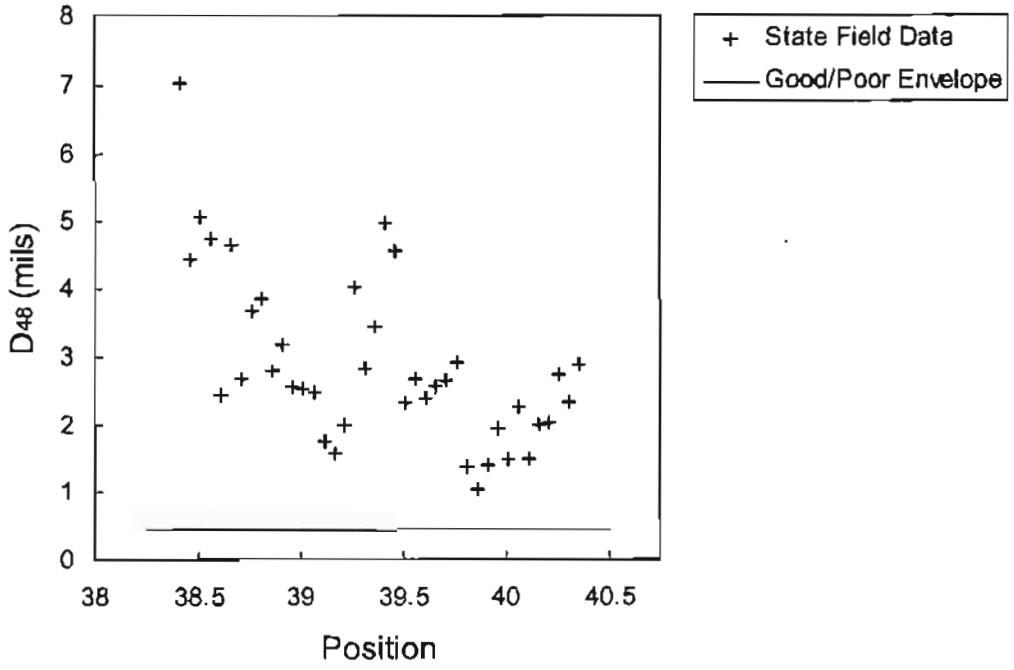

Figure C-28. D_{48} vs. position for subgrade condition determination in Montana test section 00090_p

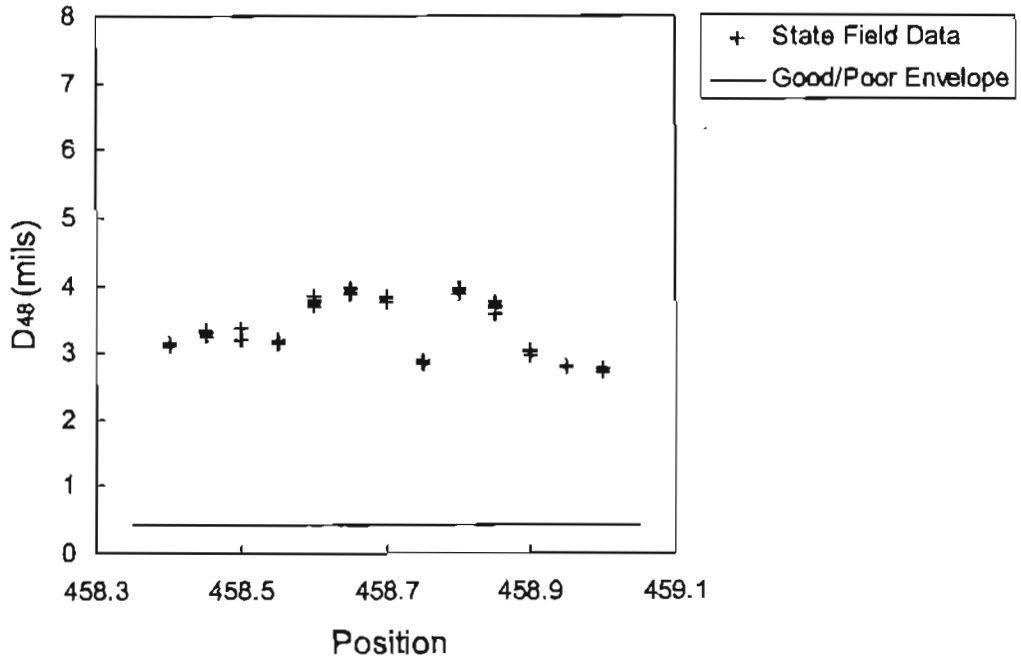

Figure C-29. D_{48} vs. position for subgrade condition determination in Washington test section Was-195-B

Depth to a Stiff Layer

In decreasing order of effectiveness, F_3, F_1, F_2, D_{48}, and D_{18} were identified by the synthetic parametric study as DBPs that are sensitive to changes in stiff layer depth in AC/PCC pavements. The same lack of field data that restricted the subgrade strength study is a factor in the determination of stiff layer depth. As before, the Ohio test sections are the only field cases available with accurate stiff layer depth measures. As a result, a direct correlation between deflection basin parameters and stiff layer depth for the field data cannot be determined. Therefore an additional synthetic data study was performed. The synthetic database was separated into categories based on subgrade depth. The F_3 values for each section were averaged and plotted against subgrade depth. A regression analysis was performed and the best-fit curve was determined. The results are shown in Figure C-30, where F_3 is seen to decrease as stiff layer depth increases. As described previously, this behavior is expected since F_3 measures the slope of the deflection bowl tail. As stiff layer depth approaches infinity, F_3 approaches zero. The best-fit synthetic regression curve was then applied to the field data. The known H_{sg} values were used to determine the DSL values based on measured upper layer thicknesses. Available field data from Ohio with known stiff layer depth was plotted in this way, and the results are shown in Figures C-31 through C-33. All data points represent deep stiff layer conditions. When subgrade thickness was unavailable, the ANN described previously was used to predict subgrade thickness and this value was used to estimate DSL using measured upper layer information. The remaining state field data are plotted in this way, and the results shown in Figures C-34 and C-35.

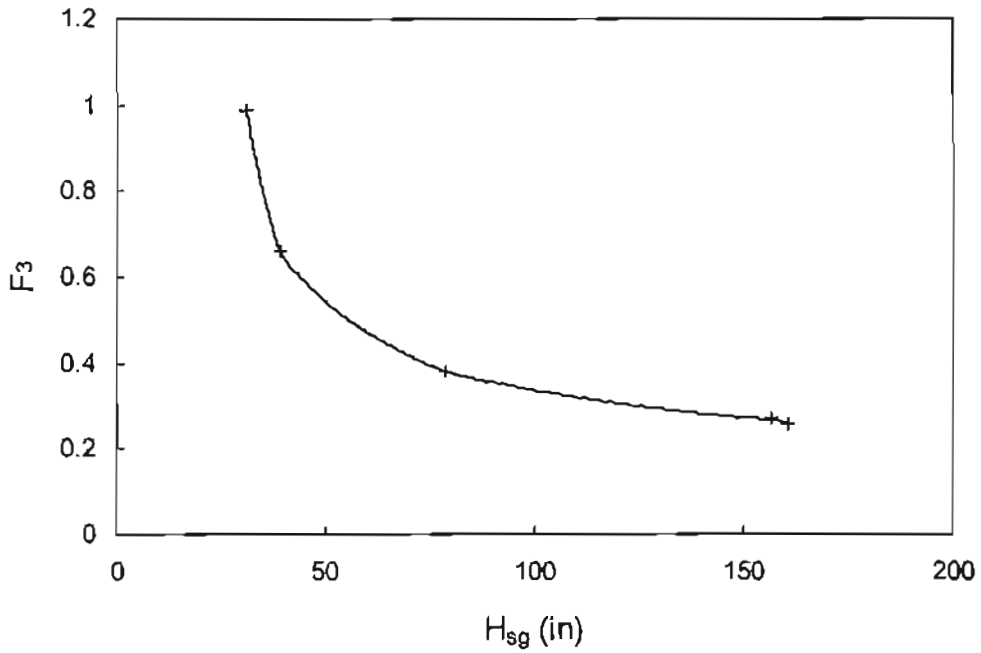

Figure C-30. F_3 vs. H_{sg} for synthetic data regression analysis

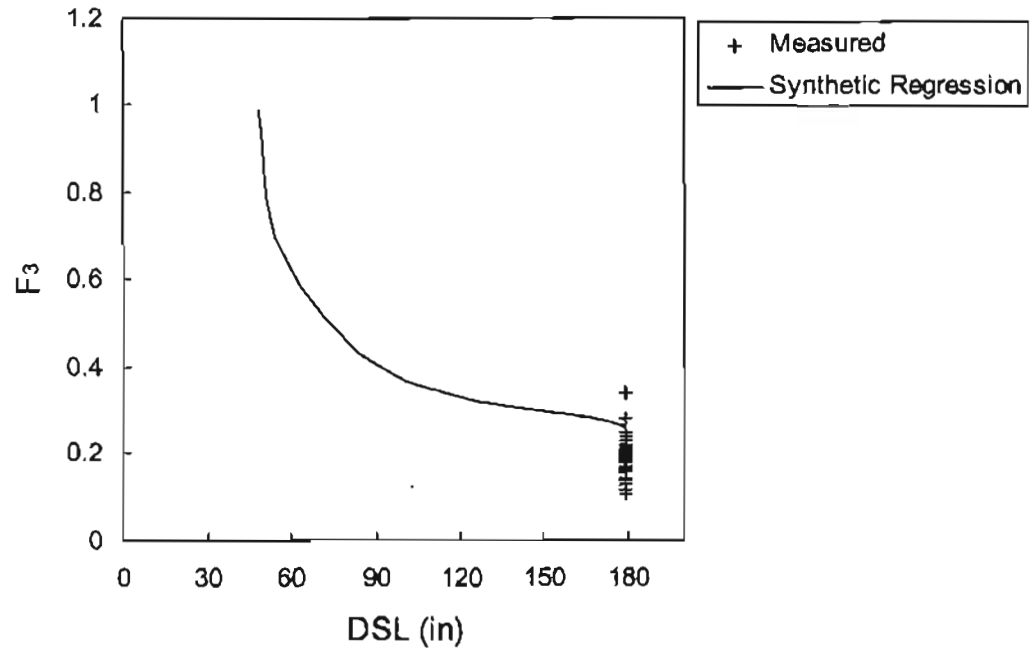

Figure C-31. F_3 vs. DSL for stiff layer depth determination in Ohio test section

0107192e

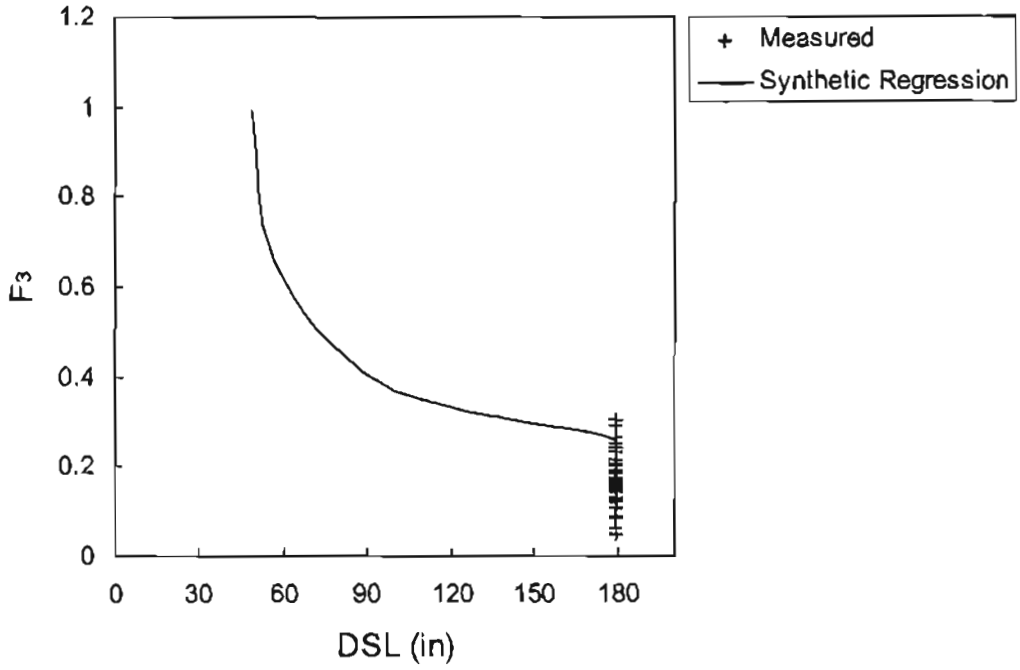

Figure C-32. F_3 vs. DSL for stiff layer depth determination in Ohio test section 0407192e

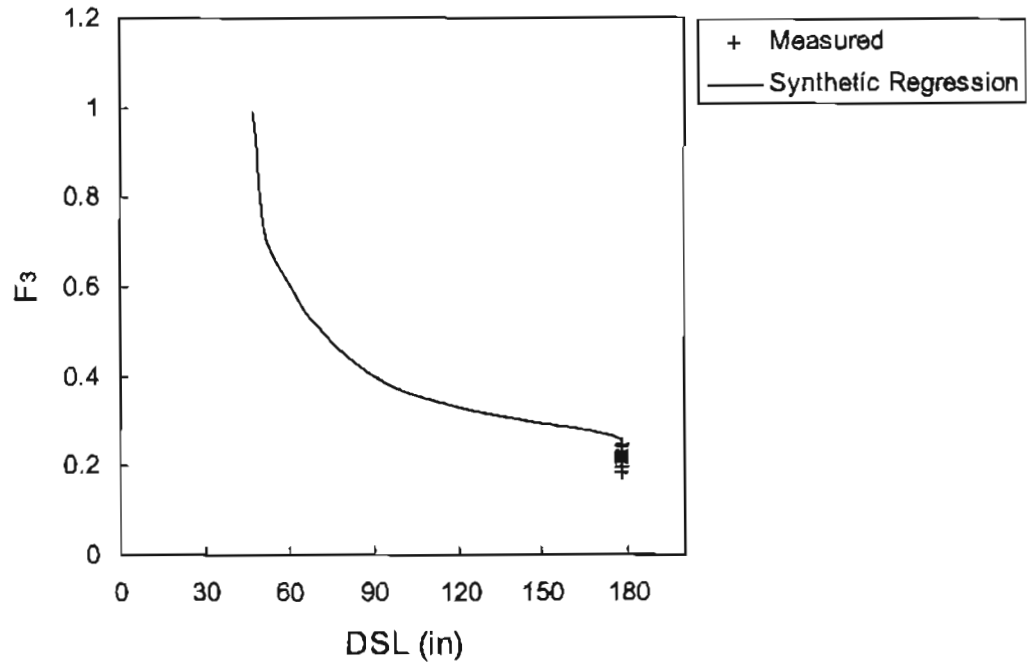

Figure C-33. F_3 vs. DSL for stiff layer depth determination in Ohio test section 0107091f

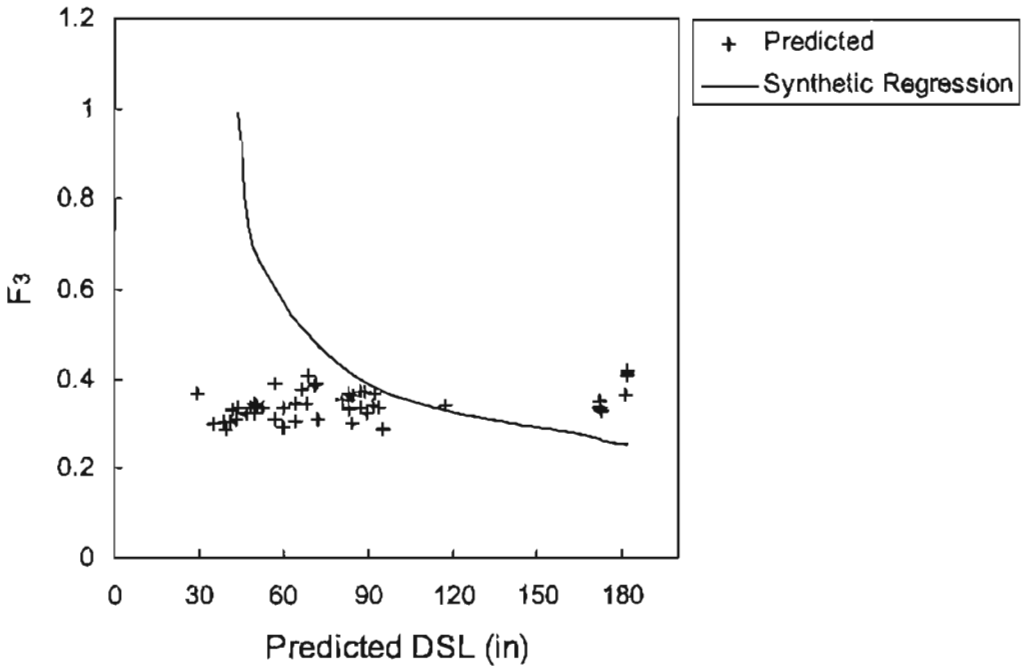

Figure C-34. F_3 vs. predicted DSL for stiff layer depth determination in Montana test section 00090_p

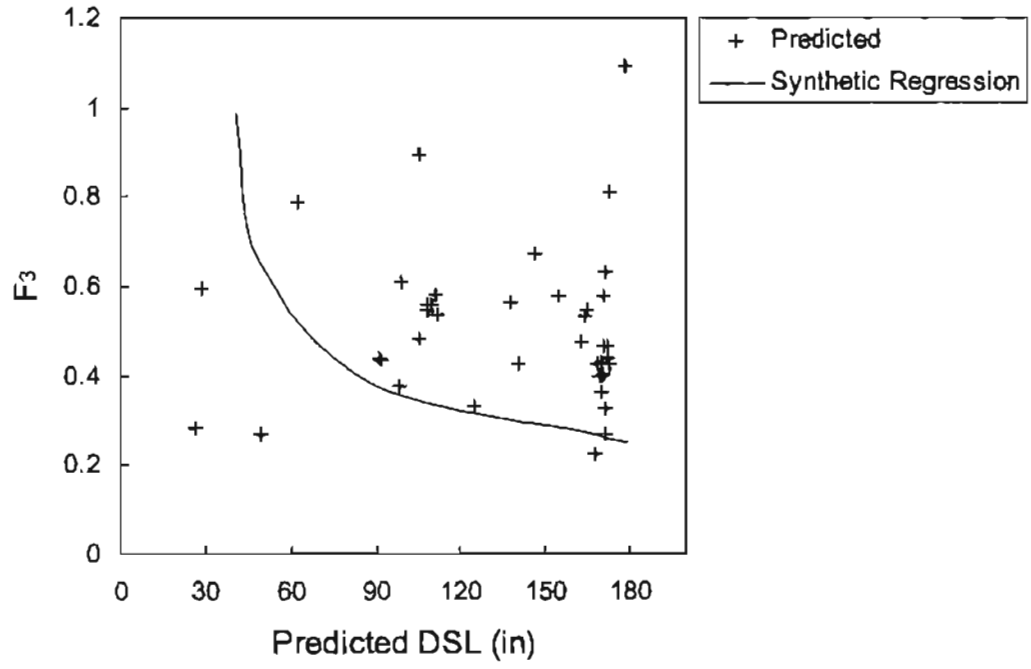

Figure C-35. F_3 vs. predicted DSL for stiff layer depth determination in Washington test section Was-195-B

SURFACE MODULUS ANALYSIS

Surface modulus is defined as the "weighted mean modulus" of layered pavement system calculated from the surface deflection of FWD testing. Based on Boussinesq's equations, the surface modulus at any radial distance under a concentrated load can be expressed as:

$$E_s(r) = \frac{(1-\mu^2)P}{\pi r d(r)} \qquad \text{(C-14)}$$

where

$E_s(r)$ = surface modulus at a distance of r from the point load,

$d(r)$ = surface deflection at a distance of r from the point load,

P = point load,

r = distance from the load, and

μ = Poisson's ratio.

For a distributed load such as the load applied by FWD, Eq. C-14 has to be modified as:

$$E_s(r) = \frac{(1-\mu^2)pa}{r_{adj} d(r)} \qquad \text{(C-15)}$$

where p is the distributed load, and a is the radius of loaded area. The adjusted radial distance r_{adj} instead of the actual radial distance r is used in Eq. C-15 to correct for the error induced by the point loading approximation. The value of r_{adj} is a function of the ratio of r to a. At the area close to the loading center, the difference between r and r_{adj} is significant. This difference decreases with increasing radial distance. After certain distance from the load, the effect of distributed load on surface deflection can be negligible. Thus, no adjustment for radial distance is needed. Johnson (C-1) presented a

table (Table C-1) for the adjusted radii used for various sensor locations of FWD test. In this research, the adjusted radii of 7.095, 11.414, 17.52, and 23.41 were used for sensors 2, 3, 4, and 5, respectively.

Typical surface modulus profiles are shown in Figures C-36 and C-37. In general, surface modulus decreases from a high value close to the load center, representing the stiffness of the entire pavement, to an asymptotic value at the outer sensor, representing the stiffness of the lower layers. Under certain conditions, such as the existence of a shallow stiff layer or strongly stress-sensitive subgrade soils, surface modulus could increase again beyond a certain radial distance. These characteristics of surface modulus profile can be explained using the stress influence line under an FWD load as shown in Figure C-38. The slope of this stress line varies from layer to layer and is mainly affected by each layer's stiffness. The stiffer the layer, the flatter the slope and, therefore, the wider the stress distribution. Surface modulus at any radial distance is considered as the effective modulus of the materials under the stress zone. Since usually subgrade has the smallest modulus value among all pavement layers, the minimum surface modulus is located at the same radial distance as the interception of FWD influence line and top boundary of the subgrade.

Using Surface Modulus Profile in Screening Deflection Basins

Irregular deflection basins, i.e., nonmonotonic changes in the deflections, are sometimes observed from FWD testing. Four irregular deflection basins from field measurements are shown in Figure C-39. The calculated surface modulus profiles are plotted in Figure C-40. Two possible reasons for irregular deflections are: incorrectly

Table C-1. Actual and adjusted geophone radii (After Johnson, 1997)

Geophone Number	Actual Distance from Load Center (in)	Adjusted Distance from Load Center (in)
2	7.9	7.095
3	11.8	11.414
4	23.6	23.410
5	35.4	Not Adjusted
6	53.1	Not Adjusted
7	70.9	Not Adjusted

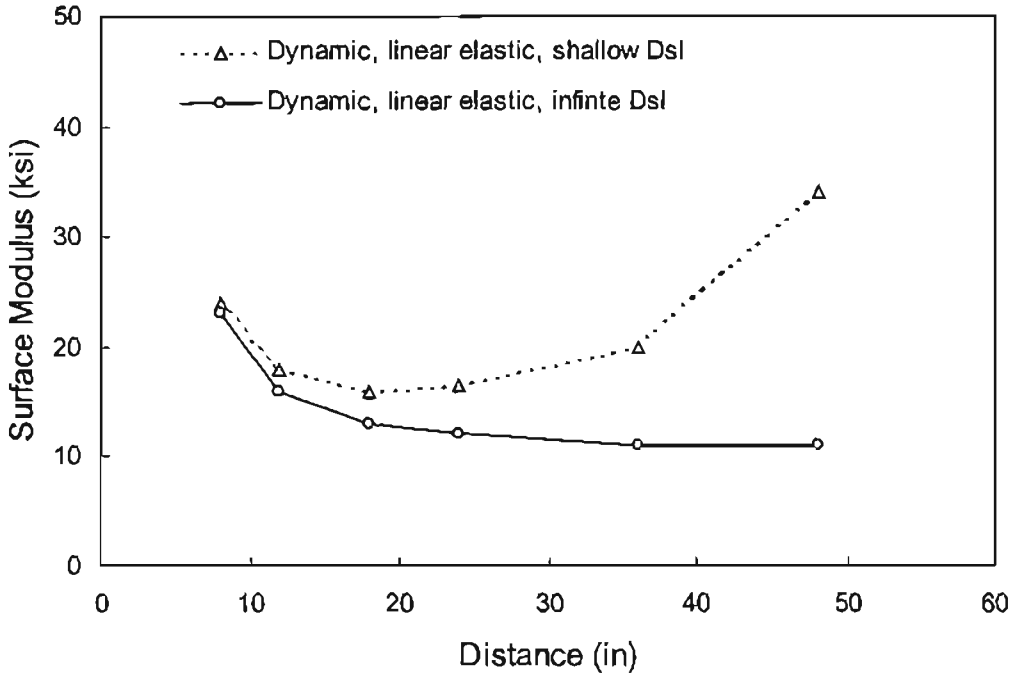

Figure C-36. Typical surface modulus profiles from linear elastic simulations of subgrade

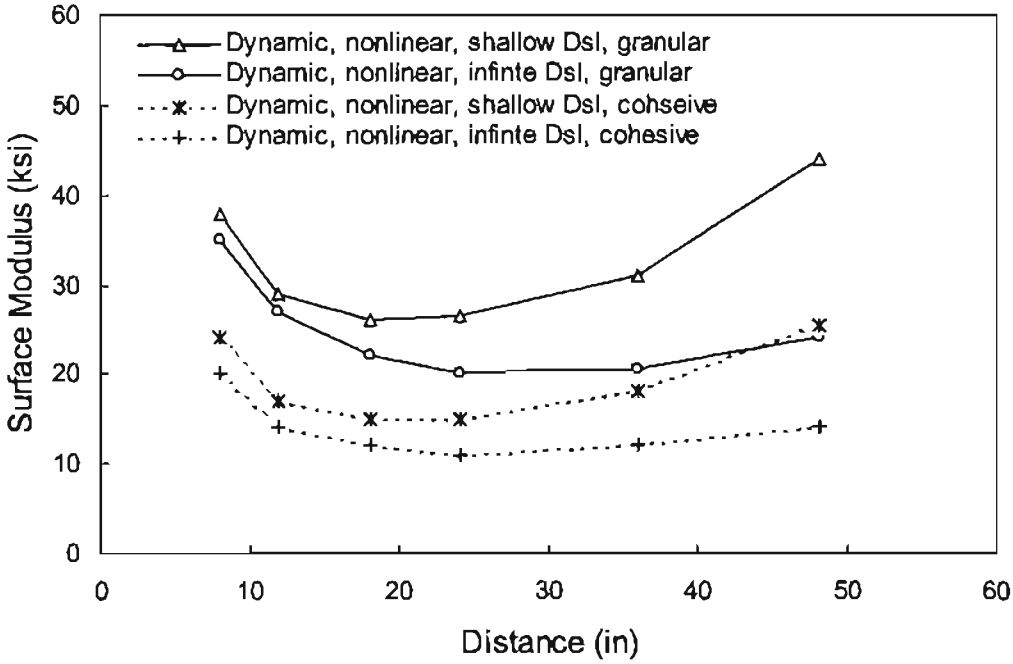

Figure C-37. Typical surface modulus profiles from nonlinear elastic simulations of subgrade

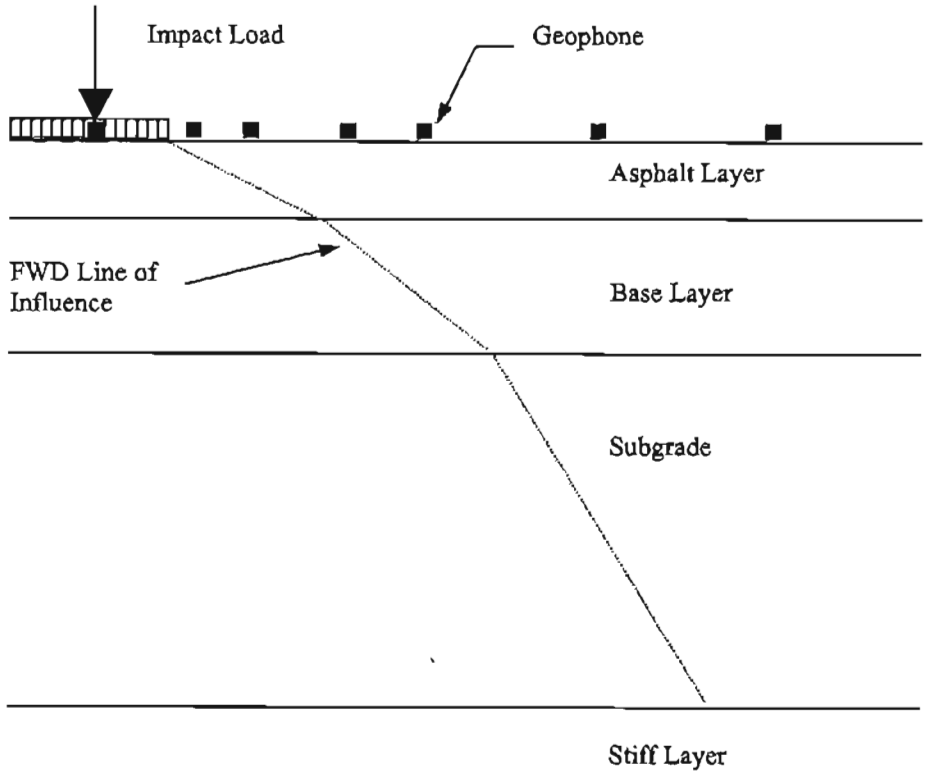

Figure C-38. Typical stress influence line under a FWD load

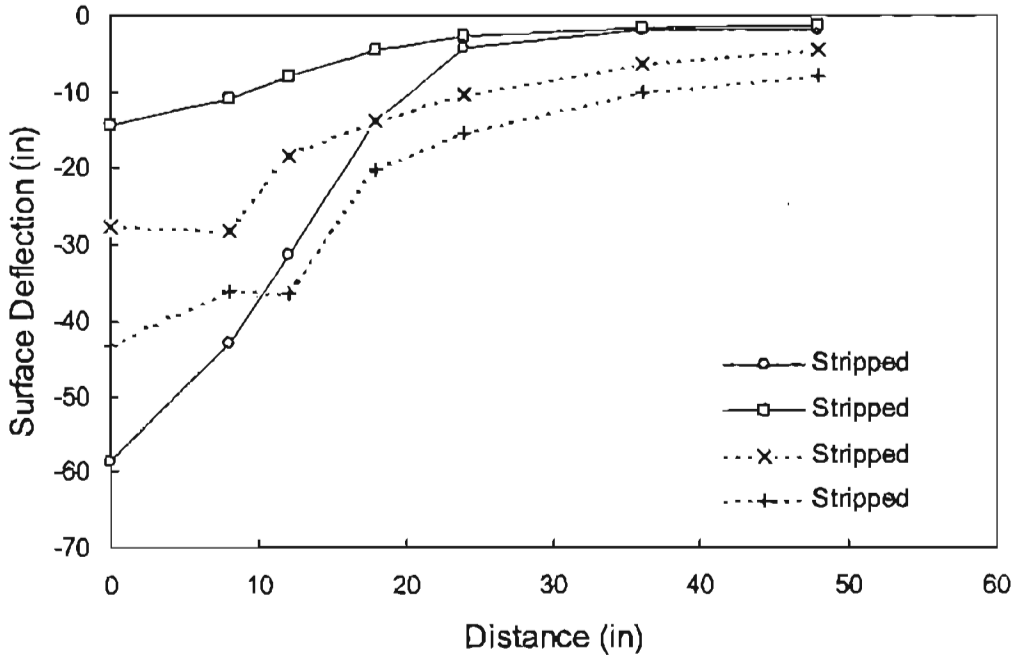

Figure C-39. Typical irregular deflection basins from field measurements

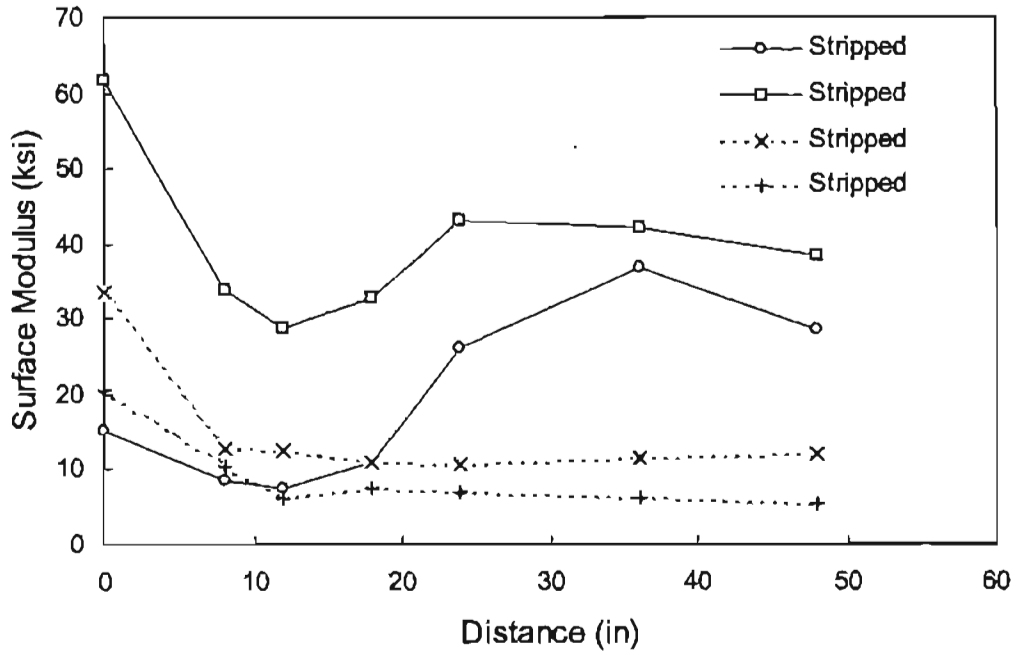

Figure C-40. Typical surface modulus profiles of irregular deflection basins from field measurements

recorded sensor spacing, and presence of discontinuities in pavement layers from cracking or stripping. Irregular deflection could cause problems in the evaluation of pavement layer conditions. Stubstad et al. (C-2) concluded that incorrectly recorded sensor locations could significantly change the moduli values estimated using backcalculation programs. Thus, it is important to first check whether one deflection basin is irregular or not. In our research, the following two simple criteria are used to detect irregular deflections:

$$\text{Criterion 1.} \quad D_i < D_{i+1}, \qquad i = 1,2,...,6 \tag{C-16}$$

$$\text{Criterion 2.} \quad E_i > E_{i+1} \;\&\; E_i > E_{i-1}, \qquad i = 2,3,...,6 \tag{C-17}$$

where D_i is the deflection at i^{th} sensor, and E_i is the surface modulus at i^{th} sensor. The deflection basin is considered irregular if any one of these two criteria is satisfied. When irregularity due to incorrect sensor location input is detected in FWD deflection basins, correction can be made before processing the deflection information for condition evaluation. One example of the method to correct surface deflections is the SLIC method from Stubstad et al. (C-2). It needs to be noted that some of the condition assessment algorithms developed in this research could be applied even if the deflection basin is irregular. This is possible because these algorithms use a portion of deflection basin for condition evaluation of different layers. For example, cracking potential of AC layer in full-depth and aggregate base pavements requires *BDI* and H_{ac} as inputs, and therefore only deflections necessary for this evaluation are deflections at 12 and 24 inches from the load center. Similarly, base and subgrade conditions can be determined with a fewer sensor deflections instead of the full deflection basin.

Using Surface Modulus Profile in Predicting E_{sg}

The minimum value of surface modulus profile, E_{smin}, and its location, d_s, provide important information relating to the stiffness of subgrade E_{sg}. To correlate E_{smin} to E_{sg}, a factor α is defined as the ratio of E_{smin} to E_{sg}:

$$\alpha = \frac{E_{s\,min}}{E_{sg}} \tag{C-18}$$

A study of the effects of layer properties on α and d_s is then conducted based on the synthetic database from dynamic, linear elastic analysis.

Full-depth Pavements

For full-depth pavements, α and d_s are mainly affected by the thickness of AC layer, the modulus of AC layer, and the thickness of subgrade (or depth to a stiff layer). Based on the equivalent thickness theory, the variable F_{ac} is defined as follows to combine the effects of the thickness and modulus of AC layer together:

$$F_{ac} = \frac{H_{ac}\sqrt[3]{E_{ac}}}{100} \tag{C-19}$$

where H_{ac} is the AC thickness in inch, and E_{ac} is the AC modulus in ksi. Table C-2 shows the effects of F_{ac} and H_{sg} on d_s, the location of the minimum surface modulus.

It was found that the stronger the AC layer, more were the cases with d_s equal to 48 inches, while the shallower depth to a stiff layer, less were the cases with d_s equal to 48 inches. Especially when F_{ac} is greater than 1 and H_{sg} is larger than 80 inches, the minimum surface modulus is located at the last sensor (48 inches offset) for all the cases. This can be explained using the stress influence line under an FWD load. When the strength of AC layer is increased, the stress influence line in AC layer becomes flatter.

Table C-2. Effects of F_{ac} and H_{sg} on d_s for full-depth pavements

	$F_{ac} \leq 1$		$1 < F_{ac} \leq 2$		$F_{ac} \geq 2$	
	H_{sg}[a] < 80	$H_{sg} \geq 80$	$H_{sg} < 80$	$H_{sg} \geq 80$	$H_{sg} < 80$	$H_{sg} \geq 80$
No. of Total Cases	360	90	160	40	40	10
No. of Cases with $d_s = 48$ inches	32	46	72	40	31	10
Percentage of Cases with $d_s = 48$ inches (%)	8.9	51.1	45.0	100.0	77.5	100.0

Thus, the location of E_{smin} moves farther away from the center of the load. A shallower stiff layer, however, reduces the relative strength of AC layer and lower layers so that the stress influence line in AC layer becomes steeper. Therefore, the location of E_{smin} moves closer to the center of load. These observations also suggest that, for strong pavements, commonly used sensor spacing for 7th sensor (48 inches) is not far enough to detect the deformation solely attributed by subgrade under FWD testing with 9000 pound load level. This is true especially when subgrade is very weak and no stiff layer exists under the subgrade.

For full-depth pavements with infinite subgrade, the variation of factor α and F_{ac} for different E_{sg} values is shown in Figure C-41. It can be seen that when AC layer is very weak, factor α is around 1, and the stronger the AC layer, the larger the factor α. For pavements with the same strength of AC layers, the stronger the subgrade, the smaller the factor α. The relationships between E_{smin} and F_{ac} for different E_{sg} values for full-depth pavements are shown in Figure C-42. A regression technique was then applied to develop the relationship among E_{smin}, E_{sg}, and F_{ac}. From Figure C-42, E_{smin} can be expressed as a 2nd order polynomial function of F_{ac} as:

$$E_{s\min} = A * F_{ac}^{\ 2} + B * F_{ac} + C \qquad \text{(C-20)}$$

Here, coefficients A, B, and C are not constants, but functions of the value of E_{sg}. The values of A, B, and C for different E_{sg} values are shown in Eqs. C-21 – C-25:

For E_{sg} = 5 ksi,

$$E_{s\min} = 0.6927 * F_{ac}^{\ 2} + 4.9759 * F_{ac} + 3.8171 \qquad \text{(C-21)}$$

$$R^2 = 0.994$$

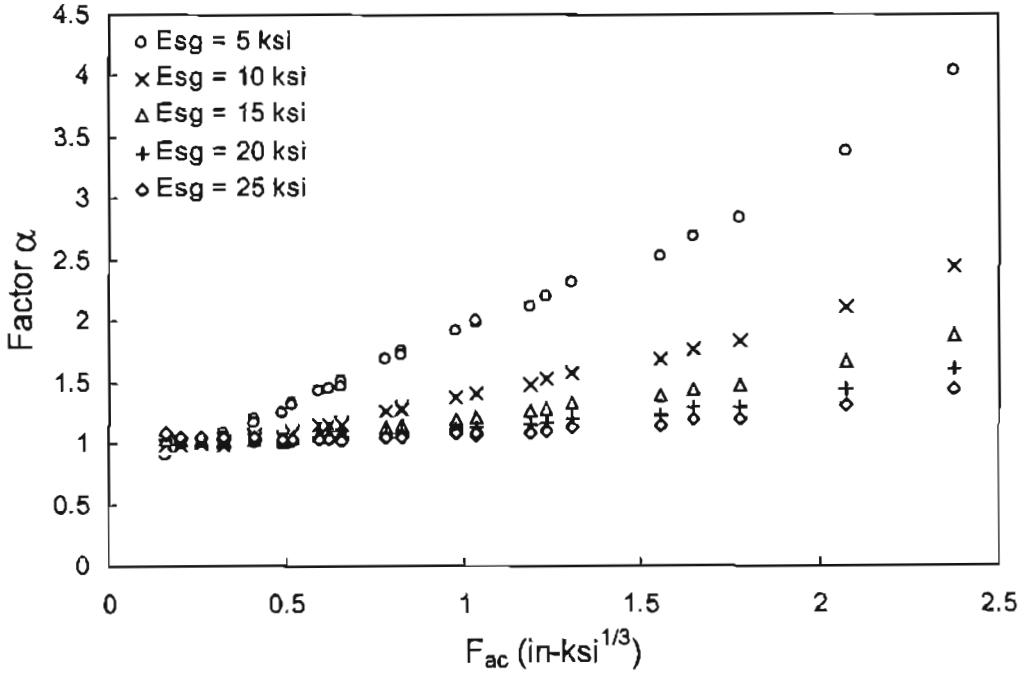

Figure C-41. Relationship of α, F_{ac} and E_{sg} for full-depth pavement with infinite subgrade

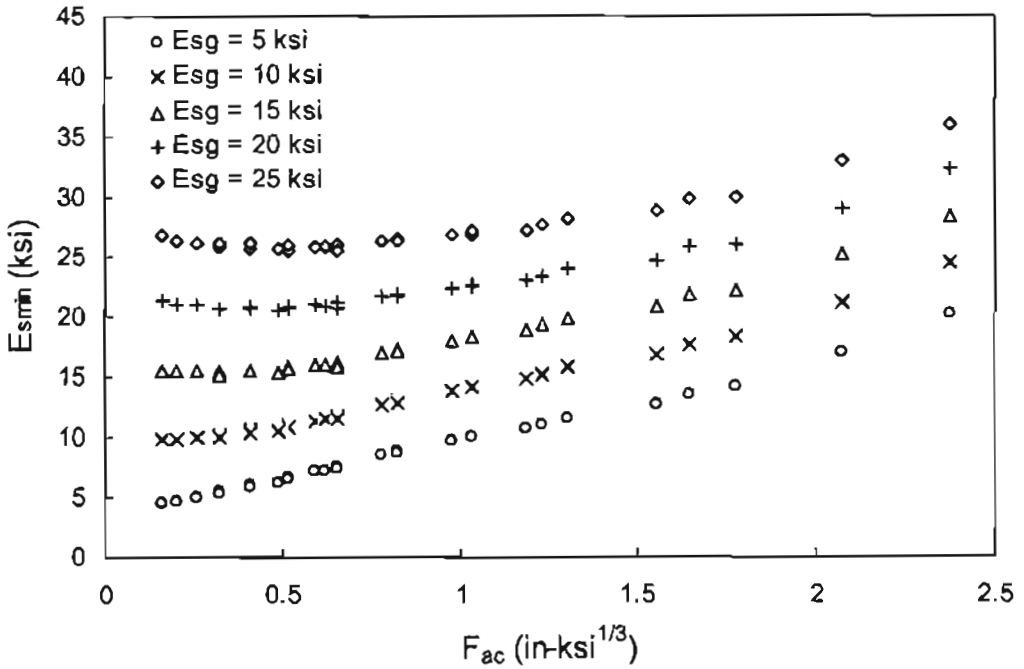

Figure C-42. Relationship of E_{smin}, F_{ac} and E_{sg} for full-depth pavement with infinite subgrade

For E_{sg} = 10 ksi,

$$E_{s\min} = 1.2237 * F_{ac}^{\ 2} + 3.4397 * F_{ac} + 8.9676 \quad \text{(C-22)}$$

$$R^2 = 0.995$$

For E_{sg} =15 ksi,

$$E_{s\min} = 1.9052 * F_{ac}^{\ 2} + 1.0610 * F_{ac} + 14.87 \quad \text{(C-23)}$$

$$R^2 = 0.992$$

For E_{sg} = 20 ksi,

$$E_{s\min} = 2.5312 * F_{ac}^{\ 2} - 1.2772 * F_{ac} + 20.915 \quad \text{(C-24)}$$

$$R^2 = 0.989$$

For E_{sg} = 25 ksi,

$$E_{s\min} = 2.8832 * F_{ac}^{\ 2} - 2.9453 * F_{ac} + 26.722 \quad \text{(C-25)}$$

$$R^2 = 0.986$$

By plotting the values of A, B, and C against the values of E_{sg}, approximate relationships, which are linear, between these variables and E_{sg} were found. The expressions for these relationships and R square values are shown in Figure C-43.Using these expressions, Eq. C-20 can now be modified as:

$$E_{s\min} = (0.1139 * E_{sg} + 0.1406) * F_{ac}^{\ 2} - (0.4112 * E_{sg} - 7.2188) * F_{ac} + (1.1551 * E_{sg} - 2.2688) \quad \text{(C-26)}$$

$$R^2 = 0.999 \qquad SEE = 0.34$$

By reorganizing Eq. C-26, α and E_{sg} can be expressed as:

$$\alpha = 0.1406 * \frac{F_{ac}^{\ 2}}{E_{sg}} + 7.12188 * \frac{F_{ac}}{E_{sg}} - 2.2688 * \frac{1}{E_{sg}} + 0.1139 * F_{ac}^{\ 2} - 0.4112 * F_{ac} + 1.1551 \quad \text{(C-27)}$$

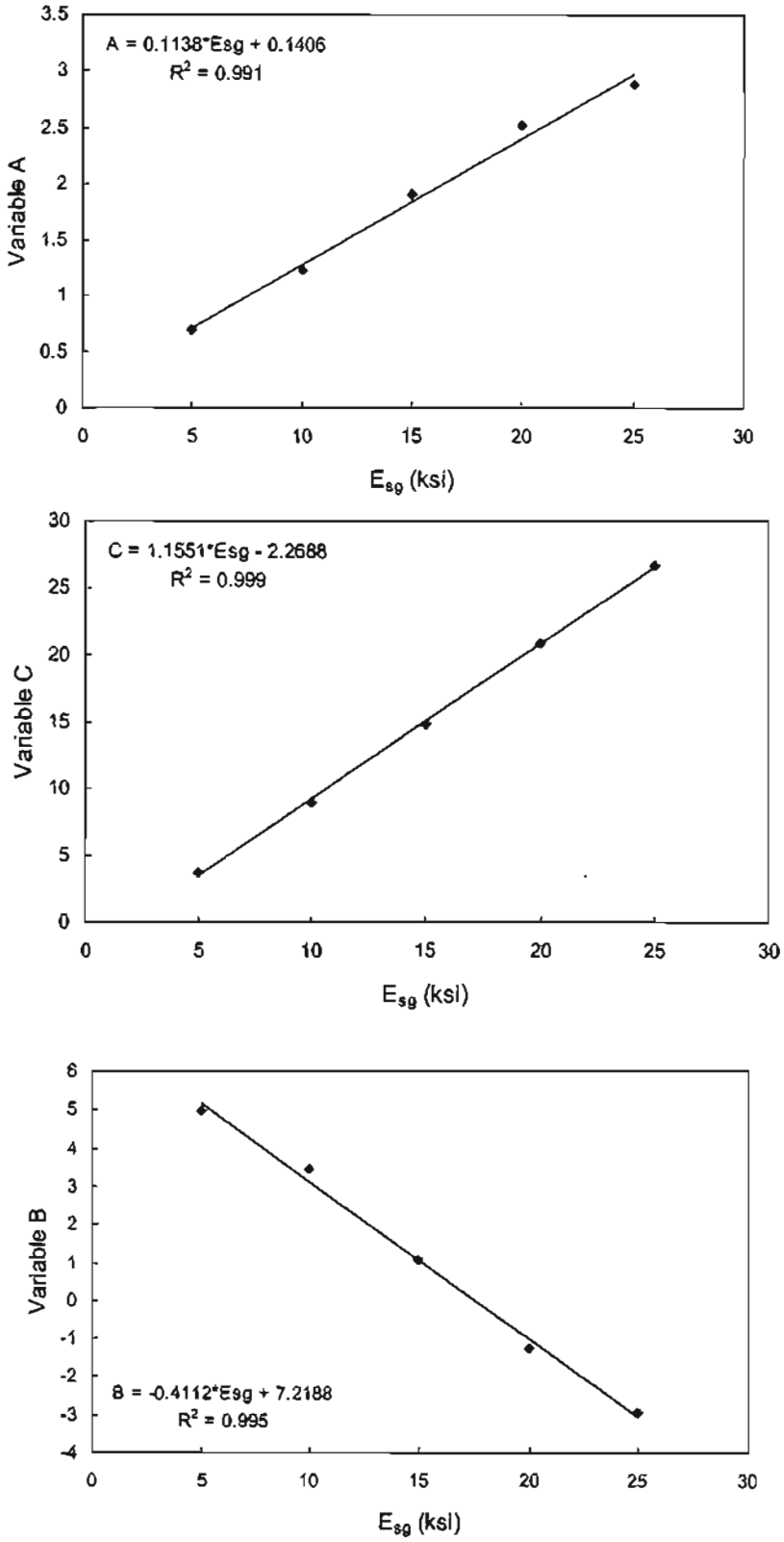

Figure C-43. Determination of coefficients A, B, and C for full-depth pavements

$$E_{sg} = \frac{E_{s\min} - 0.1406 * F_{ac}^{\ 2} - 7.2188 * F_{ac} + 2.2688}{0.1139 * F_{ac}^{\ 2} - 0.4112 * F_{ac} + 1.1551} \quad \text{(C-28)}$$

Eq. C-28 gives an easy and quick way to predict E_{sg} value for full-depth pavement with infinite subgrade. A graphical method based on Eqs. C-21 through C-25 to predict E_{sg} was also developed as shown in Figure C-44. E_{sg} can then be directly predicted by locating the point (F_{ac}, E_{smin}) in Figure C-44.

The effect of H_{sg} (or depth to a stiff layer) on factor α is shown in Figure C-45. It can be seen that α values are essentially the same when H_{sg} is larger than 160 inches. This observation is consistent with the conclusion drawn in the "Findings" chapter that a stiff layer has minimal or no effect on surface deflections if the depth to a stiff layer is greater than 15 ft. As H_{sg} decreases from 160 inches to 30 inches, the factor α increases significantly and the effect of E_{sg} on α tends to decrease, although the basic trend (i.e., the higher the value of E_{sg}, higher the factor α) remains the same. A regression equation was established to predict α for full-depth pavements as follows:

$$\alpha = 0.0186 * \frac{F_{ac}^{\ 2}}{E_{sg}} + 5.4088 * \frac{F_{ac}}{E_{sg}} - 1.0637 * \frac{1}{E_{sg}} + 0.108 * F_{ac}^{\ 2} - 0.1944 * F_{ac} + 39.5426 * \frac{F_{ac}}{D_{sg}^{\ 3}} + 1.033 \quad \text{(C-29)}$$

$R^2 = 0.979 \qquad SEE = 0.197$

Reorganizing Eq. C-29, E_{sg} can be expressed as follows:

$$E_{sg} = \frac{E_{s\min} - 0.0186 * F_{ac}^{\ 2} - 5.4088 * F_{ac} + 1.0637}{0.108 * F_{ac}^{\ 2} - 0.1944 * F_{ac} + 39.5426 * \frac{F_{ac}}{D_{sg}^{\ 3}} + 1.033} \quad \text{(C-30)}$$

where $D_{sg} = H_{sg}/12$, the thickness of subgrade in foot.

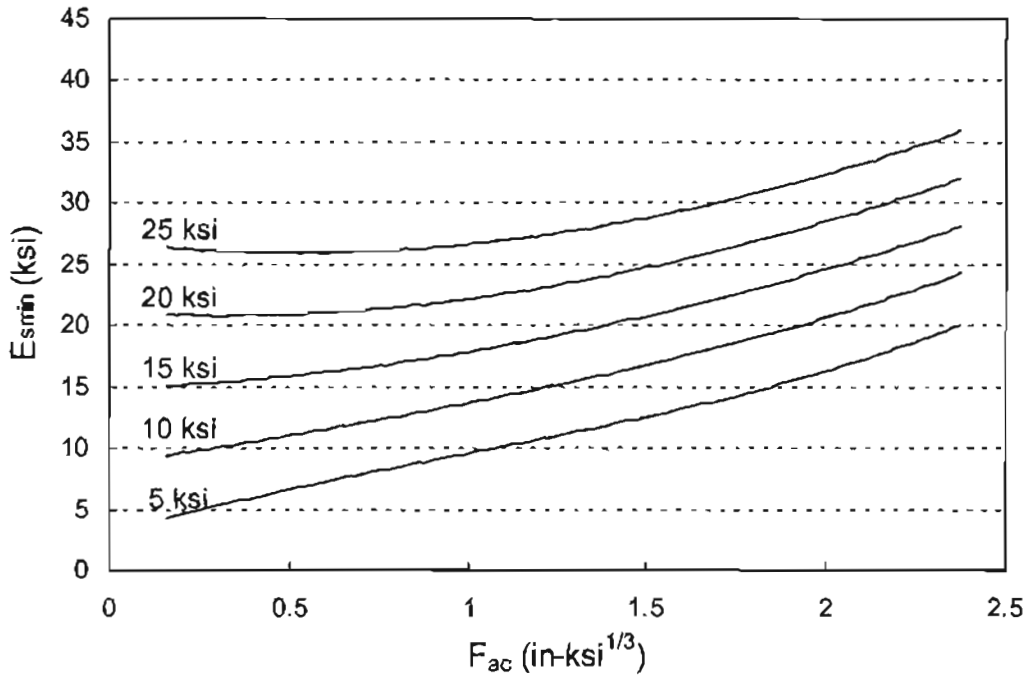

Figure C-44. Determining E_{sg} from E_{smin} and F_{ac} for full-depth pavement with infinite subgrade

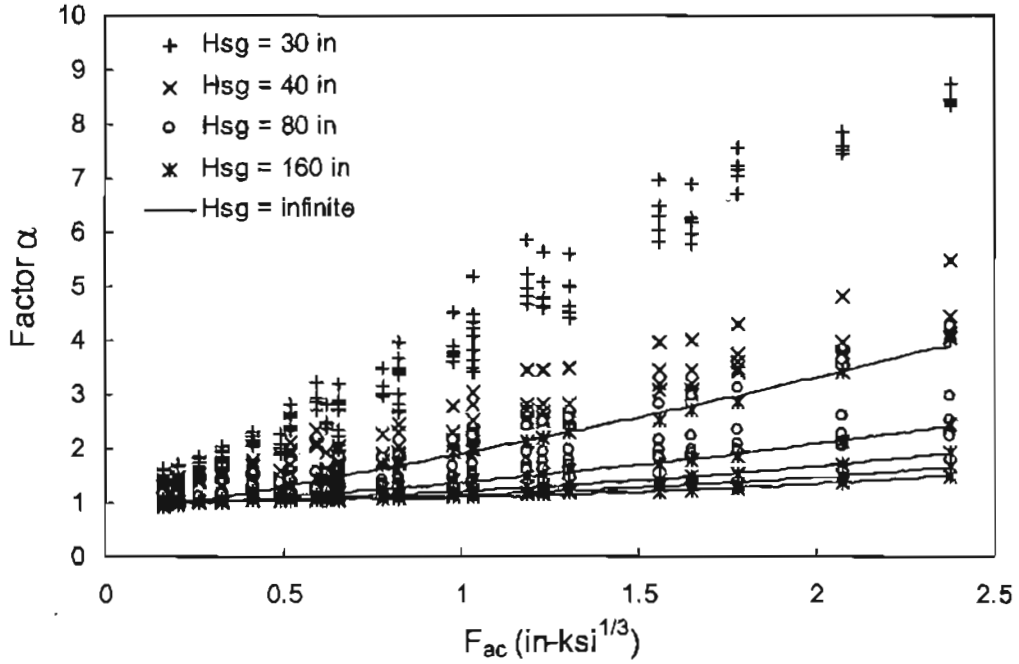

Figure C-45. Effect of H_{sg} on the relationship of α-F_{ac} for full-depth pavements

Aggregate Base Pavement

The findings from full-depth pavements can easily be extended to aggregate base pavements by incorporating the effect of base course on F_{ac}. Based on equivalent thickness theory, F_{ac} can be expressed as follows for aggregate base pavements:

$$F_{ac} = \frac{H_{ac}\sqrt[3]{E_{ac}} + H_{abc}\sqrt[3]{E_{abc}}}{100} \tag{C-31}$$

It can be seen that H_{ac} and H_{abc} affect F_{ac} more than the moduli do. Considering the relatively narrow range of base layer modulus, which is from 25 ksi to 125 ksi (corresponding to a value of 3 to 5 in the cubic root term in the equation), the effect of E_{abc} on F_{ac} is relatively minor. For practical purposes, F_{ac} can be estimated using the following equation:

$$F_{ac} = \frac{H_{ac}\sqrt[3]{E_{ac}} + cH_{abc}}{100} \tag{C-32}$$

where c is a constant, whose value equals 3, 4, or 5 corresponding to poor, marginal, or strong base, respectively.

For aggregate base pavements, the relationship between F_{ac}, H_{sg} and the radial distance, d_s, corresponding to the minimum surface modulus are similar to those of full-depth pavements. That is, greater the value of F_{ac}, larger the value of d_s, and shallower the depth to a stiff layer, smaller the value of d_s.

Figures C-46 shows the effects of F_{ac} and E_{sg} on factor α for aggregate base pavements with infinite subgrade. Figure C-47 shows the effects of F_{ac} and E_{sg} on E_{smin} for aggregate base pavements with infinite subgrade. Similar to full-depth pavements, E_{smin} can also be expressed as a 2nd order polynomial function (Eq. C-20) of F_{ac}, where

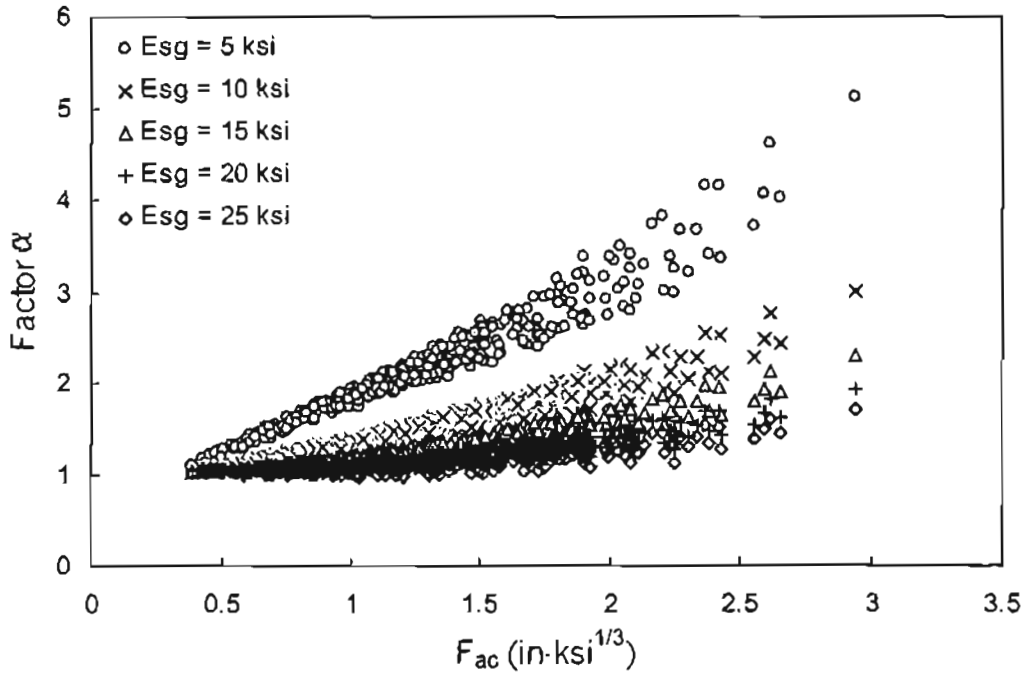

Figure C-46. Relationship of α, F_{ac},and E_{sg} for aggregate base pavements with infinite subgrade

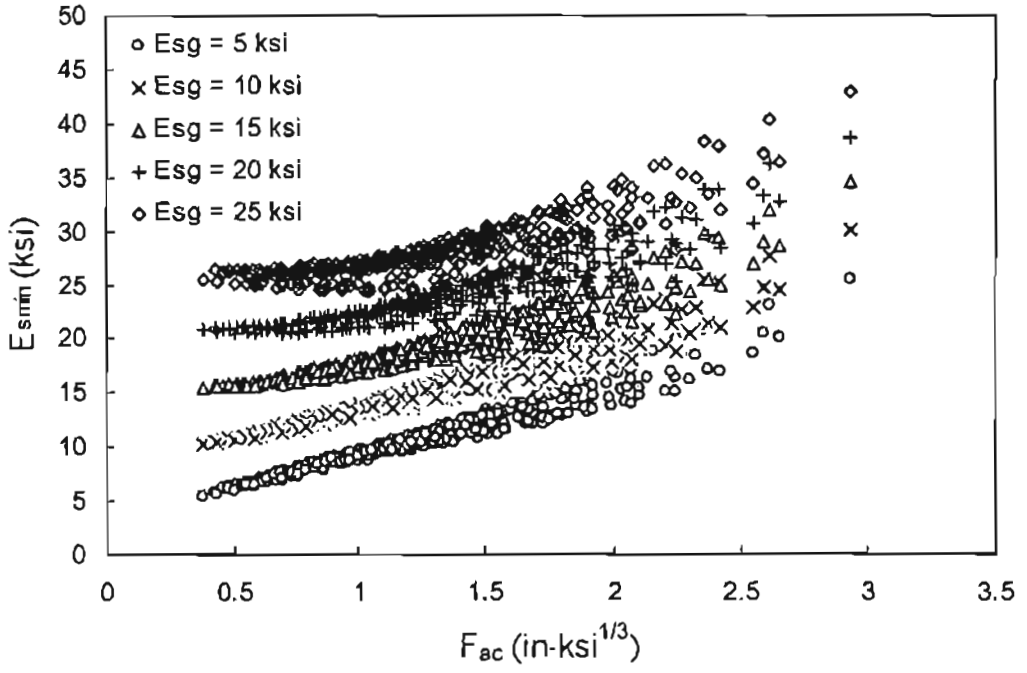

Figure C-47. Relationship of E_{smin}, F_{ac} and E_{sg} for aggregate base pavement with infinite subgrade

coefficients A, B, and C are functions of E_{sg}. Depending on the E_{sg} value, E_{smin} can be estimated as follows:

For E_{sg} = 5 ksi,

$$E_{s\min} = 0.8060 * F_{ac}^{\ 2} + 4.0203 * F_{ac} + 4.2960 \qquad \text{(C-33)}$$

$$R^2 = 0.943$$

For E_{sg} = 10 ksi,

$$E_{s\min} = 1.0497 * F_{ac}^{\ 2} + 3.3652 * F_{ac} + 8.9014 \qquad \text{(C-34)}$$

$$R^2 = 0.933$$

For E_{sg} =15 ksi,

$$E_{s\min} = 1.5243 * F_{ac}^{\ 2} + 1.6537 * F_{ac} + 14.438 \qquad \text{(C-35)}$$

$$R^2 = 0.910$$

For E_{sg} = 20 ksi,

$$E_{s\min} = 2.0526 * F_{ac}^{\ 2} - 0.4240 * F_{ac} + 20.409 \qquad \text{(C-36)}$$

$$R^2 = 0.863$$

For E_{sg} = 25 ksi,

$$E_{s\min} = 2.4581 * F_{ac}^{\ 2} - 2.1675 * F_{ac} + 26.22 \qquad \text{(C-37)}$$

$$R^2 = 0.776$$

Again, by fitting a trend for the variation of coefficients A, B, and C with E_{sg} (Figures C-48), linear regression equations were obtained. Using these equations, E_{smin} is written as:

$$E_{s\min} = (0.0861 * E_{sg} + 0.2860) * F_{ac}^{\ 2} - (0.3233 * E_{sg} - 6.1389) * F_{ac} + (1.1059 * E_{sg} - 1.7244) \qquad \text{(C-38)}$$

$$R^2 = 0.977 \qquad SEE = 1.027$$

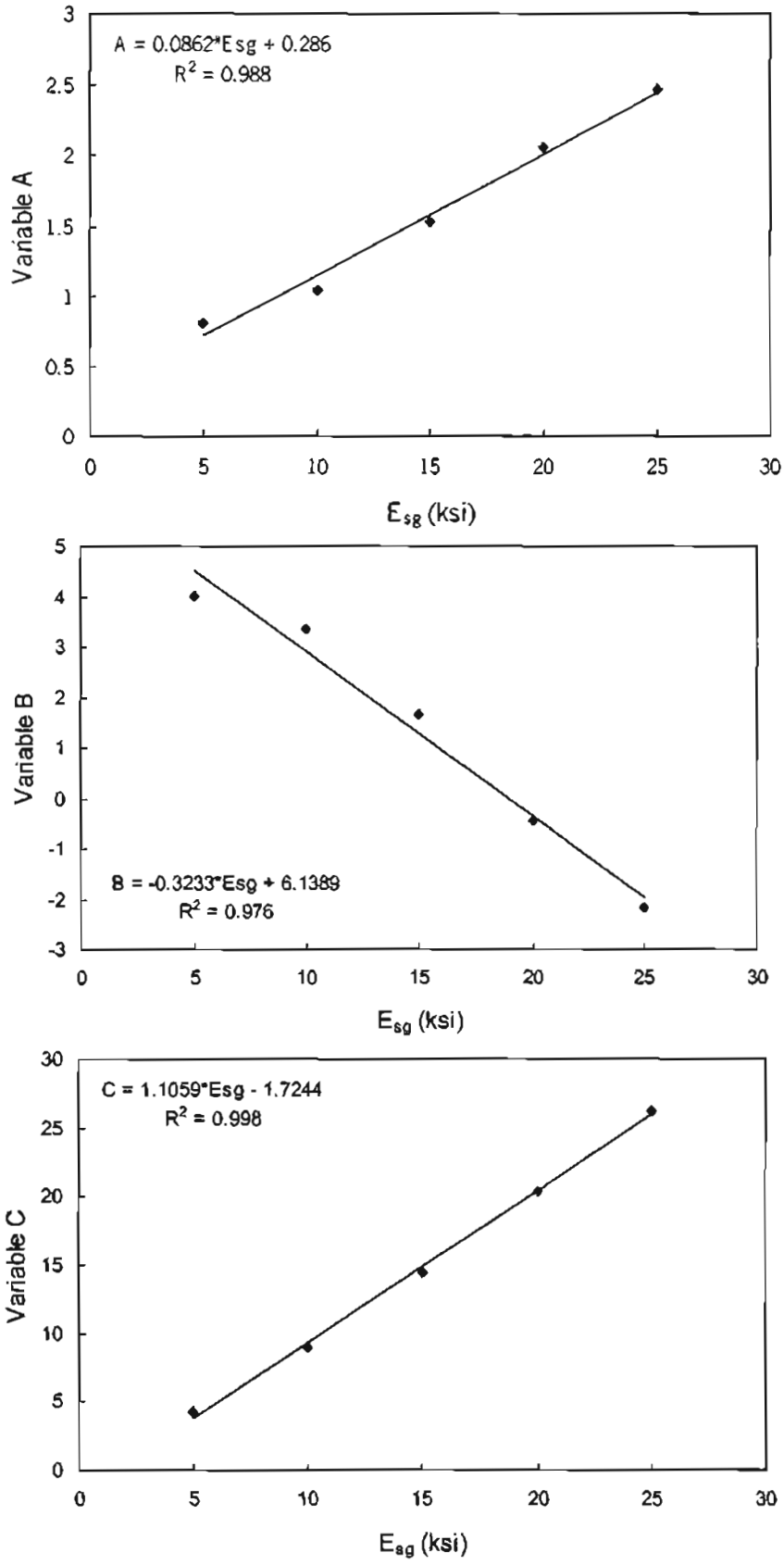

Figure C-48. Determination of coefficients A, B, and C for aggregate base pavements

By reorganizing Eq. C-38, factor a and E_{sg} for aggregate base pavements can be expressed as:

$$\alpha = 0.2860 * \frac{F_{ac}^{\ 2}}{E_{sg}} + 6.1389 * \frac{F_{ac}}{E_{sg}} - 1.7244 * \frac{1}{E_{sg}} + 0.0861 * F_{ac}^{\ 2} - 0.3233 * F_{ac} + 1.1059 \quad \text{(C-39)}$$

$$E_{sg} = \frac{E_{s\min} - 0.2860 * F_{ac}^{\ 2} - 6.1389 * F_{ac} + 1.7244}{0.0861 * F_{ac}^{\ 2} - 0.3233 * F_{ac} + 1.1059} \quad \text{(C-40)}$$

Similar to full-depth pavements, when depth to a stiff layer is not infinite (i.e., $H_{sg} < 160$ inches), the following equation was developed to predict factor α:

$$\alpha = 0.0145 * \frac{F_{ac}^{\ 2}}{E_{sg}} + 5.6922 * \frac{F_{ac}}{E_{sg}} - 0.2353 * \frac{1}{E_{sg}} + 0.045 * F_{ac}^{\ 2} - 0.115 * F_{ac} + 23.2748 * \frac{F_{ac}}{D_{sg}^{\ 3}} + 1.0091 \quad \text{(C-41)}$$

$R^2 = 0.901 \qquad SEE = 0.423$

By reorganizing Eq. C-41, E_{sg} can be expressed as:

$$E_{sg} = \frac{E_{s\min} - 0.0145 * F_{ac}^{\ 2} - 5.6922 * F_{ac} + 0.2353}{0.045 * F_{ac}^{\ 2} - 0.115 * F_{ac} + 23.2748 * \frac{F_{ac}}{D_{sg}^{\ 3}} + 1.0091} \quad \text{(C-42)}$$

Eqs. C-40 and C-42 give an easy and quick way to estimate the subgrade modulus for aggregate base pavements. If subgrade is infinite, E_{sg} can be predicted graphically by locating the point (F_{ac}, E_{smin}) in Figure C-49.

Since AC thickness in surface treated pavements is beyond the lower limit of the synthetic data range used in this research, the ANNs developed using this synthetic data

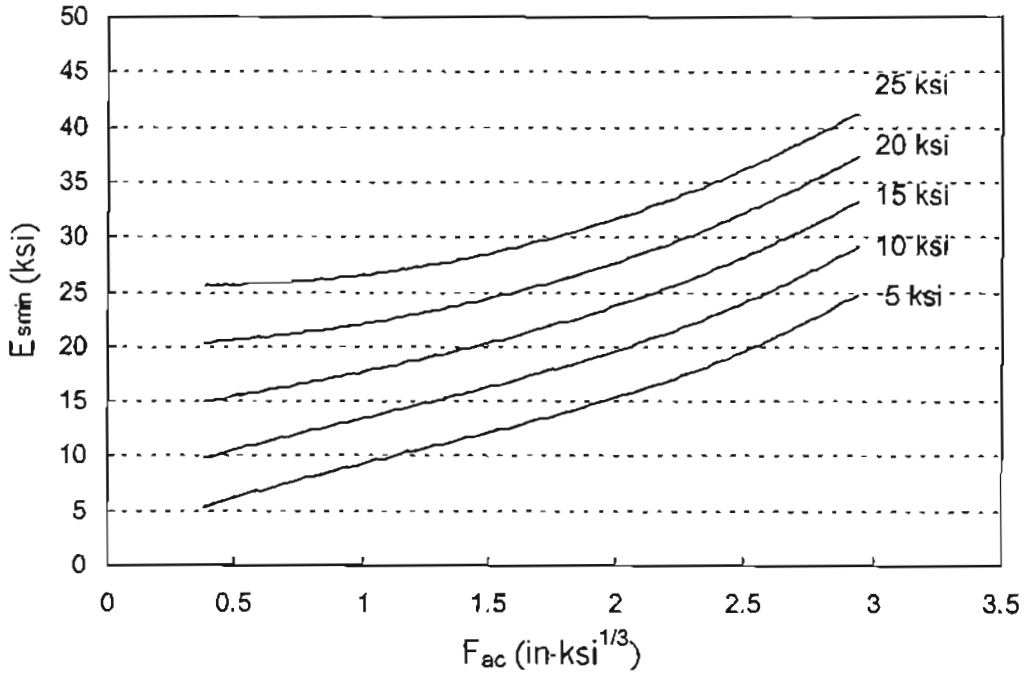

Figure C-49. Determining E_{sg} from E_{smin} and F_{ac} for full-depth pavement with infinite subgrade

do not work well in evaluating the condition of surface treated pavements. Using the surface modulus based procedures to predict E_{sg}, however, is suitable for surface treated pavements. As a surface treated pavement has a very thin AC layer, the corresponding value of F_{ac} is usually less than 0.5. From Figure C-47, it can be seen that factor α is very close to 1 when F_{ac} is less than 0.5 and the pavement does not have a shallow stiff layer. Thus, for surface treated pavements, E_{sg} can be approximately expressed as:

$$E_{sg} \approx E_{s\,min} \tag{C-43}$$

This observation is very helpful since it allows one to estimate subgrade modulus from the calculated surface modulus profile without knowing thickness and modulus information of upper layers.

REFERENCES

C-1 Andrew M. Johnson and Ronald L. Baus: Simplified Direct Calculation of Subgrade Modulus from Nondestructive Pavement Deflection Testing, TRB 1406, 1991

C-2 Stubstad, R. N., Irwin, L.H., Lukanen, E. O., and Clevenson, M.L., "It's 10 o'clock – Do You Know Where Your Sensors Are?," Transportation Research Board, 79th Annual Meeting, Washington, D., C., Jan., 2000.

APPENDIX D

ARTIFICIAL NEURAL NETWORK

INTRODUCTION

The primary goal of this activity was to facilitate several steps in the condition assessment procedure through the development of descriptive models that represent relationships among pavement condition indicators and layer properties. This development effort was necessary in cases where no known functional relationship was available. The basis for the model development is the database of FWD deflection measurements, and pavement layer properties and conditions. The model development was carried out using artificial neural networks (ANNs). ANNs, which are structured based loosely upon neurological systems prevalent in nature, provide a computational framework for acquiring meta-level information embedded in data. There are different types of ANNs, the most commonly used being the feed-forward type networks. The primary function of a feed-forward type ANN is to extract and implement a cause-effect relationship that may exist within a data set. The general structure of this type of network (Figure D-1) consists of several layers of artificial neurons, or commonly referred to as units, that are interconnected between all units in adjacent layers. One layer represents the input information and another the outputs. Intermediate layers are included to enable the network to represent collectively a general nonlinear function, which is characterized by the connection weights. An error minimization algorithm is employed to determine the best set of connection weights that correspond to the best-fit function. This process is commonly referred to as supervised training. This approach is analogous to statistical regression, except that the form of the function that is sought need not be defined a priori in the ANN-based approach.

The key steps that are commonly required when developing an ANN-based model include the following:

- *Compilation of a rich data set that represents the desired range of the relationship* - it is important that the data cover the range of typical input and output values that would be observed when using the trained ANN. Although ANNs are excellent at interpolation, their extrapolation capabilities are limited. They do, however, fail gracefully, i.e., they do not abruptly fail as a predictor when deviating marginally outside of the intended data ranges.
- *Modeling and representation of the input and output parameters* - the information that is to be predicted, i.e., the model output, is usually defined by the nature of the problem, and input may include independent variables (e.g., the deflection measurements at sensors) as well as derived descriptor variables (e.g., deflection basin parameters) of the output. The selection of input parameters to be modeled requires an understanding of the overall information being modeled and the context of the problem that is being considered. Empirical observations in practice show that including derived descriptors which are known to be related to the output improves the performance, although the derived descriptors could be implicitly captured based on the independent input parameters.
- *Setting ranges for normalizing the data* – the data used in the development of the ANN-based models are normalized a priori. This normalization is applied to both the data that is used in training as well as in post-prediction. The normalization ranges are usually set based on typical values each parameter would take in field application, and they influence the potential application of the trained ANN. Care should be taken is setting these ranges and sufficient consideration should be given to the anticipated values of a parameter during typical application of the trained ANN.

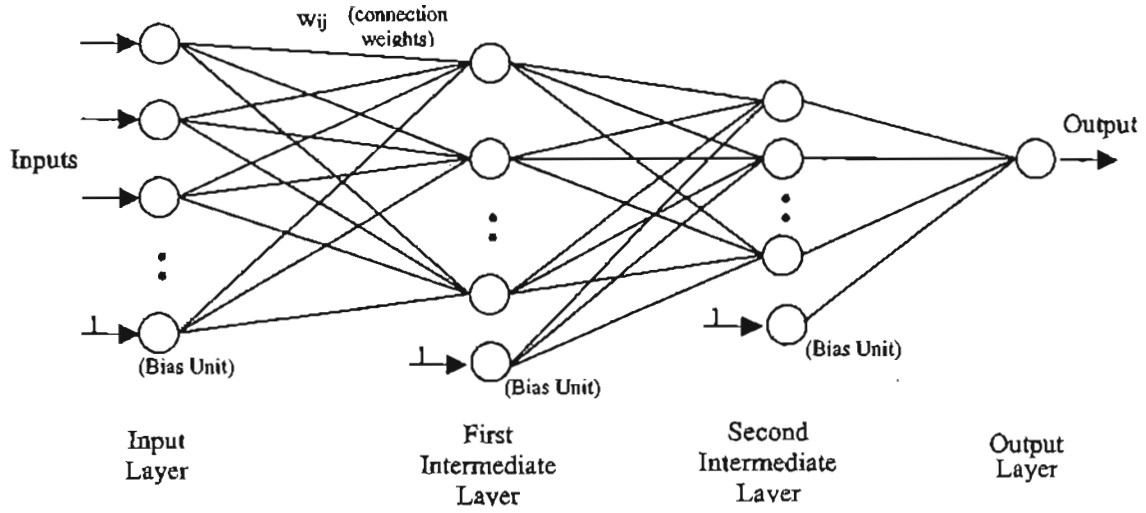

Figure D-1. Typical structure of a feed-forward type ANN

- *Determination of the best network architecture as defined by the number of intermediate units* - since the complexity of the function being mapped is not known a priori, the desirable number of functional terms, characterized by the number of units, is unknown. Typically this is identified by examining the predictive performance of several network architectures constructed by changing the number of intermediate units.
- *Testing the predictive performance* – the trained network is used to predict the output values for a set of data sets that were not used in the training of that network. Prediction error (as a function of the network predicted values and the actual values) is computed to characterize the performance of a network.

The following section describes the key information pertaining to developing the ANN-based models for pavement condition assessment.

Overview of the ANN-based approach

ANNs have been used widely in various areas, such as time series predictions, classification, pattern recognition, identification, decision-making, and vision and control systems. Also, several studies on application of ANNs in pavement engineering have been reported by researchers. For example, Merier et al.(D-1) and Lee (D-2) applied ANNs to successfully backcalculate the flexible pavement layer moduli from static and dynamic deflection basins. The report from Zaman et al. (D-3) also showed that the nonlinear behavior of cohesionless soils could be simulated accurately using ANNs.

In this research, ANNs are employed to develop models that describe the relationships between pavement condition indicators and surface deflection data as well as associated deflection basin parameters (DBPs). All ANN models were implemented and trained using the ANN libraries available within the Matlab software. Since only limited field data sets were

available, the data for developing the ANNs were augmented with synthetic data sets derived from the FEM analyses. This was necessary since the data sets need to cover the typical ranges of pavement layer characteristics, as well as they should include a large number of data points, properties that are characteristic of the FEM-based synthetic database. Ideally, it is desirable to use field data sets that implicitly incorporate noise and errors seen typically in field measurements. To ensure that the ANNs developed using the synthetic database are sufficiently robust for use in condition evaluation of field data, the trained ANNs were tested using field data where available. Although synthetic data is used in the current development, the procedures adopted here for developing the ANN-based models and their use in condition evaluation are directly applicable to new data sets that may become available in the future.

The data ranges for the parameters were chosen during the FEM analysis to include all values associated with typical pavement designs and material properties. The normalization of the data in preparation for input to the ANNs was carried out based on these data ranges. As mentioned previously, while the trained ANNs could interpolate effectively among these ranges, their extrapolation capabilities (i.e., to work outside of the chosen data ranges) are limited. Therefore, the application of the ANNs developed here should be restricted to field data that fall within the chosen data ranges. This issue, however, should not be considered limiting. If new data sets that are significantly outside of the current data ranges are available, the ANN-based model development procedure presented here could be readily applied, and new models for these updated data ranges could be implemented.

The most effective set of input information for each ANN model was determined through a systematic investigation which involved engineering judgement about the most likely descriptors of the output being predicted, the sensitivity of DBPs to the output, and the

experience gained by the research team during this research. For example, as outer sensors represent the lower layer characteristics, the ANN-based model for predicting subgrade-related parameters performed better when only the outer sensor deflections, instead of all, were used. The subsequent section lists the best set of information identified as inputs for the ANN-based models for different layer properties.

The best network architecture was determined using a systematic, but trial-and-error examination of varying number of intermediate units. All ANNs were structured to have two layers of intermediate units. The actual numbers of units in each were varied. In general, the predictive capabilities (or typically referred to as generalization capabilities) of ANN-based model when applied to new data sets improve with decreasing number of intermediate units. More intermediate units increases, however, the dimensionality of the function being fitted, enabling easier training which results from higher training capacity. This detrimentally affects, however, the generalization capabilities of the network. Considering this tradeoff and determining a number of intermediate units that provides a good ANN-based model is the goal of the trial-and-error search. The ranges of networks examined for each type of pavement and pavement layer conditions are described below.

A performance measure, indicated by the average prediction error, was used to determine when to stop training a network. The prediction error was computed for the training data set as well as a testing data set (obtained from the synthetic database and field data where available), which was not used in training. Typical variation of prediction error with increasing training iterations (or epochs) is shown in Figure D-2, which indicates that over-training (i.e., the network memorizes or fine-tunes for the training data set, losing the generalization capabilities) can potentially be harmful with respect to the prediction performance for a new data set. To avoid

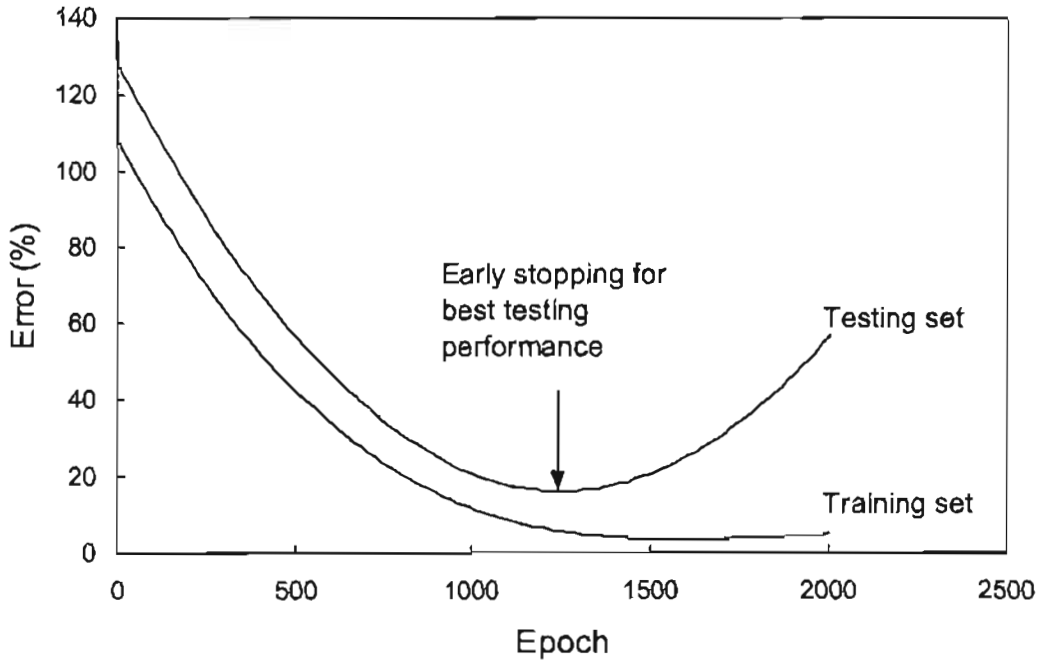

Figure D-2. Typical ANN performance variation with training iteration (epoch)

this, the testing performance of the network was checked periodically (after every 5 epochs) during training and used that information to determine the stopping criterion. It is important to note that having a low testing error computed based on synthetic data does not necessarily correlate with prediction errors estimated for field data, where available. For example, the network architecture that resulted in the lowest prediction during the ANN-based model development using synthetic data did not always give the lowest prediction error when tested using the field measurements. This could be attributed to the lack of noise and error, which is common among field measurement, in the synthetic data set. If field data were used for training the network (as previously recommended), its prediction performance for field data sets would be comparable to that of the training. Recognizing this issue, the final ANN-based model in our investigations was selected based on their performance for field data sets where available, instead of that for the synthetic data set. Again, if more field data sets become available in the future, the procedure adopted here can be applied for the new database and updated ANN-based models could be obtained.

Adopting these general steps, ANN-based models were developed and implemented for predicting pavement condition indicators associated with each pavement type. These models are incorporated into the pavement condition assessment procedures described in main text. The results of the investigation of the ANN-based predictive modeling are summarized below.

SUMMARY OF RESULTS: ANN-BASED PREDICTIVE MODELS

The tables below summarize the network architectures, defined by the input parameters, the numbers of units in the two intermediate layers, and output parameter, and their prediction performance. The prediction performance reported here is RMSE based on the synthetic database. The prediction errors for the flexible pavement cases are based on a small test data set that was not used in training, and those for the CTB and AC/PCC pavements are based on the entire data set, which was used in the training of the final networks. These tables are grouped by the different pavement types. Results associated with testing performance of the networks when applied to field data are described in Chapter 3, and are not repeated here.

Table D-1. Summary of ANN-based models for full-depth pavements[1] (developed using synthetic database for dynamic, linear elastic analysis)

Output	Inputs	Intermediate Units	Prediction Error (%)
E_{ac}	D_0-D_{48},H_{ac},*SCI*,*BDI*	11, 9	1.8
	D_0-D_{12},H_{ac},*SCI*,*BDI*	11, 9	7.6
E_{sg}	D_0-D_{48},H_{ac},AI_4,*BCI*	11, 9	6.9
	D_{24}-D_{48},H_{ac},AI_4,*BCI*	15, 12	20.5
DSL	D_0-D_{48},H_{ac},F_3,F_2	15, 12	5.6
	D_{24}-D_{48},H_{ac},F_3,F_2	19, 15	15.9

1. The database includes 1,100 data points of which 100 were saved for testing

Table D-2. Summary of ANN-based models for full-depth pavements[1] (developed using synthetic database for dynamic, nonlinear elastic analysis)

Output	Inputs	Intermediate Units	Prediction Error (%)
E_{ac}	D_0-D_{48},H_{ac},*SCI*,*BDI*	11, 9	1.9
	D_0-D_{36},H_{ac},*SCI*,*BDI*	11, 9	5.6
ε_{ac}	D_0-D_{48},H_{ac},*SCI*,*BDI*	11, 9	1.6
ε_{sg}	D_0-D_{48},H_{ac},AI_4,*BCI*	15, 12	5.6
E_{Ri}	D_0-D_{48},H_{ac},AI_4,*BCI*	19, 15	23.5
SSR	D_0-D_{48},H_{ac},AI_4,*BCI*	15, 12	15.7
DSL	D_0-D_{48},H_{ac},F_3,F_2	11, 9	16.9

1. The database includes 2,000 data points of which 100 were saved for testing

Table D-3. Summary of ANN-based models for aggregate base pavements[1] (developed using synthetic database for dynamic, linear elastic analysis)

Output	Inputs	Intermediate units	Prediction Error (%)
E_{ac}	D_0-D_{48},H_{ac},H_{abc},SCI,BDI	11, 9	7.8
	D_0-D_{24},H_{ac},H_{abc},SCI,BDI	11, 9	14.6
E_{abc}	D_0-D_{48},H_{ac},H_{abc},BDI,BCI	11, 9	12.5
	D_{12}-D_{36},H_{ac},H_{abc},BDI,BCI	19, 15	20.3
E_{sg}	D_0-D_{48},H_{ac},H_{abc},AI_4,BCI	11, 9	26.5
	D_{24}-D_{48},H_{ac},H_{abc},AI_4,BCI	15, 12	53.2
DSL	D_0-D_{48},H_{ac},H_{abc},F_3,F_2	15, 12	9.4
	D_{24}-D_{48},H_{ac},H_{abc},F_3,F_2	19, 15	19.6

1. The database includes 10,600 data points of which 100 were saved for testing

Table D-4. Summary of ANN-based models for aggregate base pavements[1] (developed using synthetic database for dynamic, nonlinear elastic analysis)

Output	Inputs	Intermediate Units	Prediction Error (%)
E_{ac}	D_0-D_{48},H_{ac},H_{abc},SCI,BDI	11, 9	5.6
	D_0-D_{24},H_{ac},H_{abc},SCI,BDI	11, 9	16.3
ε_{ac}	D_0-D_{48},H_{ac},H_{abc},SCI,BDI	11, 9	4.4
ε_{abc}	D_0-D_{48},H_{ac},H_{abc},BDI,BCI	11, 9	8.7
ε_{sg}	D_0-D_{48},H_{ac},H_{abc},AI_4,BCI	15, 12	13.4
E_{Ri}	D_0-D_{48},H_{ac},H_{abc},AI_4,BCI	19, 15	35.7
SSR	D_0-D_{48},H_{ac},H_{abc},AI_4,BCI	19, 15	22.3
DSL	D_0-D_{48},H_{ac},H_{abc},F_3,F_2	19, 15	21.1

1. The database includes 8,000 data points of which 100 were saved for testing

Table D-5. Summary of ANN-based models for CTB pavements

Output	Inputs	Intermediate Units	Prediction Error (%)
E_{ac}	D_0-D_{48},SCI,$AUPP$,H_{ac},H_{abc}	16, 13	2.4
E_{ctb}	D_0-D_{48},H_{ac},H_{ctb}	18, 15	6.5
	D_0-D_{48},BDI,BCI,H_{ac},H_{ctb}	20, 17	9.6
E_{sg}	D_0-D_{48},LSI,H_{ac},H_{ctb}	16, 13	32.1
	D_{24}-D_{48},H_{ac},H_{ctb}	12, 9	34.3
H_{sg}	D_0-D_{48},F_3,F_2,H_{ac},H_{ctb}	17, 14	21.3
	D_{24}-D_{48},F_3,F_2,H_{ac},H_{ctb}	8, 6	25.8

1. The database includes 7,797 data points

Table D-6. Summary of ANN-based models for AC/PCC pavements

Output	Inputs	Intermediate Units	Prediction Error (%)
E_{ac}	D_0-D_{48},SCI,$AUPP$,H_{ac},H_{pcc}	16, 13	2.4
E_{pcc}	D_0-D_{48},H_{ac},H_{pcc}	16, 13	4.8
E_{sg}	D_0-D_{48},H_{ac},H_{pcc}	16, 13	21.6
	D_{24}-D_{48},H_{ac},H_{pcc}	9, 7	37.6
H_{sg}	D_0-D_{48},H_{ac},H_{pcc},F_3,F_2	18, 15	11.2
	D_{24}-D_{48},H_{ac},H_{pcc},F_3,F_2	13, 11	12.9

1. The database includes 6,597 data points

ILLUSTRATIVE APPLICATIONS USING FIELD DATA

As previously mentioned testing of sufficiently complete field data (obtained from state DOTs) is presented in Chapter 3. Some additional field data from DataPave that were incomplete, however, are used in the following illustrative applications. This was carried out for data corresponding to CTB and AC/PCC pavements. As insufficient information was available, each ANN-based model output could not be confirmed fully; however, this exercise focused on examining trends in predictions and comparing them with those from AASHTO 1993 guidelines. It must be noted that the investigations carried out here are limited, and at best preliminary; this should be viewed strictly as illustrative applications. The following subsections summarize these illustrative applications and their results. More detailed testing and evaluation is needed, which is recommended as an important follow-up work.

Depth to a Stiff Layer in CTB Pavements

As the depth to stiff layer (DSL) is expected not to change with climatic conditions or pavement distress condition, it is possible to assess the prediction performance by examining the trends in the DSL predictions at a location or pavement section. The H_{sg} prediction results for some CTB pavements from DataPave are summarized in table D-7. The data represent FWD measurements from different test dates at the same pavement sections. Prediction results show that the predicted depths change very little with changes in test date. The RMSE for each test date was also quite low. This analysis seems to indicate that the ANN-based model predictions would be useful in the determination of stiff layer depth in CTB pavements. The accuracy of the predicted values cannot be confirmed since DSL measurements were not recorded for these data points.

Table D-7. H_{sg} predictions for CTB pavements from DataPave

		ANN Prediction (in)	ANN RMSE (%)
Arizona	Mar-6-89	162	2
	Mar-2-92	118	8
	Nov-4-92	112	13
	May-7-96	118	5
California	Nov-2-92	152	5
	May-26-93	168	0
	Feb-21-97	153	7
Florida	Dec-21-89	158	1
	Jul-31-90	158	2
	Nov-8-90	156	1
	May-28-91	142	2
	Nov-23-93	149	1
Maryland	Apr-20-89	47	9
	Apr-9-90	41	9
	Aug-10-92	88	14
Mississippi	Oct-11-90	92	21
	Jul-19-91	129	6
	Jun-24-92	154	1
	Aug-3-93	138	5
	Dec-1-95	103	49
North Dakota	Jun-22-89	77	3
	Sep-29-93	87	6
	Aug-23-94	80	2
Oklahoma	Jun-1-90	146	2
	Dec-7-90	113	5
	Aug-13-91	153	2
	Apr-26-93	158	1
	Jun-21-95	158	3
Texas-1050	Jun-7-89	153	1
	Jan-25-91	138	2
	Oct-18-93	161	1
	Dec-5-94	155	1
Texas-3749	Feb-27-90	164	0
	Feb-8-91	166	0
	Nov-25-91	162	1
	Apr-1-93	158	2
Virginia	Apr-14-89	102	7
	Feb-21-90	76	6
	Dec-6-93	46	8
	Sep-18-95	154	1
	Mar-24-97	95	6
Wyoming	Jun-22-89	169	0
	Sep-20-94	169	0
	Jun-17-97	167	0

Depth to a Stiff Layer in AC/PCC Pavements

An analysis as described above was conducted for several AC/PCC pavements from DataPave. The results are summarized in Table D-8. Again, the predictions (with very low RMSE) show little variation in the predictions with varying test dates, indicating that the ANN-based prediction approach is suitable for estimating depth to stiff layer in AC/PCC pavements.

PCC Layer Condition in AC/PCC Pavements

The ANN-based model for E_{pcc} prediction was applied to estimate the PCC layer modulus for several pavements from the DataPave database. The prediction results are summarized in table D-9. With the exception of damage due to traffic loads, no significant changes in base modulus, with respect to test date, are expected. Warping and curling effects that are substantial in rigid pavements are insignificant due to the continuous overlying asphalt layer. The AASHTO 1993 Pavement Design Guide includes a procedure for predicting E_{pcc}. This method was also employed for these data points and the results are also shown in Table D-7. These results show that the ANN-based prediction results are fairly consistent with respect to test date. RMSE values are also quite low in all cases, indicating consistent predictions for each test date. The AASHTO predictions, however, are unreasonably high in many cases, resulting in high RMSE. Although the trends shown in the ANN-based predictions are reasonable, field data with known base layer condition would have to be studied to make a final conclusion about the accuracy of these predictions.

Table D-8. H_{sg} predictions for AC/PCC pavements from DataPave

			ANN Prediction	ANN RMSE
Colorado	Jun-29-89	Lane Position 1	142	3
		Lane Position 2	156	3
	Apr-4-94	Lane Position 1	103	8
		Lane Position 2	78	3
	Sep-14-94	Lane Position 1	162	0
		Lane Position 2	162	0
	Aug-20-98	Lane Position 1	113	4
		Lane Position 2	71	3
Georgia	Mar-7-89	Lane Position 1	47	9
		Lane Position 2	102	14
	Jun-11-91	Lane Position 1	49	6
		Lane Position 2	66	9
	Sep-17-92	Lane Position 1	46	7
		Lane Position 2	69	8
	Mar-30-95	Lane Position 1	48	6
		Lane Position 2	65	10
	Jul-7-98	Lane Position 1	49	4
		Lane Position 2	69	6
Nebraska	Aug-17-89	Lane Position 1	142	16
		Lane Position 2	117	11
	Apr-22-95	Lane Position 1	132	4
		Lane Position 2	79	5
	Nov-13-95	Lane Position 1	163	0
		Lane Position 2	126	3
South Dakota	Jul-20-89	Lane Position 1	134	3
		Lane Position 2	76	5
	Oct-24-91	Lane Position 1	149	3
		Lane Position 2	137	4
	Oct-18-93	Lane Position 1	114	3
		Lane Position 2	92	6
	Jul-17-95	Lane Position 1	104	9
		Lane Position 2	88	3
Ontario	Aug-31-89	Lane Position 1	134	24
		Lane Position 2	129	11
	Jul-25-90	Lane Position 1	120	16
		Lane Position 2	131	12
	Apr-16-98	Lane Position 1	126	15
		Lane Position 2	120	3

Table D-9. E_{pcc} predictions for AC/PCC pavements from DataPave

			ANN		AASHTO 93	
			Prediction	RMSE	Prediction	RMSE
Colorado	Jun-29-89	Lane Position 1	3216	2	5450	3
		Lane Position 2	3680	2	5314	6
	Apr-4-94	Lane Position 1	4095	3	11232	4
		Lane Position 2	3675	2	9969	4
	Sep-14-94	Lane Position 1	5111	0	5581	3
		Lane Position 2	4937	2	5154	3
	Aug-20-98	Lane Position 1	4751	2	6801	3
		Lane Position 2	4609	2	4236	3
Georgia	Mar-7-89	Lane Position 1	4010	3	22250	8
		Lane Position 2	3880	3	22509	11
	Jun-11-91	Lane Position 1	4457	2	6921	4
		Lane Position 2	4762	2	4633	3
	Sep-17-92	Lane Position 1	4057	3	8718	3
		Lane Position 2	4402	3	5790	4
	Mar-30-95	Lane Position 1	4159	2	11902	6
		Lane Position 2	4581	2	8804	5
	Jul-7-98	Lane Position 1	4402	2	4641	5
		Lane Position 2	4948	1	4548	4
Nebraska	Aug-17-89	Lane Position 1	4557	3	8953	5
		Lane Position 2	3769	3	5806	3
	Apr-22-95	Lane Position 1	4558	3	9991	4
		Lane Position 2	4033	2	7087	3
	Nov-13-95	Lane Position 1	4739	2	31695	9
		Lane Position 2	4658	2	21050	5
South Dakota	Jul-20-89	Lane Position 1	4233	3	8491	7
		Lane Position 2	5108	0	7981	3
	Oct-24-91	Lane Position 1	4029	3	9246	8
		Lane Position 2	4098	3	15126	11
	Oct-18-93	Lane Position 1	4271	3	8179	4
		Lane Position 2	3903	3	14140	5
	Jul-17-95	Lane Position 1	5101	0	3832	6
		Lane Position 2	5111	0	3646	3
Ontario	Aug-31-89	Lane Position 1	4143	3	11213	272
		Lane Position 2	4249	3	13080	26
	Jul-25-90	Lane Position 1	4251	3	15425	18
		Lane Position 2	4310	3	9686	5
	Apr-16-98	Lane Position 1	4133	3	14603	21
		Lane Position 2	4119	3	11649	18

Subgrade Strength in AC/PCC Pavements

The ANN-based procedure and the procedure based on AASHTO 1993 Pavement Design Guide were conducted to predict E_{sg} in AC/PCC pavements. The summary of results from this application to DataPave data is given in Table D-10. In general, the AASHTO predictions are higher than the ANN predictions, but with a lower RMSE. Because subgrade condition is unknown in all DataPave cases, the results cannot be used to verify either method. Only general trends can be observed. Due to the clear differences in the state field database, the ANN-based approach is considered to more robust.

Table D-10. E_{sg} predictions for AC/PCC pavements from DataPave

			ANN		AASHTO 93	
			Prediction	RMSE	Prediction	RMSE
Colorado	Jun-29-89	Lane Position 1	31	4	43	4
		Lane Position 2	60	22	35	6
	Apr-4-94	Lane Position 1	21	7	29	2
		Lane Position 2	21	3	26	2
	Sep-14-94	Lane Position 1	50	3	35	3
		Lane Position 2	48	4	33	1
	Aug-20-98	Lane Position 1	24	3	35	2
		Lane Position 2	21	6	33	2
Georgia	Mar-7-89	Lane Position 1	10	2	83	3
		Lane Position 2	15	5	57	4
	Jun-11-91	Lane Position 1	13	3	86	2
		Lane Position 2	16	5	76	2
	Sep-17-92	Lane Position 1	12	3	84	2
		Lane Position 2	17	5	66	2
	Mar-30-95	Lane Position 1	13	4	84	2
		Lane Position 2	15	4	71	3
	Jul-7-98	Lane Position 1	14	3	89	2
		Lane Position 2	17	12	68	4
Nebraska	Aug-17-89	Lane Position 1	25	12	37	1
		Lane Position 2	13	282	30	2
	Apr-22-95	Lane Position 1	20	34	32	2
		Lane Position 2	13	32	24	2
	Nov-13-95	Lane Position 1	24	6	28	2
		Lane Position 2	19	55	22	2
South Dakota	Jul-20-89	Lane Position 1	24	8	43	2
		Lane Position 2	21	4	30	2
	Oct-24-91	Lane Position 1	31	2	35	3
		Lane Position 2	25	6	25	4
	Oct-18-93	Lane Position 1	28	7	34	1
		Lane Position 2	21	5	24	2
	Jul-17-95	Lane Position 1	20	10	37	1
		Lane Position 2	16	11	33	2
Ontario	Aug-31-89	Lane Position 1	22	19	49	5
		Lane Position 2	23	21	46	2
	Jul-25-90	Lane Position 1	21	19	52	3
		Lane Position 2	21	32	47	2
	Apr-16-98	Lane Position 1	23	20	48	2
		Lane Position 2	28	52	36	1

REFERENCES

D-1 Meier, R.W. and G. J. Rix, "Backcalculation of Flexible Pavement Moduli From Dynamic Deflection Basins Using Artificial Neural Networks," In Transportation Research Record 1473, TRB, National Research Council, Washington, D.C., 1995, pp.72-81.

D-2 Lee, Y.C., "Flexible Pavement Condition Assessment Using Deflection Data," 1997, Dissertation, North Carolina State University, Raleigh, NC

APPENDIX E

AC/PCC VOID DETECTION

INTRODUCTION

NCHRP study 10-48 involves proceedings FWD data with non-traditional back-calculation methods to identify defects in flexible and composite pavements. The goal is to evaluate methodologies that can rapidly interpret the deflection basins and identify subgrade problems. It is intended that the resulting methodologies will be readily implemented in possible spreadsheet type format.

In this section of the report an evaluation is made of the methodologies used to identify voids beneath joints in composite pavements. For the purpose of this report, a composite pavement is identified as a jointed concrete pavement with a thin (<3in.) hot mix asphalt (HMA) surfacing. It is proposed that the thin HMA layer will not have a major impact on the measured deflection bowl and that the reflection cracks will be clear in the HMA surfacing so that traditional joint deflection data can be collected. In conducting this study an evaluation is made of the appropriateness of existing void detection algorithms. As described below a new set of algorithms have been developed.

For the last two decades, several procedures have been developed for back-calculation of PCC slab and foundation moduli from measured deflections. Most procedures provide back-calculation of center or edge deflections. Interpretation of corner deflection is generally restricted to a single slab configuration, which is not the case in practice.

In this study, a unique evaluation process is proposed for direct interpretation of corner deflection in two adjacent slabs. Complex joint interaction is simplified by incorporating joint load transfer efficiency, LTE, into the deflection analysis. The process includes the dimensional analysis of structural parameters and deflection parameters of jointed concrete pavements (E-1). Structural system parameters are selected based on closed-form equations: radius of relative

stiffness (l), radius of loading plate (a), and load size ratio (a/l). Joint load transfer efficiency (LTE) is included to involve the effect of joint stiffness in corner loading condition. Corresponding response parameters are deflection basin AREA and non-dimensional maximum deflection.

On the other hand, structural evaluation is perhaps more difficult for asphalt overlaid concrete (AC/PCC) composite pavements than for any other pavement type. This complicated system may be simplified by the equivalent modulus concept. The closed-form based evaluation process also can be used for thin asphalt overlaid concrete (AC/PCC) with the application of equivalent modulus of AC and PCC layers.

To verify the proposed method, field tests were performed on experimental pavement sections at the research facility in Texas A&M University and in-service highway, US 287. The test pavements contain both PCC and thin overlaid AC/PCC. The experimental pavement section contained artificial voids underneath the pavement slab. Implementation indicated that the proposed process is convenient to practical use and gives quite reliable layer properties. It was also shown that the procedure may be used to identify joints which have subgrade deterioration, possibly voids.

VOID DETECTION

The unsupported area beneath the concrete slab, which is caused by the combination of excess moisture, pumping of fines, and erosion, is defined as voids. This type of pavement deterioration is generally created near transverse joints, working cracks, and edges. Pavement overlays will not serve the intended enhancement of service life if the voids are not properly restored prior to the rehabilitation. Experimental projects on grout sub-sealing in Illinois

revealed that the high pressure grouting without confirmed knowledge of voids could lift the slab excessively. These studies confirmed the significance of void detection.

In 1995, Texas Transportation Institute conducted a comparative study on the effectiveness of existing void detection procedures that utilize surface deflection measurements. Based on the success rate of each method, two methods, the CTR method (E-2) and the NCHRP method (E-3), were identified as most promising procedures. These two methods are readily incorporated in the concrete pavement back-calculation program RMODS, developed by Texas Transportation Institute (E-4). This section includes a brief overview on those two void detection procedures.

CTR Method

This method was developed by the Center for Transportation Research in the University of Texas at Austin. Two parameters M and Q are defined from a deflection basin, which can predict the presence of voids by empirical correlation. Figure E-1 illustrates those two deflection basin parameters. The parameter M is the angle between vertical line to the surface and the line joining maximum deflection and deflection at sensor 2. Other parameter Q is the angle between horizontal line and the line joining deflections at sensors 2 and 7. Since the actual angles are very small, a scaling factor is used to normalize them for the horizontal distances between sensors 1 and 2 and sensors 2 and 7. Empirically determined scaling factors are proposed for M and Q as 6 and 24, respectively. Empirical correlation indicated that voids are present if Q is greater than or equal to 22. The factor M may indicate the size of void. When a void exists, the smaller the value of M the larger the diameter of the void.

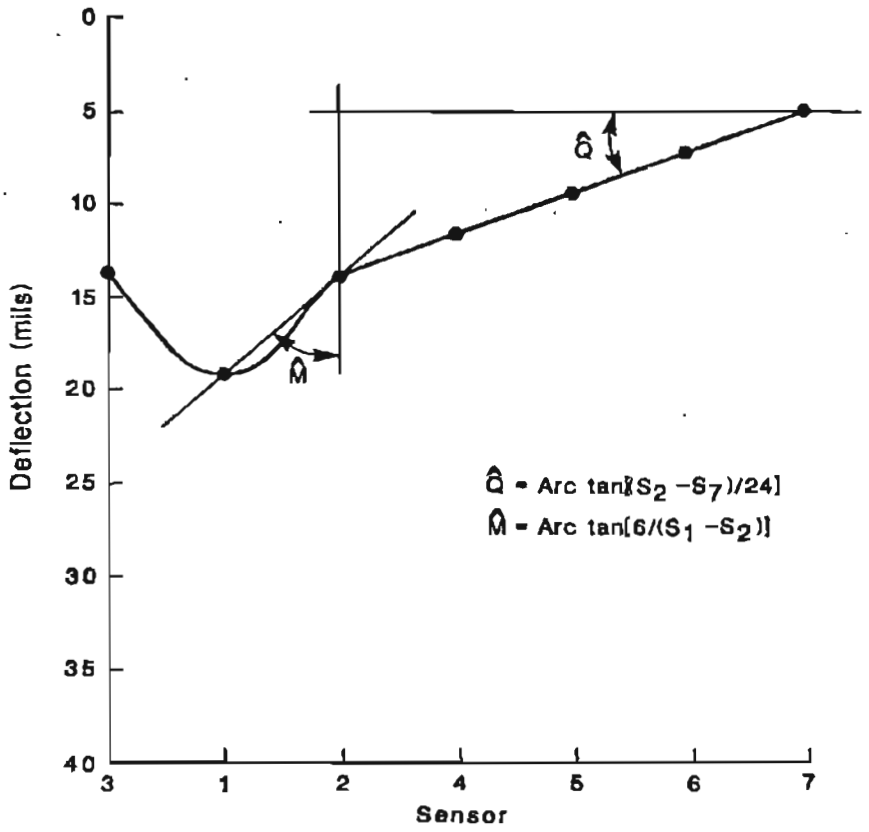

Figure E-1. Deflection basin parameters for void detection in the CTR method

NCHRP Method

This method was developed under NCHRP contract 1-21. Of the two methods outlined in the report, the proposed rapid void detection method was incorporated in RMODS. The procedure involves graphing a load-deflection diagram for FWD test and extrapolating the linear regression line through the x-intercept of the diagram. If the x-intercept is greater than 2 mils, then voids are present. Figure E-2 illustrates the NCHRP rapid void detection procedure.

DEFLECTIONS OF PCC PAVEMENTS

This section provides the fundamental background to computing deflections in PCC pavements.

Closed Form Solution

Westergaard (E-5, E-6) provided closed form solution for the load-deflection analysis of concrete pavement on the basis of slabs-on-grade system. Since then, the Westergaard solution has been the heart of the analysis and design of concrete pavement structures. The use of these classical equations includes the following assumptions:

1. The slab is acting as a plate supported uniformly by a dense liquid foundation.
2. There are no other materials between the slab and foundation.
3. The slab is of sufficient dimension such that any free edges, not connected with applied loads, are far enough away as not to influence the deflected shape of the slab.

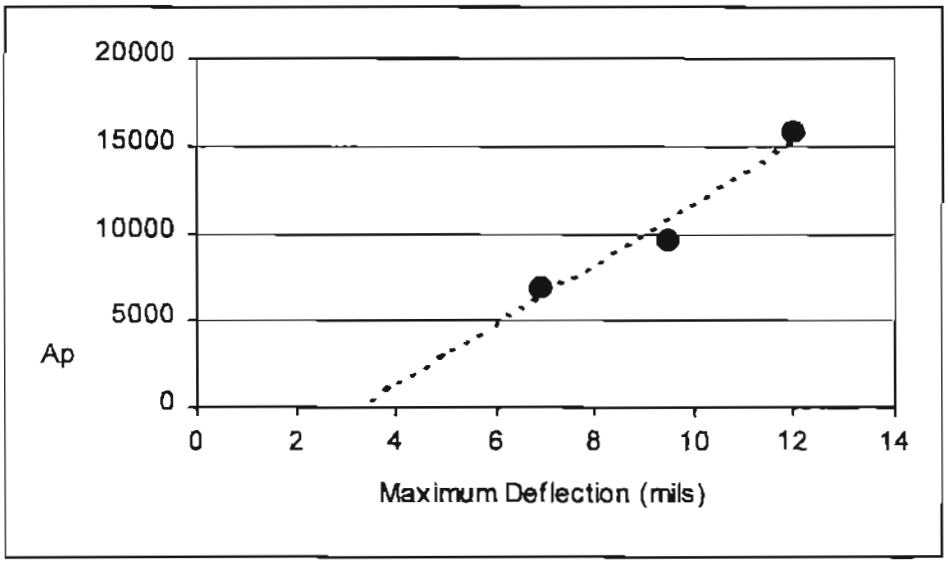

Figure E-2. The NCHRP method of void detection

The Westergaard solutions are only available for three particular loading conditions: interior, edge, and corner loading with the assumption of infinite or semi-infinite slab dimension. Here, the closed form solutions for deflections at each loading condition are described.

The Westergaard's interior loading condition is the case that a wheel load, which is uniformly distributed over the area of a small circle with radius 'a', is applied to the surface of a slab at a considerable distance from the edges. The closed form equation for interior deflection is given as follows:

$$\delta_i = \frac{P}{8kl^2}\left[1 + (1/2\pi)\left\{\ln\left((a/2l) + \gamma\right) - 5/4\right\}(a/l)^2\right] \qquad \text{(E-1)}$$

where, δ_i = interior deflection,

P = total applied load,

k = modulus of subgrade reaction,

l = radius of relative stiffness (equation 2),

a = radius of circular load, and

ln (γ) = Euler's constant (0.57721564490)

$$l^4 = \frac{Eh^3}{12(1-\nu^2)k} \qquad \text{(E-2)}$$

where, E = modulus of elasticity of concrete slab,

h = slab thickness, and ν = concrete Poisson's ratio.

Westergaard defined edge loading as the case when a wheel load is located at slab edge, but at a considerable distance from any corner. At the first equation in 1926, he assumed the pressure to be distributed uniformly over the area of small semi-circle with the center at the edge.

Equations for circular edge load were first presented in 1948. In 1960, Losberg simplified the equations to more manageable forms. Eqs. E-3, E-4 and E-5 show Westergaard's original equations in 1926, his new equations in 1948 and Losberg's simplified form in 1960, respectively.

$$\delta_e = \frac{1}{\sqrt{6}}(1+0.4\nu)\frac{P}{kl^2} \tag{E-3}$$

$$\delta_e = \frac{P\sqrt{2+1.2\nu}}{\sqrt{Eh^3k}}\left[1-(0.76+0.4\nu)(a/l)\right] \tag{E-4}$$

$$\delta_e = \frac{1}{\sqrt{6}}(1+0.4\nu)\frac{P}{kl^2}\left[1-0.76(1+0.5\nu)(a/l)\right] \tag{E-5}$$

where, δ_e = edge deflection, and

other symbols are shown under Eqs. E-1 and E-2.

Of the three fundamental cases of loading investigated by Westergaard, the corner loading is obviously the most obscure and debatable. The theoretical background for maximum corner deflection equation is particularly weak. In fact, several investigators have noted that although the Westergaard solution agreed fairly well with their observations for the interior loading condition, it failed to give even a close estimate of the response in the case of edge and corner loading. The semi-empirical and approximate nature of the Westergaard solutions for

corner loading have led to numerous revisions and modifications in an attempt to reconcile observed slab behavior with theory.

The first attempt was made in 1926 to solve the problem of corner break of concrete pavement slabs with a concentrated load acting at the corner of a slab. Few years later, Westergaard took up the problem again, trying to account for the effect of a load distributed over some area, whose resultant could be represented by a point load P acting at a small distance $a1$ from the corner, along the bisector of the corner. Using a simple approximate process involving the use of the principle of minimum potential energy, he hoped to achieve an improved approximation to corner stress. Then he arrived at Eq. E-6 for corner deflection. He quotes this equation as being approximately applicable for plausible ranges of $a1$ and l.

$$\delta_c = \frac{P}{kl^2}\left(1.1 - 0.88\frac{a1}{l}\right) \qquad \text{(E-6)}$$

where, δ_c = corner deflection, and

$a1$ = distance to point of action of resultant along corner angle bisector,

$= \sqrt{2}a$

other symbols are shown under Eqs. E-1 and E-2.

Non-Dimensional Maximum Deflection

Closed form equations described in previous section tell us that the Westergaard solutions may be reproduced as a function of non-dimensional load size ratio, a/l, when the deflection response is expressed in dimensionless term as in Eq. E-7. Introducing the non-dimensional

deflection yields more manageable forms of the closed form equations. For instance, the corner deflection (Eq. E-6) can be re-expressed as Eq. E-8 with its dimensionless term.

$$\Delta_j = \left(\frac{\delta_j k l^2}{P} \right) \tag{E-7}$$

where, Δ_j = non-dimensional deflections at each loading conditions, and

$j = i$ for interior, e for edge, or c for corner loading conditions.

$$\Delta_c = 1.1 - 1.2445(a/l) \tag{E-8}$$

where, Δ_c = non-dimensional maximum corner deflection.

Deflection Parameter AREA

Various deflection analysis methods introduce various descriptive parameters of the deflected surface shape. One such parameter is the geometrical deflection parameter AREA. The concept of AREA was originally defined by Hoffman and Thompson (E-7). They proposed a simple two-parameter approach to back-calculation of two layer flexible pavements by the use of AREA. AREA represents the trapezoidal cross sectional area of deflection basin normalized by the maximum deflection so that it has the dimension of length. Figure E-3 illustrates an extension of this AREA concept to any sensor configuration, calculated with the general equation:

$$AREA = \left(\frac{1}{\delta_1} \right) \sum_{i=1}^{n} \left[(R_{i+1} - R_i) \frac{(\delta_i + \delta_{i+1})}{2} \right] \tag{E-9}$$

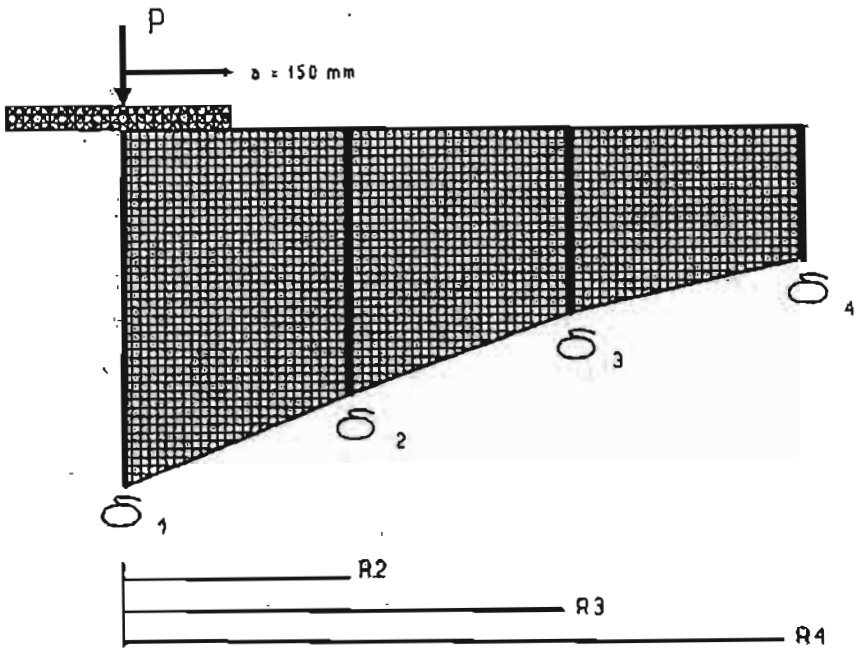

Figure E-3. Deflection basin AREA concept

where, R_i = Radial distance between sensor i and the center of loading plate

δ_i = Surface deflection measured at sensor i.

The AREA concept was subsequently applied to backcalculation of PCC slab elastic modulus (E_c) and the modulus of subgrade reaction (k). Further investigation of this concept has produced a forward solution procedure to replace the traditional iterative and graphical procedures. This solution is based on the fact that, for a given load radius and sensor arrangement, a unique relationship exists between AREA and the radius of relative stiffness, l.

Joint Load Transfer Efficiency

For corner loading condition, obviously the stiffness of adjacent slab will affect the deflection of loaded slab through joint stiffness. Joint load transfer efficiency, LTE, may reflect the effect of joint stiffness. As a preliminary study, the relationship between joint stiffness and LTE is examined with a set of finite element analysis and a subsequent non-linear regression study. The data plot and corresponding regression equation are presented in Figure E-4.

Since LTE is dimensionless as in Eq. E-10, the joint stiffness should be related with LTE in its non-dimensional form of S/kl, where S is the joint stiffness in the dimension of FL^{-2}. The coefficient 0.95 in Eq. E-10 takes account the deflection ratio of two locations at the same distance to δ_l and δ_u for center loading condition. The distance between the two locations is normally 12 inches apart.

The deflection basin shape at corner is not continuous, due to the geometric discontinuity of joint. In fact, the maximum corner deflection does not occur at the center of loading plate.

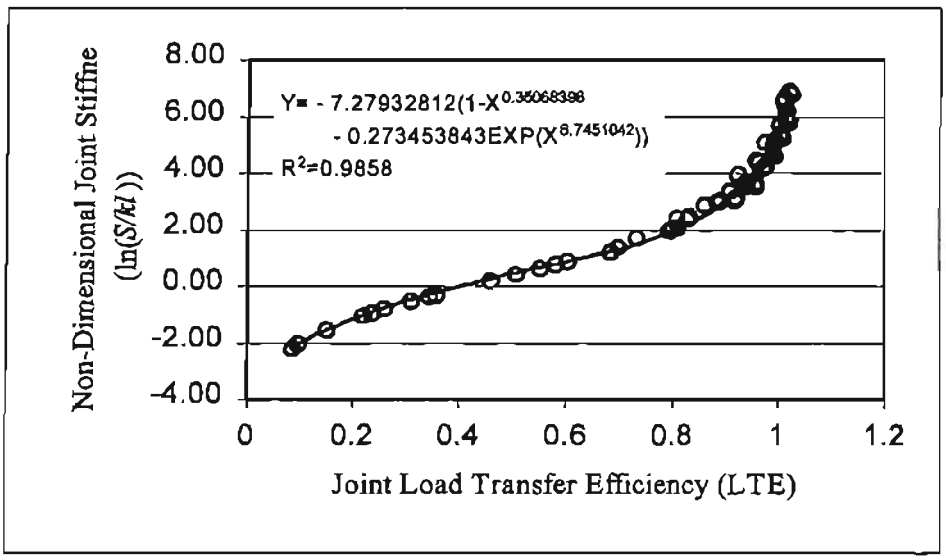

Figure E-4. Relationship between joint load transfer efficiency and non-dimensional joint siffness

Instead it occurs in between d_l and d_u so that the two values may be close to unity. Therefore, the *LTE* value calculated by equation 10 may be greater than unity.

$$LTE = \frac{\delta_u / \delta_l}{0.95} \tag{E-10}$$

where, δ_l = deflection of loaded side (d_1)

δ_u = deflection of unloaded side at the same distance from the joint (d_4).

FINITE ELEMENT ANALYSIS

The new methodology developed in this study is presented in this section of the report. As described below, it is based on extensive finite element analysis. The results of which are combined into a series of regression analysis.

Framework for interpreting deflection data

Theoretical review indicates that the load size ratio, *a/l*, is the key factor of characterizing the load-deflection behavior of concrete pavements, where *a* is the radius of loaded area and *l* is the radius of relative stiffness. Obviously, joint stiffness, S, is another important influencing factor for corner loading condition. By introducing the relationship shown in Figure E-4, measured LTE can be simply used in lieu of the joint stiffness.

With a fixed *a* value, the deflection due to a selected level of FWD loading is solely a function of *l*-value of given PCC slab and foundation system. This *l*-value can be identified from deflection basin parameter AREA by adopting the fact that a unique relationship exists between *a/l* and AREA for any particular deflection measurement on any PCC pavements. Since the relationship is based on the Westergaard's solutions, slab size effect should be incorporated in the relationship. However, a typical size of highway pavement slab (20ft × 12ft) was selected in

this study rather than introducing correction factor for size effect. This direct calculation may enhance the accuracy of the relationship.

By defining the above relationship, the structural system of PCC pavement can be identified. The procedure starts with deflection measurement. The proposed framework for interpreting deflection data is summarized as follows:

1. Calculate AREA and/or LTE from FWD deflection measurements (Eq. E-9)
2. Estimate radius of relative stiffness, l, from the relationship between AREA and l (Eq. E-11 – E-13)
3. Estimate non-dimensional maximum deflection, Δ_1, from the estimated a/l and/or LTE (Eq. E-14 - E-16)
4. Estimate k using estimated non-dimensional maximum deflection, Δ_1, measured maximum deflection, δ_1, applied total load, P, and estimated l value (Eq. E-7)
5. Estimate E_c using estimated k and l values and slab thickness, h (Eq. E-2)
6. Estimated system parameters may give additional information on tested pavement such as void underneath the slab.

Finite Element Model

Load-deflection behavior of concrete pavements is identified through a set of finite element analysis. Finite element program ILLISLAB was used in this study. ILLISLAB is specially developed finite element analysis program for concrete pavement applications. It is based on classical medium thick plate theory and employs 4-node, 12-dof, linear 2-dimensional plate bending elements.

Pavement structure was modeled as a 2-layer system composed with PCC slab and Winkler foundation. The FWD impact load is simply modeled as an equivalent static pressure loaded on a 10.5x10.5 in (26.25x26.25 cm) square area. Since there is no information on joint details, the joint effect is modeled with interlocking stiffness only. Slab size is fixed in all calculation as 150x240 inch (375x600 cm). It is very typical slab size of highway pavements. Concrete Poisson's ratio is assumed to be 0.15.

Table E-1 shows case matrix for the analysis with various input parameters which gives the l values from 13.6 to 61.9, covering almost all cases of practical highway pavements. Each set of input variables produces an unique deflection basin and corresponding AREA. This unique relationship was identified with regression analysis. For center and edge loading condition, 45 runs were made for each with various values of the radius of relative stiffness, l.

Table E-1. Input variables for finite element analysis

Input Variables	Slab thickness, h (in)	Concrete Young's modulus, Ec (ksi)	Modulus of subgrade reaction, k (pci)	Joint stiffness, S (ksi)
Used Values	10 12 14	2000, 2500, 3000, 3500, 4000, 4500, 5000	50, 100, 200, 400, 1000, 2000, 5000	10, 100, 500, 1000, 2000, 2500, 3000, 3500

In the case of corner loading, a total of 57 runs were made with different l values and joint stiffness.

Formulating the Relationships

Figures E-5, E-6 and E-7 show the relationship between calculated deflection AREA and the radius of relative stiffness in each loading condition. Identified regression equations are given below, Eqs. E-11 to E-13. Using these equations the radius of relative stiffness was back-calculated and compared to its initial input value. As shown in Figures E-8, E-9 and E-10, estimated values show very good agreement with initial values in all three loading cases.

for center loading (R^2=0.999)

$$l = 0.0007(AREA)^3 - 0.0566(AREA)^2 + 2.2285(AREA) - 14.792 \qquad \text{(E-11)}$$

for edge loading (R^2=0.999)

$$l = 0.0006(AREA)^3 - 0.0539(AREA)^2 + 2.3194(AREA) - 19.037 \qquad \text{(E-12)}$$

for corner loading (R^2=0.999)

$$l = 0.0008(AREA)^3 - 0.0565(AREA)^2 + 2.2586(AREA) - 15.057 \qquad \text{(E-13)}$$

The next step is to estimate the theoretical non-dimensional maximum deflection with the estimated l-value. The relationships between non-dimensional maximum deflections and load size ratio are shown in Figures E-11 and E-12, for center and edge loading. Center and edge deflections are related to the load size ratio in 6th degree polynomials. These regression equations are given in Eqs. E-14 and E-15.

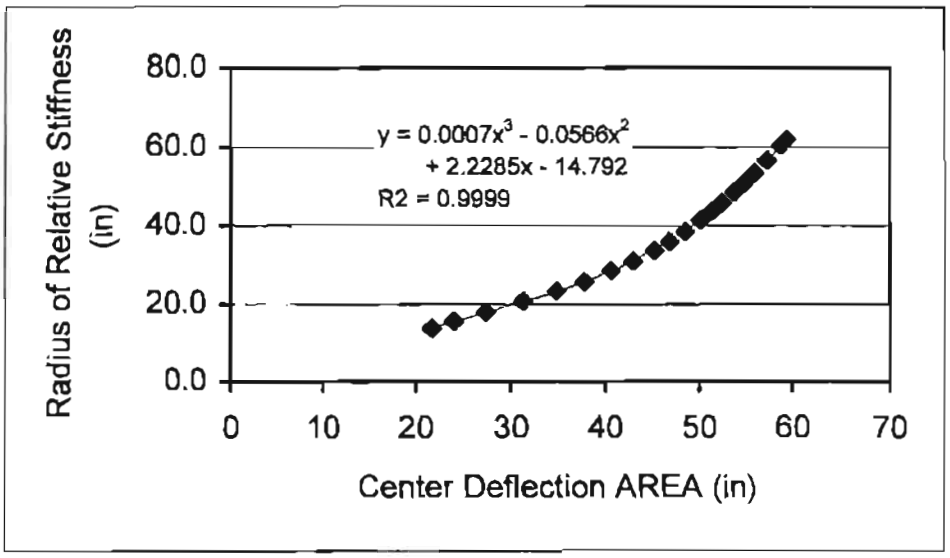

Figure E-5. Relationship between center deflection AREA and radius of relative stiffness

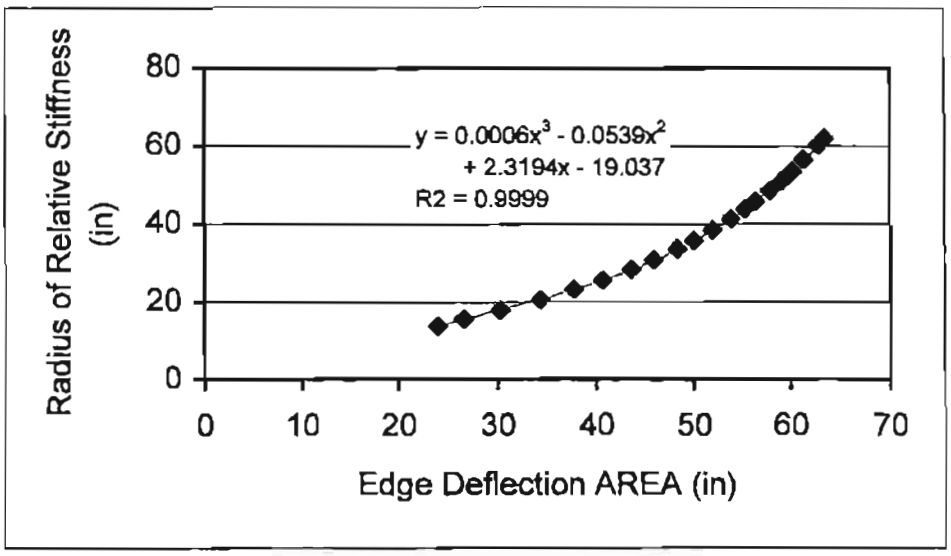

Figure E-6. Relationship between edge deflection AREA and radius of relative stiffness

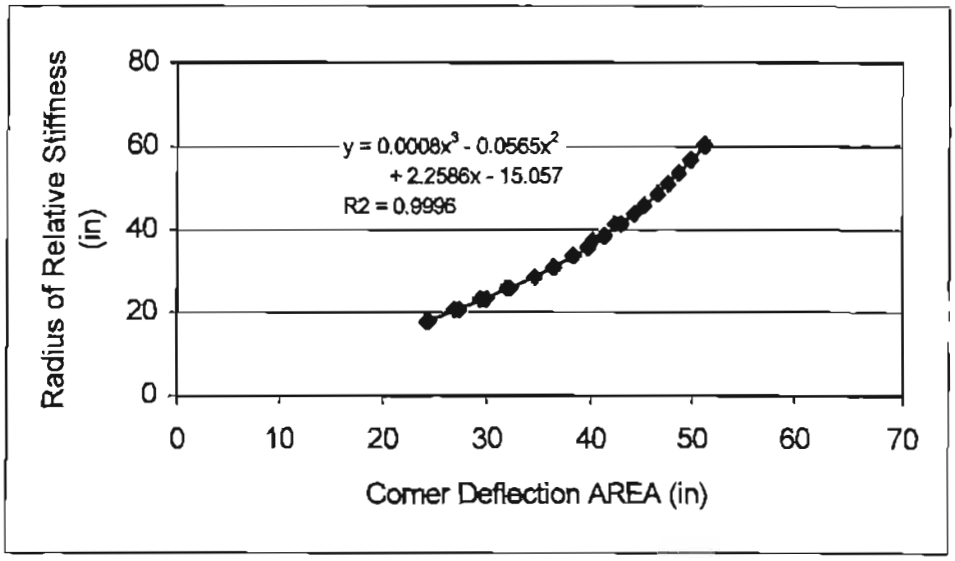

Figure E-7. Relationship between corner deflection AREA and radius of relative stiffness

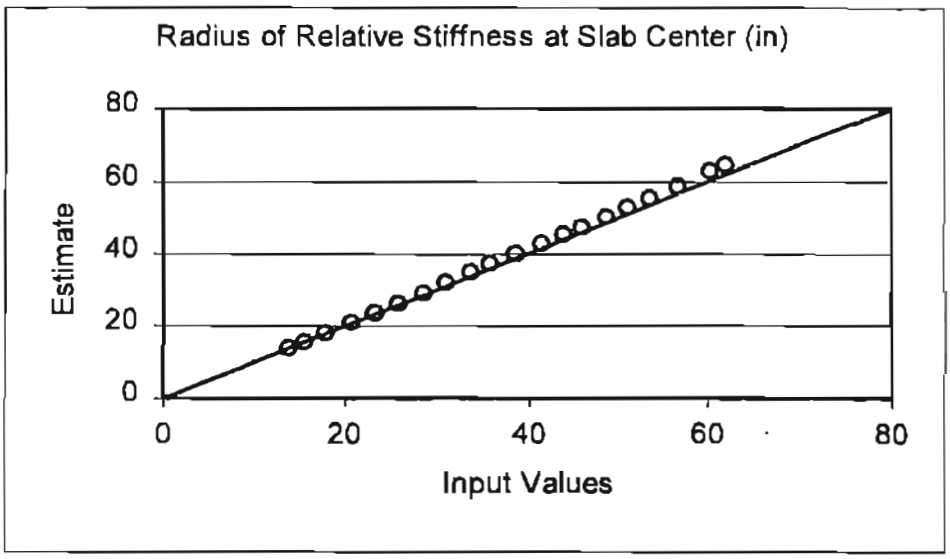

Figure E-8. Comparison between estimated and input radius of relative stiffness at center

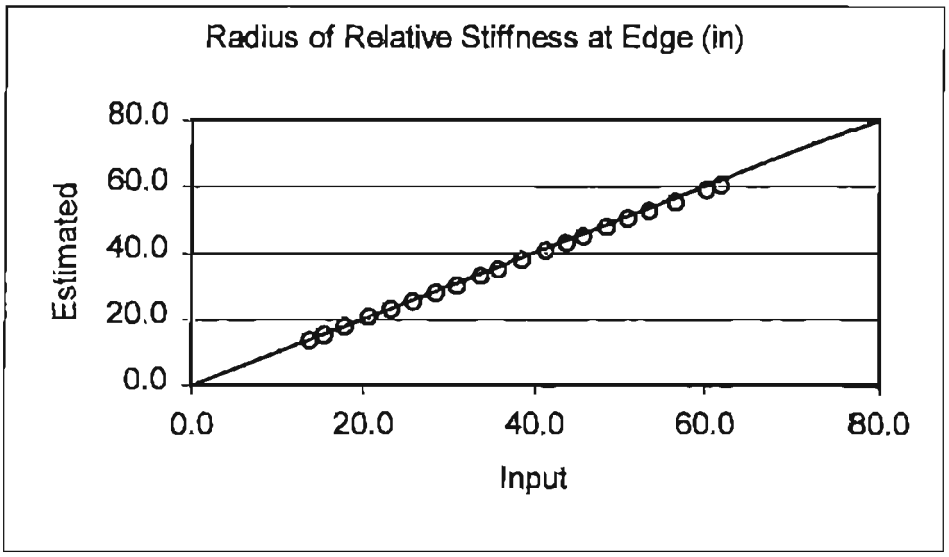

Figure E-9. Comparison between estimated and input radius of relative stiffness at edge

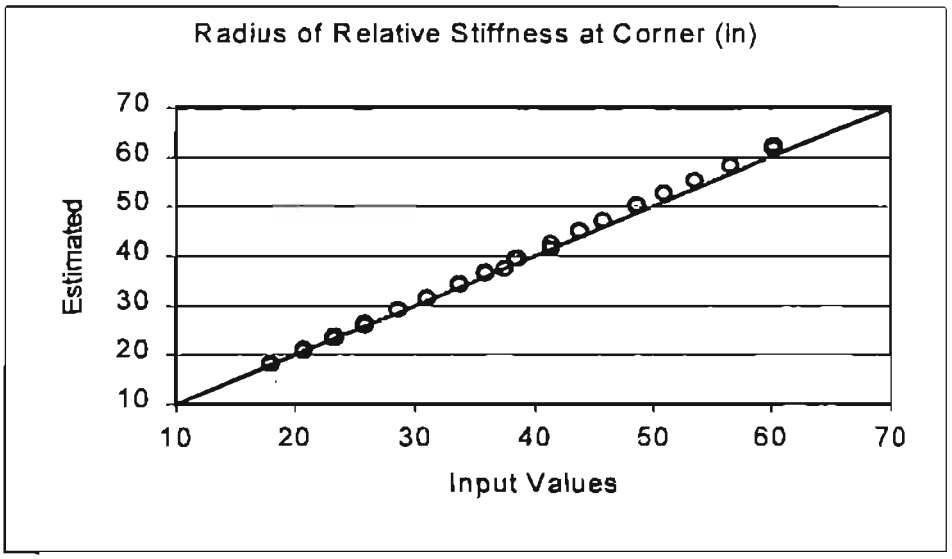

Figure E-10. Comparison between estimated and input radius of relative stiffness at corner

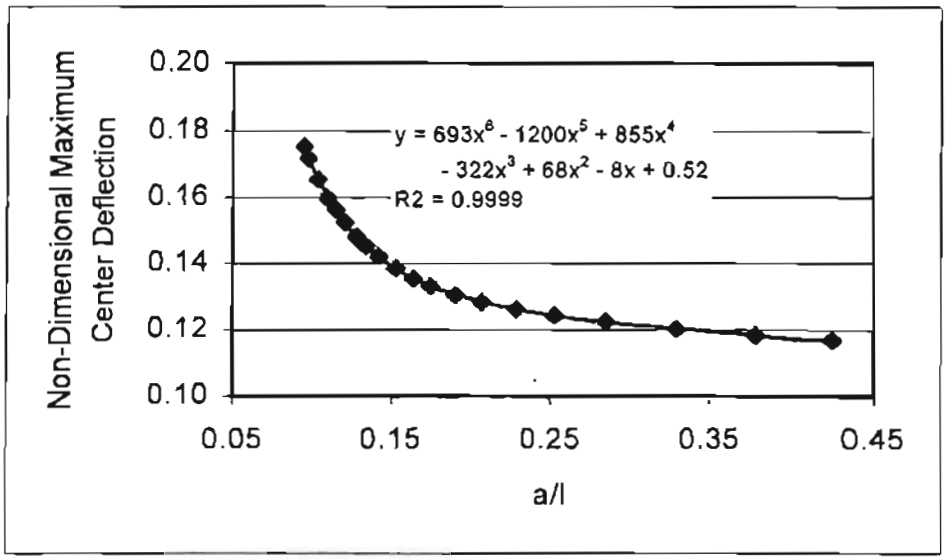

Figure E-11. Relationship between non-dimensional maximum center deflection (Δ_1-center) and load size ratio (*a/l*)

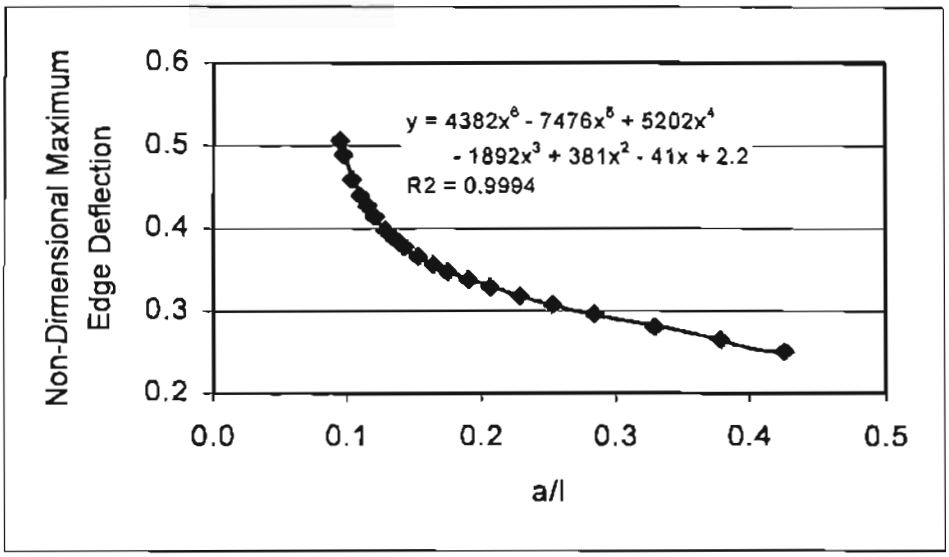

Figure E-12. Relationship between non-dimensional maximum edge deflection (Δ_1-edge) and load size ratio (*a/l*)

for center loading (R^2=0.999) (E-14)

$$\Delta_1 = 0.52 + 693(a/l)^6 - 1200(a/l)^5 + 855(a/l)^4 - 322(a/l)^3 + 68(a/l)^2 - 8(a/l)$$

for edge loading (R^2=0.999) (E-15)

$$\Delta_1 = 2.2 + 4382(a/l)^6 - 7476(a/l)^5 + 5202(a/l)^4 - 1892(a/l)^3 + 381(a/l)^2 - 41(a/l)$$

for corner loading (R^2=0.991) (E-16)

$$\Delta_1 = 1.265 - 8.507(a/l) + 49.043(a/l)^2 - 137.84(a/l)^3 - 0.2423(LTE)$$

Beside *a/l* value, LTE should be incorporated in the relationship for corner loading condition. The relationship for corner deflection was identified through multiple linear regression analysis. Eq. E-16 gives the estimation of non-dimensional corner deflection. Comparison of input and estimated Δ_1 values for each loading condition are presented in Figures E-13 through E-15. The estimate of Δ_1 is also very close to the original input values.

With applied load (P), measured maximum deflection (δ_1), and estimated *l*-value, the modulus of subgrade reaction, *k*, can be estimated by equation E-8. With these estimated values, the elastic modulus of PCC slab (E_c) also can be estimated by Eq. E-2, if slab thickness is known and concrete Poisson's ratio is pre-determined. Figures E-16 to E-18 and E-19 to E-21 show the good agreement between initial input and estimated *k*-value and E_c, respectively.

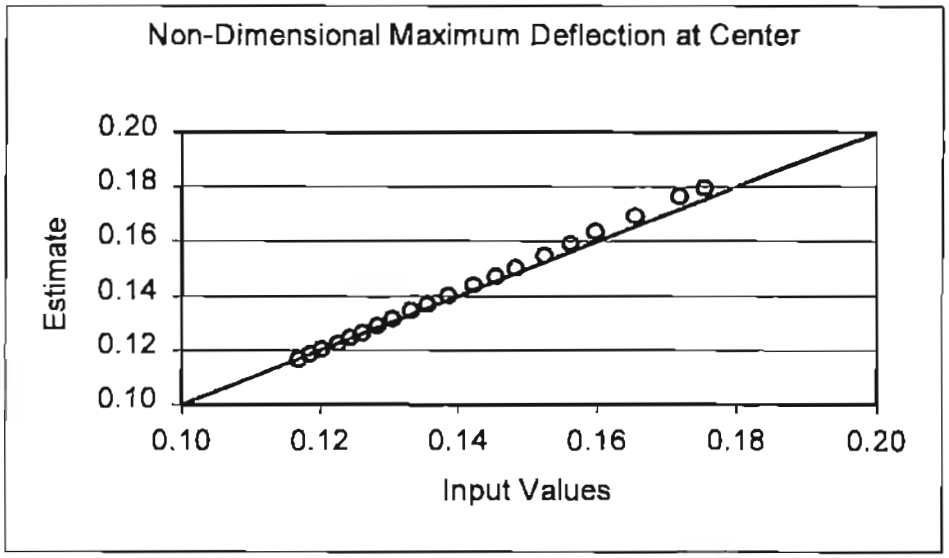

Figure E-13. Comparison between estimated and input non-dimensional maximum center deflection (Δ_1 -center)

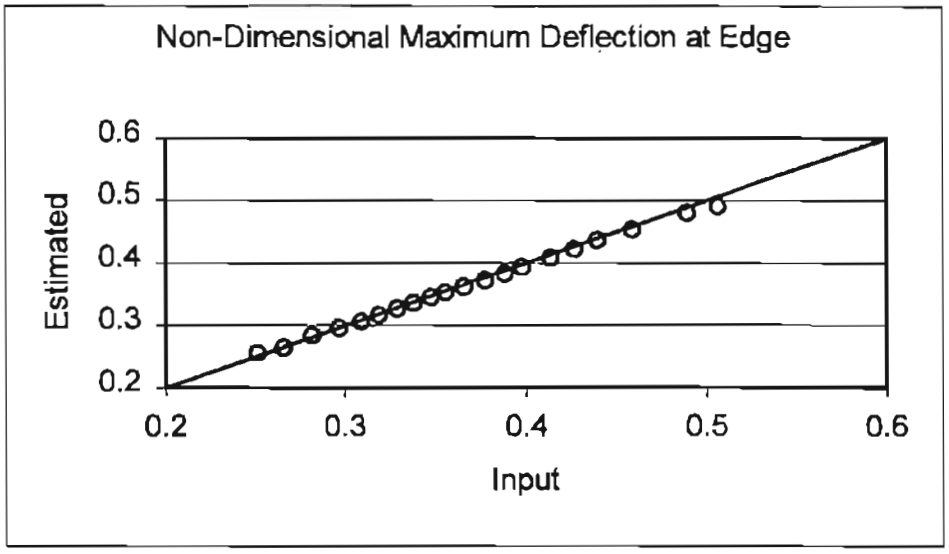

Figure E-14. Comparison between estimated and input non-dimensional maximum edge deflection (Δ_1 -edge)

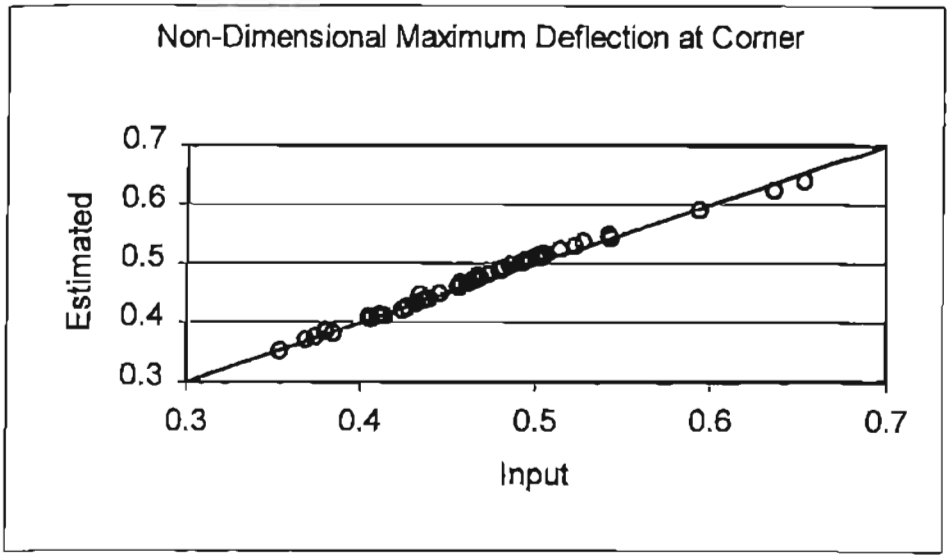

Figure E-15. Comparison between estimated and input non-dimensional maximum corner deflection (Δ_t -corner)

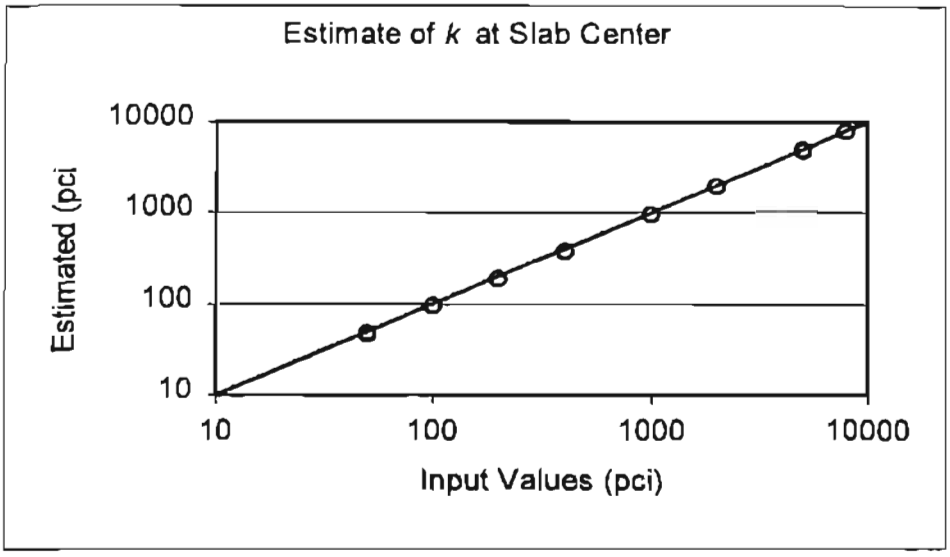

Figure E-16. Comparison between input and estimated *k*-values at slab center

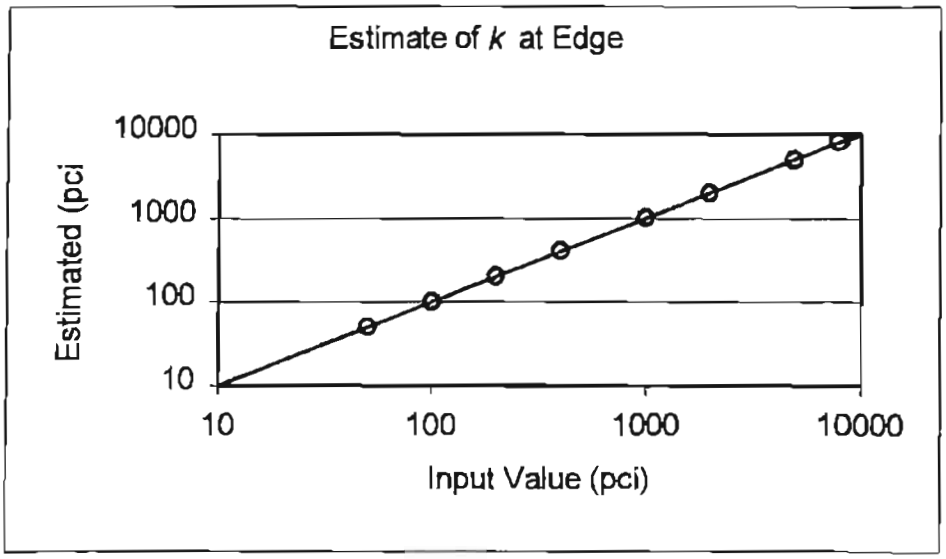

Figure E-17. Comparison between input and estimated *k*-values at slab edge

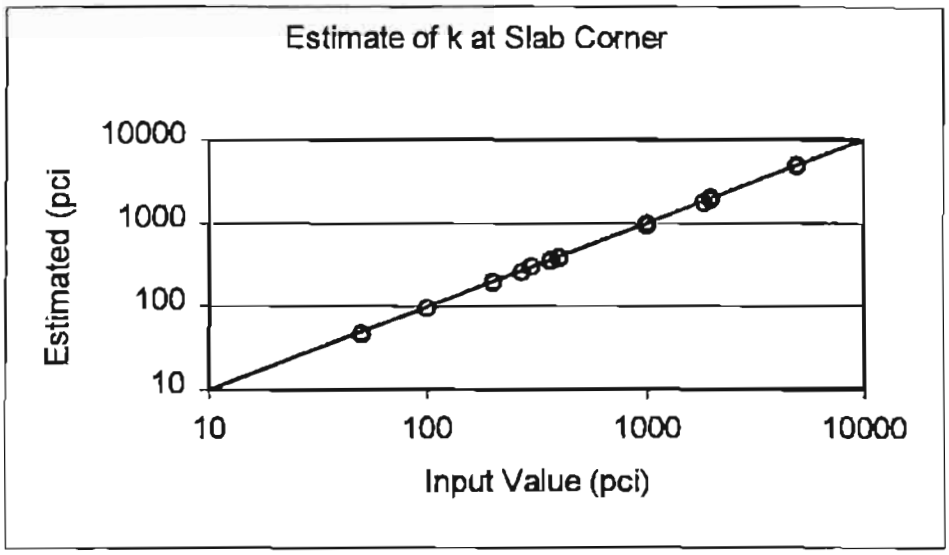

Figure E-18. Comparison between input and estimated *k*-values at slab corner

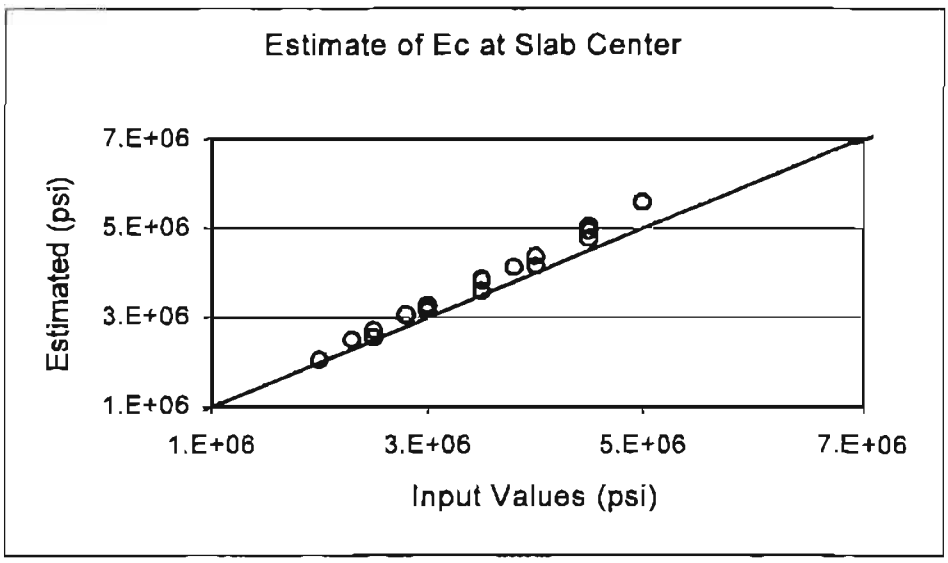

Figure E-19. Comparison between input and estimated concrete modulus of elasticity, E_c at slab corner

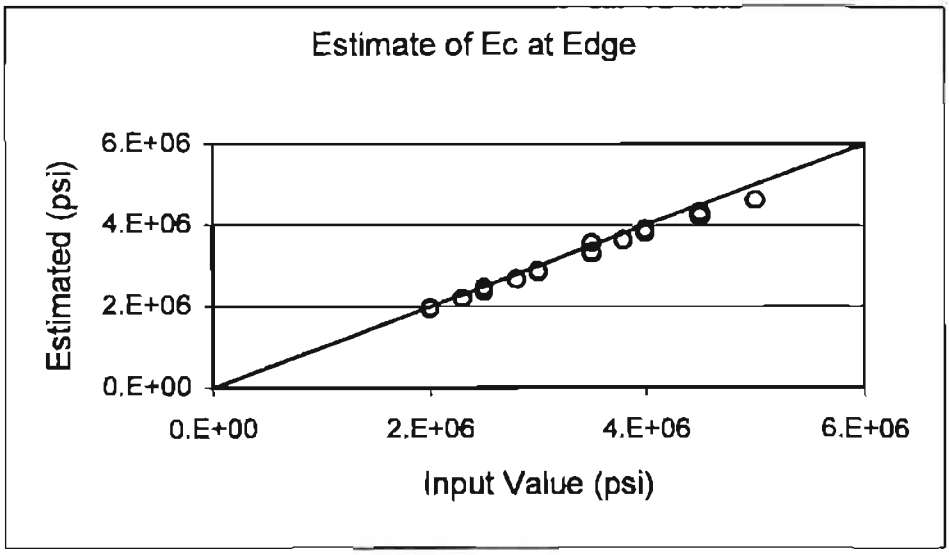

Figure E-20. Comparison between input and estimated concrete modulus of elasticity, E_c at slab edge

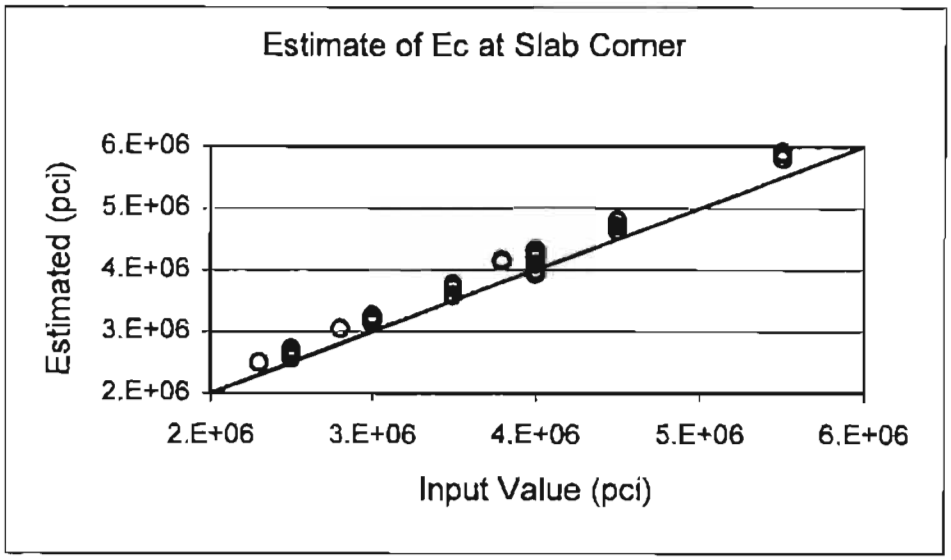

Figure E-21. Comparison between input and estimated concrete modulus of elasticity, E_c at slab corner

FIELD TESTS

Test Pavements

A test section was specially prepared at the Riverside Campus of Texas A&M University which was used for a military airport in 50's and 60's. Unfortunately, visible dimensions are the only information on the test pavements. The geometry of the test section is shown in Figure E-22. The test section contains one control slab and six test slabs. The control slab is a part of PCC pavement section, while six test slabs have 2" (5cm) asphalt concrete overlay on PCC slab. All slabs have identical dimension of 12" (30cm) thickness, 150" (375cm) width and 240" (600cm) length. Figure E-23 shows the cross sections of the test pavements.

Artificial voids were made underneath the slabs 2, 4, and 5. Slab 2 has an up-stream void and slab 4 has a void under down-stream joint. Slab 5 has both. Drilling auger (ϕ8×36") was used to build the voids (Figure E-24). Figure E-25 shows a completed void. After completion, profile of each void was measured. Void length measured in longitudinal is 36~46 inches and width varies longitudinally from 22 to 44 inches. The void depth is between 8~14 inches. Finally, the shoulder was replaced (Figure E-26) and the profiles of voids were marked on the surface (Figure E-27). The completeness of artificial voids was checked with ground penetrating radar (GPR). Figure E-28 presents a captured image of GPR signal. It clearly shows the existence of voids.

Eleven sets of FWD test were performed in two different days. In day 1, four sets of data were collected from the control slab and other four sets were collected from the test slabs. In day 2, additional three sets of data were obtained from the test slabs in the morning. Table E-2 gives summarized description of each test set.

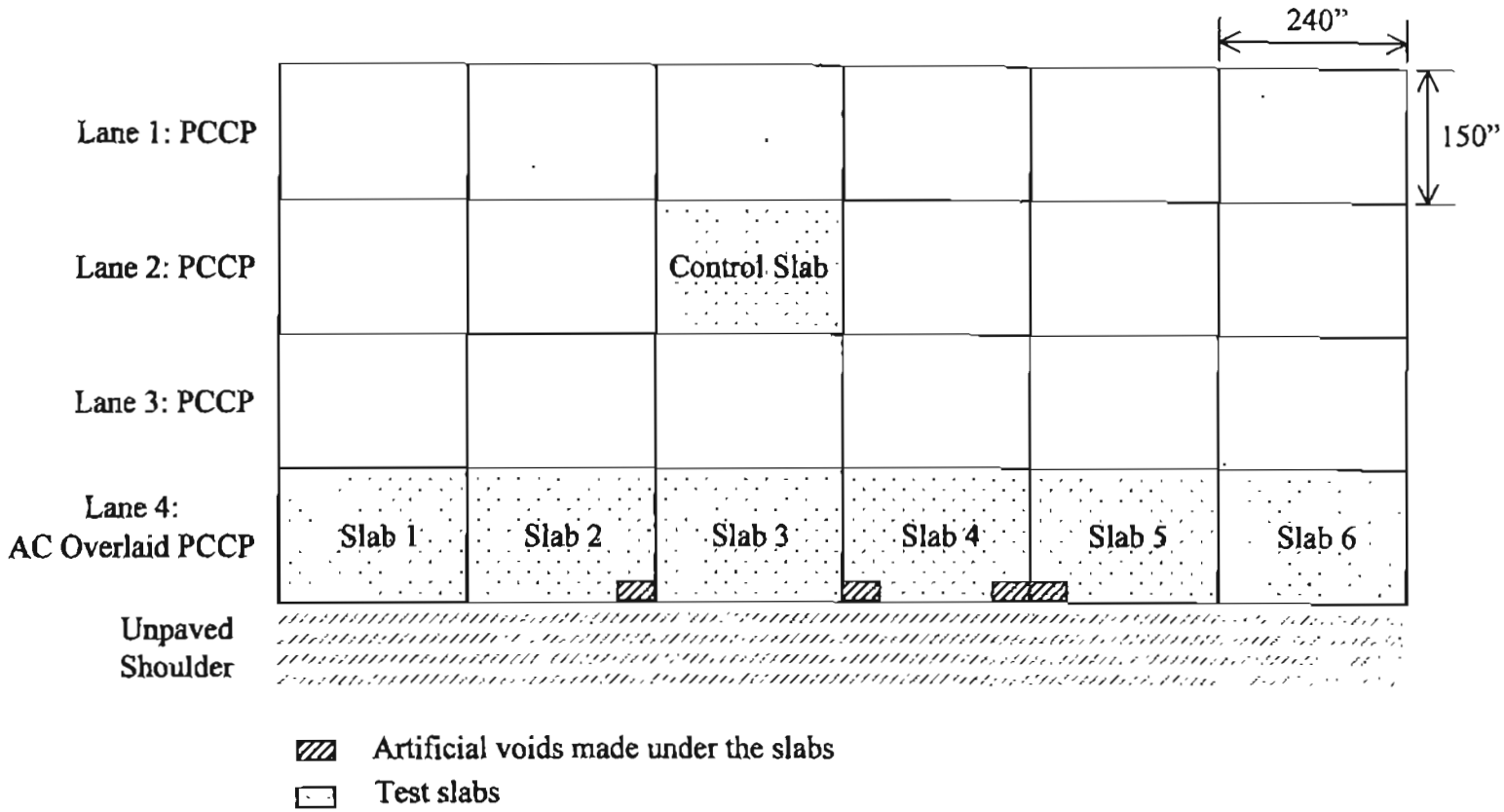

Figure E-22. Geometry of Test Pavements

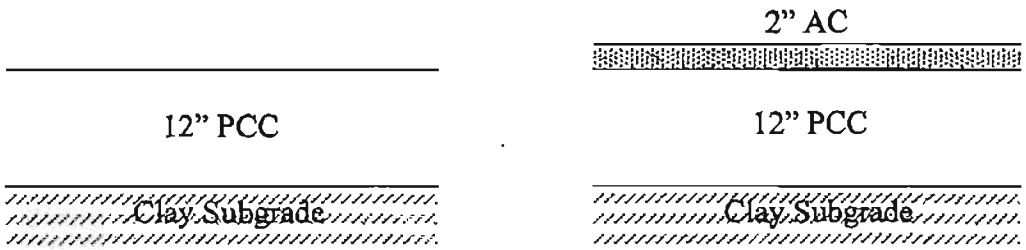

(a) PCC slab (b) AC Overlaid PCC slab

Figure E-23. Cross Section of the Test Pavements

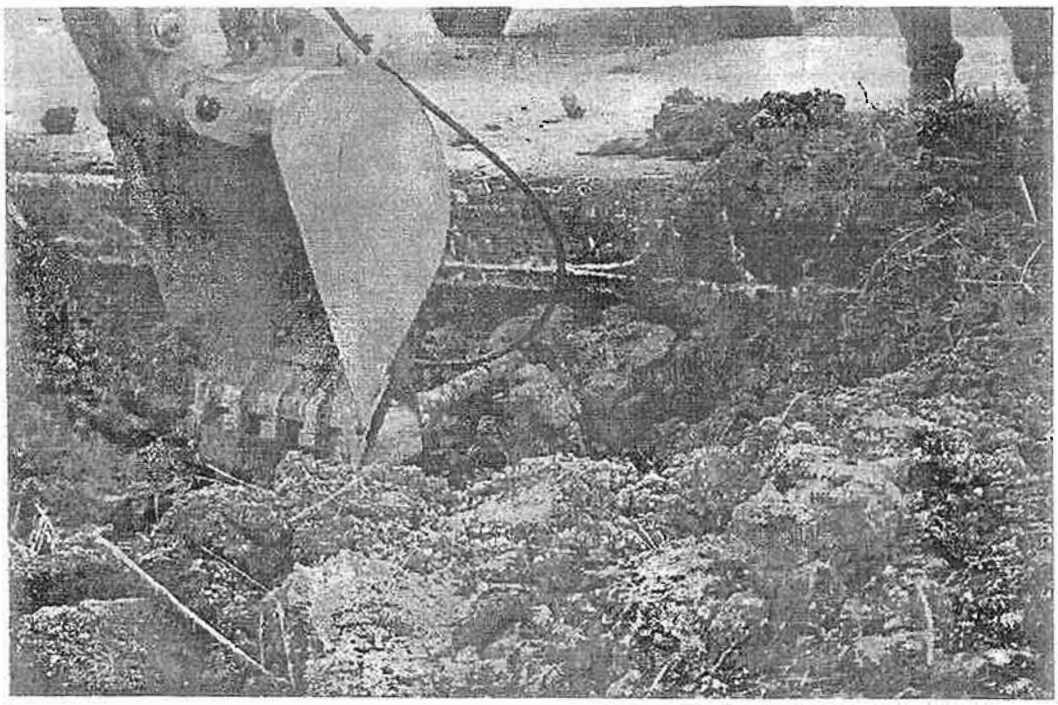

Figure E-24. Making artificial void with auger drill

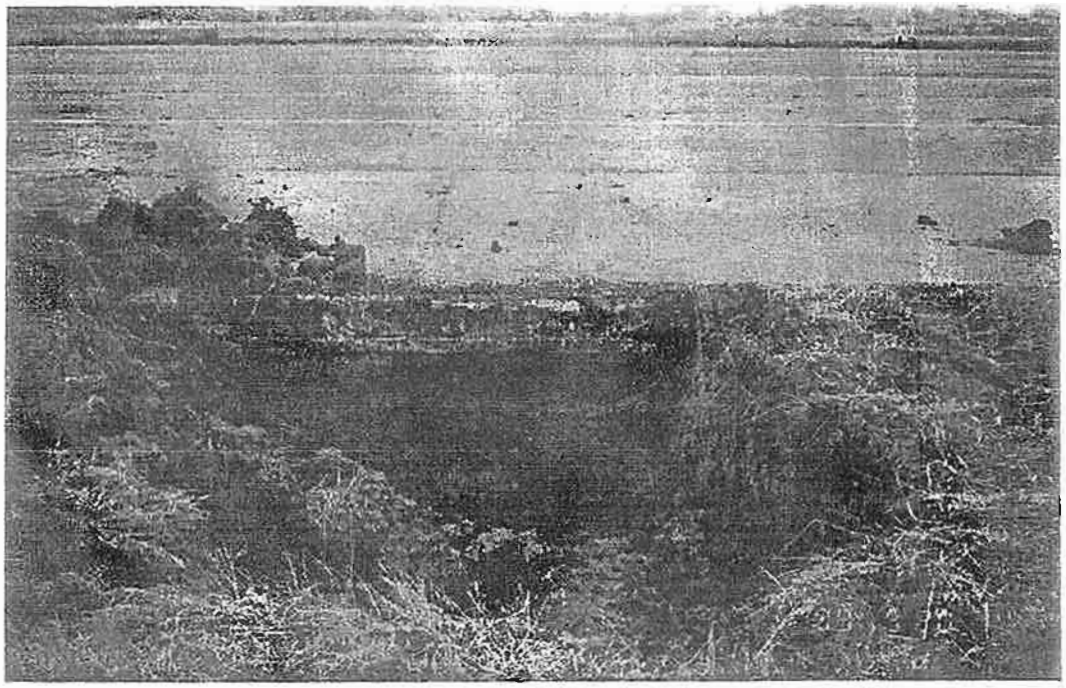

Figure E-25. Completed view of an artificial void

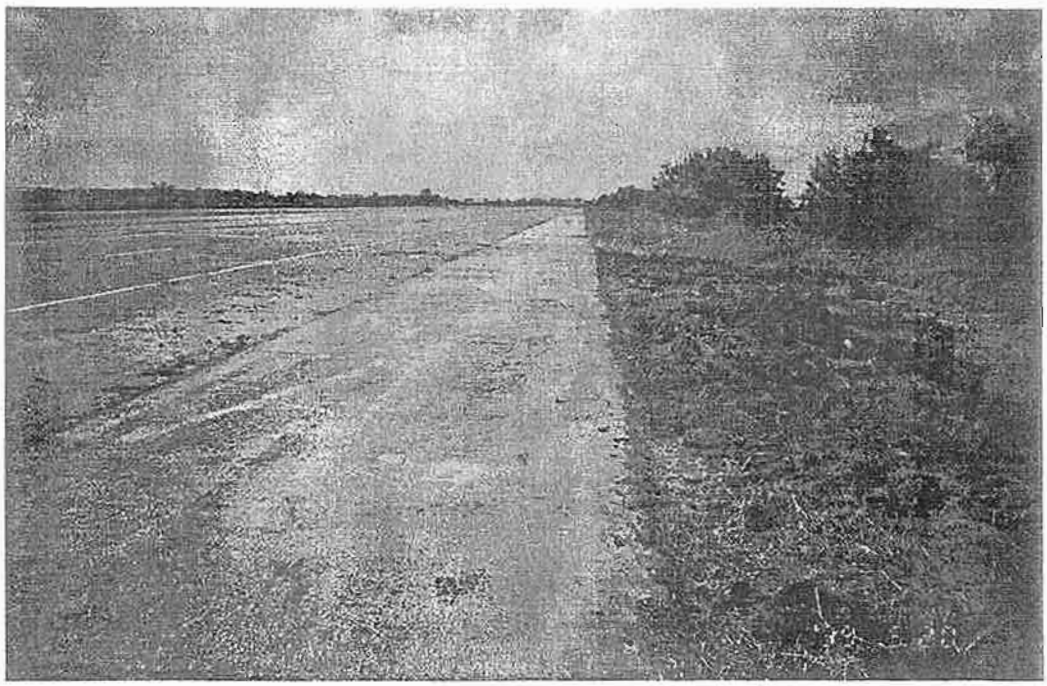

Figure E-26. Replacement of shoulder after the completion of voids

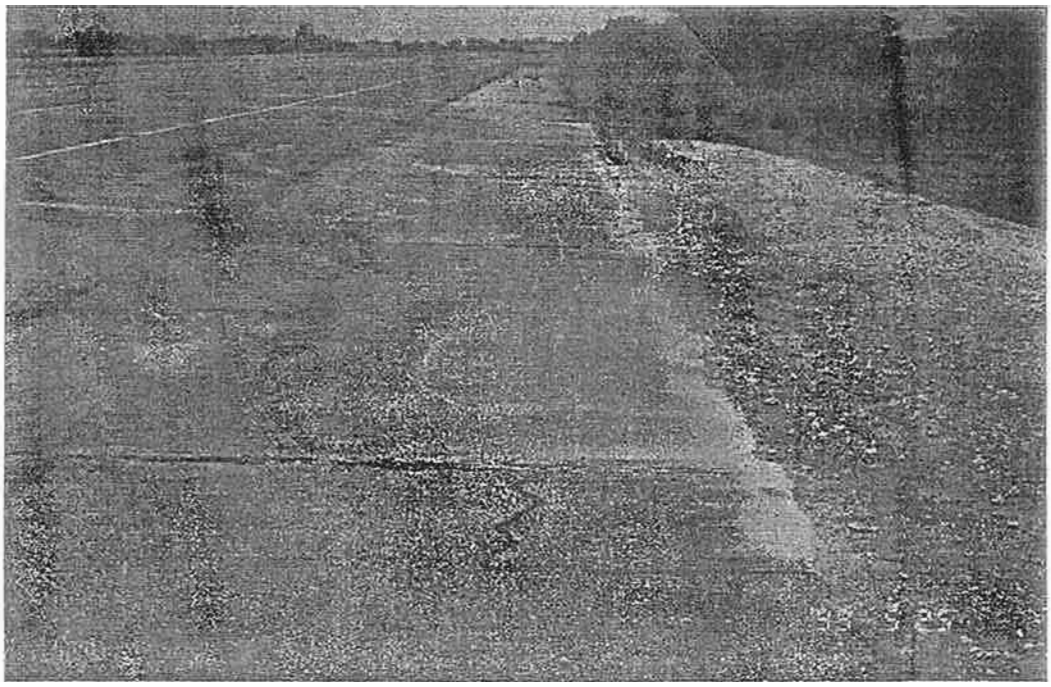

Figure E-27. Marked profile of the artificial voids

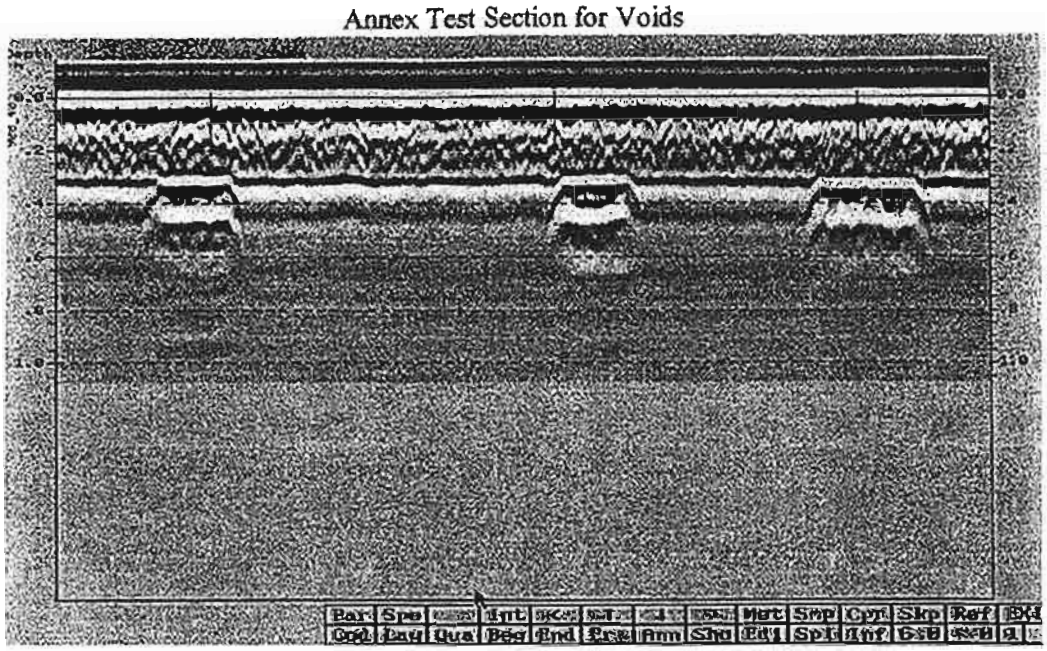

Figure E-28. Processed image of Ground Penetrating Radar (GPR) test over the experimental section

Table E-2. Summary of test set description

Test set	Test day	Test points	Test time
Test 1	Day 1	Control slab center	Morning
Test 2		Control slab corner, edge	
Test 3		Control slab center	Afternoon
Test 4		Control slab corner, edge	
Test 5		Test slabs center	Morning
Test 6		Test slabs corner, edge	
Test 7		Test slabs center	Afternoon
Test 8		Test slabs corner, edge	
Test 9	Day 2	Test slabs center	Morning
Test 10		Test slabs corner, edge	
Test 11		Test slabs corner, edge	

For corner and edge tests in the test slabs (Test 6, 8, 10 and 11), the loading plate was located with some offset distance from the exact edge line because there is some spalling along the edge of overlaid surface. The offset distance varies from test to test. All tests in the test set 6 and 8 have 18 inches of offset from the edge to the right side of plate. During test 10, the loading plate was located as close as possible to the edge so that the offset varies from 2 to 6 inches. Test 11 has 14~17 inches of offset distances. A typical view of FWD deflection testing is given in Figure E-29.

For each test set, four levels of impulse load ranging from 5.5 to 16 kips (24.5 to 71.2 kN) were applied at each testing point. The weight was dropped twice at each of four different levels, whereas the first drop at each level is for secure bedding of the loading plate. The FWD contains a 12" (30cm) diameter loading plate and rear extended bar. Geophones are located at -12, 0, 12, 24, 48, 60, 72 inches (-30, 0, 30, 60, 120, 150, 180 cm) from the center of loading plate. FWD trailer always traveled in the direction from slab 1 to slab 6 throughout the tests. Edge and corner loading was located along the right side edge of the slabs in view of traveling direction. As shown in Figure E-22, the control slab was selected in lane 2. The right side edge of the control slab can be regarded as a free edge since a construction joint was placed between lanes 2 and 3. Very little joint load transfer is expected from this longitudinal joint.

US 287

A set of FWD test data was also collected from in-service highway, US 287. The US 287 data contains three groups. One is measured at slab center, other is from joints in good condition and the last group is measured at joints in poor condition. Whole section in US 287 consists of 10" PCC slab, 4 " cement treated base (CTB), and subgrade. Two different load levels were

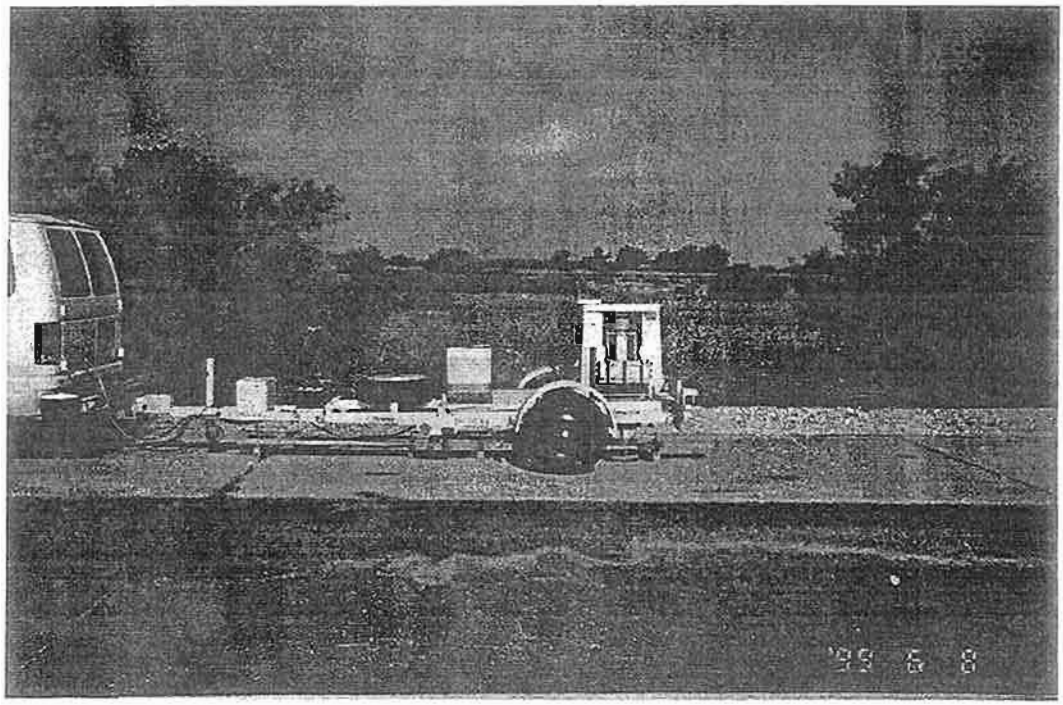

Figure E-29. A typical view of FWD testing

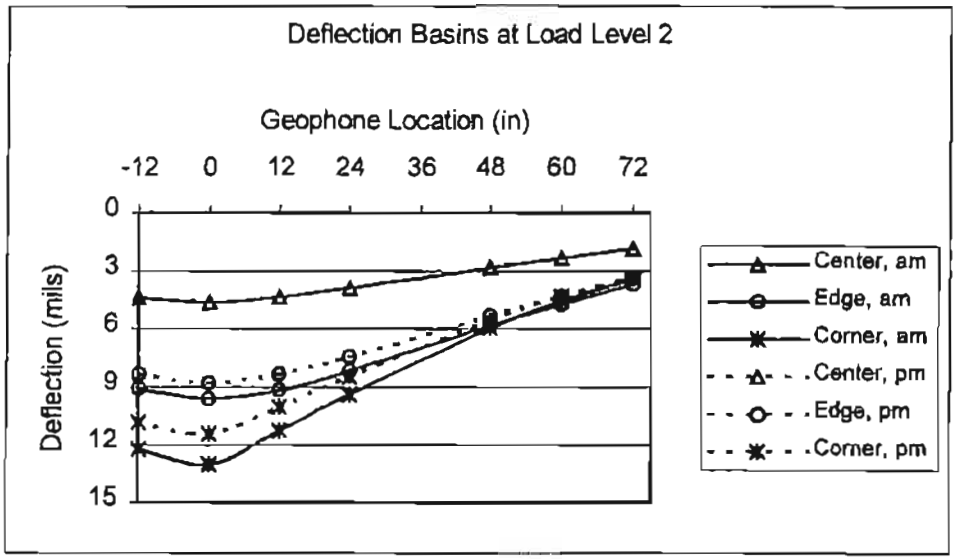

Figure E-30. Deflection basins from control slab; Measured at load level 2

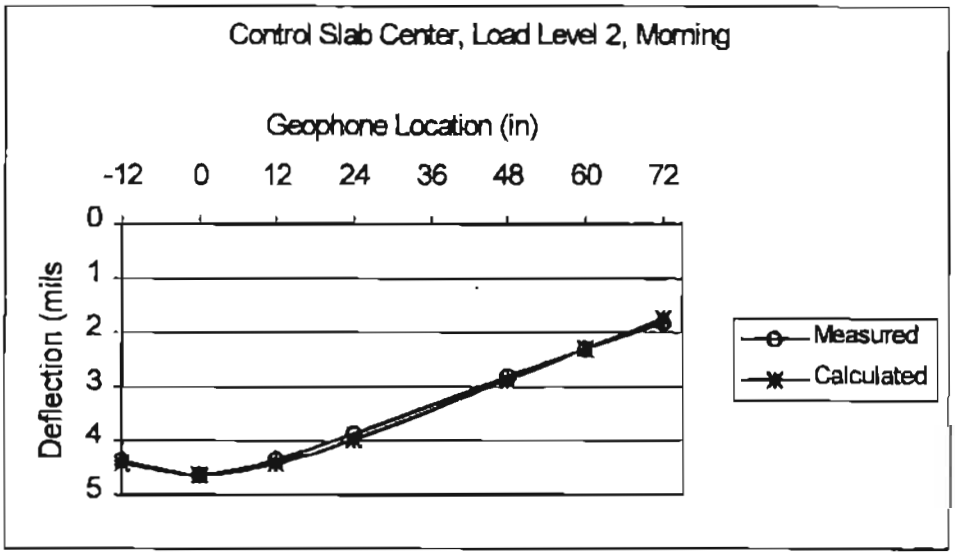

Figure E-31. Comparison between measured and calculated center deflections at control slab; Measured at load level 2, morning

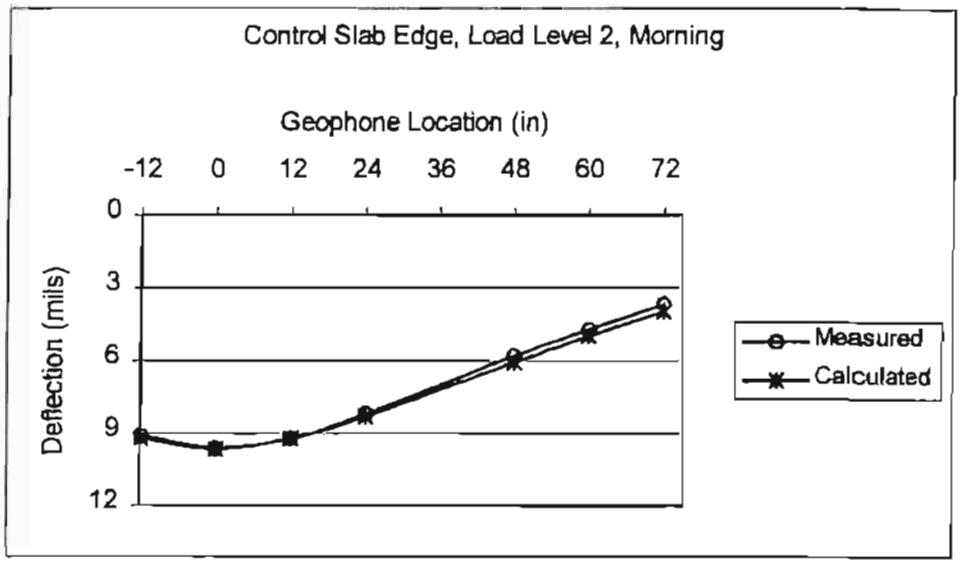

Figure E-32. Comparison between measured and calculated edge deflections at control slab; Measured at load level 2, morning

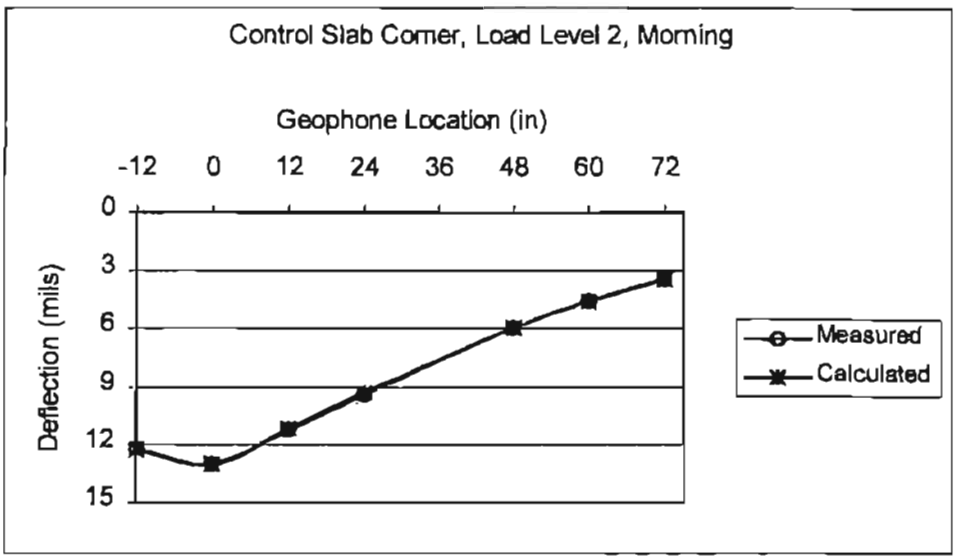

Figure E-33. Comparison between measured and calculated corner deflections at control slab; Measured at load level 2, morning

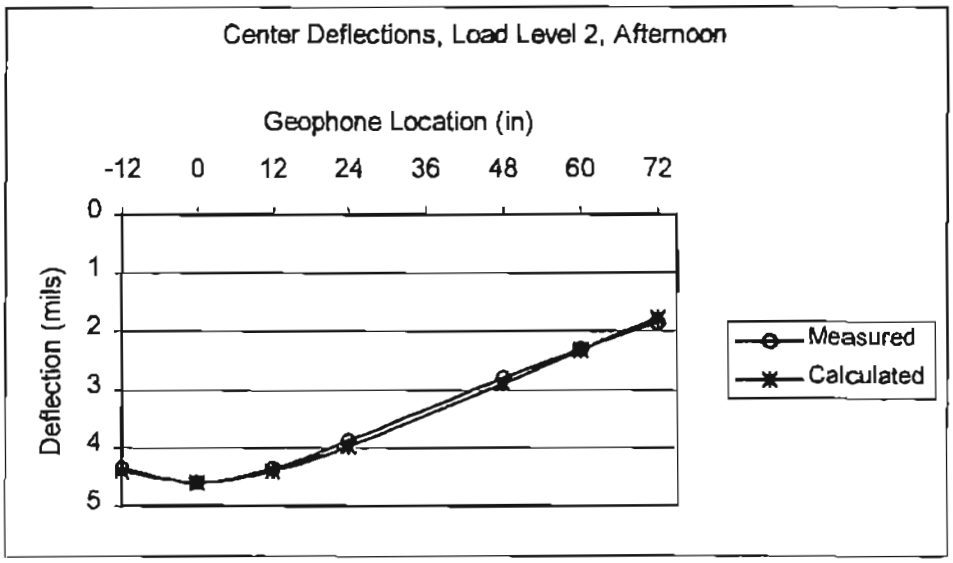

Figure E-34. Comparison between measured and calculated center deflections at control slab; Measured at load level 2, afternoon

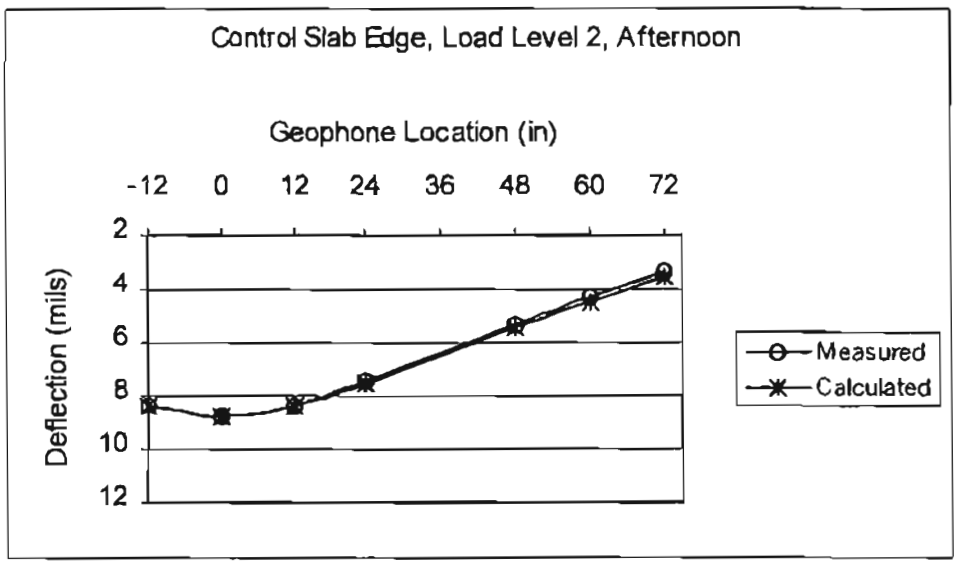

Figure E-35. Comparison between measured and calculated edge deflections at control slab; Measured at load level 2, afternoon

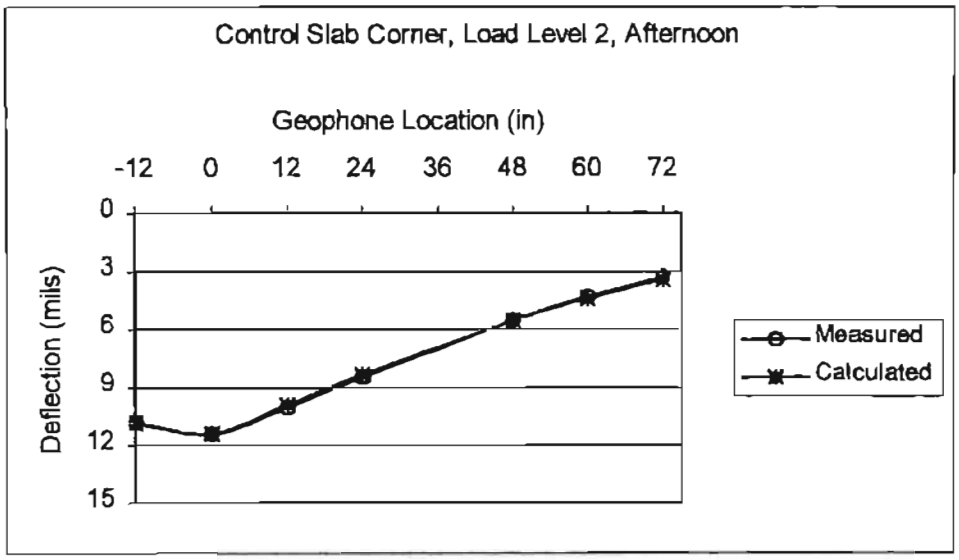

Figure E-36. Comparison between measured and calculated corner deflections at control slab; Measured at load level 2, afternoon

Table E-3. Evaluation of control slab from the center and edge deflection measurements

Test Point	Time	Load, P (lbs)	Deflections at each Geophone location (mils)							AREA (in)	l (in)	a/l	Δ_1	k (pci)	E_c ($\times 10^6$psi)
			d_{12}	d_0	d_{12}	d_{24}	d_{48}	d_{60}	d_{72}						
Center	AM	5967	2.80	3.03	2.83	2.51	1.81	1.49	1.18	51.109	44.710	0.132	0.146	144.3	3.914
		9244	4.37	4.63	4.35	3.88	2.81	2.30	1.81	51.590	45.649	0.129	0.148	141.6	4.175
		12601	5.82	6.21	5.76	5.15	3.71	3.03	2.39	50.976	44.454	0.133	0.146	150.0	3.977
		16585	7.39	7.91	7.39	6.58	4.76	3.89	3.03	51.216	44.917	0.131	0.147	152.5	4.215
	PM	5879	2.82	2.96	2.83	2.50	1.80	1.47	1.17	51.953	46.374	0.127	0.149	137.5	4.317
		9224	4.36	4.59	4.35	3.87	2.80	2.30	1.84	51.948	46.364	0.127	0.149	139.2	4.365
		12577	5.80	6.11	5.78	5.14	3.71	3.05	2.43	51.800	46.068	0.128	0.148	144.0	4.401
		16510	7.44	7.89	7.39	6.60	4.77	3.89	3.09	51.445	45.364	0.130	0.147	149.9	4.309
Edge	AM	5848	5.82	6.15	5.88	5.23	3.73	3.00	2.34	51.834	39.930	0.148	0.371	221.3	3.818
		9256	9.11	9.61	9.19	8.18	5.81	4.73	3.67	51.877	39.977	0.148	0.371	223.5	3.883
		12625	12.26	12.92	12.33	10.98	7.83	6.36	4.93	51.854	39.962	0.148	0.371	227.1	3.931
		16422	15.94	16.80	16.00	14.29	10.19	8.29	6.42	51.871	39.988	0.148	0.371	226.9	3.939
	PM	5736	5.22	5.60	5.33	4.71	3.35	2.68	2.06	51.279	39.071	0.151	0.368	246.6	3.901
		9069	8.36	8.80	8.36	7.44	5.30	4.29	3.33	51.580	39.533	0.149	0.369	243.6	4.039
		12426	11.09	11.74	11.18	9.92	7.07	5.76	4.52	51.675	39.681	0.149	0.370	248.7	4.186
		16240	14.37	15.19	14.37	12.85	9.14	7.42	5.84	51.579	39.532	0.149	0.369	252.7	4.189

* l : Radius of relative stiffness (Eq. E-2); a : Radius of loading plate (5.9 in); Δ_1 : Non-dimensional maximum deflection (Eq. E-8)
k : Modulus of subgrade reaction; E_c : Concrete modulus of elasticity

Table E-4. Evaluation of control slab from the corner deflection measurements

Test Time	Load, P (lbs)	Deflections at each Geophone location (mils)							AREA (in)	LTE	l (in)	a/l	Δ_1	k (pci)	E_c ($\times 10^6$psi)
		d_{-12}	d_0	d_{12}	d_{24}	d_{48}	d_{60}	d_{72}							
Morning	5828	7.85	8.39	7.19	6.07	3.91	2.89	2.26	43.445	0.985	42.026	0.140	0.473	186.0	3.938
	9149	12.20	13.04	11.23	9.39	5.95	4.56	3.42	43.279	0.985	41.716	0.141	0.472	190.1	3.909
	12490	16.17	17.35	15.00	12.45	7.89	6.04	4.56	43.231	0.981	41.627	0.142	0.472	196.1	3.998
	16272	20.77	22.32	19.20	15.98	10.09	7.79	5.80	43.094	0.980	41.373	0.143	0.471	200.8	3.993
Afternoon	5685	6.92	7.26	6.41	5.41	3.52	2.73	2.08	44.967	1.003	45.000	0.131	0.481	186.1	5.180
	9010	10.81	11.43	10.04	8.47	5.52	4.30	3.29	44.814	0.996	44.690	0.132	0.482	190.1	5.149
	12374	14.64	15.36	13.40	11.30	7.35	5.69	4.33	44.461	1.003	43.986	0.134	0.477	198.6	5.046
	16184	18.88	19.84	17.24	14.56	9.51	7.30	5.57	44.365	1.002	43.797	0.135	0.476	202.6	5.061

• l : Radius of relative stiffness (Eq. E-2); LTE : Joint load transfer efficiency; a : Radius of loading plate (5.9 in);
Δ_1 : Non-dimensional maximum deflection (Eq. E-8); k : Modulus of subgrade reaction; E_c : Concrete modulus of elasticity

Table E-5. Evaluated structural parameters at each test points of control slab and their comparison to the evaluation from RMODS

Test Point	Test Time	Load, P (lbs)	This Study		RMODS	
			k (pci)	E_c ($\times 10^6$psi)	k (pci)	E_c ($\times 10^6$psi)
Center	AM	5967	144.3	3.914	117.0	3.560
		9244	141.6	4.175	116.7	3.595
		12601	150.0	3.977	140.0	3.029
		16585	152.5	4.215	135.3	3.360
	PM	5879	137.5	4.317	112.5	3.675
		9224	139.2	4.365	116.7	3.618
		12577	144.0	4.401	141.4	3.054
		16510	149.9	4.309	142.8	3.164
Edge	AM	5848	221.3	3.818	200.5	3.603
		9256	223.5	3.883	201.3	3.694
		12625	227.1	3.931	205.8	3.718
		16422	226.9	3.939	205.2	3.734
	PM	5736	246.6	3.901	225.3	3.712
		9069	243.6	4.039	213.1	4.077
		12426	248.7	4.186	224.5	4.032
		16240	252.7	4.189	225.7	4.149
Corner	AM	5825	186.0	3.938	N/A	
		9149	190.1	3.909		
		12490	196.1	3.998		
		16272	200.8	3.993		
	PM	5685	186.1	5.180	N/A	
		9010	190.1	5.149		
		12374	198.6	5.046		
		16184	202.6	5.061		

applied for every test points. The FWD device used in US 287 also has rear extension bar so that the 4th geophone is placed 12" behind the center of loading plate.

PAVEMENT EVALUATION

Control Slab

Figure E-30 shows typical deflection basins obtained at the center, edge and corner of the control slab. Solid and dashed lines present the basins obtained in the morning and afternoon, respectively. Though Figure E-30 contains only the deflections at load level 2, identical basin shapes are obtained at different load levels but in different magnitude. The complete set of measured data and corresponding estimation of k and E_c are presented in Table E-3 and Table E-4. Table E-3 contains center and edge data while corner measurements and estimates are given in Table E-4. As shown in the tables, the estimated k and E_c values appear to be reasonable for the typical clayey subgrade and concrete. Using those estimated parameters, deflections were calculated by ILLISLAB and compared to the measured values. Figures E-31 through E-36 show the comparison between measured and calculated deflection basins at each test point. Figures E-31 to E-33 are for morning data and Figures E-34 to E-36 are for afternoon. Only load level 2 data was used for the comparison. As shown in the figures, good agreements exist between measured and calculated deflection basins at all test points.

Table E-5 shows comparison of the parameters estimated by the method proposed in this study and program RMODS. Program RMODS is a rigid pavement evaluation and back-calculation system developed by the Texas Transportation Institute. Back-calculation models adopted in RMODS are the layered elastic and Hertz models for processing center slab deflection data and the Westergaard model for free edge deflection data. Corner deflection analysis is not

available in RMODS. The Hertz and Westergaard theories adopt the Winkler foundation model, while the layered elastic model assumes all layers as a linear elastic continuous material. All of these models assume that the longitudinal and lateral slab dimensions are infinite or semi-infinite. As shown in Table E-5, both procedures produce similar values of k and E_c for all cases. The proposed back-calculation gives slightly higher estimates than RMODS. This difference is mostly because of the effect of finite slab dimensions. Table E-5 also indicates that the estimated E_c values are consistent in all test points for morning data, while greater k-values are produced from edge and corner than center deflection analysis. Increased E_c values are obtained from afternoon data compared to morning due to curling effect. Presumably, the greatest curling effect exists at corner.

On the other hand, as shown in Figure E-30, the corner deflection has its distinguishable basin shape compared to center or edge deflections. The basin shape at the corner is convex and it has a discontinuous nature at the joint, whereas the basin at center or edge has continuous concave shape. This geometrical discontinuity produces difficulties in load-deflection analysis at joints. In fact, most previous studies have restricted themselves to a single slab boundary based on free corner deflection due to the complexity at the joint. However, free corner deflection is in fact not available in practice. Rather an approximation has been applied by so called the total deflection concept, which is defined as the sum of the maximum deflection at the center of loading plate on the loaded slab and the deflection on the unloaded slab. On the assumption that the total corner deflection remains a relative constant regardless of joint discontinuity, the free corner deflection for a single slab can be approximated by this total deflection. However, this approximation could not provide a sufficient accuracy for the evaluation of PCC pavements directly from corner deflection measurements.

With respect to this problem, this study uniquely provides the direct interpretation of corner deflections. Factors contributing to the joint complexity are aggregate interlocking, dowel bar action, as well as support condition and structural dimensions of pavement structure. Interactions between these factors may be involved in a single parameter, the non-dimensional joint stiffness, S/kl, where S is joint stiffness, k is modulus of subgrade reaction, and l is radius of relative stiffness. As previously stated, the relationship between non-dimensional joint stiffness and measurable joint load transfer efficiency was identified in this study through finite element analysis (Figure E-4). Interpretation of measured joint load transfer efficiency, LTE, simplifies the complex joint interaction and consequently permits a direct interpretation of corner deflection (Eq. E-16). Comparisons of the estimated parameters from center and corner (Tables E-3 and E-4) indicate that the direct interpretation of corner deflection is reasonable. The comparison between measured and calculated corner deflections supports the efficiency of direct interpretation of corner deflections (Figures E-33 and E-36).

Another fact that has to be considered carefully in the interpretation of corner deflection is the curling effect. Referring to Figure E-30 again, it gives the evidence of curling effect on the edge and corner deflection measurements. It shows that corner and edge deflections measured in the afternoon are less than morning measurements due to the downward curling of the heated slab. It is a well known phenomena that a downward curing occurs when the slab surface is heated in the afternoon so that the upper-slab temperature is higher than bottom, whereas upward curling occurs in the opposite way. These up and downward curling cause greater and smaller deflections as measured in FWD test when compared to the deflections measured on a flat slab. Experiences indicate that there is the least curling in morning at which the temperature distribution in a slab is closely uniform.

Obviously, the rate of curling is to be different according to the point of interest in a slab. It would be greater along the four edges of a slab than inside area and greatest at the corner. For FWD testing, therefore, the rate of difference in deflection measurements between the curled and flat slab, equivalently afternoon and morning tests, depend on the geophone location. Figure E-30 also shows this location dependency. For the center deflections, the two basins obtained in the morning and afternoon are fairly close to each other. Edge deflections measured in the afternoon are less than the morning measurements. However, the rate of difference at each geophone is close to the other sensor points. For corner deflections, the rate of difference is also dependent on the sensor location such that the closer to the corner the greater the rate of difference. This inconsistent rate of difference induces another difference between basin AREAs obtained in the morning and afternoon, and therefore the subsequent estimation of k and E_c will be different.

All AREA values obtained from morning and afternoon tests are fairly close in both center and edge (Table E-3). Close estimations of k and E_c are therefore produced from morning and afternoon data for both cases. However, as shown in Table E-4 corner deflections measured in the afternoon produce greater values of AREA and subsequently greater E_c than those measured in the morning. The estimate of E_c from the afternoon data gives about 25 % greater values than morning data. Since the maximum deflection term (δ_1) in the calculation of non-dimensional maximum deflection (Δ_1) compromises the difference between deflections at morning and afternoon, the estimation of k is not sensitive to the curling effect.

Test Pavements

Center loading

Typical deflection basins measured at the center of test slabs are shown in Figure E-37. It contains deflections at load level 2 of test set 5. All basins exhibit similar curves in their shape and magnitude. Measured deflections and corresponding structural evaluation are presented in Table E-6. Table E-6 also includes structural parameters evaluated by the Hertz theory, which is incorporated in RMODS program. Since test slabs consist of three layers, the concept of equivalent stiffness is applied to estimate the top two layers, overlaid asphalt and concrete slab, as a single slab. Compared to the estimates in control slab (Table E-5), estimated *k* value and equivalent modulus E_{eq} are in their legitimate ranges. With the assumption that the properties of concrete are identical in control slab and test slabs, the stiffness of asphalt layer can be easily calculated.

The variances of estimated k and E_{eq} for each slab are drawn with their averaged values in Figures E-38 and E-39, respectively. As shown in Figure E-38, both evaluation processes exhibit stable estimation of subgrade modulus, whereas the proposed method produces about 20~40% higher values. This difference is mainly caused by the effect of finite slab dimension. Though little fluctuations exist in the estimation of equivalent modulus (Figure E-39), the estimated values are all fairly reasonable. Close investigation of Table E-6 indicates that, for a fixed test point, the proposed method provides more stable estimations of equivalent modulus without regard to applied load levels than RMODS.

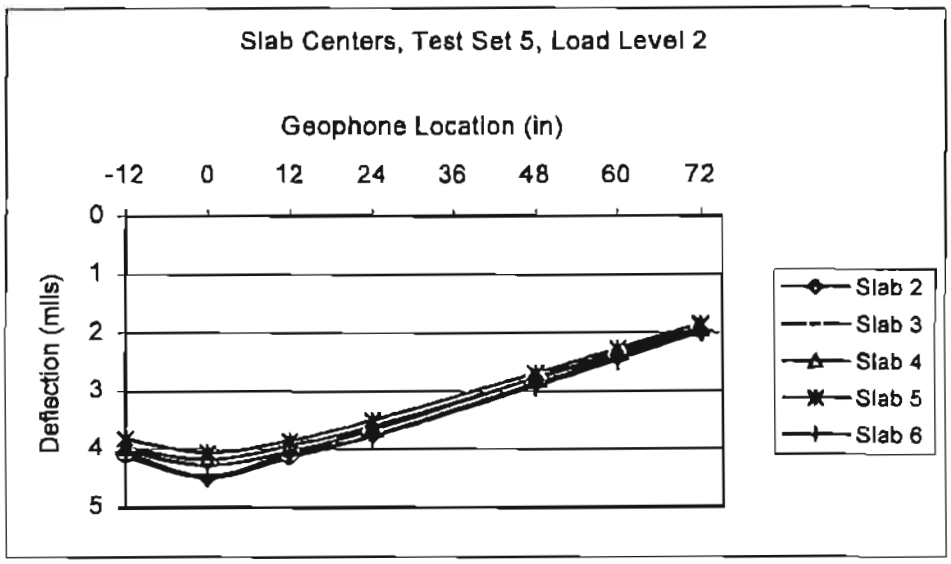

Figure E-37. Typical deflection basins obtained at the center of test slabs; Measured at load level 2 in test set 5

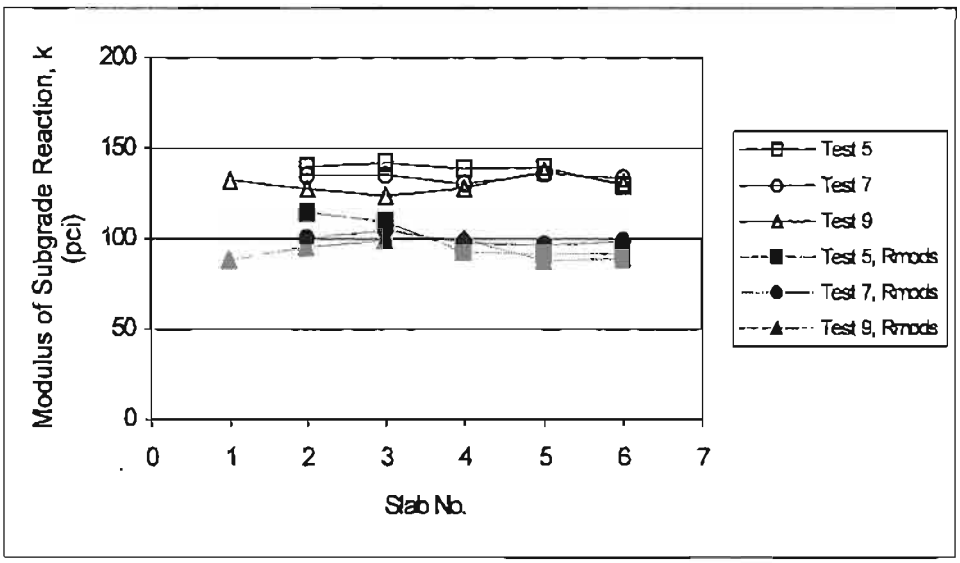

Figure E-38. Variation of *k*-values estimated at the center of test slabs

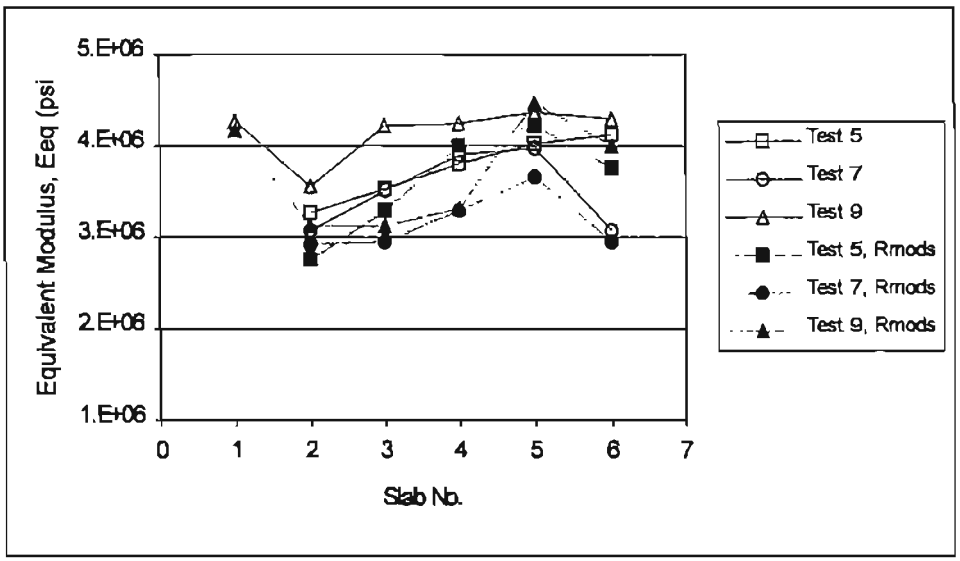

Figure E-39. Variation of equivalent modulus, E_{eq} estimated at the center of test slabs

Table E-6. Evaluation of test slabs from the center deflection measurements

Test Set	Slab	Load	Deflection at each location (mils)							Evaluation						RMODS	
		(lbs)	d-12	d0	d12	d24	d48	d60	d72	AREA	l (in)	a/l	Del l	k (pci)	Eeq (psi)	k (pci)	Eeq (psi)
Test 5 (AM)	Slab 2	5732	2.61	2.75	2.58	2.35	1.76	1.48	1.20	53.24	49.05	0.120	0.153	132.5	3.28E+06	105.0	2.73E+06
		9105	4.04	4.32	4.03	3.64	2.74	2.30	1.87	52.76	48.04	0.123	0.151	138.3	3.15E+06	106.4	2.83E+06
		12454	5.38	5.71	5.34	4.84	3.65	3.05	2.45	52.97	48.48	0.122	0.152	141.1	3.33E+06	100.4	3.25E+06
		16490	6.91	7.36	6.86	6.22	4.68	3.90	3.13	52.75	48.02	0.123	0.151	147.1	3.34E+06	146.7	2.22E+06
	Slab 3	5820	2.50	2.67	2.51	2.28	1.72	1.42	1.16	53.24	49.05	0.120	0.153	138.6	3.43E+06	100.0	3.22E+06
		9089	3.89	4.14	3.89	3.55	2.67	2.22	1.78	53.33	49.26	0.120	0.153	138.7	3.49E+06	105.2	3.10E+06
		12454	5.19	5.51	5.22	4.72	3.56	2.96	2.35	53.42	49.45	0.119	0.154	142.0	3.63E+06	149.7	2.20E+06
		16514	6.68	7.12	6.70	6.09	4.57	3.80	2.99	53.17	48.90	0.121	0.153	148.2	3.62E+06	83.2	4.62E+06
	Slab 4	5736	2.43	2.62	2.46	2.23	1.71	1.45	1.21	53.75	50.17	0.118	0.155	134.6	3.64E+06	100.3	3.25E+06
		9010	3.82	4.08	3.83	3.49	2.67	2.26	1.85	53.81	50.30	0.117	0.155	135.2	3.70E+06	105.2	3.09E+06
		12402	5.08	5.39	5.08	4.64	3.54	2.98	2.43	53.97	50.65	0.116	0.156	139.5	3.92E+06	95.3	3.78E+06
		16422	6.52	6.94	6.51	5.96	4.54	3.81	3.07	53.73	50.13	0.118	0.155	145.6	3.93E+06	70.2	5.83E+06
	Slab 5	5673	2.41	2.53	2.40	2.18	1.67	1.43	1.17	54.33	51.48	0.115	0.157	132.7	3.98E+06	103.5	3.21E+06
		9053	3.73	3.99	3.76	3.43	2.63	2.23	1.82	54.09	50.93	0.116	0.156	136.4	3.92E+06	71.8	5.18E+06
		12355	4.94	5.26	4.97	4.54	3.48	2.93	2.38	54.18	51.14	0.115	0.156	140.4	4.10E+06	82.1	4.73E+06
		16442	6.33	6.78	6.36	5.81	4.46	3.75	3.04	53.85	50.39	0.117	0.155	148.1	4.08E+06	108.5	3.71E+06
	Slab 6	5752	2.47	2.64	2.51	2.31	1.78	1.52	1.27	55.09	53.24	0.111	0.160	122.8	4.22E+06	95.0	3.26E+06
		9053	3.83	4.15	3.89	3.58	2.78	2.36	1.94	54.46	51.77	0.114	0.157	128.0	3.93E+06	92.6	3.54E+06
		12434	5.09	5.50	5.15	4.76	3.69	3.13	2.58	54.53	51.94	0.114	0.158	132.1	4.11E+06	99.2	3.42E+06
		16418	6.53	7.04	6.60	6.10	4.76	4.00	3.26	54.61	52.12	0.113	0.158	135.5	4.28E+06	80.6	4.81E+06
Test 7 (PM)	Slab 2	5732	2.66	2.87	2.67	2.42	1.83	1.54	1.26	52.89	48.31	0.122	0.152	129.9	3.03E+06	99.9	2.70E+06
		9081	4.13	4.49	4.14	3.77	2.87	2.42	1.99	52.81	48.14	0.123	0.152	132.3	3.04E+06	95.6	3.02E+06
		12458	5.56	5.99	5.52	5.02	3.81	3.22	2.64	52.69	47.88	0.123	0.151	137.1	3.08E+06	102.6	2.91E+06
		16383	7.09	7.68	7.06	6.43	4.88	4.12	3.38	52.62	47.74	0.124	0.151	141.3	3.14E+06	103.1	3.10E+06
	Slab 3	5780	2.59	2.73	2.56	2.33	1.77	1.48	1.19	53.41	49.42	0.119	0.154	133.1	3.39E+06	104.3	2.84E+06
		9069	4.03	4.28	4.04	3.67	2.77	2.33	1.92	53.64	49.92	0.118	0.154	131.2	3.48E+06	103.9	2.84E+06
		12438	5.37	5.69	5.36	4.88	3.69	3.09	2.51	53.58	49.79	0.118	0.154	135.9	3.57E+06	100.6	3.19E+06
		16403	6.94	7.30	6.87	6.26	4.70	3.94	3.19	53.42	49.44	0.119	0.154	141.2	3.61E+06	112.1	2.97E+06
	Slab 4	5716	2.56	2.66	2.56	2.31	1.78	1.52	1.22	54.83	52.64	0.112	0.159	123.1	4.04E+06	98.6	3.02E+06
		9014	3.98	4.18	3.94	3.61	2.78	2.35	1.93	54.34	51.50	0.115	0.157	127.5	3.84E+06	100.0	3.05E+06
		12363	5.33	5.57	5.26	4.81	3.68	3.14	2.54	54.27	51.33	0.115	0.157	131.9	3.92E+06	100.0	3.26E+06
		16339	6.76	7.16	6.71	6.14	4.70	3.98	3.23	53.87	50.45	0.117	0.155	139.2	3.85E+06	92.9	3.87E+06
	Slab 5	5689	2.44	2.58	2.46	2.24	1.70	1.44	1.20	54.42	51.67	0.114	0.157	129.8	3.96E+06	101.5	3.15E+06
		8986	3.83	4.06	3.85	3.50	2.69	2.26	1.85	54.24	51.26	0.115	0.156	131.8	3.89E+06	100.2	3.26E+06
		12347	5.07	5.36	5.08	4.63	3.53	2.97	2.44	54.16	51.08	0.116	0.156	137.9	4.01E+06	82.5	4.50E+06
		16339	6.52	6.88	6.50	5.92	4.50	3.80	3.07	53.90	50.51	0.117	0.155	144.5	4.02E+06	102.1	3.73E+06
	Slab 6	5728	2.60	2.89	2.62	2.41	1.86	1.57	1.30	52.69	47.89	0.123	0.151	130.6	2.94E+06	94.3	2.94E+06
		8994	4.06	4.47	4.09	3.78	2.91	2.46	1.98	53.18	48.93	0.121	0.153	128.4	3.15E+06	99.7	2.74E+06
		12323	5.48	6.00	5.48	5.04	3.85	3.27	2.65	52.82	48.16	0.123	0.152	134.2	3.09E+06	100.0	2.91E+06
		16355	6.94	7.71	7.01	6.45	4.94	4.17	3.36	52.61	47.72	0.124	0.151	140.6	3.12E+06	100.6	3.16E+06

Table E-6. (Con'd)

Test Set	Slab	Load	Deflection at each location (mils)							Evaluation						RMODS	
		(lbs)	d-12	d0	d12	d24	d48	d60	d72	AREA	*l* (in)	a/*l*	Del 1	*k* (pci)	Eeq (psi)	*k* (pci)	Eeq (psi)
Test 9 (AM)	Slab 1	7079	2.96	2.94	2.72	2.57	2.04	1.81	1.51	55.80	54.94	0.107	0.163	129.7	5.05E+06	80.4	5.18E+06
		9404	4.28	4.30	3.78	3.61	2.94	2.51	2.12	53.93	50.57	0.117	0.155	132.9	3.71E+06	91.7	3.40E+06
		12553	5.44	5.70	5.20	4.87	3.79	3.24	2.63	53.88	50.47	0.117	0.155	134.2	3.72E+06	100.0	3.19E+06
		16467	6.63	7.00	6.74	5.96	4.75	4.10	3.47	55.10	53.25	0.111	0.160	132.5	4.56E+06	81.7	4.92E+06
	Slab 2	6901	2.93	3.18	3.02	2.70	2.01	1.75	1.45	53.40	49.39	0.119	0.154	136.5	3.47E+06	101.2	3.17E+06
		9197	4.30	4.50	4.29	3.87	3.04	2.56	2.09	54.69	52.31	0.113	0.158	118.2	3.78E+06	94.5	2.90E+06
		12391	5.74	6.06	5.68	5.17	4.01	3.41	2.82	54.06	50.86	0.116	0.156	123.2	3.52E+06	93.6	2.99E+06
		16399	7.14	7.62	7.13	6.50	4.91	4.23	3.47	53.57	49.78	0.119	0.154	133.8	3.51E+06	92.6	3.45E+06
	Slab 3	6864	2.95	3.00	2.90	2.62	2.08	1.83	1.30	55.72	54.75	0.108	0.162	123.9	4.76E+06	102.8	3.27E+06
		9221	4.32	4.39	4.18	3.73	2.98	2.48	2.03	54.49	51.84	0.114	0.157	123.0	3.80E+06	95.0	3.03E+06
		12367	5.70	5.85	5.63	5.06	3.97	3.32	2.73	54.94	52.89	0.112	0.159	120.3	4.02E+06	95.0	3.05E+06
		16407	7.15	7.26	6.99	6.31	4.93	4.07	3.41	54.97	52.95	0.111	0.159	128.4	4.31E+06	104.7	3.15E+06
	Slab 4	6777	2.77	2.90	2.91	2.61	1.97	1.66	1.33	56.09	55.66	0.106	0.164	123.6	5.07E+06	101.5	3.50E+06
		9181	4.10	4.22	4.02	3.63	2.85	2.41	1.99	54.75	52.45	0.112	0.158	125.3	4.05E+06	97.4	3.16E+06
		12304	5.43	5.68	5.38	4.93	3.82	3.21	2.64	54.67	52.24	0.113	0.158	125.5	4.00E+06	100.1	3.04E+06
		16260	6.83	7.16	6.71	6.09	4.76	3.98	3.30	53.96	50.63	0.117	0.155	137.7	3.87E+06	99.7	3.54E+06
	Slab 5	6782	2.67	2.74	2.65	2.40	1.85	1.54	1.25	55.01	53.04	0.111	0.159	140.3	4.75E+06	104.0	3.84E+06
		9145	3.83	3.97	3.79	3.47	2.65	2.21	1.81	54.62	52.14	0.113	0.158	133.8	4.23E+06	73.2	5.05E+06
		12164	5.24	5.31	5.03	4.61	3.56	2.96	2.42	54.49	51.83	0.114	0.157	134.3	4.14E+06	100.1	3.45E+06
		16073	6.48	6.64	6.35	5.79	4.41	3.67	3.02	54.49	51.83	0.114	0.157	141.8	4.38E+06	74.6	5.54E+06
	Slab 6	6880	2.80	2.85	2.71	2.52	1.97	1.58	1.39	55.35	53.85	0.110	0.161	133.8	4.81E+06	79.8	4.97E+06
		9184	4.05	4.19	3.99	3.58	2.81	2.33	2.00	54.42	51.67	0.114	0.157	129.0	3.93E+06	96.6	3.26E+06
		12164	5.31	5.56	5.33	4.80	3.73	3.12	2.61	54.67	52.25	0.113	0.158	126.7	4.04E+06	97.3	3.24E+06
		16221	6.57	6.96	6.69	6.08	4.67	3.87	3.27	54.83	52.62	0.112	0.159	133.6	4.38E+06	82.5	4.52E+06

* *l* : Radius of relative stiffness (Eq. E-2)
k : Modulus of subgrade reaction

a : Radius of loading plate (5.9 in)
E_{eq} : Equivalent modulus of top two layers

Del 1 : Non-dimensional maximum deflection (Eq. E-8)

Edge loading

Figures E-40 and E-41 present the edge deflection basins of test slabs at load level 2 in test set 6 and test set 10, respectively. All tests in test set 6 have 18 inches of offset of loading point from the edge. The offset varies 1.5 ~ 10 inches in test set 10. Obviously, the deflections increase as offset decreases. Measured deflections and corresponding structural evaluation are presented in Table E-7. As shown in Table E-7, offset effect induces overestimates of *k* and Eeq. In fact, the proposed regression equations are developed for the case of zero offset loading. Therefore deflections should be measured on the exact edge to effective use of the proposed equations. If offsets can not be avoided, certain type of correction should be drawn to produce absolute estimations. This will be discussed in corner deflection analysis.

As discussed in the previous section, the equivalent modulus should be consistent in all of center, edge and corner estimations, while edge and corner estimates produce higher k values. Evaluations in test set 10, which has the least offsets, indicate that the edge estimation of E_{eq} converges to the center estimations as the offset approaches to zero. It supports the applicability of the proposed back-calculation equations for edge deflections. The variances of average k and E_{eq} for each slab are presented in Figures E-42 and E-43.

Corner loading

Interpretation of corner deflection is more complicated than at the center or edge. Since the proposed regression equations are based on the closed form solutions, for back-calculation of edge and corner deflections, they have an inherent restriction on the loading point; the loading plate should be located along the exact edge line. This requirement is, however, frequently violated in practice due to geometrical restrictions of the road. In fact, a few inches of offset

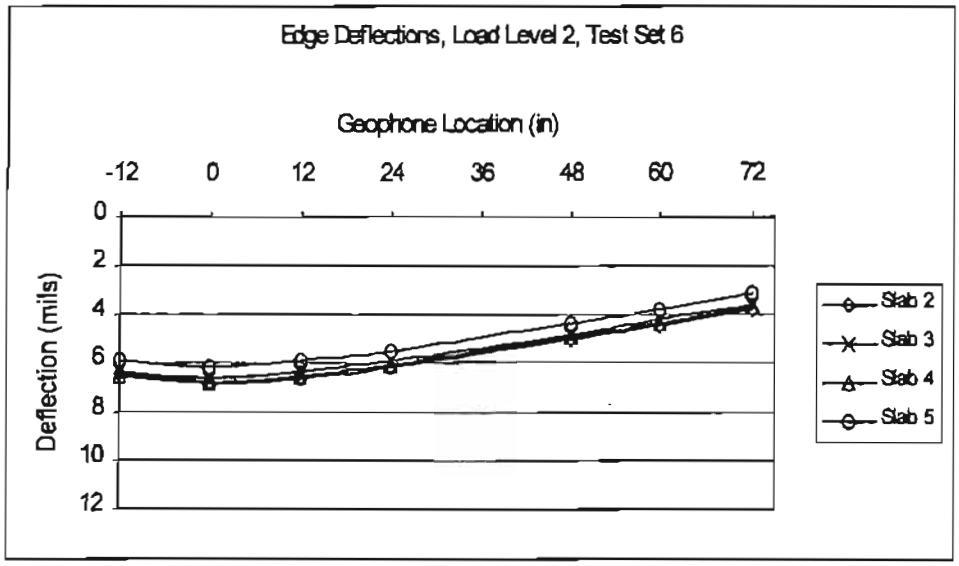

Figure E-40. Typical deflection basins obtained at the edge of test slabs; Measured at load level 2 in test set 6, Offset (D) = 18"

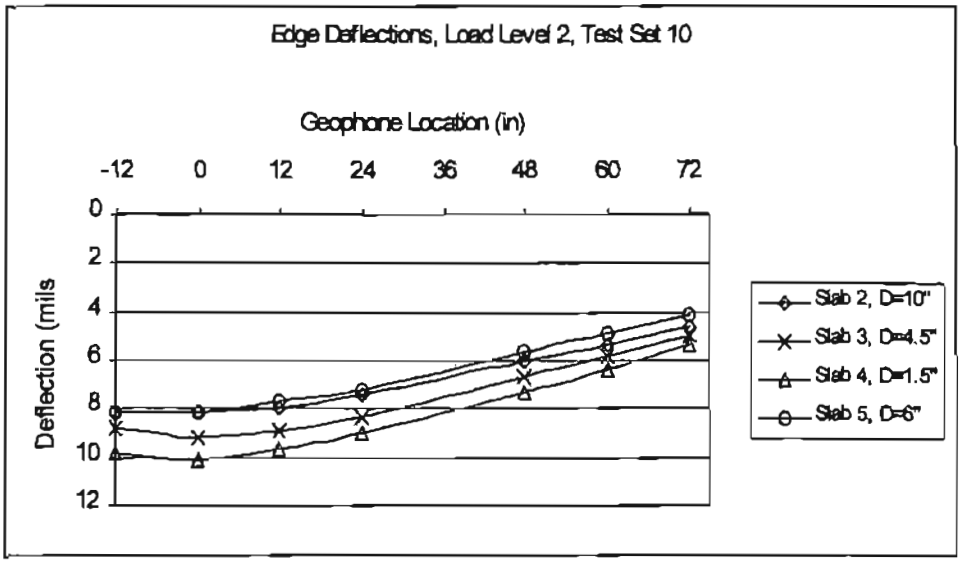

Figure E-41. Typical deflection basins obtained at the edge of test slabs; Measured at load level 2 in test set 10, Offset (D) = 1.5 ~ 10"

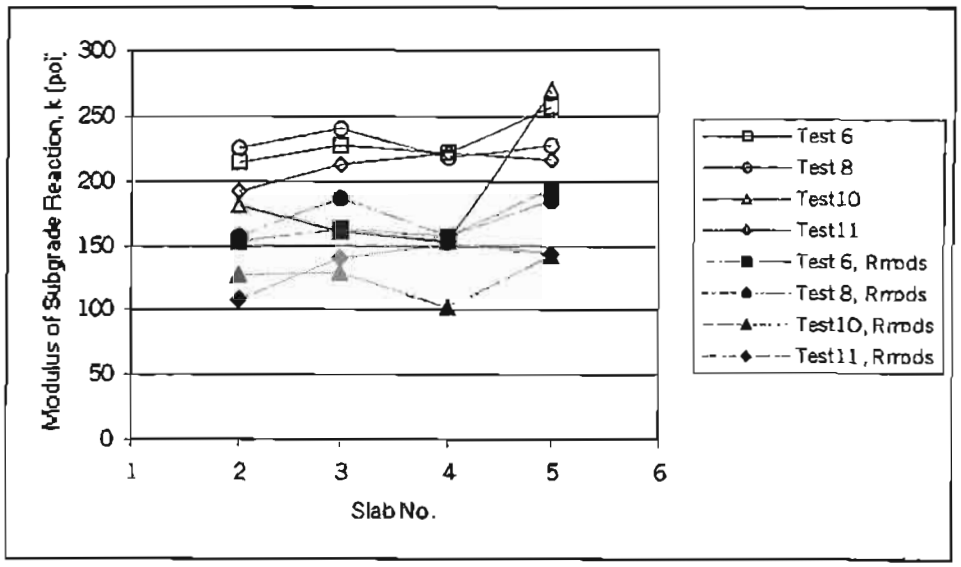

Figure E-42. Variation of *k*-values estimated at the edge of test slabs

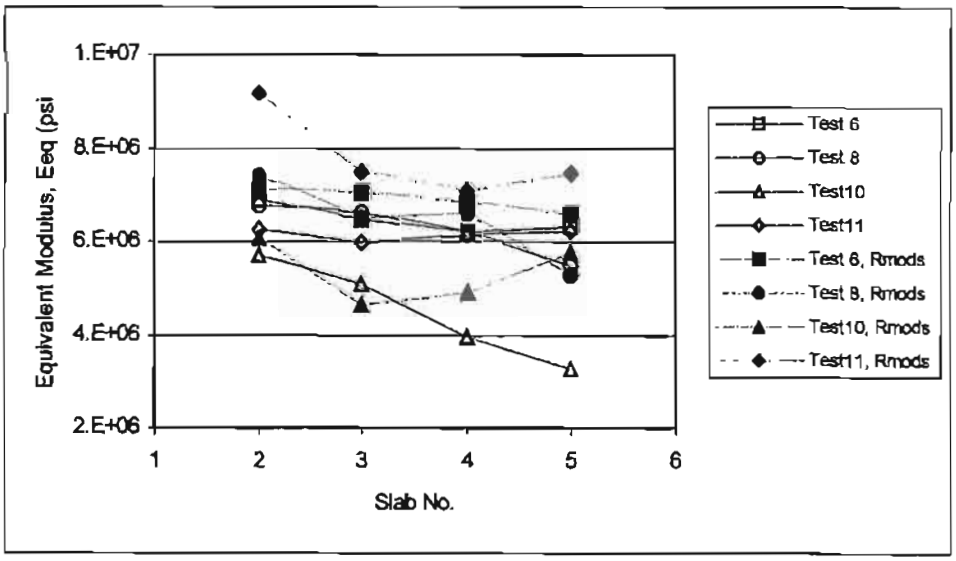

Figure E-43. Variation of equivalent modulus, E_{eq} estimated at the edge of test slabs

Table E-7. Evaluation of test slabs from the edge deflection measurements

Test Set	Slab	Offset (in)	Load (lbs)	Deflection at each location (mils)							Evaluation						RMODS	
				-12	0	12	24	48	60	72	AREA	l (in)	a/l	Del 1	k (pci)	Eeq (psi)	k (pci)	Eeq (psi)
Test 6 (AM)	Slab 2	18"	5748	4.08	4.28	4.16	3.87	3.15	2.76	2.34	58.21	51.67	0.114	0.429	215.9	6.58E+06	158.3	6.56E+06
			8994	6.46	6.76	6.57	6.10	5.01	4.42	3.76	58.43	52.16	0.113	0.432	211.4	6.69E+06	147.1	7.19E+06
			12287	8.65	9.06	8.76	8.23	6.76	5.94	5.06	58.60	52.53	0.112	0.435	213.5	6.95E+06	152.6	7.08E+06
			16315	11.18	11.66	11.30	10.62	8.76	7.72	6.59	58.88	53.15	0.111	0.438	217.1	7.41E+06	149.8	7.71E+06
	Slab 3	18"	5701	4.00	4.17	4.04	3.75	3.04	2.64	2.23	57.74	50.69	0.116	0.423	225.2	6.36E+06	158.7	7.01E+06
			8946	6.30	6.57	6.33	5.90	4.81	4.17	3.55	57.76	50.73	0.116	0.424	224.0	6.35E+06	153.5	7.14E+06
			12287	8.43	8.81	8.48	7.91	6.46	5.62	4.75	57.80	50.81	0.116	0.424	229.0	6.53E+06	151.1	7.79E+06
			16268	10.88	11.37	10.92	10.22	8.35	7.27	6.17	57.85	50.92	0.116	0.425	234.3	6.73E+06	183.3	6.31E+06
	Slab 4	18"	5637	4.11	4.26	4.10	3.81	3.10	2.69	2.28	57.54	50.26	0.117	0.421	220.4	6.01E+06	160.8	6.36E+06
			8887	6.55	6.78	6.49	6.05	4.93	4.30	3.66	57.49	50.16	0.118	0.420	218.9	5.92E+06	160.8	6.24E+06
			12223	8.76	9.08	8.70	8.12	6.71	5.78	4.93	57.79	50.80	0.116	0.424	221.1	6.29E+06	152.8	7.09E+06
			16319	11.35	11.73	11.23	10.51	8.61	7.53	6.41	57.81	50.84	0.116	0.424	228.3	6.52E+06	151.3	7.73E+06
	Slab 5	18"	5661	3.71	3.85	3.68	3.43	2.76	2.37	2.00	56.91	48.99	0.120	0.413	253.2	6.24E+06	200.4	6.04E+06
			8910	5.85	6.11	5.83	5.44	4.37	3.75	3.12	56.78	48.72	0.121	0.412	253.0	6.09E+06	196.6	6.10E+06
			12196	7.85	8.13	7.79	7.25	5.83	5.02	4.17	56.94	49.05	0.120	0.414	257.9	6.38E+06	178.0	7.51E+06
			16216	10.06	10.52	10.03	9.37	7.65	6.49	5.37	57.03	49.22	0.120	0.415	263.8	6.62E+06	203.8	6.66E+06
Test 8 (PM)	Slab 2	18"	5720	3.94	4.14	4	3.74	3.04	2.65	2.26	58.03	51.30	0.115	0.427	224.1	6.63E+06	161.4	6.92E+06
			8946	6.2	6.52	6.28	5.88	4.83	4.2	3.59	58.16	51.58	0.114	0.429	221.1	6.69E+06	158.7	7.00E+06
			12216	8.37	8.76	8.41	7.87	6.46	5.65	4.83	58.01	51.26	0.115	0.427	226.4	6.68E+06	152.0	7.76E+06
			16216	10.71	11.26	10.82	10.17	8.37	7.35	6.28	58.35	51.98	0.114	0.431	229.8	7.17E+06	156.1	8.01E+06
	Slab 3	18"	5693	3.8	3.99	3.83	3.58	2.89	2.53	2.18	57.59	50.38	0.117	0.421	236.9	6.52E+06	186.4	6.14E+06
			8950	5.99	6.3	6.05	5.64	4.57	4.01	3.43	57.60	50.39	0.117	0.421	235.8	6.50E+06	190.0	5.94E+06
			12251	8.02	8.45	8.07	7.56	6.13	5.38	4.61	57.54	50.26	0.117	0.421	241.4	6.59E+06	195.2	6.01E+06
			16244	10.32	10.83	10.38	9.72	7.88	6.94	5.94	57.73	50.68	0.116	0.423	247.2	6.97E+06	171.7	7.94E+06
	Slab 4	18"	5689	4.22	4.4	4.2	3.92	3.2	2.79	2.39	57.45	50.08	0.118	0.420	216.3	5.82E+06	161.3	6.05E+06
			8879	6.56	6.8	6.52	6.11	5.02	4.37	3.73	57.97	51.17	0.115	0.426	212.5	6.23E+06	168.0	5.73E+06
			12227	8.81	9.2	8.78	8.23	6.76	5.92	5.06	57.80	50.82	0.116	0.424	218.2	6.22E+06	149.3	7.14E+06
			16212	11.39	11.84	11.31	10.63	8.77	7.67	6.55	58.03	51.34	0.115	0.427	221.9	6.59E+06	149.8	7.55E+06
	Slab 5	18"	5629	4.17	4.39	4.18	3.87	3.09	2.67	2.28	56.38	47.92	0.123	0.407	227.4	5.13E+06	174.1	5.46E+06
			8879	6.57	6.88	6.58	6.12	4.88	4.24	3.6	56.79	48.74	0.121	0.412	223.8	5.40E+06	173.6	5.45E+06
			12243	8.85	9.25	8.85	8.23	6.59	5.72	4.84	56.88	48.92	0.121	0.413	228.4	5.59E+06	199.3	4.78E+06
			16184	11.41	11.89	11.38	10.61	8.5	7.37	6.23	57.00	49.16	0.120	0.414	233.3	5.83E+06	188.5	5.45E+06

Table E-7. (Con'd)

Test Set	Slab	Offset (in)	Load (lbs)	Deflection at each location (mils)							Evaluation						RMODS	
				-12	0	12	24	48	60	72	AREA	*l* (in)	a/*l*	Del 1	*k* (pci)	Eeq (psi)	*k* (pci)	Eeq (psi)
Test 10 (AM)	Slab 2	10"	6806	5.57	5.65	5.48	5.1	4.18	3.66	3.08	58.25	51.76	0.114	0.430	193.2	5.93E+06	118.0	7.62E+06
			9113	8.11	8.2	7.96	7.41	6.04	5.35	4.58	58.35	51.99	0.113	0.431	177.3	5.54E+06	132.9	5.33E+06
			12061	10.88	11.1	10.75	10.03	8.21	7.29	6.25	58.46	52.22	0.113	0.433	172.4	5.48E+06	126.4	5.39E+06
			16030	13.64	13.98	13.52	12.71	10.44	9.21	7.88	58.70	52.75	0.112	0.436	179.6	5.94E+06	127.9	5.99E+06
	Slab 3	4.5"	6610	5.87	6.18	6.07	5.74	4.56	4.02	3.39	58.88	53.15	0.111	0.438	166.0	5.66E+06	131.1	4.88E+06
			9110	8.77	9.19	8.91	8.32	6.7	5.82	4.96	57.89	51.01	0.116	0.425	162.0	4.69E+06	159.2	3.29E+06
			11989	11.87	12.4	12.04	11.26	9.12	7.94	6.77	58.20	51.65	0.114	0.429	155.5	4.73E+06	99.8	5.73E+06
			15850	15.01	15.56	15.21	14.29	11.58	10.08	8.59	58.74	52.84	0.112	0.436	159.2	5.31E+06	123.8	4.75E+06
	Slab 4	1.5"	6714	6.68	6.92	6.58	6.13	4.98	4.33	3.67	57.00	49.16	0.120	0.414	166.3	4.15E+06	104.0	5.66E+06
			9081	9.8	10.09	9.63	8.96	7.29	6.38	5.38	57.23	49.63	0.119	0.417	152.4	3.95E+06	106.5	4.56E+06
			11648	13.28	13.74	13.04	12.18	9.92	8.63	7.41	57.11	49.39	0.119	0.416	144.4	3.67E+06	96.0	4.58E+06
			15477	16.83	17.31	16.53	15.44	12.63	11.05	9.48	57.59	50.38	0.117	0.421	148.4	4.09E+06	100.6	4.80E+06
	Slab 5	6"	6841	5.55	5.66	5.33	4.96	3.96	3.39	2.87	55.90	46.99	0.126	0.402	220.2	4.59E+06	108.9	9.13E+06
			9062	8.11	8.17	7.67	7.19	5.67	4.92	4.13	55.86	46.92	0.126	0.402	202.5	4.19E+06	157.1	4.45E+06
			11894	10.83	11.02	10.35	9.69	7.72	6.59	5.5	55.88	46.95	0.126	0.402	196.8	4.09E+06	150.6	4.43E+06
			15882	13.7	27.85	13.15	12.27	9.79	8.33	6.93	31.01	18.95	0.311	0.291	462.9	2.55E+05	150.9	5.06E+06
Test 11 (AM)	Slab 2	15"	6671	5.26	5.17	4.74	4.65	3.91	3.47	3.06	58.41	52.11	0.113	0.432	205.2	6.47E+06	103.5	1.14E+07
			8999	7.48	7.53	7.09	6.8	5.71	5.09	4.35	58.78	52.92	0.111	0.437	186.4	6.25E+06	107.4	8.71E+06
			11843	10.09	10.22	9.58	9.18	7.7	6.82	5.91	58.46	52.21	0.113	0.433	183.8	5.84E+06	119.2	6.95E+06
			15731	12.65	12.82	12.11	11.63	9.75	8.63	7.47	58.93	53.25	0.111	0.439	190.0	6.53E+06	102.2	9.69E+06
	Slab 3	16"	6806	4.85	5	4.74	4.44	3.59	3.32	2.83	57.65	50.50	0.117	0.422	225.3	6.26E+06	150.9	7.53E+06
			9026	7.08	7.06	6.75	6.39	5.21	4.52	3.79	57.95	51.13	0.115	0.426	208.3	6.09E+06	151.6	6.16E+06
			11867	9.5	9.61	9.17	8.63	7.04	6.23	5.22	57.84	50.90	0.116	0.424	202.3	5.80E+06	100.9	9.96E+06
			15795	11.98	12.28	11.61	10.99	8.83	7.93	6.67	57.41	49.99	0.118	0.419	215.7	5.76E+06	152.2	6.37E+06
	Slab 4	18"	6663	4.63	4.79	4.54	4.19	3.43	3.14	2.63	57.17	49.51	0.119	0.416	236.3	6.07E+06	149.6	8.08E+06
			9030	6.78	6.81	6.48	6.04	5.05	4.44	3.75	57.86	50.94	0.116	0.425	217.1	6.25E+06	160.2	6.27E+06
			11827	9.11	9.25	8.76	8.24	6.74	6.08	5.09	57.70	50.61	0.117	0.423	211.0	5.92E+06	146.2	6.73E+06
			15696	11.49	11.68	11.1	10.38	8.56	7.69	6.52	57.84	50.90	0.116	0.425	220.2	6.32E+06	150.4	7.32E+06
	Slab 5	14"	6737	4.78	4.76	4.61	4.28	3.6	3.01	2.76	58.49	52.28	0.113	0.433	224.2	7.16E+06	150.3	7.88E+06
			9050	6.89	7.04	6.64	6.15	5.31	4.33	3.93	57.35	49.88	0.118	0.418	216.2	5.72E+06	150.0	6.64E+06
			11846	9.33	9.42	8.99	8.31	7.07	5.9	5.18	57.66	50.51	0.117	0.422	208.1	5.79E+06	121.0	8.47E+06
			15668	11.64	11.81	11.31	10.52	8.87	7.41	6.53	57.89	51.01	0.116	0.425	216.8	6.27E+06	154.2	6.80E+06

* *l* : Radius of relative stiffeness (Eq. E-2)
k : Modulus of subgrade reaction
a : Radius of loading plate (5.9 in)
Del 1 : Non-dimensional maximum deflection (Eq. E-8)
E_{eq} : Equivalent modulus of top two layers

distance from the exact corner may bring large difference, in the order of FWD testing, in deflection measurements and subsequent analysis. Figure E-44 indicates how large the effect of offset distance is in measure of corner deflections. The ordinate represents the ratio of deflections at each sensor location measured with some offset distance D to the deflections measured with zero offset. The abscissa is also presented in dimensionless offset distance term in which the offset distance, D, is divided by the radius of relative stiffness, l, of the slab. Data points in Figure E-44 were obtained by another set of finite element analysis using ILLISLAB. Relevant non-linear regression analysis gives Eq. E-17 for the trends of the deflection ratio at each sensor location. Estimated regression parameters for the Eq. E-17 is valid when the value of D/l is less than 1.5.

As shown in the Figure E-44, the degree of influence of the offset distance is different for each sensor location. The outer sensors present the steeper reductions in the deflection ratio as the offset increases. Naturally, the offset also influences the computed corner deflection AREA. Figure E-45 shows the change of corner deflection AREA at various offset distances. The trend in Figure E-45 is explained by equation E-18, which is also valid when D/l is less than 1.5. Considering highway geometry, possible offset distance would be less than 40 inches so that Eqs. E-17 and E-18 may be applied to most of highway pavements.

$$\delta_{iD} / \delta_{i0} = k_1 \left(\left(\frac{D}{l} \right)^{k_2} - k_3 \exp\left(\frac{D}{l} \right)^{k_4} \right) \qquad \text{(E-17)}$$

where, D = offset distance from slab edge to the edge of loading plate (in),

l = radius of relative stiffness (in),

δ_{i0} = deflection at i^{th} sensor with zero offset (D = 0),

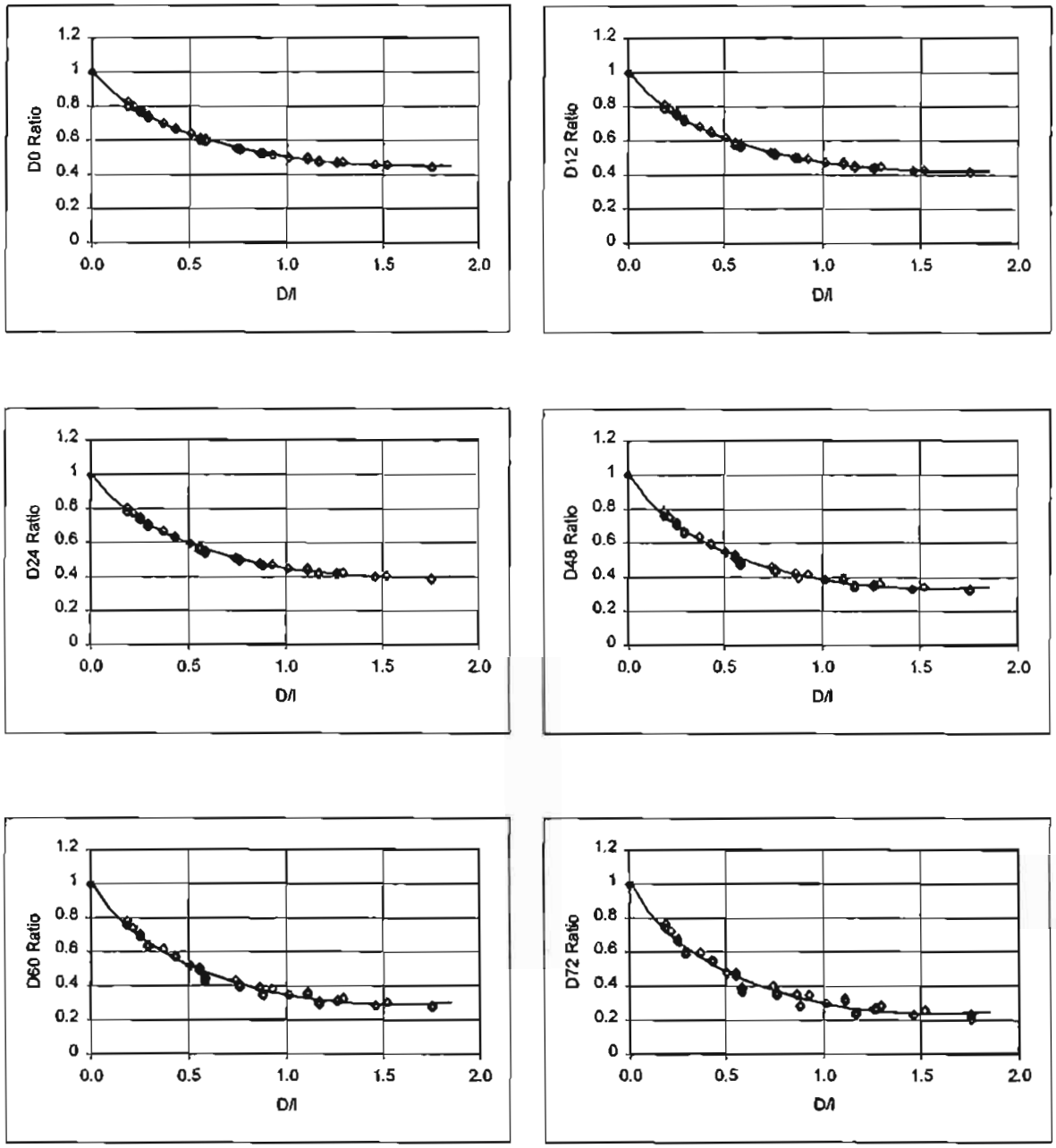

Figure E-44. Effect of offset distance on corner deflection measurements at each sensor location

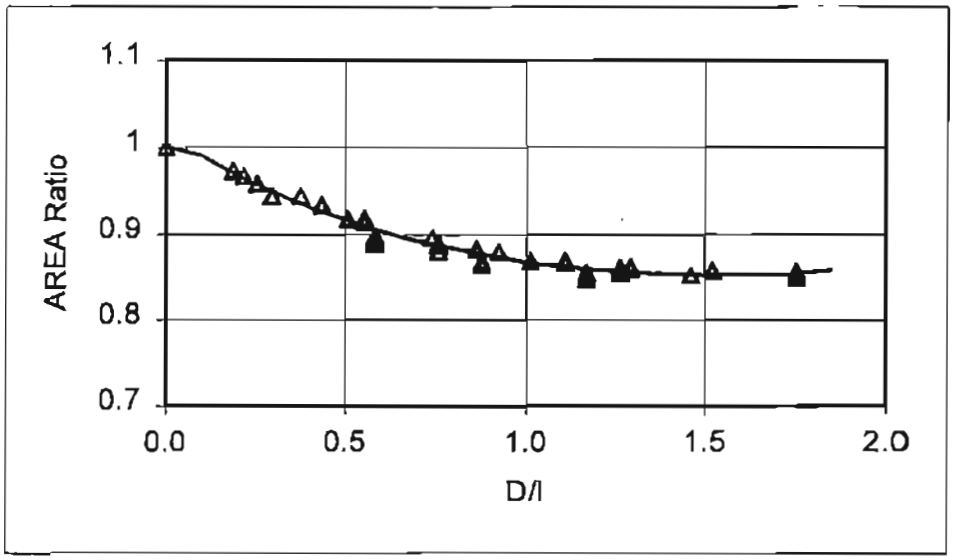

Figure E-45. Effect of offset distance on the corner deflection AREA

$\delta_{i\text{-}D}$ = deflection at i^{th} sensor with some offset (D < 1.5l),

Regression parameters ($k_1 \sim k_4$);

Sensors	k_1	k_2	k_3	k_4	R^2
δ_1 (at 0")	-2.2230	0.56552	0.45114	0.39979	0.997
δ_2 (at 12")	-2.2531	0.57103	0.44572	0.40785	0.996
δ_3 (at 24")	-2.2844	0.58125	0.44029	0.41933	0.995
δ_4 (at 48")	-2.3580	0.60296	0.42826	0.44503	0.991
δ_5 (at 60")	-2.4060	0.61229	0.42097	0.45829	0.986
δ_6 (at 72")	-2.4673	0.61200	0.41240	0.46333	0.975

$$AREA_D / AREA_0 = k_1\left(1-\left(\frac{D}{l}\right)^{k_2} + k_3 \exp\left(\frac{D}{l}\right)^{k_4}\right) \qquad \text{(E-18)}$$

where, $AREA_D$ = corner deflection AREA measured at some offset (D < 1.5l),

$AREA_0$ = corner deflection AREA measured at exact corner (D = 0),

and Regression parameters (R^2 = 0.978) k_1, k_2, k_3, and k_4 are 0.68227, 0.70424, 0.46806, and 0.48343, respectively.

To use Eqs. E-17 and E-18, one must know D and l in advance. The offset distance can be measured during test. The radius of relative stiffness is identified by iterative process. Theoretically, the radius of relative stiffness of a PCC slab and subgrade system is unique throughout the slab so that we may adopt the center l value as the initial value for the iteration. The proposed calculation process to account for FWD load plate offset effect is as follows.

With initial center l value from Eq. E-11, calculate D/l and the corresponding correction factor for AREA using Eq. E-18. With this revised AREA, calculate revised l again using the proposed AREA-l relationship at the given LTE (Eq. E-13), and iterate the process to calculate next revised AREA and corresponding l until revised l becomes same to input l. Here, it is

assumed that the load transfer efficiency remains constant throughout the joint. As an example, Figure E-46 shows the convergence of corner *l*-value in this iteration process for the load level 2 in test set 6. Although the correction for the offset effect on each deflection is automatically included in the correction of AREA, an individual correction for the maximum deflection (d0) should be provided for further evaluation, for example, calculation of non-dimensional maximum deflection. Estimated corner *l*-values and corresponding correction factors for test slabs at each test set are summarized in Table E-8. All tests were conducted at the leave slab corner. For example, corner test on slab number 2 indicates that the test was performed at the joint between slab 1 and 2 and the loading plate was located at slab 2 corner. Although one test point has one offset, each test at that point at different load level would produce different correction factor since the *l*-estimate is different. Correction factors in Table E-8 were calculated with deflections measured at load level 2 at each test point. Dividing measured deflections or basin AREA by relevant correction factors will give the values corrected for the offset effect.

Deflection basins before and after the correction are drawn in Figures E-47 and E-48 for tests 6 and 10. The post index 'C' in the figure represents 'corrected' so that solid lines are the basins of raw measured deflections and dotted lines are for corrected deflections. It is assumed that the deflection across the joint, d-12, has same correction factor with the deflection at the 2nd sensor location, d12. The comparison of the basins indicates that they are divided into two groups with their magnitudes in accordance with the existence of void under the slab. As described in previous chapter, all slabs except slab 2 have artificial voids under the slabs. However, due to the rigidity of concrete slab, the shape of deflection basin does not show any perceivable difference between slab 2 and other slabs.

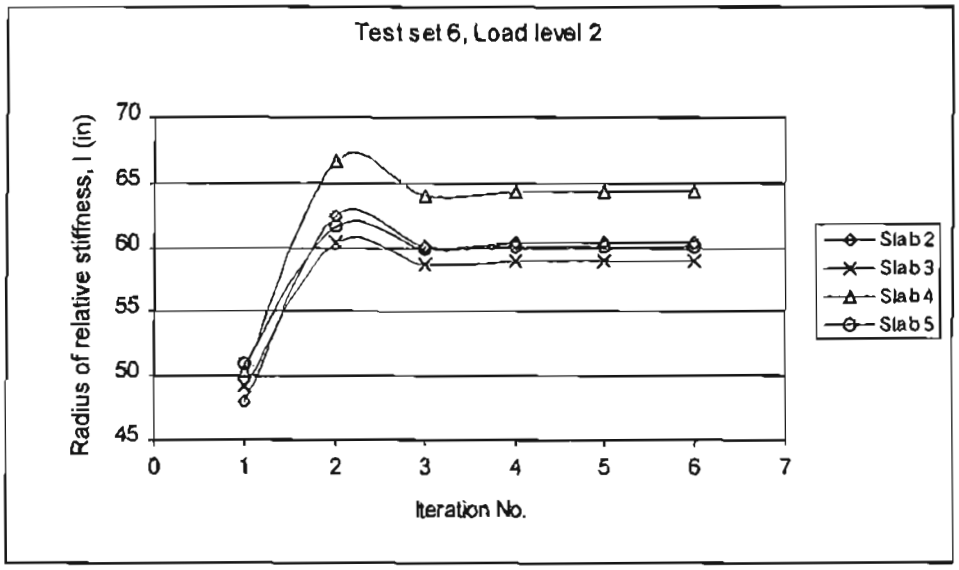

Figure E-46. Estimation of corner l value with the AREA correction for the offset effect; Load Level 2, Test Set 6

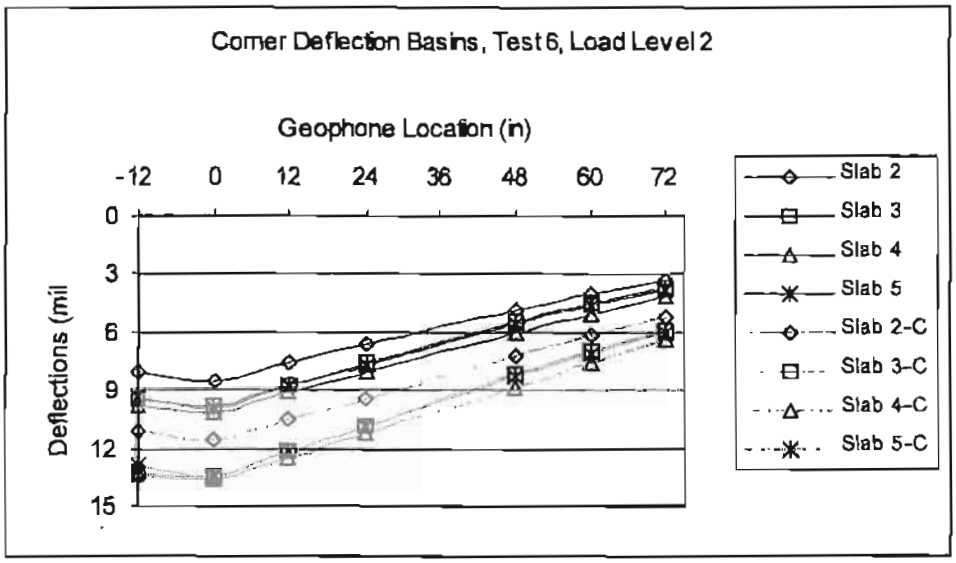

Figure E-47. Deflection basins obtained at the corner of test slabs at load level 2 in test set 6, Offset (D) = 18"

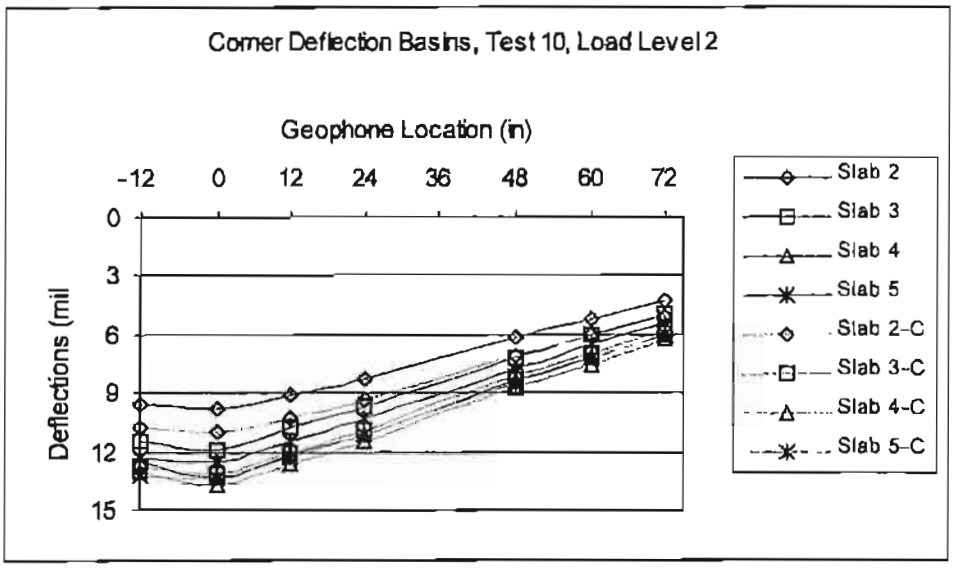

Figure E-48. Deflection basins obtained at the corner of test slabs at load level 2 in test set 10, Offset (D) = 2 ~ 6"

Table E-8. Correction factors for the offset effect for corner deflections and AREA

Test Set	Slab No.	Offset, D (in)	Estimated *l*-corner (in)	*D/l*	Correction factors for each sensor location and AREA						
					d0	d12	d24	d48	d60	d72	AREA
Test 6	2	18	60.38	0.298	0.736	0.720	0.706	0.673	0.652	0.624	0.949
	3	18	58.92	0.305	0.732	0.716	0.701	0.668	0.646	0.618	0.947
	4	18	64.30	0.280	0.747	0.732	0.718	0.687	0.666	0.639	0.952
	5	18	60.14	0.299	0.736	0.719	0.705	0.673	0.651	0.623	0.949
Test 8	2	18	68.74	0.262	0.759	0.744	0.730	0.701	0.681	0.655	0.956
	3	18	66.80	0.269	0.754	0.738	0.725	0.695	0.675	0.648	0.954
	4	18	73.11	0.246	0.769	0.754	0.742	0.713	0.694	0.669	0.959
	5	18	68.17	0.264	0.757	0.742	0.729	0.699	0.679	0.653	0.955
Test 10	2	6	64.07	0.094	0.896	0.887	0.880	0.866	0.856	0.842	0.993
	3	5	59.84	0.084	0.907	0.898	0.892	0.879	0.869	0.856	0.995
	4	2	62.85	0.032	0.974	0.969	0.965	0.958	0.953	0.947	1.000
	5	3.5	61.22	0.057	0.938	0.931	0.926	0.916	0.909	0.899	1.000
Test 11	2	14	71.28	0.196	0.804	0.791	0.780	0.756	0.739	0.717	0.969
	3	14	67.39	0.208	0.796	0.782	0.771	0.746	0.729	0.706	0.967
	4	16	64.25	0.249	0.767	0.752	0.740	0.711	0.692	0.667	0.958
	5	17	69.19	0.246	0.769	0.755	0.742	0.713	0.694	0.670	0.959

Measured deflections and corresponding structural evaluations with corrections for each offset are shown in Table E-9. Corrections were made on the basin AREA and maximum deflection, d0, for the structural evaluation presented in Table E-9. Estimated *k*-values are close to the center evaluations, while higher E_{eq}-values are produced in corner estimations. This high estimate of modulus of elasticity may be induced from the limitation on the range of variables in proposed regression equations. Back to Figure E-7, the range of corner AREA in the relationship is about from 25 to 50 inches and corresponding *l*-estimate is between 20 and 60 inches. Corrected AREA values in test slabs are mostly at or above the range limit of the regression. In addition, Figure E-10 indicates the possibility of overestimate in high ranges of *l*-value, which will invoke the overestimate of modulus of elasticity. Therefore, simple extrapolation of given regression will produce higher estimates of E-values as presented in Table E-9. To extend the regression range, another set of FE analysis should be performed with extended ranges of input variables. However, additional FE analysis was not conducted in this study. This study proposed the methodology of direct interpretation of corner deflection measurements for the structural evaluation of JCP, and confirmed its applicability from the test and analysis of control slab. Formulation of the regression equation for extended ranges of corner AREA and *l*-values should be performed in further study on this subject.

Void Detection

Several procedures to identify voids using surface deflections have been proposed, and their application has produces mixed results. Based on a comparative study (E-4) on existing procedures, the CTR method (E-2) and the NCHRP method (E-3) were identified as the most promising procedures. Both give empirical criteria for identifying voids. The CTR method uses

Table E-9. Evaluation of test slabs from the corner deflection measurements with correction for the offset effect

Test Set	Slab	Offset (in)	Load (lbs)	Deflection at each location (mils)							LTE	AREA	Corrected		Evaluation				
				d-12	d0	d12	d24	d48	d60	d72			AREA	d0	*l* (in)	*a/l*	Del 1	*k* (pci)	Eeq (psi)
Test 6 (AM)	2	18	5796	5.04	5.29	4.82	4.14	3.06	2.57	2.12	1.003	49.67	52.34	7.19	63.07	0.094	0.543	110.0	7.44E+06
			9137	8.00	8.55	7.54	6.63	4.87	4.04	3.27	0.985	48.76	51.38	11.62	60.34	0.098	0.535	115.5	6.54E+06
			12470	10.76	11.37	10.08	8.87	6.46	5.41	4.37	0.996	48.92	51.55	15.45	60.83	0.097	0.534	116.5	6.82E+06
			16287	13.85	14.67	12.96	11.42	8.33	6.99	5.65	0.994	48.86	51.49	19.93	60.65	0.097	0.534	118.6	6.86E+06
	3	18	5736	5.91	6.17	5.48	4.73	3.39	2.85	2.31	1.008	48.14	50.83	8.43	58.83	0.100	0.522	102.6	5.25E+06
			9041	9.46	9.85	8.72	7.59	5.46	4.51	3.65	1.011	48.19	50.89	13.46	58.98	0.100	0.522	100.8	5.21E+06
			12315	12.79	13.46	11.88	10.27	7.37	6.15	4.97	1.000	47.88	50.56	18.39	58.10	0.102	0.520	103.2	5.03E+06
			16220	16.80	17.71	15.59	13.49	9.68	8.10	6.53	0.999	47.81	50.49	24.19	57.92	0.102	0.520	103.9	5.00E+06
	4	18	5665	6.00	6.28	5.68	5.00	3.70	3.08	2.65	1.006	50.21	52.74	8.41	64.26	0.092	0.547	89.3	6.51E+06
			8930	9.80	10.15	9.12	8.07	6.06	5.04	4.11	1.016	50.23	52.76	13.59	64.33	0.092	0.545	86.5	6.33E+06
			12251	13.38	13.79	12.40	10.99	8.16	6.86	5.65	1.021	50.21	52.75	18.46	64.28	0.092	0.543	87.3	6.37E+06
			16172	17.44	18.07	16.24	14.40	10.74	9.02	7.37	1.016	50.26	52.80	24.19	64.44	0.092	0.545	87.8	6.47E+06
	5	18	5748	5.82	6.10	5.41	4.77	3.51	2.80	2.27	1.004	48.82	51.44	8.29	60.51	0.097	0.531	100.5	5.76E+06
			9149	9.30	9.89	8.79	7.67	5.57	4.63	3.77	0.990	48.67	51.28	13.44	60.08	0.098	0.532	100.4	5.59E+06
			12378	12.85	13.56	12.02	10.51	7.69	6.30	5.11	0.998	48.63	51.25	18.42	59.97	0.098	0.530	99.0	5.47E+06
			16184	17.09	18.09	16.06	14.01	10.16	8.45	6.88	0.994	48.59	51.20	24.58	59.85	0.099	0.530	97.4	5.34E+06
Test 8 (PM)	2	18	5824	4.46	4.59	4.45	4.03	2.68	2.44	2.11	1.023	53.08	55.53	6.05	73.12	0.081	0.578	104.0	1.27E+07
			9085	7.07	7.51	7.04	6.29	4.44	3.87	3.3	0.991	51.79	54.17	9.89	68.66	0.086	0.569	110.7	1.05E+07
			12363	9.55	10.04	9.33	8.33	6.16	5.31	4.43	1.001	52.12	54.52	13.23	69.79	0.085	0.570	109.5	1.11E+07
			16244	12.5	13.03	12.11	10.76	7.87	6.92	5.72	1.010	51.90	54.28	17.17	69.03	0.085	0.565	112.3	1.09E+07
	3	18	5709	4.81	5.01	4.54	4.06	3.05	2.62	2.13	1.011	51.25	53.72	6.64	67.24	0.088	0.558	106.1	9.27E+06
			9014	7.63	7.97	7.22	6.46	4.84	4.11	3.37	1.008	51.12	53.58	10.57	66.82	0.088	0.557	106.4	9.07E+06
			12311	10.38	10.83	9.8	8.74	6.54	5.57	4.57	1.009	50.96	53.42	14.36	66.31	0.089	0.555	108.2	8.94E+06
			16204	13.69	14.28	12.89	11.46	8.57	7.28	5.96	1.009	50.70	53.15	18.94	65.48	0.090	0.551	110.0	8.65E+06
	4	18	5673	5.22	5.41	5	4.5	3.5	2.96	2.48	1.016	53.02	55.29	7.04	72.32	0.082	0.576	88.9	1.04E+07
			8938	8.34	8.65	8.02	7.25	5.59	4.78	3.97	1.015	53.23	55.51	11.25	73.04	0.081	0.579	86.3	1.05E+07
			12212	11.38	11.79	10.92	9.87	7.63	6.53	5.43	1.016	53.24	55.52	15.33	73.09	0.081	0.579	86.4	1.05E+07
			16172	15	15.53	14.36	13	10.04	8.59	7.14	1.017	53.20	55.47	20.20	72.93	0.081	0.578	87.1	1.05E+07
	5	18	5716	5.65	5.85	5.41	4.82	3.65	3.11	2.57	1.017	52.17	54.63	7.73	70.15	0.084	0.568	85.4	8.84E+06
			9002	9.09	9.5	8.68	7.73	5.87	4.96	4.11	1.007	51.59	54.02	12.55	68.20	0.087	0.563	86.8	8.03E+06
			12331	12.54	13.13	11.93	10.63	8.06	6.8	5.63	1.005	51.31	53.73	17.34	67.28	0.088	0.560	87.9	7.70E+06
			16184	16.68	17.41	15.83	14.1	10.69	9.02	7.48	1.008	51.34	53.75	23.00	67.36	0.088	0.559	86.7	7.63E+06

Table E-9. (Con'd)

Test Set	Slab	Offset (in)	Load (lbs)	Deflection at each location (mils)							LTE	AREA	Corrected		Evaluation				
				d-12	d0	d12	d24	d48	d60	d72			AREA	d0	l (in)	a/l	Del l	k (pci)	Eeq (psi)
Test10 (AM)	2	6	7116	6.63	6.91	6.33	5.70	4.26	3.62	2.99	1.010	51.82	52.19	7.71	62.64	0.094	0.539	126.7	8.34E+06
			9399	9.57	9.85	9.13	8.21	6.16	5.17	4.27	1.023	52.28	52.65	10.99	64.00	0.092	0.542	113.1	8.11E+06
			12053	13.09	13.51	12.34	11.07	8.34	7.03	5.82	1.020	51.65	52.01	15.08	62.14	0.095	0.534	110.6	7.05E+06
			16030	16.43	16.86	15.51	13.96	10.49	8.77	7.28	1.026	51.98	52.34	18.82	63.09	0.094	0.537	114.9	7.78E+06
	3	5	6687	7.74	8.04	7.33	6.54	4.85	4.12	3.44	1.013	51.16	51.41	8.86	60.44	0.098	0.528	109.1	6.22E+06
			9026	11.48	11.91	10.80	9.65	7.20	6.04	4.99	1.015	50.95	51.20	13.13	59.85	0.099	0.525	100.8	5.53E+06
			11954	15.76	16.36	14.82	13.22	9.83	8.25	6.80	1.014	50.78	51.03	18.04	59.38	0.099	0.523	98.3	5.22E+06
			15816	20.33	21.00	19.04	16.98	12.66	10.57	8.75	1.019	50.83	51.08	23.15	59.52	0.099	0.522	100.7	5.40E+06
	4	2	6626	8.60	9.15	8.37	7.60	5.72	4.95	4.12	0.989	52.37	52.37	9.39	63.18	0.093	0.546	96.5	6.58E+06
			8914	12.57	13.30	12.20	11.12	8.43	7.21	5.98	0.995	52.67	52.67	13.66	64.05	0.092	0.549	87.3	6.28E+06
			11703	17.26	18.24	16.64	15.21	11.54	9.89	8.18	0.996	52.54	52.54	18.73	63.68	0.093	0.547	84.3	5.92E+06
			15434	22.09	23.40	21.29	19.71	14.86	12.58	10.54	0.994	52.66	52.66	24.02	64.04	0.092	0.549	86.0	6.18E+06
	5	3.5	6607	8.26	8.36	7.68	6.94	5.25	4.39	3.64	1.040	52.18	52.18	8.91	62.63	0.094	0.532	100.5	6.61E+06
			8986	12.33	12.52	11.45	10.31	7.75	6.52	5.40	1.037	51.78	51.78	13.35	61.46	0.096	0.527	94.0	5.73E+06
			11822	17.23	17.56	15.95	14.40	10.82	9.04	7.52	1.033	51.50	51.50	18.72	60.68	0.097	0.525	90.0	5.21E+06
			15541	22.32	22.94	20.67	18.56	13.93	11.72	9.74	1.024	50.98	50.98	24.46	59.25	0.100	0.520	94.1	4.96E+06
Test11 (AM)	2	14	7047	5.54	5.80	5.41	4.87	3.74	3.21	2.62	1.005	53.27	54.97	7.21	71.25	0.083	0.575	110.6	1.22E+07
			9515	8.15	8.44	7.87	7.13	5.43	4.60	3.87	1.016	53.27	54.97	10.50	71.26	0.083	0.572	102.2	1.13E+07
			11787	11.00	11.47	10.67	9.61	7.32	6.20	5.19	1.009	52.93	54.63	14.27	70.13	0.084	0.570	95.7	9.90E+06
			15866	13.94	14.51	13.45	12.15	9.26	7.82	6.53	1.011	52.85	54.54	18.05	69.85	0.084	0.568	102.4	1.04E+07
	3	14	6912	6.35	6.49	5.95	5.31	3.97	3.39	2.81	1.030	51.61	53.37	8.15	66.16	0.089	0.549	106.4	8.71E+06
			9200	9.43	9.53	8.79	7.79	5.97	5.00	4.15	1.042	51.97	53.74	11.97	67.31	0.088	0.551	93.4	8.20E+06
			11843	12.83	13.11	11.92	10.58	8.11	6.74	5.60	1.030	51.30	53.06	16.47	65.21	0.090	0.545	92.2	7.12E+06
			15850	16.43	16.81	15.23	13.53	10.31	8.66	7.22	1.029	51.16	52.90	21.12	64.76	0.091	0.543	97.3	7.31E+06
	4	16	6817	6.49	6.72	5.80	5.34	4.08	3.49	2.70	1.017	50.23	52.43	8.76	63.36	0.093	0.540	104.8	7.22E+06
			9081	9.47	9.67	8.19	7.70	5.97	5.06	4.25	1.031	50.53	52.74	12.61	64.27	0.092	0.541	94.3	6.88E+06
			11592	13.07	12.96	11.27	10.55	8.18	6.89	5.76	1.062	51.50	53.75	16.90	67.35	0.088	0.546	82.6	7.27E+06
			15466	15.92	16:60	14.80	13.56	10.44	8.83	7.43	1.010	51.79	54.06	21.64	68.32	0.086	0.563	86.1	8.02E+06
	5	17	6973	6.00	6.40	5.94	5.19	3.99	3.34	2.87	0.987	51.91	54.13	8.32	68.53	0.086	0.569	101.5	9.57E+06
			9351	9.04	9.25	8.37	7.61	5.88	4.89	4.07	1.029	52.09	54.32	12.03	69.14	0.085	0.561	91.3	8.92E+06
			11716	12.39	12.90	11.61	10.60	8.09	6.78	5.62	1.011	51.80	54.01	16.78	68.17	0.087	0.562	84.4	7.79E+06
			15715	16.02	16.62	15.09	13.68	10.42	8.76	7.31	1.015	51.96	54.18	21.61	68.70	0.086	0.563	86.7	8.26E+06

the geometric characteristics of deflection basin and the NCHRP method uses maximum deflection at multi load levels.

The CTR method asserts that a void exists when the geometric parameter Q is greater than 22. The parameter Q is determined from the angle between horizontal line and the line joining d12 and d72. Figures E-49 and E-50 represent the corner deflection basins normalized with the minimum deflection (d72) at the slabs with and without void in test pavements. The deflections are corrected for the loading offset in each test. Slab 2 has sound contact between concrete slab and subgrade, while slab 4 has a void at the loading point under the slab. Solid lines represent the basins at load level 2 and dashed lines are for load level 4. Obviously, the decisive parameter Q is influenced by applied load level. However, the CTR method does not specify the load level for application.

Figure E-51 shows examples of applying the NCHRP void detection process. The NCHRP method specifies that a void exists when the x-axis intercept of linear regression line for a load vs. deflection plot is greater than 2 mils. Figure E-51 contains the test data for slab 2, which has sound subgrade, and slab 4, in which a void exists, in test sets 6 and 10. Although a large void exists under the slab 4, corresponding regression lines pass through the x-axis well below the NCHRP criteria.

The results of the two current void detection processes are presented in Table E-10. It indicates that, in general, the CTR method gives more promising results out of the given tests. However, it is required for effective use of the CTR method that the applied load should be high at 16000 lbs. and loading plate should be located as close as to the exact corner. Also, test at morning when curling effect is not dominant would enhance the effectiveness of the process.

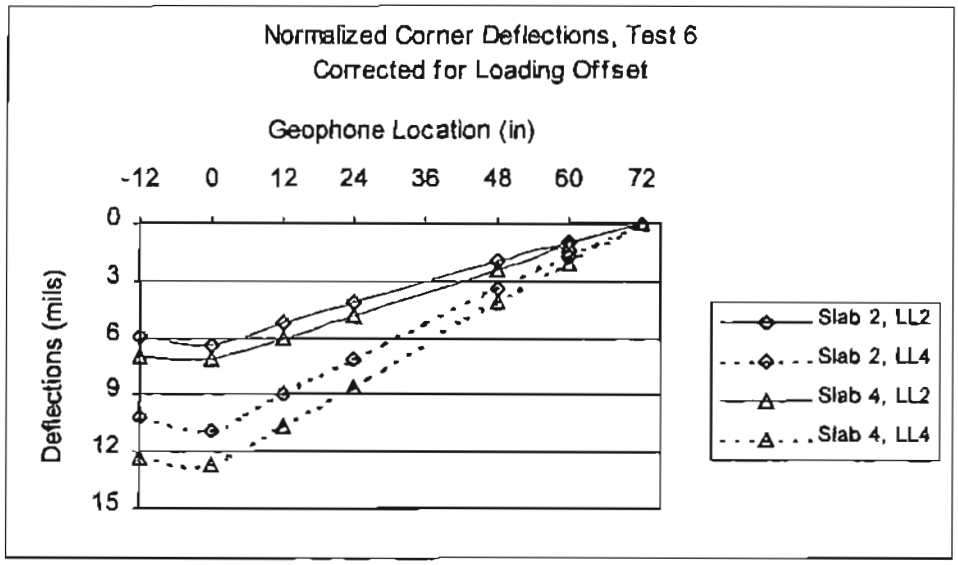

Figure E-49. Normalized corner deflection basins of test slabs 2 and 4 in test set 6; Deflections are corrected for the offsets

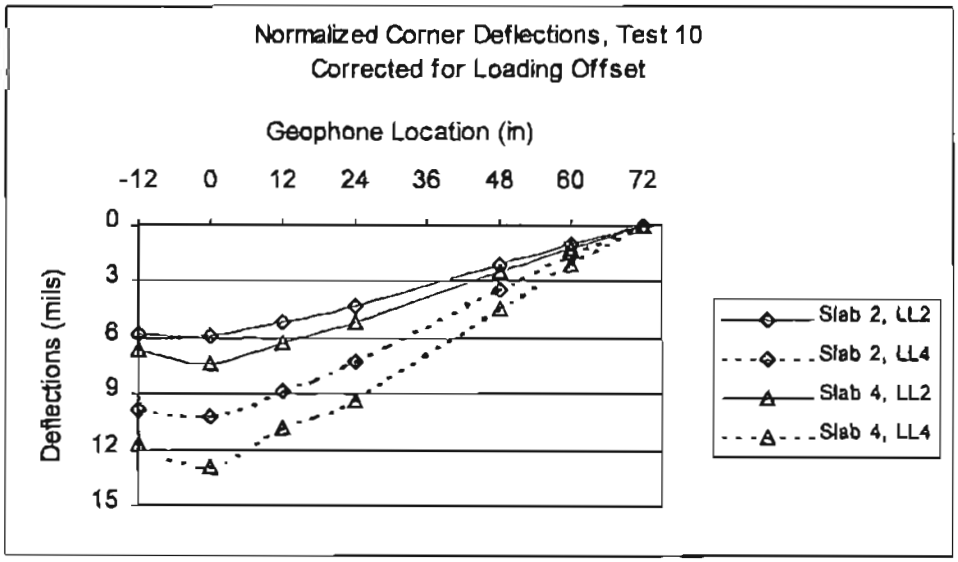

Figure E-50. Normalized corner deflection basins of test slabs 2 and 4 in test set 10; Deflections are corrected for the offsets

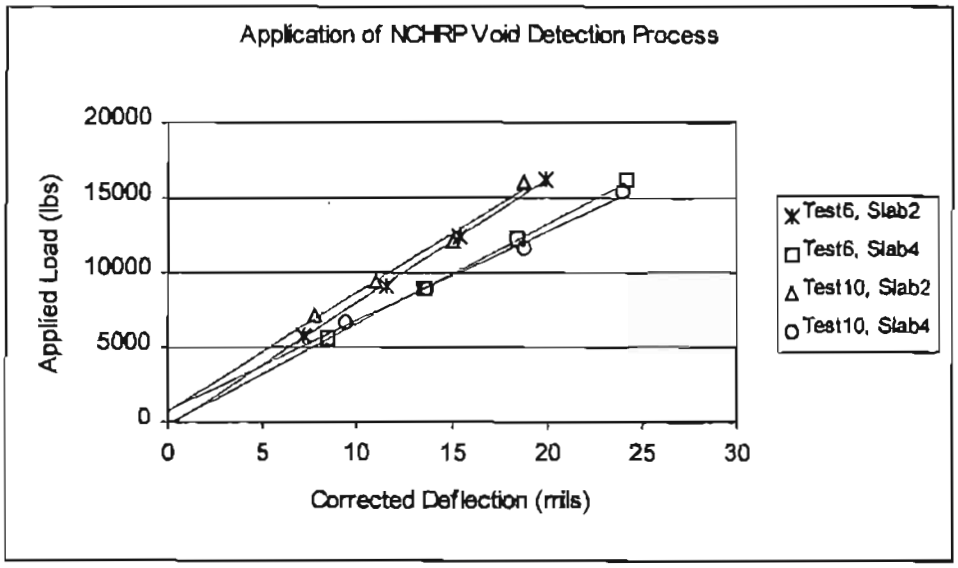

Figure E-51. Application of the NCHRP void detection process with corrected deflections; Slab 2 and Slab 4 in Test Set 6 and Test Set 10

Table E-10. Results of current void detection processes

Test Set	Slab	Offset (in)	Load (lbs)	Deflections (mils)						Void Detection without Correction					Void Detection with Correction				
				Measured			Corrected for offset			CTR			NCHRP		CTR			NCHRP	
				d0	d12	d72	d0	d12	d72	Q	M	void	x-int.	void	Q	M	void	x-int.	void
Test 6 (AM)	2	18	5796	5.29	4.82	2.12	7.19	6.69	3.40	6.42	85.52	N			7.82	85.30	N		
			9137	8.55	7.54	3.27	11.62	10.47	5.24	10.09	80.44	N			12.30	79.20	N		
			12470	11.37	10.08	4.37	15.45	14.00	7.00	13.38	77.87	N			16.25	76.43	N		
			16287	14.67	12.96	5.65	19.93	18.00	9.05	16.94	74.09	N	0.25	N	20.44	72.15	N	0.34	N
	3	18	5736	6.17	5.48	2.31	8.43	7.65	3.74	7.52	83.44	N			9.27	82.64	N		
			9041	9.85	8.72	3.65	13.46	12.18	5.91	11.93	79.33	N			14.65	77.98	N		
			12315	13.46	11.88	4.97	18.39	16.59	8.04	16.06	75.25	N			19.61	73.34	N		
			16220	17.71	15.59	6.53	24.19	21.77	10.57	20.68	70.54	N	-0.12	N	25.03	68.03	[redacted]	-0.17	N
	4	18	5665	6.28	5.68	2.65	8.41	7.76	4.15	7.20	84.29	N			8.56	83.84	N		
			8930	10.15	9.12	4.11	13.59	12.46	6.43	11.79	80.26	N			14.10	79.35	N		
			12251	13.79	12.40	5.65	18.46	16.94	8.84	15.71	76.96	N			18.65	75.78	N		
			16172	18.07	16.24	7.37	24.19	22.19	11.53	20.28	73.04	N	0.03	N	23.93	71.53	[redacted]	0.05	N
	5	18	5748	6.10	5.41	2.27	8.29	7.52	3.64	7.45	83.44	N			9.18	82.75	N		
			9149	9.89	8.79	3.77	13.44	12.23	6.05	11.81	79.61	N			14.43	78.58	N		
			12378	13.56	12.02	5.11	18.42	16.72	8.20	16.06	75.60	N			19.54	74.13	N		
			16184	18.09	16.06	6.88	24.58	22.34	11.04	20.93	71.31	N	-0.57	N	25.20	69.51	[redacted]	-0.77	N
Test 8 (PM)	2	18	5824	4.59	4.45	2.11	6.05	5.98	3.22	5.57	88.66	N			6.56	89.37	N		
			9085	7.51	7.04	3.30	9.89	9.46	5.04	8.86	85.52	N			10.44	85.88	N		
			12363	10.04	9.33	4.43	13.23	12.54	6.76	11.54	83.25	N			13.53	83.46	N		
			16244	13.03	12.11	5.72	17.17	16.28	8.73	14.91	81.28	N	0.02	N	17.45	81.56	N	0.02	N
	3	18	5709	5.01	4.54	2.13	6.64	6.15	3.29	5.73	85.52	N			6.81	85.30	N		
			9014	7.97	7.22	3.37	10.57	9.78	5.20	9.11	82.87	N			10.81	82.53	N		
			12311	10.83	9.80	4.57	14.36	13.28	7.05	12.29	80.26	N			14.54	79.76	N		
			16204	14.28	12.89	5.96	18.94	17.47	9.20	16.11	76.96	N	-0.01	N	19.01	76.21	N	-0.01	N
	4	18	5673	5.41	5.00	2.48	7.04	6.63	3.71	5.99	86.09	N			6.95	86.15	N		
			8938	8.65	8.02	3.97	11.25	10.64	5.93	9.58	84.01	N			11.09	84.18	N		
			12212	11.79	10.92	5.43	15.33	14.48	8.12	12.88	81.75	N			14.86	81.95	N		
			16172	15.53	14.36	7.14	20.20	19.05	10.67	16.74	78.97	N	-0.01	N	19.23	79.15	N	-0.01	N
	5	18	5716	5.85	5.41	2.57	7.73	7.29	3.94	6.75	85.81	N			7.96	85.84	N		
			9002	9.50	8.68	4.11	12.55	11.70	6.29	10.78	82.22	N			12.69	81.92	N		
			12331	13.13	11.93	5.63	17.34	16.08	8.62	14.71	78.69	N			17.26	78.08	N		
			16184	17.41	15.83	7.48	23.00	21.33	11.45	19.18	75.25	N	-0.45	N	22.37	74.50	[redacted]	-0.59	N

Table E-10. (Con'd)

Test Set	Slab	Offset (in)	Load (lbs)	Deflections (mils)						Void Detection without correction					Void Detection with correction				
				Measured			Corrected for offset			CTR			NCHRP		CTR			NCHRP	
				d0	d12	d72	d0	d12	d72	Q	M	void	x-int.	void	Q	M	void	x-int.	void
Test10 (AM)	2	6	7116	6.91	6.33	2.99	7.71	7.14	3.55	7.92	84.48	N			8.50	84.52	N		
			9399	9.85	9.13	4.27	10.99	10.29	5.07	11.45	83.16	N			12.27	83.34	N		
			12053	13.51	12.34	5.82	15.08	13.91	6.91	15.20	78.97	N			16.26	79.00	N		
			16030	16.86	15.51	7.28	18.82	17.49	8.65	18.93	77.32	N	-0.92	N	20.22	77.49	N	-1.02	N
	3	5	6687	8.04	7.33	3.44	8.86	8.16	4.02	9.21	83.25	N			9.80	83.33	N		
			9026	11.91	10.80	4.99	13.13	12.03	5.83	13.61	79.52	N			14.48	79.57	N		
			11954	16.36	14.82	6.80	18.04	16.50	7.94	18.48	75.60	N			19.63	75.66	N		
			15816	21.00	19.04	8.75	23.15	21.20	10.22	23.21	71.91	[redacted]	-1.17	N	24.59	71.99	[redacted]	-1.29	N
	4	2	6626	9.15	8.37	4.12	9.39	8.64	4.35	10.04	82.59	N			10.13	82.81	N		
			8914	13.30	12.20	5.98	13.66	12.59	6.31	14.53	79.61	N			14.65	79.94	N		
			11703	18.24	16.64	8.18	18.73	17.17	8.64	19.42	75.07	N			19.58	75.47	N		
			15434	23.40	21.29	10.54	24.02	21.97	11.13	24.13	70.62	[redacted]	-1.35	N	24.31	71.11	[redacted]	-1.38	N
	5	3.5	6607	8.36	7.68	3.64	8.91	8.25	4.05	9.56	83.53	N			9.93	83.69	N		
			8986	12.52	11.45	5.40	13.35	12.30	6.01	14.15	79.89	N			14.69	80.08	N		
			11822	17.56	15.95	7.52	18.72	17.13	8.36	19.35	74.98	N			20.07	75.17	N		
			15541	22.94	20.67	9.74	24.46	22.20	10.83	24.49	69.28	[redacted]	-2.29	N	25.34	69.41	[redacted]	-2.44	N
Test11 (AM)	2	14	7047	5.80	5.41	2.62	7.21	6.84	3.65	6.63	86.28	N			7.56	86.43	N		
			9515	8.44	7.87	3.87	10.50	9.95	5.40	9.46	84.57	N			10.74	84.78	N		
			11787	11.47	10.67	5.19	14.27	13.49	7.24	12.86	82.41	N			14.60	82.62	N		
			15866	14.51	13.45	6.53	18.05	17.00	9.11	16.08	79.98	N	-1.14	N	18.21	80.13	N	-1.42	N
	3	14	6912	6.49	5.95	2.81	8.15	7.61	3.98	7.45	84.86	N			8.60	84.81	N		
			9200	9.53	8.79	4.15	11.97	11.24	5.88	10.94	82.97	N			12.59	83.04	N		
			11843	13.11	11.92	5.60	16.47	15.24	7.93	14.75	78.78	N			16.94	78.44	N		
			15850	16.81	15.23	7.22	21.12	19.48	10.23	18.46	75.25	N	-1.32	N	21.08	74.69	N	-1.65	N
	4	16	6817	6.72	5.80	2.70	8.76	7.71	4.05	7.36	81.28	N			8.68	80.09	N		
			9081	9.67	8.19	4.25	12.61	10.89	6.37	9.32	76.14	N			10.66	74.03	N		
			11592	12.96	11.27	5.76	16.90	14.99	8.64	12.93	74.27	N			14.82	72.34	N		
			15466	16.60	14.80	7.43	21.64	19.68	11.14	17.07	73.30	N	-0.89	N	19.59	71.89	N	-1.16	N
	5	17	6973	6.40	5.94	2.87	8.32	7.87	4.28	7.29	85.62	N			8.49	85.66	N		
			9351	9.25	8.37	4.07	12.03	11.09	6.07	10.16	81.66	N			11.79	81.07	N		
			11716	12.90	11.61	5.62	16.78	15.38	8.39	14.01	77.87	N			16.24	76.89	N		
			15715	16.62	15.09	7.31	21.61	19.99	10.91	17.96	75.69	N	-1.80	N	20.72	74.84	N	-2.35	N

With respect to void detection process, it is a common idea that the objective of surface deflection analysis would be limited to identify the uniformity of support qualitatively rather than to determine exact void dimensions. As a qualitative measure, a comparative examination on the estimated *k*-values can be used for the identification of voids. Figure E-52 shows a comparison of *k*-values estimated at the corner of test slabs in test set 6 and test set 10. It is plotted with the results presented in Table E-9. Four plotting points in one slab represent *k*-estimates at the four different load levels. It is shown that decreased *k*-values are produced with the slabs containing void. Table E-11 presents a comparison on the *k*-values obtained at the center and corner of test slabs. Listed value for each slab is the averaged value of four estimates at four different load levels.

Table E-11 indicates explicitly that the support condition along the corner of test slabs is not uniform compared to that of centers. The ratio of *k*-values at corner to center is specified as a comparative index for the support condition. This relative support condition index can be used to identify slab corner in which weak subgrade or void exists. In the table, slab 4 and slab 5 show large decrease in *k*-values at corner and therefore less *k*-ratios than other slabs. This trend well matches to the physical condition of test slabs. Although slab 3 also contains void, it is upstream void under the neighboring corner of slab 2, not under the loading point. It must be remembered that the FWD loading plate was placed on the downstream only. Slabs 4 and 5 are containing voids right under the loading points. Slab 4 has downstream void and slab 5 has voids under both sides. An upstream void under unloaded slab would not significantly affect to the response of loaded corner. As a consequence, the *k*-value from the corner of slab 3 shows moderate decrease compared to the slabs containing downstream voids. If a test is intended to

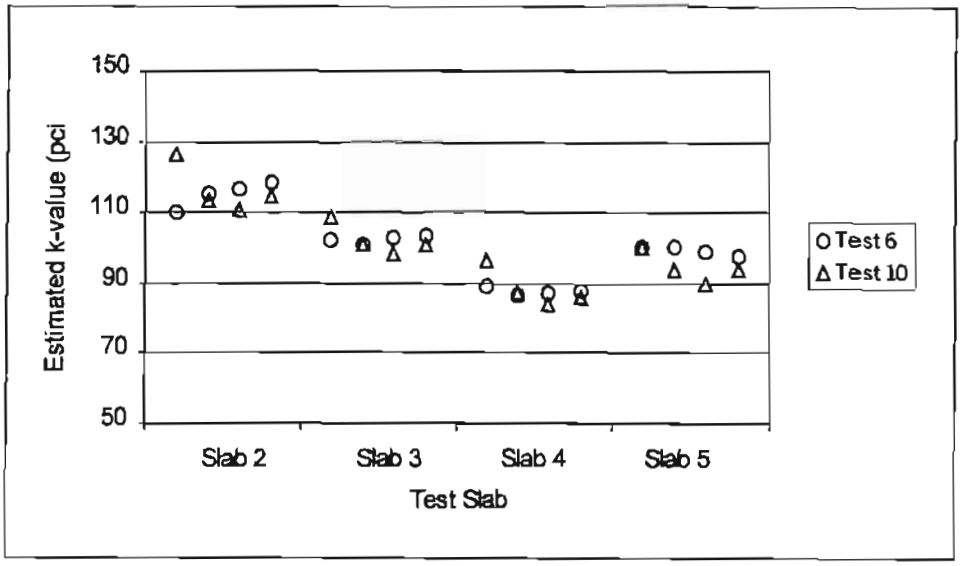

Figure E-52. Comparison of the estimated k-values of test slabs at each load level in test set 6 and test set 10

Table E-11. Comparison of averaged *k*-estimates from slab center and corner

Test set	Slabs	Void	*k*-estimates (pci)		*k*-ratio (corner/center)
			Center*	Corner**	
Test 5 & Test 6	Slab 2	No	139.8	115.2	0.824
	Slab 3	Yes	141.9	102.6	0.723
	Slab 4	Yes	138.7	87.7	0.632
	Slab 5	Yes	139.4	99.3	0.712
Test 9 & Test 10	Slab 2	No	127.9	116.3	0.909
	Slab 3	Yes	123.9	102.2	0.825
	Slab 4	Yes	128.0	88.5	0.691
	Slab 5	Yes	137.6	94.7	0.688

* Refer to Table E-6,

** Refer to Table E-9

investigate both side of a joint, the test should be performed on both of the up and downstream corners.

The *k*-ratio itself, however, would not be a proper index for the criteria. Its range varies depending on the structural system of pavements. For instance, the *k*-ratio in the control slab was greater than unity (Table E-5), while the test slabs have the ratios below 1.0. Rather the relative difference of *k*-ratios to a control value would be consistence even in different pavement structures. Provided known physical condition of subgrade, it is clear to select control value of *k*-ratio. For the test slabs the control value would be the ratio of slab 2, since it is known that slab 2 has sound subgrade. But in general, the control *k*-ratio should be determined based on the trend of *k*-ratio of whole test section.

The change of *k*-ratio in test slabs is shown in Figure E-53. Each plotting point represents calculated ratio of *k*-values at corner to center at four different load levels. The solid line is the trend of average *k*-ratio along the test slabs. As the ratio of slab 2 being a control value, other slabs have lower *k*-ratio than the control value. Slab 3 has an upstream void under the unloaded corner and the *k*-ratio for the loaded corner of slab 3 is about 10% less than the control value. Slab 4 and slab 5 have voids under the loaded corner so that they produced more greatly decreased *k*-ratios than slab 3. In general, the *k*-ratios of slabs 4 and 5 show more than 20% decrease relative to the control value. From this observation it is concluded that locally weakened subgrade or void exists when the *k*-ratio is less than 20% of control value. It is also indicated that voids under unloaded corner do not significantly affect to the evaluation of loaded corner.

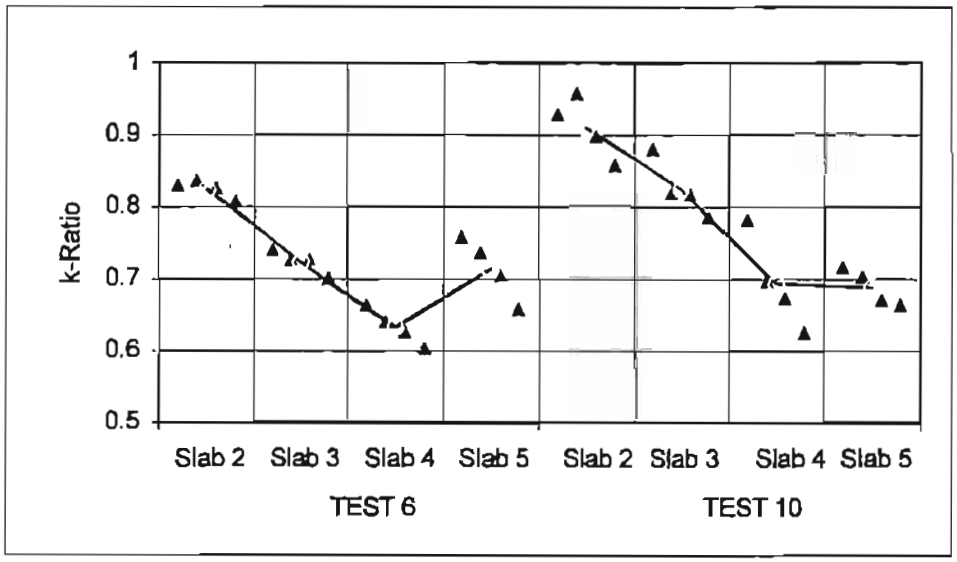

Figure E-53. Changes in *k*-ratio along the test slabs

US 287

Proposed evaluation process is applied to the deflection data of in-service highway, US 287. The US 287 data contains three groups. One is measured at the slab center and other is measured at the slab corner of joints in good condition. As the third data group, another corner deflections were measured at joints in poor condition. For the convenience of comparison, six sections from each group were selected for the evaluation such that the sections are neighboring to each other. Pavement layer consists of 10" PCC slab, 4" cement treated base (CTB) and subgrade. Two different load levels were applied to every test points. The FWD used in US 287 also has rear extension bar so that the 4^{th} geophone is placed 12" behind the center of loading plate.

Table E-12 presents the measured center deflections and corresponding pavement evaluations. The results from RMODS are also included in the table for comparison. Figure E-54 shows the trends of averaged k and E_c estimates along the test points. Both evaluation tools produced close results, though the variance of estimates in RMODS is somewhat higher than the proposed method.

The evaluation from corner deflection measurements is presented in Table E-13. Among the analysis of corner deflections at poor joints, negative non-dimensional maximum deflection, $\Delta 1$, was produced for the slabs at 59, 120, and 180R1. Negative non-dimensional maximum deflection invokes also meaningless negative k-value. This strange result in fact conforms to the physical condition of given joints. Most of joints in poor condition have structural deterioration at the joint such as cracks, corner break or through thickness patching. Under this condition, a slab is no longer continuous or linear system and therefore the proposed evaluation process, which assumes the geometry of a slab is to be continuous within given dimension, will be limited

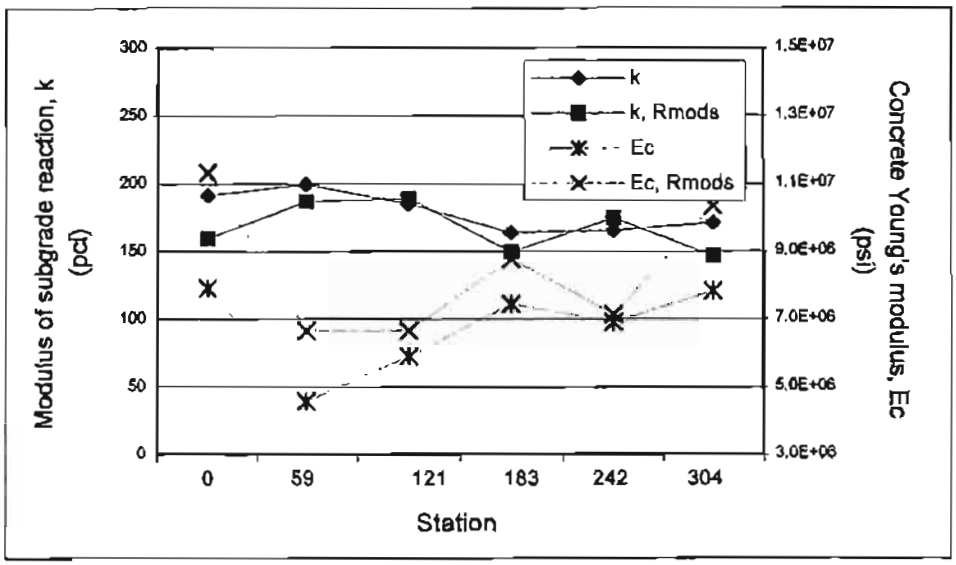

Figure E-54. Trends along stations for k and Ec estimates at slab centers in US 287

Table E-12. Evaluation of test sections in US 287 from the center deflection measurement

Station	Load	Deflections (mils)							Evaluation						RMODS	
	(lbs)	d-12	d0	d12	d24	d48	d60	d72	AREA	l (in)	a/l	Dell	k (pci)	Ec (psi)	k (pci)	Ec (psi)
0R1	6638	1.97	2.24	2.02	1.81	1.29	1.08	0.85	49.795	42.27	0.140	0.119	196.8	7.37E+06	146.0	1.28E+07
	9717	2.93	3.25	2.99	2.69	1.93	1.62	1.26	50.935	44.38	0.133	0.123	186.4	8.48E+06	173.5	9.86E+06
59R1	6666	2.52	2.63	2.35	2.02	1.39	1.20	0.94	47.681	38.67	0.153	0.112	189.1	4.96E+06	170.8	6.93E+06
	9693	3.66	3.76	3.36	2.88	1.81	1.56	1.16	46.005	36.10	0.163	0.106	210.6	4.20E+06	203.2	6.41E+06
121R1	6694	2.36	2.52	2.29	1.99	1.38	1.17	0.90	48.690	40.34	0.146	0.115	187.5	5.82E+06	189.0	6.73E+06
	9713	3.44	3.67	3.34	2.93	2.02	1.73	1.31	48.997	40.86	0.144	0.116	183.6	6.01E+06	190.0	6.62E+06
183R1	6634	2.30	2.50	2.34	2.03	1.49	1.26	1.06	51.168	44.83	0.132	0.124	163.3	7.73E+06	149.0	8.76E+06
	9713	3.40	3.73	3.46	3.02	2.19	1.83	1.56	50.670	43.88	0.134	0.122	164.7	7.16E+06	150.0	8.79E+06
242R1	6594	2.36	2.58	2.37	2.11	1.54	1.25	1.02	50.674	43.89	0.134	0.122	161.6	7.03E+06	193.3	5.97E+06
	9645	3.30	3.70	3.40	3.02	2.12	1.79	1.46	50.205	43.01	0.137	0.120	169.2	6.79E+06	156.1	8.32E+06
304R1	6543	2.14	2.39	2.15	1.89	1.47	1.29	1.07	51.264	45.01	0.131	0.124	167.6	8.07E+06	139.1	1.09E+07
	9621	3.16	3.48	3.16	2.78	2.06	1.75	1.56	50.655	43.85	0.135	0.122	175.0	7.59E+06	153.9	9.77E+06

Table E-13. Evaluation of test sections in US 287 from the corner deflection measurements

Test Point		Load	Deflections (mils)							Evaluation							CTR			NCHRP	
		(lbs)	d-12	d0	d12	d24	d48	d60	d72	AREA	LTE	l (in)	a/l	Dell	k (pci)	Ec (psi)	Q	M	Void	x-int	Void
Joint (good)	0R1	6729	3.26	5.29	3.79	2.98	1.70	1.26	0.94	34.45	0.65	28.40	0.208	0.221	349.1	2.66E+06	6.77	75.96	N		
		9701	4.62	7.59	5.43	4.26	2.48	1.86	1.37	34.59	0.64	28.58	0.206	0.231	361.4	2.83E+06	9.60	70.20	N	0.08	N
	62R1	8434	3.45	4.07	3.21	2.65	1.69	1.45	1.11	40.57	0.89	37.00	0.159	0.380	575.9	1.27E+07	5.00	81.84	N		
		11310	4.98	6.03	4.73	3.97	2.51	2.03	1.61	40.40	0.87	36.72	0.161	0.382	531.2	1.13E+07	7.41	77.77	N	-1.68	N
	121R1	6785	3.52	4.40	3.61	2.91	1.83	1.47	1.13	40.79	0.84	37.35	0.158	0.398	439.5	1.00E+07	5.90	82.50	N		
		9840	5.22	6.47	5.37	4.35	2.69	2.15	1.65	41.06	0.85	37.81	0.156	0.402	427.9	1.03E+07	8.81	79.61	N	-0.20	N
	181R1	6837	3.27	3.83	3.23	2.72	1.77	1.43	1.09	43.41	0.90	41.96	0.141	0.438	443.6	1.61E+07	5.10	84.29	N		
		9935	4.92	5.73	4.84	4.09	2.68	2.17	1.69	43.72	0.90	42.54	0.139	0.442	423.3	1.63E+07	7.48	81.56	N	-0.36	N
	241R1	7524	3.67	4.16	3.58	3.00	1.89	1.48	1.17	43.44	0.93	42.02	0.140	0.431	441.3	1.61E+07	5.73	84.48	N		
		10317	5.41	6.09	5.31	4.44	2.80	2.24	1.76	44.01	0.94	43.10	0.137	0.439	400.6	1.62E+07	8.41	82.59	N	-1.04	N
	301R1	6737	2.70	2.99	2.65	2.25	1.43	1.26	0.93	45.71	0.95	46.54	0.127	0.464	482.2	2.65E+07	4.10	86.76	N		
		9717	4.00	4.41	3.92	3.37	2.20	1.87	1.39	46.38	0.95	47.98	0.123	0.473	452.6	2.81E+07	6.02	85.33	N	-0.22	N
Joint (poor)	0R1	6920	2.40	3.85	2.98	2.35	1.45	1.18	0.87	38.09	0.66	33.21	0.178	0.370	602.5	8.59E+06	5.02	81.75	N		
		9709	3.51	5.50	4.36	3.43	2.07	1.67	1.25	38.52	0.67	33.83	0.174	0.379	584.8	8.99E+06	7.38	79.24	N	-0.24	N
	59R1	7151	3.23	8.71	4.09	3.17	1.79	1.42	0.99	24.52	0.39	18.15	0.325	-1.147	0.0	N/A	7.36	52.40	N		
		9709	4.66	11.09	5.90	4.59	2.56	2.05	1.40	26.96	0.44	20.45	0.289	-0.525	0.0	N/A	10.62	49.14	N	2.06	[redacted]
	120R1	6539	2.44	7.02	4.41	3.14	1.24	0.98	0.85	27.17	0.37	20.65	0.286	-0.466	0.0	N/A	8.44	66.49	N		
		9494	3.83	9.83	6.37	4.52	1.76	1.43	1.21	27.76	0.41	21.22	0.278	-0.372	0.0	N/A	12.13	60.03	N	0.80	N
	180R1	6447	1.61	11.56	6.55	5.02	2.70	1.95	1.40	27.57	0.15	21.03	0.281	-0.340	0.0	N/A	12.11	50.14	N		
		9379	2.88	14.15	8.64	6.62	3.60	2.61	1.92	29.36	0.21	22.79	0.259	-0.093	0.0	N/A	15.64	47.44	N	5.87	[redacted]
	242R1	7198	2.01	5.76	4.28	3.37	1.89	1.44	1.14	35.54	0.37	29.76	0.198	0.343	484.0	4.46E+06	7.45	76.14	N		
		9764	3.11	7.99	6.11	4.83	2.75	2.14	1.69	36.74	0.41	31.33	0.188	0.382	476.1	5.38E+06	10.44	72.60	N	-0.50	N
	303R1	6575	1.23	9.67	7.02	4.52	2.47	1.96	1.50	31.09	0.13	24.59	0.240	0.111	124.4	5.33E+05	12.95	66.17	N		
		9494	1.83	12.40	9.24	6.00	3.42	2.63	1.99	32.12	0.16	25.71	0.229	0.192	222.7	1.14E+06	16.81	62.23	N	3.52	[redacted]

in its application. This physical constraint also can be observed from deflection basins. Figures E-55 and E-56 show corner deflection basins at load level 2 obtained from the joints in good and bad conditions, respectively. For the measurements in poor joints, near joint deflections of loaded side is much greater than those of the joints in good condition. Subsequently, the deflection basins of poor joints exhibit abrupt slope changes near the joint. Considering high stiffness of concrete, this abrupt slope change might be interpreted as the concrete slab has geometrical non-linearity around the inflection point. Since the proposed evaluation process can not take account this geometric non-linearity, the *k*-value is replaced with zero in this case and further analysis for E_c is halted.

Table E-13 also contains the results of void detection using the CTR and NCHRP methods. As shown, no void was detected in the good joints. Even for the poor joints, the CTR method does not indicate any void. Here it needs to be noted that the applied load is not high enough for effective void evaluation. As stated in the previous section, applied load should be around 16000 lbs. for effective use of the CTR method. The NCHRP method produced three voided corners out of six poor joints. They are the points at station 59R1, 180R1 and 303R1. Referring to Figure E-56, the three highest maximum deflections are produced at these three points and their precedence coincides with the order of x-axis interception in the points (Table E-13).

To apply the proposed method of void detection, the ratio of *k*-center (Table E-12) and *k*-corner (Table E-13) was calculated for each test points and compared to each other. For the calculation of *k*-ratio, it is assumed that *k*-values at the center of neighboring test points are identical. Figure E-57 presents calculated *k*-ratios for each test points. The control value of *k*-ratio should be determined in such a way that it may provide the allowable lower limit as to the

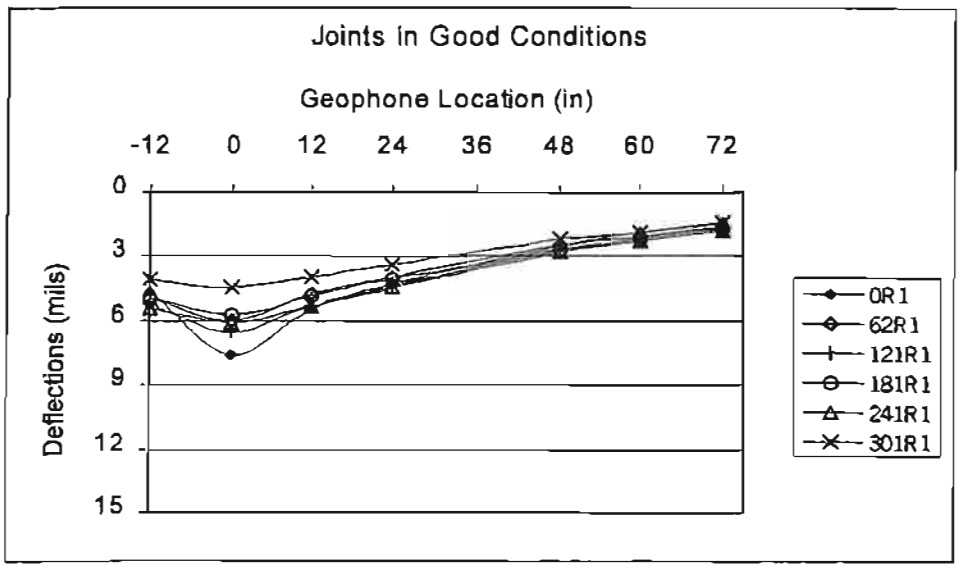

Figure E-55. Corner deflection basins from the joint in good conditions, US 287

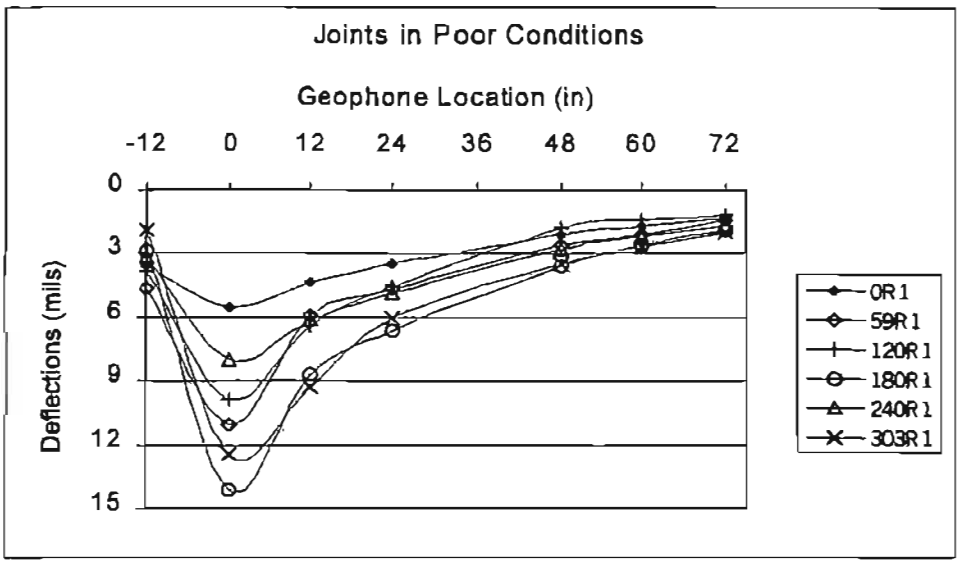

Figure E-56. Corner deflection basins from the joint in poor conditions, US 287

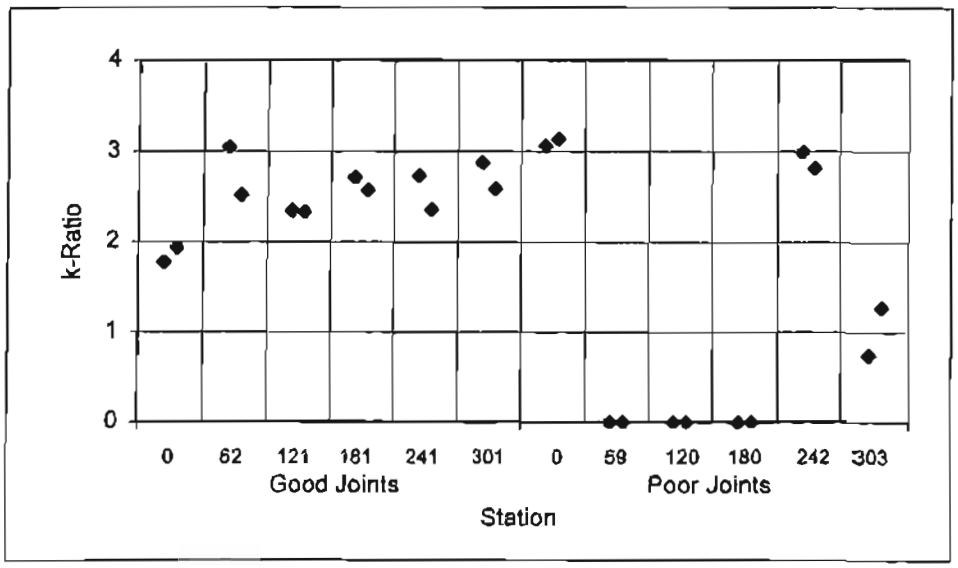

Figure E-57. Changes in *k*-ratio along the test sections in US 287

normal support condition. Figure E-57 indicates that the control *k*-ratio would be around 2.0. According to the proposed method, therefore, the slab corners at the station of 59R1, 120R1, 180R1 and 303R1 in the poor joints are identified as voided. By the application of proposed method the point 120R1 is added as voided to the result of NCHRP method. This point in fact has great possibility of void based on its load-deflection behavior and corresponding analysis. The point produced next highest maximum deflection to the other three (Figure E-56). Its deflection basin exhibits excessive slope change (Figure E-58). For the convenience of comparison, selected deflection basins from the poor joints are repeatedly plotted in Figure E-58. Moreover the structural evaluation at that point produces zero subgrade modulus. These joined results highly indicate the possibility of void under the corner of slab at the station of 120R1, in addition to the other three possible slabs identified by the NCHRP method.

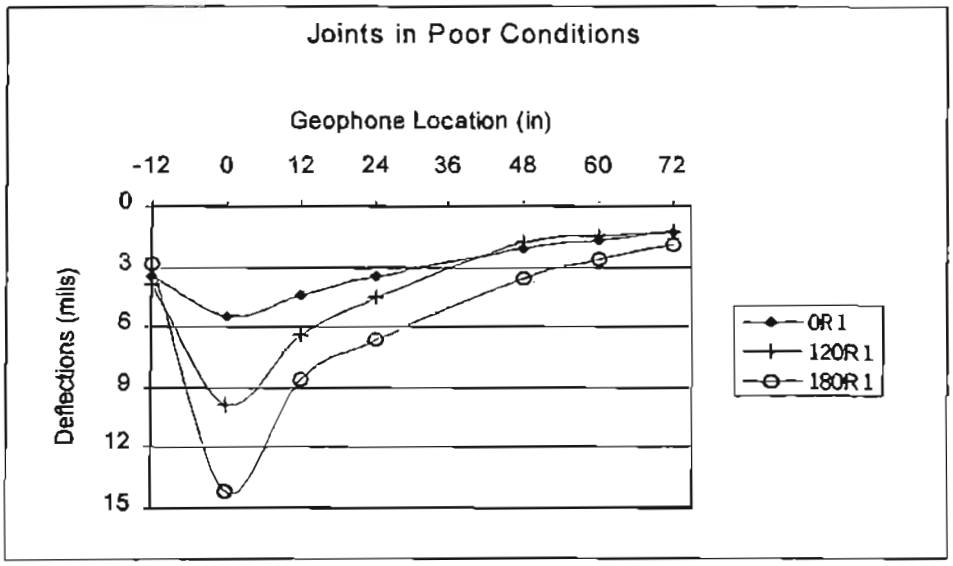

Figure E-58. Selected corner deflections at poor joints in US 287; Station 0R1, 120R1 and 180R1

REFERENCES

E-1 Ioannides, A. M., "Dimensional Analysis in NDT Rigid Pavement Evaluation," Journal of Transportation Engineering, ASCE, Vol. 116, No. 1, 1990, pp. 23-36.

E-2 Ricci, E. A., et al., "The Falling Weight Deflectometer for Nondestructive Evaluation of Rigid Pavements," Research Report 387-3F, Center for Transportation Research, The University of Texas, Austin, TX., Nov., 1985

E-3 Crovetti, J. A and Darter, M. I., "Void Detection Procedures," NCHRP Report 1-21, Appendix C, March 1985

E-4 Uzan, J., Kodavali, S. and Scullion, T., "Rigid Pavement Evaluation System: Implementation of RMODS," Research Report1939-3F, Texas Transportation Institute, Texas A&M University, College Station, TX., Nov., 1995

E-5 Westergaard, H. M., "Computation of Stresses in Concrete Roads," HRB Proceedings, 5th Annual Meeting, Vol. 5, Part I, 1926, pp. 90-112.

E-6 Westergaard, H. M., "New Formulas for Stresses in Concrete Pavements of Airfields," Transactions, ASCE, Vol. 113, 1948, pp. 425-439

E-7 Hoffman, M. S. and Thompson, M. R., "Mechanistic Interpretation of Nondestructive Testing Deflections," Civil Engineering Studies, Transportation Engineering Series No. 32, University of Illinois, Urbana, IL, 1981